UNIVERSITÉ LIBRE DE BRUXELLES
Faculté des Sciences
Département de Physique

Neutron measurements in a proton therapy facility and comparison with Monte Carlo shielding simulations

Thèse présentée par

Valérie De Smet

En vue de l'obtention du grade de

Docteur en Sciences

Bruxelles, 2016

Research conducted at the

Interuniversity Institute for High Energies (IIHE),
Université Libre de Bruxelles (ULB), Belgium,

in association with

Ion Beam Applications (IBA),
Louvain-la-Neuve, Belgium.

Doctoral examination commission:

Prof. Dr. Gilles De Lentdecker (supervisor)
        IIHE, ULB

Dr. Frédéric Stichelbaut (co-supervisor)
        IBA

Prof. Dr. Laurent Favart (president)
        IIHE, ULB

Prof. Dr. Alain Dubus (secretary)
        Ecole Polytechnique de Bruxelles, ULB

Prof. Dr. Nicolas Pauly
        Ecole Polytechnique de Bruxelles, ULB

Dr. Marco Silari
        CERN

Acknowledgements

Abstract

Proton therapy uses proton beams with energies of 70 – 230 MeV to treat cancerous tumours very effectively, while preserving surrounding healthy tissues as much as possible. During nuclear interactions of these protons with matter, secondary neutrons can be produced. These neutrons can have energies ranging up to the maximum energy of the protons and can thus be particularly difficult to attenuate. In fact, the rooms of a proton therapy facility are generally surrounded by concrete walls of at least ~2 m in thickness, in order to protect the members of the staff and the public from the stray radiation. Today, the design of the shielding walls is generally based on Monte Carlo simulations. Amongst the numerous parameters on which these simulations depend, some are difficult to control and are therefore selected in a conservative manner. Despite these conservative choices, it remains important to carry out accurate neutron dose measurements inside proton therapy facilities, in order to assess the effectiveness of the shielding and the conservativeness of the simulations. There are, however, very few studies in literature which focus on the comparison of such simulations with neutron measurements performed outside the shielding in proton therapy facilities. Moreover, the published measurements were not necessarily acquired with detectors that possess a good sensitivity to neutrons with energies above 20 MeV, while these neutrons actually give an important contribution to the total dose outside the shielding. A first part of this work was dedicated to the study of the energy response function of the WENDI-2, a rem meter that possesses a good sensitivity to neutrons of more than 20 MeV. The WENDI-2 response function was simulated using the Monte Carlo code MCNPX and validation measurements were carried out with ^{252}Cf and AmBe sources as well as high-energy quasi-monoenergetic neutron beams. Then, WENDI-2 measurements were acquired inside and outside four rooms of the proton therapy facility of Essen (Germany). MCNPX simulations, based on the same conservative choices as the original shielding design simulations, were carried out to calculate the neutron spectra and WENDI-2 responses in the measurement positions. A relatively good agreement between the simulations and the measurements was obtained in front of the shielding, whereas overestimates by at least a factor of 2 were obtained for the simulated responses outside the shielding. This confirmed the conservativeness of the simulations with respect to the neutron fluxes transmitted through the walls. Two studies were then carried out to assess the sensitivity of the MCNPX simulations to the defined concrete composition and the selected physics models for proton and neutron interactions above 150 MeV. Both aspects were found to have a significant impact on the simulated neutron doses outside the shielding. Finally, the WENDI-2 responses measured outside the fixed-beam treatment room were also compared to measurements acquired with an extended-range Bonner Sphere Spectrometer and a tissue-equivalent proportional counter. A satisfactory agreement was obtained between the results of the three measurement techniques.

Résumé

La protonthérapie utilise des faisceaux de protons de 70 – 230 MeV pour traiter efficacement des tumeurs cancéreuses tout en préservant le plus possible les tissus sains environnants. Lors d'interactions nucléaires de ces protons avec la matière, des neutrons peuvent être produits. Ceux-ci peuvent avoir jusqu'à l'énergie maximale des protons et être particulièrement difficiles à atténuer. Pour cette raison, les salles d'un centre de protonthérapie sont généralement entourées de murs de béton d'environ 2 m d'épaisseur au minimum, afin de protéger le personnel et le public. Aujourd'hui, le dimensionnement des murs de blindage s'effectue souvent à partir de simulations Monte Carlo. Parmi les nombreux paramètres dont dépendent ces simulations, certains sont difficilement maîtrisables et sont dès lors choisis de manière conservative. Malgré cette démarche conservative, il est important d'effectuer des mesures exactes de doses neutrons dans les centres de protonthérapie, afin de valider l'efficacité des blindages et d'évaluer le caractère conservateur des simulations. Dans la littérature, des études portant sur la comparaison de ce type de simulations avec des mesures de neutrons effectuées autour des salles sont très peu nombreuses. En outre, certaines mesures présentées ont été effectuées avec des détecteurs qui ne possèdent pas une bonne sensibilité aux neutrons de plus de 20 MeV, alors que ces derniers contribuent de manière importante à la dose totale derrière le blindage. Les travaux présentés dans cette thèse portent premièrement sur l'étude de la réponse en énergie du WENDI-2, un rem meter possédant une bonne sensibilité aux neutrons de plus de 20 MeV. La fonction de réponse du WENDI-2 a été simulée à l'aide du code Monte Carlo MCNPX et des mesures de validation de cette fonction ont été effectuées avec des sources d'AmBe et ^{252}Cf ainsi qu'avec des faisceaux quasi-monoénergétiques de haute énergie. Des mesures ont ensuite été acquises avec un WENDI-2 à l'intérieur et autour de quatre salles du centre de proton thérapie d'Essen (Allemagne), et des simulations de ces salles ont été réalisées avec le code MCNPX pour calculer les spectres de neutrons et la réponse du WENDI-2 aux positions de mesure. Un assez bon accord entre mesures et simulations a été obtenu en amont des blindages tandis que, en aval de ceux-ci, les résultats de simulation surestiment les mesures d'au moins un facteur 2, ce qui confirme le caractère conservateur des simulations pour la transmission des neutrons au travers des murs. Deux études ont ensuite été réalisées pour évaluer la sensibilité des simulations MCNPX à la composition de béton sélectionnée et au choix des modèles physiques utilisés pour les interactions des protons et neutrons de plus de 150 MeV. Ces deux aspects peuvent influencer de manière significative les doses neutrons simulées derrière les blindages. Enfin, les mesures du WENDI-2 effectuées autour de la salle à faisceau fixe ont également été comparées à des mesures effectuées avec un compteur proportionnel équivalent-tissus et un système de spectrométrie par sphères de Bonner étendu au domaine des hautes énergies. Un accord très satisfaisant a été obtenu entre les résultats des trois systèmes de mesure.

Contents

CHAPTER I
Introduction

I-1 Introduction to proton therapy

I-1.1 Cancer

Deoxyribonucleic acid (DNA) is a long macromolecule that contains all the instructions for the development and functioning of a living cell. Lasting alterations of the DNA structure, called mutations, can occur either spontaneously or due to external factors such as radiation or chemicals [1]. Mutations can sometimes cause a cell to start proliferating in an uncontrolled way, initiating a growth of abnormal cells called 'tumour' [2].

Cancer is the potentially fatal disease that arises from the development of a *malignant* tumour. Malignancy is defined as the capacity to invade adjoining normal tissues and to create new tumours at distant sites (metastases) by spreading via the circulatory or lymphatic system [2].

Cancer is a major cause of morbidity and mortality in the world. According to the World Health Organization, about 14 million new cancer cases and 8.2 million cancer-related deaths were reported in 2012 and the number of annual new cancer cases is expected to rise to approximately 22 million over the next two decades [3]. Continuing to improve the prevention and the treatment of cancer is thus of paramount importance.

Cancer treatment is most often based on surgery, radiation therapy, drugs, or a combination of these [4][5]. Radiation therapy and surgery constitute local treatments. Drugs, however, are mainly used as a whole body treatment for cancers with metastases (chemotherapy). The choice of the treatment depends on many factors which include:

- the type and location of the cancer,
- the stage of the disease,
- the patient's age and general health.

I-1.2 General aspects of radiation therapy

I-1.2.1 General principle

When traversing matter, ionizing radiation deposits energy in discrete amounts of energy, which cause either the excitation or the ionization of the hit atoms or molecules. The excitation is the process in which a bound electron is raised into a higher energy level. In the ionization, however, an electron receives enough energy to be ejected from the atom or molecule. The most important impact of ionizing radiation on living cells is, as the name suggests, caused by the induced ionizations [6], as they result in the breaking of molecular bonds and the creation of free radicals. The latter, which are highly reactive chemical species, rapidly cause damage to nearby molecules as well.

With respect to cell death caused by ionizing radiation, the chromosomal DNA is regarded as the most vulnerable target within a mammalian cell [7][8]. The first reason for this is that the DNA contains the instructions for all cellular functions, including its own repair mechanisms. The second is that the cell only contains two copies of the DNA, which moreover cannot be as quickly regenerated as other types of biomolecules numerously present in the cell. Cell death can occur when the repair mechanisms fail to correctly repair critical DNA sequences, either because these mechanisms were altered or because they are overtaken by the high damage rate [8].

Radiation therapy uses ionizing radiation with the aim to kill tumour cells while preserving as much as possible the surrounding normal tissues [9]. Limiting the ionizations inside the surrounding healthy tissues is important in order to reduce the side-effects of the therapy. These include not only rapidly manifesting effects (e.g. nausea, fatigue, skin problems *etc.*), but also the risk of developing late effects such as, for instance, second cancers [10].

I-1.2.2 Main types of radiation therapy

Radiation therapy techniques can be classified according to the type of ionizing radiation and the delivery method used. In some techniques, such as e.g. brachytherapy [11] and unsealed radionuclide therapy [12], a radioactive source is introduced inside the patient's body. More common, however, is external beam radiotherapy, in which the radiation source is located outside the body [13].

Today, the most widespread form of radiation therapy is external beam therapy based on megavoltage X-rays (1 – 25 MVp) produced with a linear electron accelerator [13]. To treat superficial tumours, X-ray photons of lower maximum energies (50 – 500 kVp) produced with an X-ray tube, are also used.

Other types of external beam therapy use for instance gamma photons, electrons (4 MeV – 25 MeV [14]) or specific hadrons, such as e.g. protons (50 MeV – 250 MeV [10]), neutrons and heavy ions (e.g. carbon ions of 100 – 450 MeV/u). Amongst hadron therapies, the most common form today is proton therapy [15].

I-1.3 Physics of radiation therapy

I-1.3.1 Fluence

An important quantity which is used to describe the number of particles at a given point in an ionizing radiation field is the particle fluence (or 'fluence') Φ, defined as "the quotient of dN by da, where dN is the number of particles incident upon a small sphere of cross-sectional area da" [16–18]:

$$\Phi = \frac{dN}{da}$$

This quantity is expressed in units of m^{-2}. Since the definition considers a spherical surface, the fluence is independent of the direction in which the individual particles are moving. Also, the fluence refers to a given exposure (of a given duration), which should be specified when stating a value of fluence.

The time-derivative of the fluence is called the fluence rate, the flux density or simply, as in the rest of this work, the flux.

To describe the energy-distribution of the particles which constitute the radiation field, one usually uses the spectral fluence, which is the energy-derivative of the fluence. The spectral fluence given as a function of energy is commonly referred to as the 'energy spectrum', or simply the 'spectrum'.

I-1.3.2 Absorbed dose

Generally, the biological effects of exposure to ionizing radiation are to a certain degree related to the energy deposited by the radiation per unit mass of the irradiated tissues, a quantity which is called 'absorbed dose' (or 'dose'). According to the International Commission on Radiation Units and measurements (ICRU), the absorbed dose D at a point P is formally defined as:

$$D = \frac{d\bar{\varepsilon}}{dm} \quad \left[Gy = \frac{J}{kg} \right]$$

where $d\bar{\varepsilon}$ is the statistical average of the energy imparted by the ionizing radiation to the matter of mass dm around P [17]. The mass element dm in this definition is a very small mass but does not approach zero in the mathematical sense, because it is supposed to include many atoms or molecules [17]. The energy imparted ε to a finite

volume *V* of matter during a finite period of time is a stochastic quantity defined as [17]:

$$\varepsilon = \mathrm{R}_{in} - \mathrm{R}_{out} + \mathit{\Sigma}\mathrm{Q} \quad [\mathrm{J}] \qquad (\mathrm{I}.1)$$

in which

R_{in} = the sum of the energies, excluding rest energies, of all charged and uncharged particles entering *V*,

R_{out} = the sum of the energies, excluding rest energies, of all charged and uncharged particles leaving *V*,

ΣQ = the net energy derived from rest mass variations within *V*. ΣQ is positive if the sum of rest masses decreases and negative for the reverse process.

On a practical level, the mean energy imparted $d\bar{\varepsilon}$ can simply be regarded as the mean energy lost by charged particles in causing ionizations and excitations inside d*m*, This stems from the mechanisms in which ionizing particles – charged or uncharged – interact with matter at the energies of interest here:

- ***Charged particles*** – including the very light ones, like electrons, as well as the 'heavy' charged particles such as protons, α-particles, carbon ions, etc. – interact with the traversed medium mostly through Coulomb interactions with orbital electrons [19]. The majority of these interactions are glancing collisions, also called 'soft' collisions, in which the energy lost by the incident charged particle is small (a few eV or, at most, a few tens of eV). This transferred energy is expended either in the excitation of the hit atom or in the ejection of one of its valence electrons, which receives little kinetic energy. In the worst case, the ejected electron can cause a few excitations or ionizations very close to the original ion, in a local cluster. Often, however, the electron just loses energy by causing interatomic motion (heat production), before being captured. Therefore, in the initial soft collision, the energy lost by the incident charged particle is considered as locally absorbed by the medium: it directly results in absorbed dose. At rare occasions, when interacting with a single orbital electron instead of with the atom as a whole, the initial charged particle undergoes a knock-on ('hard') collision, in which it loses a significant fraction of its kinetic energy. An inner electron of the hit atom can then be ejected and may receive sufficient kinetic energy (at least ~100 eV) to produce its own significant track of excitations and ionizations through the medium. In these rather infrequent cases, the energy lost by the initial charged particle is not locally absorbed by the medium, but deposited elsewhere by the secondary electron called 'δ-ray'. However, because δ-rays are relatively rare [20], charged particles are commonly regarded as *directly ionizing radiation* [21]. Figure **I-1** schematically illustrates a track of ionizations and excitations caused by a charged particle that traverses matter.

- **_Uncharged particles_**, such as photons and neutrons, are called _indirectly ionizing radiation_ because they barely ionize the medium themselves, but undergo interactions in which at least one energetic secondary charged particle is released [21]. The secondary charged particles will lose their kinetic energy as described above, by causing several excitations and ionizations along their track. Generally speaking, the absorbed dose due to the incident uncharged particles is not delivered in the points where these particles themselves interact but rather in the many interaction points of their secondary charged particles.
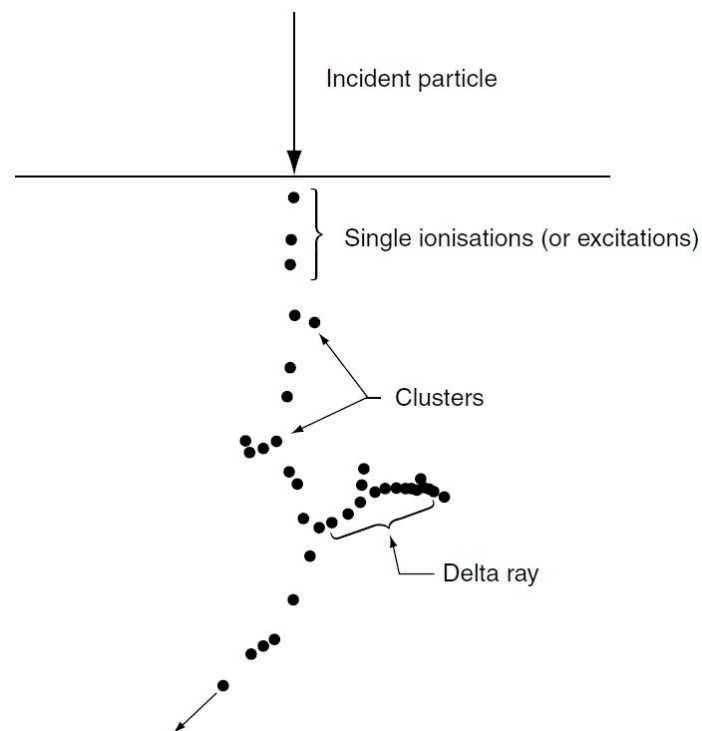
Figure I-1 - Schematic representation of a track of ionizations and excitations caused by a charged particle that traverses matter [22]_._

I-1.3.3 Energy loss mechanisms of charged particles

For charged particles used in radiation therapy, electromagnetic interactions with orbital electrons, causing ionizations and excitations, represent the most frequent interaction type. These interactions are responsible for the so-called 'collisional' energy losses of the charged particles.

When passing sufficiently close to an atomic nucleus, a charged particle may also interact with this nucleus instead of with an orbital electron. Most interactions of heavy charged particles with nuclei are electromagnetic in nature, although nuclear interactions are also possible (but less probable). We will come back on these nuclear interactions later, in Section **I-3.1**. Most of the electromagnetic interactions with

nuclei are elastic collisions. Since the differential elastic scattering cross-section strongly decreases for increasing scattering angles of the projectile, most single elastic scattering events only lead to a very tiny angular deflection and a negligible kinetic energy transfer to the nucleus. As for the infrequent inelastic collisions, the acceleration of the heavy charged particle in the electromagnetic field of the nucleus is not large enough to cause significant radiative energy losses through the production of *bremsstrahlung* (emission of X-ray photons) [23]. Thus, in the considered energy range, the energy losses of heavy charged particles due to interactions with atomic nuclei are generally considered to be negligible.

Electrons, which are much lighter particles, follow more tortuous paths through matter than heavy charged particles. Due to their light mass, they cannot transfer any significant amount of kinetic energy to a nucleus during elastic scattering. However, significant radiative energy losses through the emission of *bremsstrahlung* can occur in inelastic scattering events because the acceleration in the electromagnetic field of the nucleus is much larger than for a heavy charged particle. The intensity of these radiative losses increases with the energy of the incident electron and with the atomic number of the nucleus [23]. At high energies, e.g. above ~10 MeV in tungsten or above ~100 MeV in water [24], the emission of *bremsstrahlung* even becomes the most important energy loss mechanism for electrons.

I-1.3.4 Linear Energy Transfer of charged particles

The **stopping power *S*** is a quantity which describes the rate at which charged particles progressively lose their energy along their track through matter. It is defined as the average kinetic energy lost by the charged particle, -d*E*, per unit path length d*x* [25]:

$$S = -\frac{dE}{dx}$$

The stopping power can be expressed as the sum of the **collision stopping power** and the **radiative stopping power**, referring to the abovementioned collisional and radiative energy losses (see Section **I-1.3.3**).

The collision stopping power, also called the **'Linear Energy Transfer' (LET)**, is thus the average kinetic energy lost by a charged particle per unit path length due to ionizations and excitations. Note that for heavy charged particles in the therapeutic energy range, the stopping power is approximately equal to the LET, since the radiative losses are completely negligible.

The LET of charged particles is obviously closely related to the concept of dose. The absorbed dose *D* due to charged particles can indeed be calculated from the LET as follows [22]:

$$D = \frac{1}{\rho} \int \frac{d\Phi}{dE}(E) \, S_{coll}(E) \, dE$$

where $S_{coll}(E)$ is the LET as a function of energy, $(d\Phi/dE)(E)$ is the energy spectrum of the fluence, and ρ is the density of the material.

The energy dependence of the LET is accurately described by the well-known modern version of the Bethe-Bloch formula [26]. In the figure **I-2,** the LET divided by the density, also called the **mass collision stopping power**, is shown as a function of energy for electrons, protons and carbon ions (^{12}C)$^{6+}$ passing through liquid water.
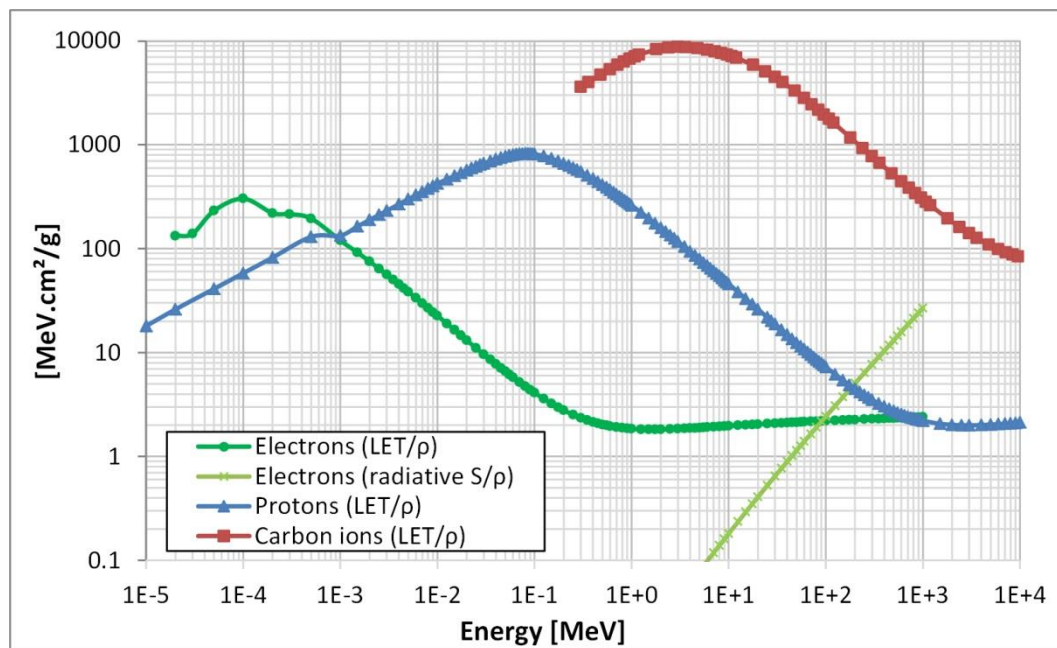
Figure I-2 - Mass collision stopping power in liquid water for electrons (values below 1 keV from [22], values above 1 keV from [24]), protons (values below 1 keV from [22], values above 1 keV from [27]) and carbon ions [28], and mass radiative stopping power in liquid water for electrons [24].

I-1.3.5 Range of charged particles

The **range *R*** of a charged particle of a given type, with a given initial energy, inside a given medium, is the expectation value of the path length that it follows until it comes to rest (discounting thermal motion) [29]. *R* is thus an average value, defined for a beam of particles. The corresponding **projected range <*t*>** is the expectation value of the farthest depth of penetration t_{max} of a particle in its initial direction [29].

The path of heavy charged particles, such as protons or carbon ions, is nearly a straight line. Most of the particles are progressively slowed down by means of many collisions with electrons, in which they do not suffer large angular deviations. Eventually, when they run out of energy, they get neutralized by picking up electrons from the medium. For a heavy charged particle beam, the path length of most

particles is almost equal to the range, which is not much larger than the projected range (see figure **I-3**).

Electrons, however, undergo more often large deviations in their collisions and their range may be much longer than their projected range, depending on the medium. For an electron beam, the distribution of projected path lengths is typically broader than for heavy charged particles.

Uncharged particles, such as neutrons and photons, tend to undergo fewer interactions with matter than charged particles and they do not necessarily lose their energy gradually. Details on photon interactions can be found in, for example, [30,31]. Neutron interactions will be discussed in section **I-3.3**. Unlike a charged particle, an uncharged particle has a significant probability of passing through a macroscopic layer of matter without interacting with it at all. A beam of uncharged particles does not have a finite range in matter. The beam fluence typically decreases as a function of depth in a progressive and exponential-like manner.
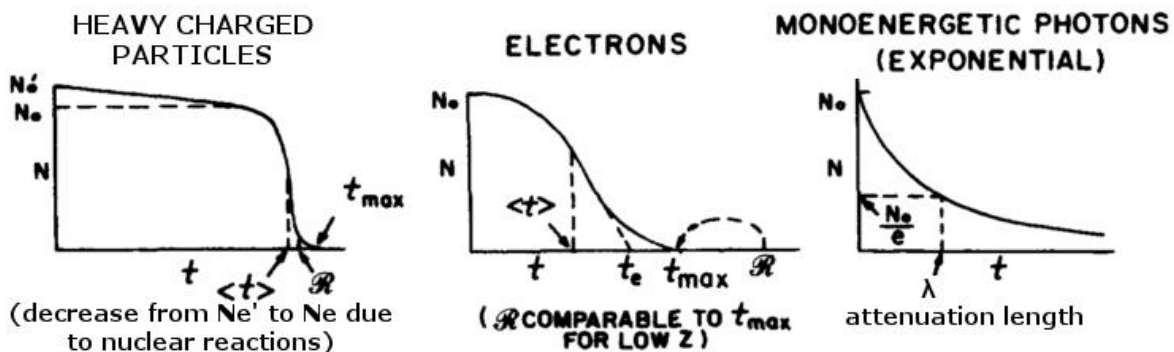
*Figure I-3 – Typical evolution of the particle fluence of an (initially) mono-energetic beam as a function of the depth t in an absorbing medium: for heavy charged particles (left), electrons (middle) and photons (right). For the charged particles, $\mathcal{R}$ represents the range and **<t>** the projected range. (adapted from [29]).*

I-1.3.6 Depth-dose distributions

Thanks to their energy loss mechanisms and well-defined range in matter, heavy charged particles have more advantageous depth-dose distributions for the treatment of deep-seated tumours than e.g. photons (see figure **I-4**). The LET of heavy charged particles progressively increases as the particles lose energy along their nearly straight path through the patient. As a consequence, the largest absorbed dose is delivered just before the end of their trajectory, in what is commonly called the Bragg peak. By selecting the appropriate initial energy of the particles, the range of the beam can be adjusted so that the Bragg peak falls into the tumour. Healthy tissues located at larger depths will be spared from dose deposition by the beam itself (primary particles). Only secondary particles, produced during the relatively infrequent nuclear reactions, will deliver a small dose to these tissues. Tissues located in front of the tumour inside the treatment field also benefit from a smaller dose

deposition than with a photon beam, because the maximum of the dose deposition by photons occurs at a relatively small depth (with the build-up of the secondary electrons). In short, using heavy charged particles instead of photons, for delivering a same dose to the tumour, can in principle result in a reduced total-body dose, and thus reduced side-effects for the patient.
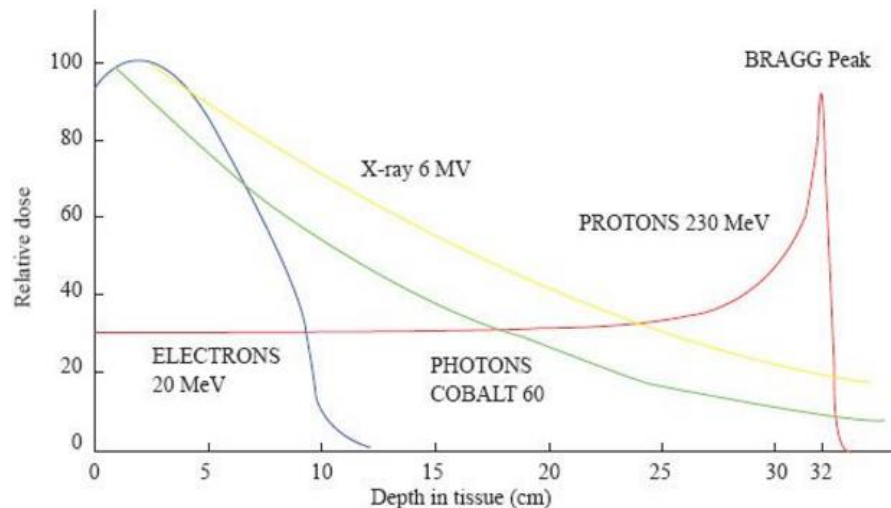
Figure I-4 – Relative depth-dose distributions of 230MeV protons (red), 6 MV X-ray photons (yellow), ^{60}Co gamma photons (green) and 20 MeV electrons (blue) [32].

Compared to protons, heavier ions (e.g. carbon ions) have a Bragg peak that is even sharper. The dose deposition beyond the distal edge of the Bragg peak is however significantly larger, because the nuclear interactions result in the fragmentation of the primary ions into lighter ions with long ranges. On the other hand, the lateral dose fall-off may be sharper than for protons thanks to reduced scattering. The main advantage of heavier ions is however related to their higher Relative Biological Effectiveness (see section **I-1.3.7**).

As for electrons, their depth-dose distribution is not a Bragg peak due to their tortuous paths in matter. It is rather a broad-peaked distribution, nevertheless with a rapid fall-off thanks to their finite range. Electron beams are particularly indicated for the treatment of superficial tumours extending into the patient's skin.

I-1.3.7 Relative Biological Effectiveness

In practice, the biological effects caused by ionizing radiation depend on more parameters than only the absorbed dose [33]. The dose rate and fractionation play for example an important role as well. The biological effects also typically depend on the LET of the radiation, which in turn depends on the type of particles, their energy and the density and composition of the tissue. For a same absorbed dose, radiation with a higher LET causes a higher ionisation density and the resulting cell damage tends to be more clustered and difficult to repair. Furthermore, because of biological reasons,

different tissues may react differently under identical irradiation conditions (some tissues being more radiosensitive than others).

The Relative Biological Effectiveness (RBE) is a ratio of the absorbed doses of two types of radiation producing the same specified biological effect in identical irradiation conditions [18]. In this definition, the denominator is the dose delivered by the radiation of interest (e.g. protons) while the numerator is the dose delivered by a reference radiation (of which the characteristics should be specified when giving the RBE value).

Because of the large clinical experience gained with photon therapy, such photon beams are typically used as a reference for the RBE of proton therapy beams. The prescribed doses in proton therapy are actually based on those of photon therapy. The proton beams are however more biologically effective than the photon beams and this is accounted for by means of the RBE. Although the RBE is not constant along the proton path, its variation with the LET is generally not calculated in the treatment planning. As a reasonable approximation, a single average value of 1.1 is used for simplicity. To determine the dose prescription of a proton treatment, the dose that would have been prescribed in photon therapy is thus divided by 1.1 [34].

Heavier ions used in hadron therapy have larger RBE values than protons (typical RBEs are in the range of 1.5 – 4) [35]. Such beams have the advantage of being more effective against particularly radio-resistant tumours. With heavier ions, the dependency of the RBE on the LET is however much stronger and needs to be taken into account in the treatment planning.

I-1.4 The advent of proton therapy

The idea of using accelerated protons and heavier ions in radiotherapy was first proposed in 1946 by Robert R. Wilson, from Harvard University [36]. The first treatments of patients with proton beams were started in 1954 at the Lawrence Berkeley Laboratory (California, USA) [37]. By the early 1990s, about ten nuclear physics research laboratories throughout the world were delivering proton therapy to patients [38].

The first hospital-based proton therapy facility was opened in 1990 at the Loma Linda University Medical Center (California) [39]. Since then, the number of new clinical facilities designed and built exclusively for proton therapy has been growing increasingly fast. According to the Particle Therapy Co-Operative Group (PTCOG), at the end of June 2015 the total number of operating proton therapy facilities around the world had reached 49 (including 15 in Europe [40]), while 32 new facilities were also under construction [41].

I-2 The proton therapy facility of Essen, Germany

Many of the measurements reported in this thesis were acquired at the West German Proton therapy facility of Essen (WPE). This centre was designed and equipped by Ion Beam Applications (IBA).

I-2.1.1 Structure of the facility

A floor plan of the Essen proton therapy facility is shown in figure **I-5**. This centre possesses:

- a ®C230 isochronous cyclotron,
- an Energy Selection System (ESS) and a beam transport line,
- 1 fixed-beam treatment room, and
- 3 gantry treatment rooms.
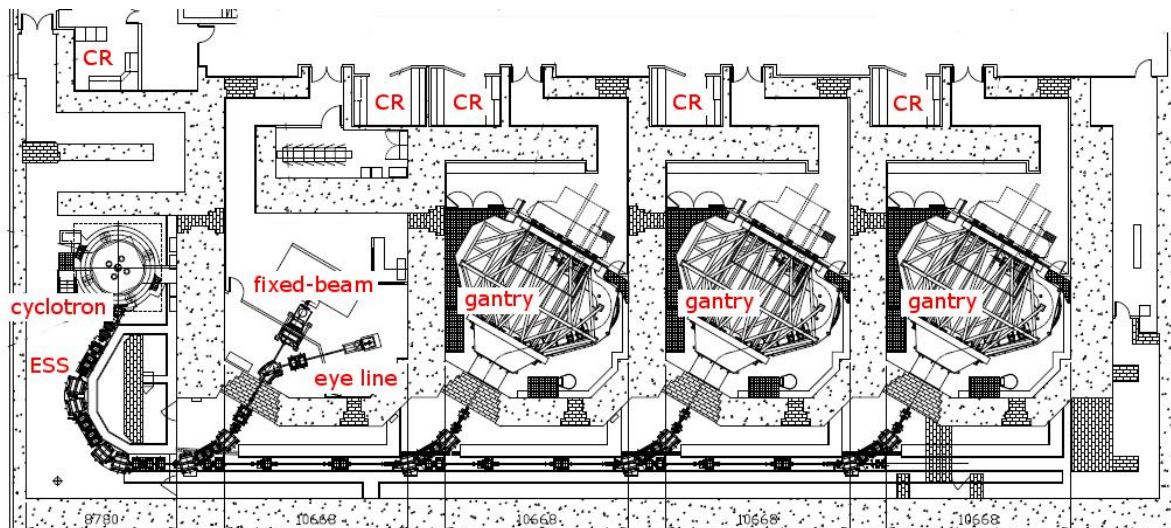
Figure I-5 – Floor plan of the proton therapy facility of Essen (courtesy of IBA).

The cyclotron accelerates protons up to a fixed energy of ~230 MeV. The cyclotron-extracted beam first passes through the ESS, which allows reducing the energy of the protons to the required value in the range of 70 MeV – 230 MeV. The layout of the ESS is shown in figure **I-6**. It is mainly composed of [42]:

- a set of quadrupoles to focus the cyclotron-extracted beam,
- the energy degrader: a graphite wheel with variable thickness. Rotating the wheel into position allows selecting the average energy of the transmitted beam. A nickel beam stop, which can fully block the proton beam, is also present on this wheel.
- a tantalum collimator: to limit the emittance of the beam transmitted through the degrader.
- another set of quadrupoles to refocus the beam,

- two sets of two dipoles, which bend the beam towards the treatment rooms and also act like a magnetic spectrometer. In between of them, an energy analyser and momentum slits (nickel) serve indeed to limit the beam energy spread $\Delta E/E$ to at most 0.6%.

The fixed-beam treatment room contains two beam lines: a multi-purpose fixed-beam treatment line and an eye treatment line. The multi-purpose fixed-beam line can be used for e.g. intracranial, head and neck, and prostate treatments [43].

Gantry treatment rooms (see picture in figure **I-7**) are useful for delivering treatment fields to a patient from any direction. A gantry, such as those installed at Essen, is a large electromechanical structure that can rotate at 360° around its central horizontal axis [43]. A picture of this structure is shown in figure **I-8**. At its entrance in the treatment room, the proton beam is aligned with this horizontal axis. The transport line mounted on the gantry includes a large dipole magnet and bends the beam so that it is delivered perpendicularly to the gantry axis. During a treatment, the targeted tumour is positioned at the gantry isocentre, defined as the intersection of the gantry axis and the central axis of the delivered proton beam.
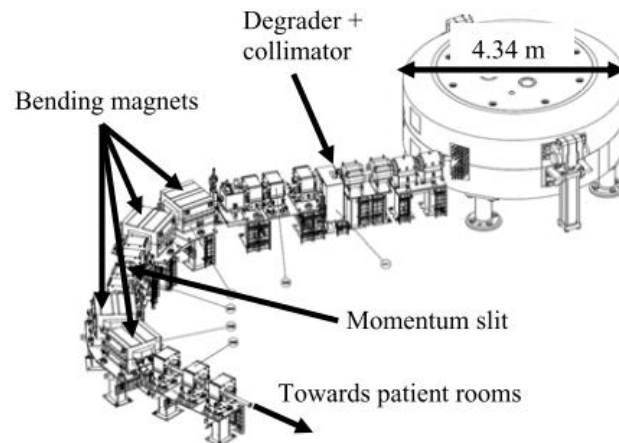
Figure I-6 – Drawing of the ®C230 cyclotron and the ESS (design by IBA) [42]*.*

Figure I-7 – Picture taken inside a gantry treatment room at Essen.
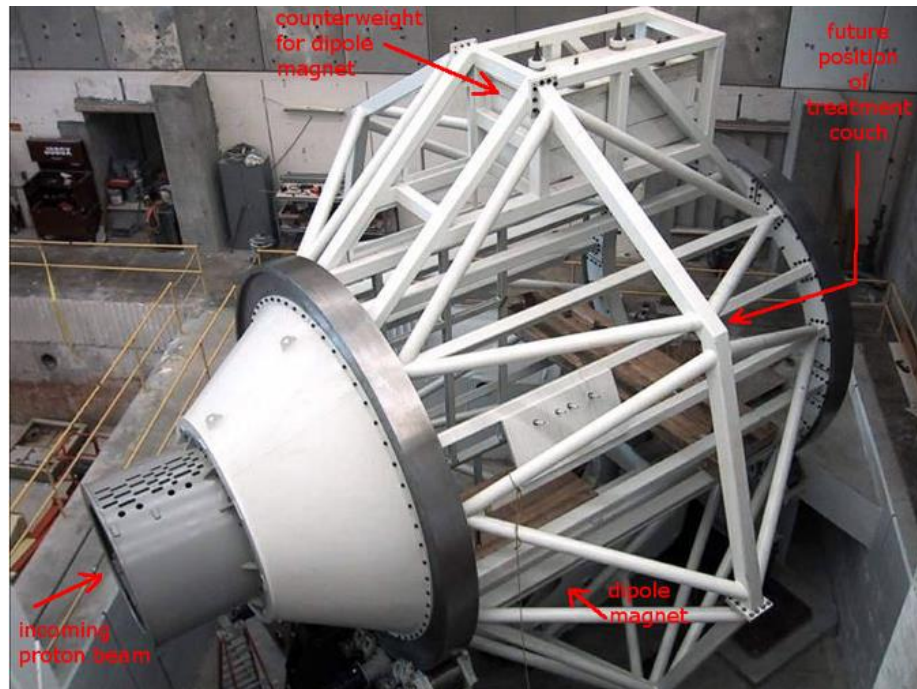
Figure I-8 – 360° gantry (IBA design) [44].

I-2.1.2 Available beam delivery modes

Different beam delivery techniques have been developed over the past decades to ensure an optimal dose delivery to the entire tumour volume, while also sparing surrounding healthy tissues.

To deliver a homogeneous dose to the tumour volume in the depth direction, different proton energies – and thus proton ranges – may typically be needed. Via beam energy modulation, a Spread-Out Bragg Peak (SOBP) can be constructed by adding appropriately weighted Bragg peaks with different ranges (see figure **I-9**).

To cover the lateral extent of the tumour, passive or active beam delivery techniques can be employed. The oldest and most common techniques are passive delivery modes, which are based on an enlargement of the proton field by means of scattering materials. Active delivery modes are more recent techniques that rely on scanning magnets to dynamically scan the proton beam in two transverse directions, so as to progressively "paint" the entire tumour volume with the beam.

At the proton therapy facility of Essen, "Double Scattering" is available as a passive delivery mode, and "Uniform Scanning" and "Pencil Beam Scanning" as active modes. These irradiation techniques are described in the following subsections.
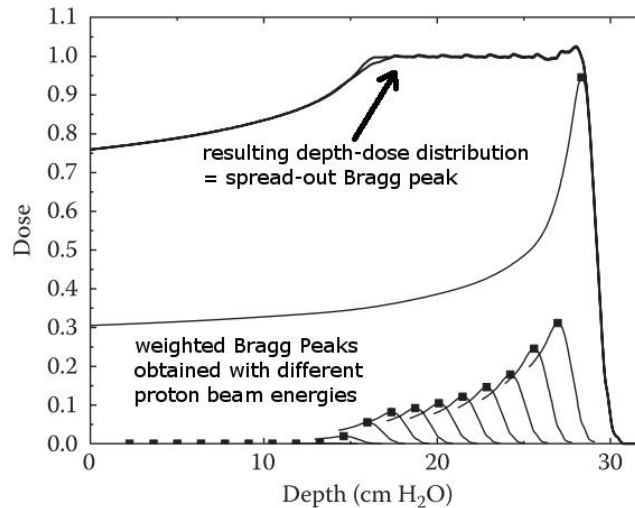
Figure I-9 - Spread-Out Bragg Peak (SOBP) (adapted from [45]*).*

I-2.1.2.1 Double Scattering

In the Double Scattering (DS) mode, the beam inside the treatment nozzle passes through a first scatterer, a range modulator, a second scatterer and two sets of collimating jaws (along the two transverse directions X and Y). This is illustrated in figure **I-10**. The function of the first scatterer is simply to enlarge the beam. The range modulator is a wheel with sectors of different thicknesses (see figure **I-11**). It serves, as its name indicates, to modify the proton range. The wheel is rotated at a constant frequency of ~10 Hz and the beam intensity is modulated as a function of the angular wheel position in order to produce the required SOBP. The second scatterer (see figure **I-10**) is contoured, *i.e.* its shape was optimized to flatten the lateral beam profile.

After the collimator, the beam exits the treatment nozzle through the snout on which a patient-specific aperture and range compensator are mounted. The aperture delineates the lateral shape of the treated volume, whereas the range compensator adjusts the dose distribution to the distal profile of this volume (see figure **I-12**). The snout is retractable and allows positioning these patient-specific accessories close to the patient's skin in order to reduce the lateral scattering that degrades the penumbra.

This delivery mode has the following disadvantages:

- the dose profile at the proximal edge of the target is the same as at the distal edge (see figure **I-10**), which implies that non-targeted tissues located very close to the proximal edge may receive a full treatment dose.

- Individual treatment accessories need to be manufactured for each patient.

- Secondary neutrons (see section **I-3**) are produced by nuclear interactions of the protons inside the scattering elements of the nozzle.
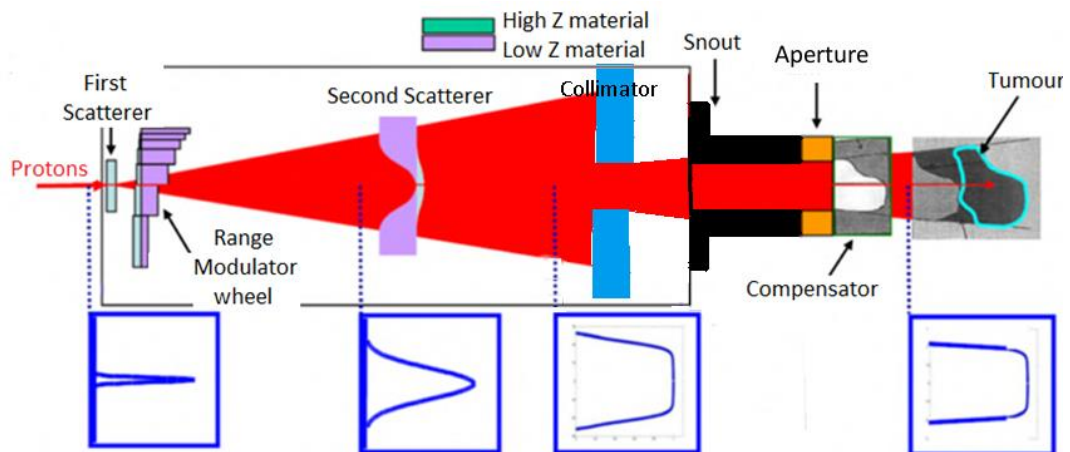
Figure I-10 – Principle of double scattering (adapted from [46]*)*

Figure I-11 – Picture of a range modulator wheel with three range modulation tracks (IBA)
[47]*.*
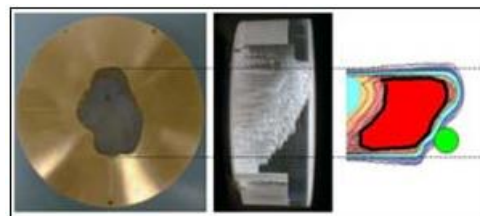
Figure I-12 - Pictures of a brass aperture and a Lucite range compensator [48]*.*

I-2.1.2.2 Uniform Scanning

Uniform Scanning (US) is similar to DS, but does not involve a second scatterer (see figure **I-13**) [49]. Instead, magnets in the nozzle are used to scan the beam over the entire field, in a regular 2D pattern schematized in figure **I-14**. The scatterer and the range modulator enlarge the beam width so that, in air at the isocentre, the standard deviation of the Gaussian beam profile is of a few cm. The range modulator serves the same purpose as in DS but does not rotate at the same speed. The dose is delivered to the tumour "layer by layer", so the range modulator only switches to another step after one layer is fully covered [50]. As in DS, a patient-specific aperture

and compensator are used to conform the dose distribution to the lateral and distal edges of the tumour.
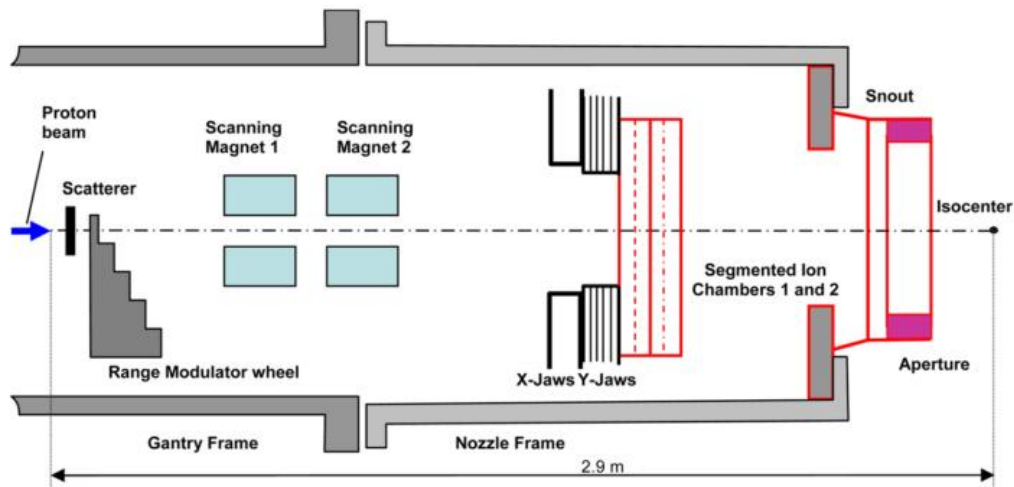
Figure I-13 – Schematic representation of a uniform scanning nozzle (IBA design) [49]*.*
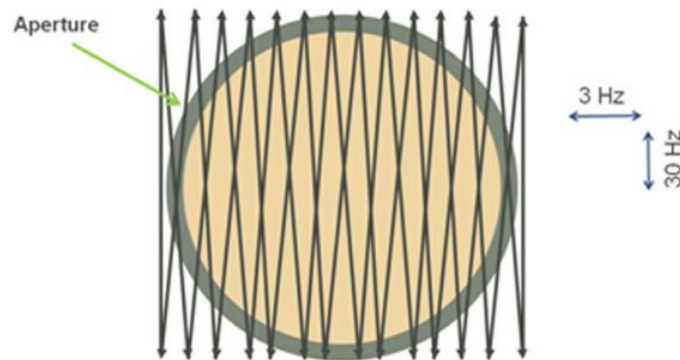
Figure I-14 – Example of a uniform scanning pattern (produced with an IBA nozzle) [49]*.*

I-2.1.2.3 Pencil Beam Scanning

Pencil Beam Scanning (PBS) is the newest beam delivery mode. A schematic representation of the PBS technique is shown in figure **I-15**. A highly focussed "pencil" beam, with a standard deviation of 3 – 6 mm in air at the isocentre, is steered laterally across the tumour by means of the scanning magnets inside the nozzle [51]. The dose distribution is progressively delivered by consecutive "spots" and the beam is briefly switched off every time the magnets are reconfigured for the next position of the pencil beam. As in US, the dose is delivered layer by layer, but the modulation of the beam energy is done entirely at the level of the ESS. The use of a patient-specific aperture and compensator is not necessary because the beam is narrow enough to correctly address small curvatures on the tumour edges [50]. Compared to US and DS, this technique also has the advantage that the production of secondary neutrons in the treatment nozzle is virtually inexistent.
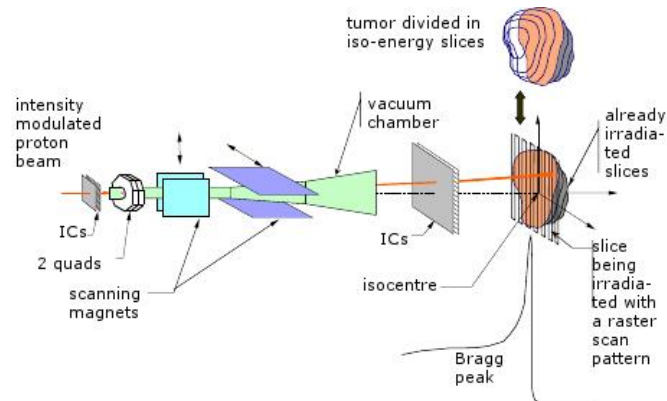
Figure I-15 - Pencil Beam Scanning (adapted from [51]*).*

I-3 Secondary neutrons in proton therapy

I-3.1 Nuclear interactions of protons

When the kinetic energy of the protons becomes large enough to overcome the electrical repulsion of the nucleus (the Coulomb barrier), nuclear interactions become possible. The probability for a proton to undergo a nuclear interaction increases as a function of the energy up to ~1 GeV. Depending on the target material, this probability is of approximately 20 – 35% for protons of 200 MeV – 250 MeV impinging on a stopping length target [52].

Nuclear interactions can be elastic or non-elastic. In elastic scattering, the total kinetic energy of the system (projectile + target nucleus) is conserved and no excitation energy is thus given to the target nucleus. In non-elastic interactions, the target nucleus is brought to an excited state.

I-3.1.1 Classification of reaction mechanisms

A comprehensive theoretical model for all types of nuclear reactions does not exist. For proton energies of a few MeV to ~1 GeV, the description of proton-nucleus non-elastic interactions is generally based on three main reaction mechanisms: direct reactions, compound reactions and pre-equilibrium emissions.

I-3.1.1.1 Direct reactions

Direct reactions are characterised by a very short time span, approximately equal to the transit time of the projectile across the nucleus ($\sim 10^{-22}$ s) [53,54]. No intermediate system is formed, so that the outgoing channel is directly linked to the incoming channel. The emitted particles have therefore a strongly forward-peaked angular distribution. The projectile may interact with a single nucleon without inferring with other nucleons, or it may cause a collective excitation of the nucleus but without being amalgamated with it. Examples of direct reactions are [55]:

- Inelastic scattering: the incoming particle is scattered but the total kinetic energy of the system is not conserved. The nucleus is left in a low-lying excited state and subsequently emits one or more gamma rays to return to its ground state. For an incoming proton: X(p,p')X*.

- Charge-exchange reactions: the number of nucleons in the target nucleus is unchanged but the outgoing particle has a different electric charge as the incoming particle. For an incoming proton: X(p,n)Y.

- Transfer reactions: one or more nucleons are transferred between the projectile and the target nucleus (stripping or pick-up reactions). For an incoming proton, pick-up reactions are possible: e.g. X(p,d)Y, X(p,t)Z ...

I-3.1.1.2 Compound reactions

Compared to direct reactions, the time span of compound reactions is much longer ($\sim 10^{-18}$ s – 10^{-16} s) [53,54]. The projectile is captured by the nucleus and a compound nucleus system is formed through a complex process which involves all nucleons. The kinetic energy of the projectile thus gets shared amongst all nucleons and the system reaches a state of statistical equilibrium. When this dynamic equilibrium is established, the compound starts to decay through particle emissions. From time to time, sufficient energy is indeed concentrated on a nucleon or a group of nucleons so that one or more particles are emitted. Gamma ray emission may also compete, or become the only possible decay mode once the remaining excitation energy is not sufficient for particle emission. The emissions in compound reactions are approximately isotropic because the system has lost the "memory" of the momentum of the incoming particle.

Two different types of models exist for the description of the decay process of a statistically equilibrated excited nucleus:

- **Evaporation models**, such as the theories of Weisskopf-Ewing [56] and Hauser-Feshbach [57], which treat the decay process as a sequence of two-body break-ups (*i.e.* one particle is emitted at each step). The Hauser-Feshbach theory, unlike the Weisskopf-Ewing theory, considers the conservation of the angular momentum and provides the angular distribution of the emitted particles.

- **Fermi break-up models**, which considers break-ups in two or more products [58].

I-3.1.1.3 Pre-equilibrium emissions

In some cases, particles are emitted after a time which is intermediate to the durations of direct and compound reactions [53,59,60]. These emissions occur before the compound system has reached statistical equilibrium. The pre-equilibrium stage

is in this case described as a series of nucleon-nucleon interactions, by which the kinetic energy of the projectile is progressively spread over an increasing number of nucleons. During the interactions, nucleons are occasionally ejected (individually or grouped inside light clusters). The angular distribution of the emitted particles tends to be forward-peaked despite the fact that the time span of the pre-equilibrium is longer than that of direct reactions. At the end of the pre-equilibrium stage, the excited compound nucleus is statistically equilibrated and continues its decay as described in the previous section.

Nuclear physicists have developed many kinds of pre-equilibrium models, a review of which can be found in [59]. Two types of models will essentially be referred to in this thesis:

- **Exciton models** [61,62]: these models do not follow trajectories of nucleons in the nucleus, but only focus on the partition of excited particles (above the Fermi energy) and holes (in the Fermi sea). The Fermi energy is the highest energy state occupied by a nucleon when the nucleus is in its ground state. The Fermi sea refers to all energy levels below the Fermi energy. In the pre-equilibrium stage, a projectile can excite a nucleon from the Fermi sea and create a "particle-hole" pair. Excited particles and holes are both called excitons. Due to nucleon-nucleon interactions, the number of excitons varies over time until the statistical equilibrium state is reached. Exciton models follow this evolution and determine the particle emission probability at each exciton configuration by making use of the inverse reaction cross-section.

- **Intranuclear cascade models** [63–65]: The nucleons are considered as point-like objects that have straight classical trajectories inside a nucleus described by a degenerate Fermi gas model. This model considers independent particles, subjected to the Pauli exclusion principle, inside a spherical square well potential. Here, the potential represents an average for the interactions of a nucleon with all its partners. A nucleon can be emitted if it reaches the surface of the nucleus with sufficient kinetic energy.

  Several intranuclear cascade models (e.g. Bertini [66,67], CEM [68,69]) are based on a space-like approach. In this case, the nucleus is seen as a continuous medium in which the incoming projectile – and all the subsequently involved nucleons – systematically undergo a collision with another nucleon after having travelled a distance equal to their mean free path. The latter is calculated as the inverse of the product of the nucleon density and the experimental free nucleon-nucleon cross-section.

  Other intranuclear models (e.g. Isabel [70,71], INCL [72,73]) use a time-like approach. The projectile and each nucleon are followed in coordinate and momentum space. Collisions occur when two nucleons approach each other at a distance that is smaller than the square root of the experimental free nucleon-nucleon cross-section divided by $\pi^{1/2}$.

The intranuclear cascade models use free nucleon-nucleon cross-sections because they are based on the assumption of independent binary collisions. As explained in detail in [74], this assumption is not valid when the kinetic energy of the projectile is lower than 100 – 200 MeV. In fact, intranuclear cascade models are generally considered as valid for projectile energies ranging from a few hundred MeV to a few GeV.

I-3.1.2 Influence of the projectile energy

For projectiles of a few MeV, the nuclear reactions proceed mainly through the compound reaction mechanism, but direct reactions can also occur [54]. The spectra of the emitted particles are mostly characterised by a low-energy component, from the decay of the statistically equilibrated compound nucleus, and by a high-energy component (close to the projectile energy) from direct reactions.

When the projectile energy increases above ~10 MeV, pre-equilibrium emissions become increasingly probable [59]. To illustrate this, examples of proton and neutron total emission spectra are shown in figure I-16, for the nuclear reactions with lead nuclei of protons of 10 MeV (on the left) and 100 MeV (on the right).
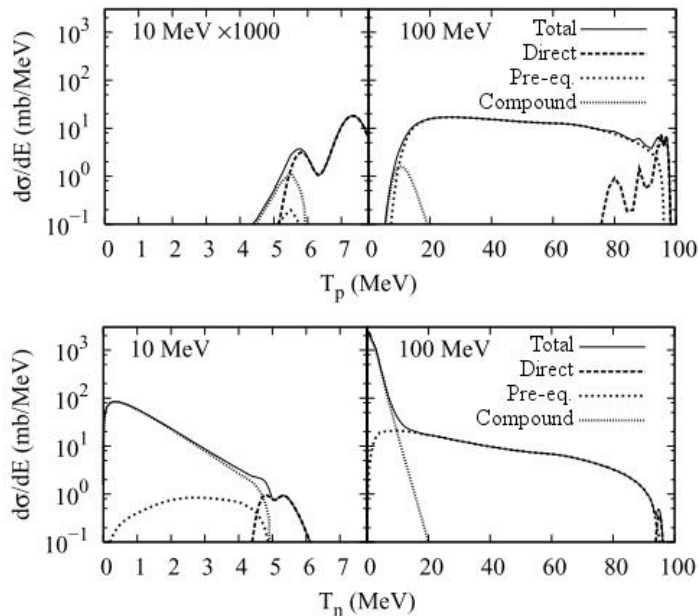
Figure I-16 – Differential cross-sections of the proton production (above) and the neutron production (below) in nuclear reactions of protons of 10 MeV (left) and 100 MeV (right) with ^{208}Pb nuclei [75]. Distinction between the contributions from direct reactions, pre-equilibrium emissions and the decay of statistically equilibrated compound nuclei.

Up to energies of ~150 MeV, pre-equilibrium emissions are often predicted by means of an exciton model. Intranuclear cascade models are preferably used only for projectile energies above ~150 MeV.

Despite the different calculation models, the underlying physical process of the pre-equilibrium emissions is thought to be the same for projectile energies of 10 MeV – 230 MeV. In the rest of this chapter, we will therefore simply refer to all pre-equilibrium reactions as "intranuclear cascades".

I-3.2 Secondary particles in proton therapy

As mentioned in the sections **I-1.3.3** and **I-3.1**, electromagnetic and nuclear interactions of protons with energies up to 230 MeV lead to the production of various types of secondary particles:

- electromagnetic interactions produce secondary electrons and X-ray photons;

- nuclear interactions create secondary neutrons, protons, other light ions (d, t, ^{3}He, α …) and gamma-ray photons.

The most energetic secondary particles are those produced in direct nuclear reactions or intranuclear cascades. Neutrons and charged particles produced by these mechanisms can have high kinetic energies ranging almost up to the primary proton energy (which can be of 230 MeV, at most). The gammas, however, have energies limited to at most ~10 MeV.

Inside the patient, the secondary electrons produced by the electromagnetic interactions of the protons allow delivering the therapeutic dose to the tumour. The other secondary particles may, depending on their penetrating power, also deposit an unwanted dose in the patient's healthy tissues outside the treatment field. Neutrons and gammas, which tend to be more penetrating than the charged particles, typically give the largest contribution to the secondary dose in out-of-field organs [46]. They are usually considered as the main causes for the induction of second cancers in patients treated with proton therapy [76,77]. With beam delivery techniques such as DS or US, more secondary particles are produced than with PBS, because nuclear interactions also occur inside elements of the treatment nozzle. The secondary doses delivered to the patient are thus unfortunately larger in these cases. Proton therapy (in PBS, especially) is nevertheless considered as a better treatment than intensity-modulated X-ray therapy in several cases, even when taking the risks related to the secondary neutron/photon doses into account [76,78].

Besides the risk of inducing second cancers in patients, other consequences of the production of secondary particles are:

- the need for radiation protection measures for members of the staff and the public visiting the proton therapy facility;

- induced radioactivity in the equipment and walls, which impacts the decommissioning process of the facility.

This thesis is related to the first of these two aspects and focusses on the shielding against prompt radiation. In this context, we can underline the fact that treatment rooms are not the only areas in which secondary particles are produced. Protons may also interact with matter inside the cyclotron, the ESS and the transport lines. An overview of the main production sites of secondary particles is shown in figure **I-17**.
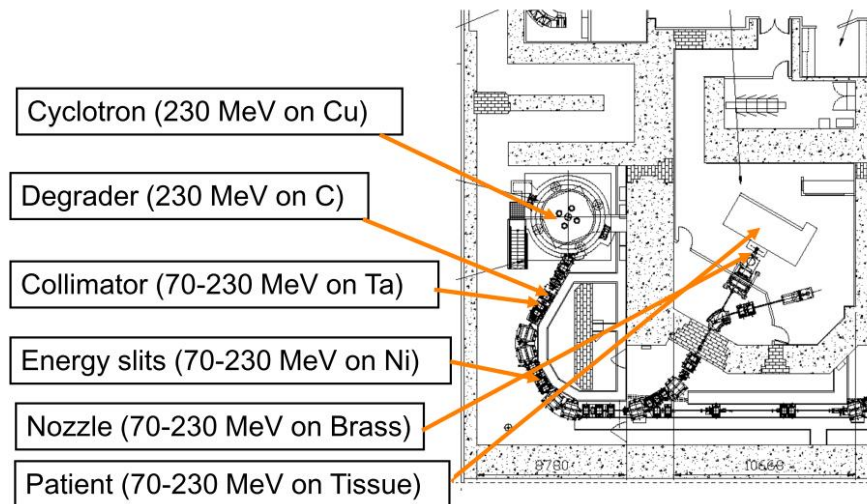
Figure I-17 – Main production sites of secondary particles in the cyclotron room and a treatment room [79].

I-3.3 Interactions of neutrons

Amongst the secondary particles produced in proton therapy, the high-energy neutrons constitute the most penetrating radiation and essentially determine the minimum required shielding thickness [55]. Neutrons are electrically neutral and can only interact with the atomic nuclei in matter.

I-3.3.1 Neutrons with energies below ~1 MeV

Thermal neutrons have kinetic energies typically below ~0.5 eV and are in approximate thermal equilibrium with their surroundings. Their velocities follow roughly a Maxwell-Boltzmann distribution, with an average kinetic energy of 0.025 MeV at 20°C [80]. The main interaction mechanisms of thermal neutrons with matter are [81]:

- Elastic scattering, *i.e.* scattering in which the total kinetic energy is conserved. By means of elastic scattering, thermal neutrons can lose or gain small amounts of kinetic energy.

- Radioactive capture: the neutron is absorbed by the nucleus, which subsequently decays by emitting a gamma ray.

Neutrons with energies in the range of 0.5 eV – 100 keV are referred to as intermediate neutrons, and neutrons between 100 keV and ~10 MeV as fast neutrons. Evaporation neutrons, which are emitted in the evaporation stage of nuclear reaction (section **I-3.1.1.2**), are typically fast neutrons [81].

Intermediate neutrons and fast neutrons of less than ~1 MeV interact with matter mainly through elastic scattering. The probability of radioactive capture is generally smaller than for thermal neutrons. The most likely scenario is thus one in which a neutron is progressively slowed down to thermal energies through several elastic collisions, before being eventually captured.

I-3.3.2 Neutrons with energies above ~1 MeV

For neutrons of at least a few MeV, elastic and non-elastic nuclear interactions can both occur. The non-elastic nuclear interactions follow the same mechanisms as those described for protons in section **I-3.1.** A difference lies however in the fact that the Coulomb barrier is inexistent for neutrons.

I-4 Radiation protection

I-4.1 System of quantities used in radiation protection

According to the International Commission on Radiological Protection (ICRP), the adverse effects of ionizing radiation on the human body can generally be classified into deterministic and stochastic effects [18]. Deterministic effects are the consequence of situations in which high radiation doses induce sufficient cell killings to cause detectable tissue reactions (malfunctioning or tissue death). A threshold dose generally has to be attained for this to be the case. The severity of the injury then increases with the received dose.

With lower radiation doses, there may be no detectable tissue reactions, but a single or a few cells might be affected by mutations (see Section **I-1.1**). Some mutations may evolve into a cancer or a heritable disease, which are called the stochastic health effects of ionizing radiation. The probability of occurring of a stochastic effect – but not its severity – is considered to be a linear function of the dose without a threshold. This function depends on the biological effectiveness of the radiation type and on the radiation sensitivity of the tissue type.

The present system of quantities used in radiation protection against external irradiation is articulated around three categories of quantities [16,18]:

- **Physical quantities**, which are defined at a point and are measurable. The fluence (already defined in Section **I-1.3.1**), the absorbed dose (defined in Section **I-1.3.2**) and the kerma (definition in [18]) belong to this category. For

the assessment of deterministic health effects, the absorbed dose serves as the reference quantity.

- **Radiation protection quantities**, in terms of which national legal dose limits for low dose exposure are defined. These quantities are linked to the risk of developing stochastic health effects. They are expressed in Sievert (Sv) in order to distinguish them easily from the absorbed dose expressed in Gy, although both units are equivalent to J/kg. Their definitions [18] are based on the mean absorbed dose to individual organs or tissues, which are not directly measurable but ought to be calculated using a computational anthropomorphic voxel phantom recommended by the ICRP:

  - The *equivalent dose H_T* to a tissue or organ is a weighted sum of the absorbed doses averaged over the tissue or organ caused by the different types of radiation involved. The appropriate radiation-weighting factors w_R [18] were determined by the ICRP on the basis of experimental data for the RBE (defined in section **I-1.3.7**) relative to photon radiation at low doses (therefore, w_R=1 for photons). The w_R factors are intended to be roughly consistent with the quality factor function *Q(L)*, which will be defined in section **I-4.2.1** [82].

  - The *effective dose E* to a person is a weighted sum of the equivalent doses H_T to the different tissues and organs of the body. The tissue-weighting factors w_T [18], which are normalized to their sum, were established by the ICRP "based on epidemiological studies of cancer induction as well as on experimental genetic data after radiation exposure, and on judgements" [18].

  The shielding design of a proton therapy facility, for instance, is based on calculations of the expected annual effective doses, which have to remain below the corresponding legal limits of the hosting country.

- **Operational quantities**, against which radiation measuring devices are calibrated. They were defined by the ICRU based on well-defined (but theoretical) tissue-equivalent phantoms and irradiation conditions. The definition of the ambient dose equivalent *H*(10)*, used for area monitoring of strongly penetrating radiation, is given below in Section **I-4.2**. Other operational quantity definitions can be found in the ICRU Report 51 [16]. Initially, the operational quantities were meant to serve as measurable quantities which provide conservative estimates for the radiation protection quantities [18]. It should be noted, however, that they are in fact non-directly measurable either [83,84] and that the ambient dose equivalent *H*(10)* may underestimate the effective dose *E* in the vicinity of high energy particle accelerators and in cosmic ray fields [18]. Despite these limitations, common neutron ambient dosimeters still in use today are devices that were designed for measuring the neutron *H*(10)*. This is for instance the case of the WENDI-2

(see section **I-6.1**), a detector with which many of the measurements reported in this thesis were performed.

I-4.2 The ambient dose equivalent H*(10)

I-4.2.1 Definition

Following the definition of the ICRU [16], the ambient dose equivalent *H*(10)* at a point in a strongly penetrating radiation field is the dose equivalent that would be produced by the corresponding expanded and aligned field in the ICRU sphere at a depth of 10 mm on the radius vector opposing the direction of the aligned field.

The dose equivalent *H* at a point is given by [16]:

$$H = \int Q(L)\frac{dD}{dL}(L)dL$$

where

L is the LET of the secondary charged particles produced by the incident radiation field (see Section **I-1.3.4** for the definition of LET),

$\frac{dD}{dL}(L)$ is the spectral distribution in terms of LET of the absorbed dose *D*,

$Q(L)$ is the quality factor function. It reflects the biological effectiveness of the secondary charged particles in low dose exposures. The values were determined based on experimental RBE data as well as judgements (concerning the extrapolation towards lower doses, and concerning the biological endpoints that are important in the context of stochastic health effects [82]). The following definition of $Q(L)$ published in 1991 in ICRP Publication 60 [85] is still of application today [18]:

$$Q(L) = \begin{cases} 1 & L < 10\,\dfrac{keV}{\mu m} \\[2mm] 0.32L - 2.2 & 10\,\dfrac{keV}{\mu m} \leq L \leq 100\,\dfrac{keV}{\mu m} \\[2mm] \dfrac{300}{\sqrt{L}} & L > 100\,\dfrac{keV}{\mu m} \end{cases}$$

This quality factor function from ICRP Publication 60 is shown in figure **I-18**, together with its earlier version from ICRP Publication 26.
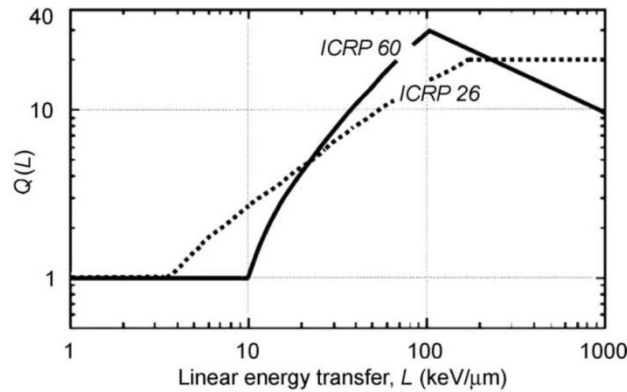
Figure I-18 - Quality factor Q as a a function of the LET (L): current convention (ICRP 60) and earlier convention (ICRP 26) [82].

The 'ICRU sphere' is a theoretical phantom defined as "a 30-cm diameter tissue-equivalent sphere with a density of 1 g cm^{-3} and a mass composition of 76.2% oxygen, 11.1% carbon, 10.1% hydrogen and 2.6% nitrogen" [16]. The 'expanded and aligned field' refers to a theoretical unidirectional field in which the fluence and its energy distribution are constant throughout the entire volume of interest (a 30 cm diameter sphere) and equal to the fluence and its energy distribution at the point of reference in the actual field. This concept is schematized in Figure **I-19**.

Like the effective dose (see Section **I-4.2**), the ambient dose equivalent is expressed in units of *Sv*.
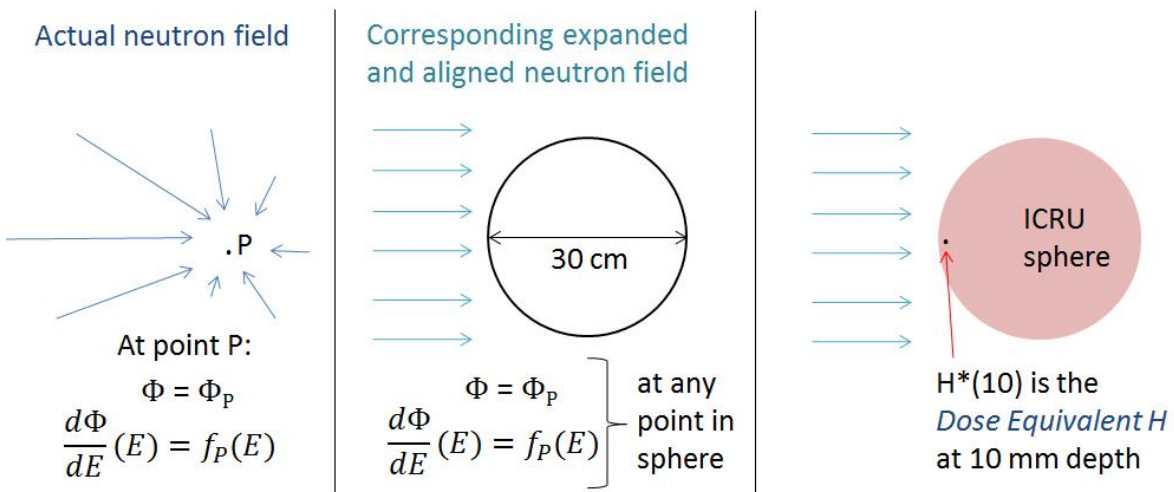
Figure I-19 - Expanded and aligned field in the definition of H(10).*

I-4.2.2 Fluence-to-H*(10) conversion coefficients

If the energy spectrum of the fluence is known (through calculation or measurement), the radiation protection quantities and the operational quantities can be calculated by folding that spectrum with the appropriate conversion coefficients recommended by the ICRP. These conversion coefficients are based on the results of Monte Carlo simulations for monoenergetic irradiations of reference phantoms, more

specifically anthropomorphic phantoms for the radiation protection quantities and the ICRU sphere or slab for the operational quantities. The latest versions of the conversion coefficients are given in ICRP Publication 116 [86] for the organ-absorbed dose and the effective dose in five idealized whole-body irradiation geometries, and in ICRP Publication 74 [87] for *H*(10)* and the other operational quantities.

In this work, the fluence-to-*H*(10)* conversion coefficients for neutrons from ICRP Publication 74 were used to compute the neutron *H*(10)* in several Monte Carlo simulations. These ICRP coefficients, shown on a log-log scale in figure **I-20,** are given up to 200 MeV. Their definition is based on the quality factor function *Q(L)* from ICRP Publication 60.

It can be noted that extensions above 200 MeV were also calculated by two groups of authors [88,89] using two different Monte Carlo codes, but their results differ from each other by a factor of 1.30 – 1.45 in the range of 200 MeV – 500 MeV (probably reflecting to a certain degree the relatively large uncertainties that affect the physics models in this energy range). However, not having clearly established conversion coefficients above 200 MeV has been of negligible importance in this work, because the maximum neutron energy was limited to 230 MeV and the fraction of neutrons with energies larger than 200 MeV was expected to be very small in all considered neutron spectra (<2% of the total neutron fluence according to the simulated spectra).
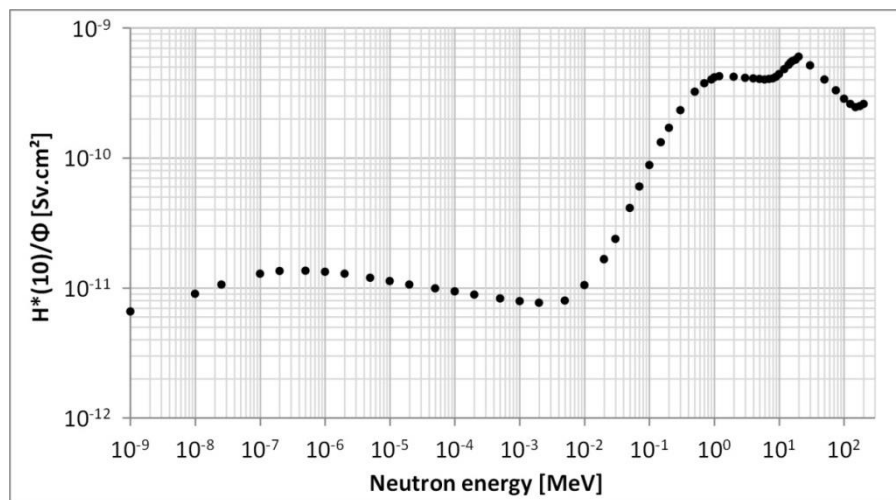
Figure I-20 - Fluence-to-H*(10) conversion coefficients from ICRP Publication 74 [87].

I-4.4 Shielding in proton therapy

As mentioned earlier, the high-energy neutrons are the most penetrating secondary particles produced inside a proton therapy facility. As a consequence, neutrons constitute the main radiation hazard for members of the staff and the public in this facility. Shielding against this prompt radiation is usually achieved by means of thick concrete walls. Wall thicknesses of at least ~2 m are common around the accelerator room and the treatment rooms. Concrete is a popular shielding material for such facilities because [81]:

- it contains hydrogen. Hydrogen is a very effective neutron moderator because of its high elastic scattering cross-section and its small mass as a target nucleus which allows for large energy transfers during an elastic collision.

- it also effectively attenuates photons.

- it has sufficient structural strength to support a building and can be poured in almost any configuration.

- it is relatively inexpensive.

The attenuation of the neutrons through such thick shields is relatively complex because the source spectra are continuous (ranging from 0 MeV to the initial energy of the primary protons) and neutrons of different energies are attenuated differently. As shown in figure **I-21**, neutrons of less than ~1 MeV, and especially thermal neutrons, have larger probabilities of interacting with nuclei of the concrete than neutrons of more than ~1 MeV. Moreover, the attenuation process of energetic neutrons by means of non-elastic nuclear reactions regenerates additional neutrons inside the shield (see reaction mechanisms in sections **I-3.1.1.2** and **I-3.1.1.3**). These additional neutrons can have very different energies depending on the reaction mechanism by which they were produced. During an intranuclear cascade, for instance, a large fraction of the energy is often transferred to a single nucleon. Therefore, intranuclear cascades induced by projectiles of more than ~50 MeV can generate high-energy neutrons that are themselves able to induce new intranuclear cascades deeper in the shield. That process is sometimes referred to as "internuclear cascades" [55].

The shape of the source spectra in front of the shielding depends strongly on the angle to the proton beam direction, due to the anisotropy of the intranuclear cascade emissions. As shown in figure **I-22** (left side), at forward angles, the emission of high-energy neutrons is large and the peak maximum typically lies above 100 MeV. As the angle to the proton beam increases, the amplitude of the high-energy peak decreases and its maximum progressively shifts to lower energies. At 180° of the proton beam direction, the high-energy peak is not distinguishable any more.
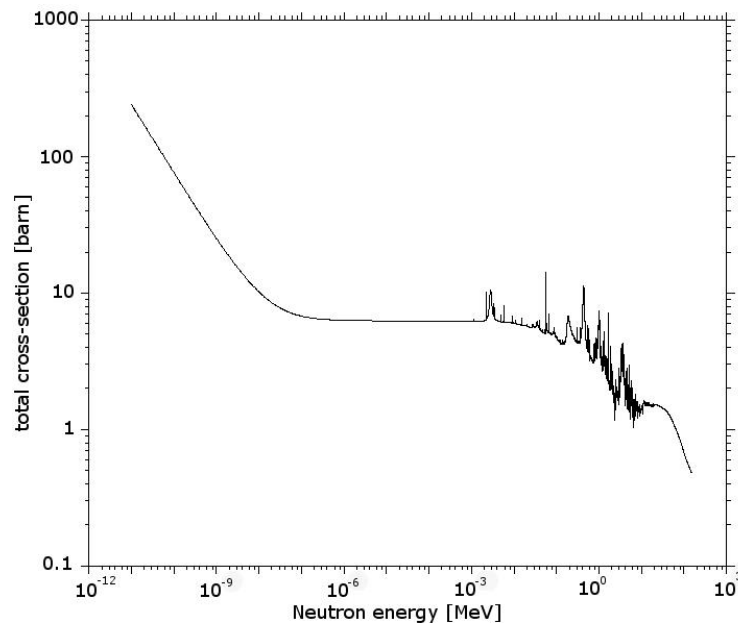
Figure I-21 - Total interaction cross-section for neutrons in NIST Portland concrete (MCNPX, nuclear data from ENDF/B-VII.0 evaluation).

Inside the concrete shield, the shape of the neutron spectrum typically changes as a function of depth, but an equilibrium shape is generally reached after a certain depth [90]. This equilibrium shape, represented in figure **I-22** (right side), is characterised by a high-energy peak around ~100 MeV (produced by intranuclear cascades), a peak of evaporation neutrons around ~2 MeV, and a peak at thermal energies. For 2 – 3 m thick shields, the magnitude of this spectrum strongly depends on the fraction of neutrons of more than ~100 MeV in the source spectrum [81].
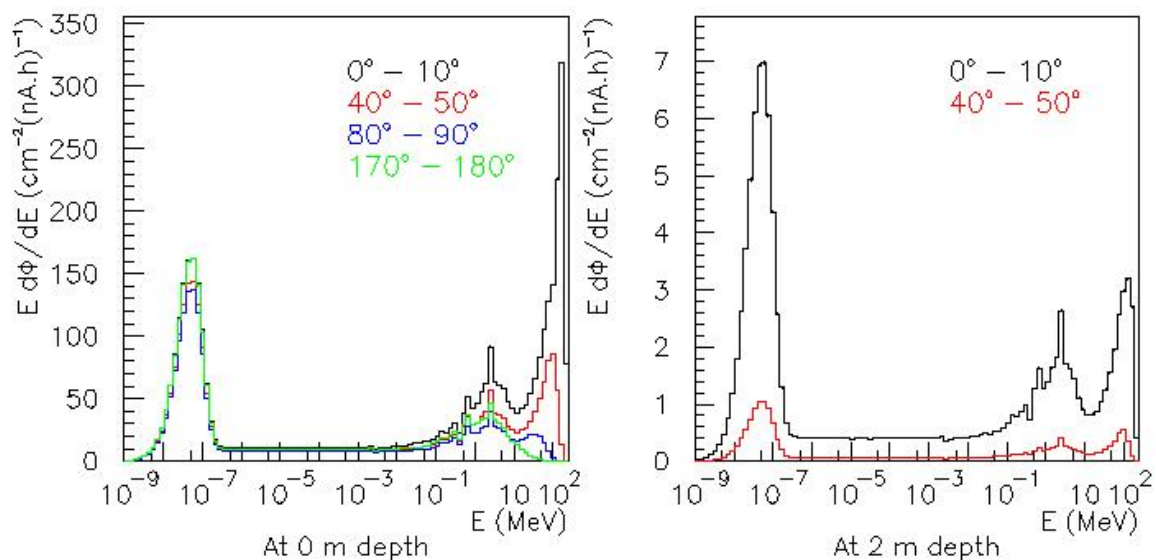
Figure I-22 – Lethargy plots of the neutron fluence produced at various emission angles by a 230 MeV proton beam impinging on a large water phantom. The spectra were calculated at 0 m depth (left) and 2 m depth (right) in a large spherical concrete shield. (Simulated with MCNPX).

The spectra in figure **I-22** are represented as lethargy plots [91], which show the fluence per unit lethargy (on a linear scale) as a function of the neutron energy (on a logarithmic scale). The fluence in each energy bin [E_i, E_{i+1}] has thus been normalized by the corresponding bin lethargy, which is defined as:

$$bin\ lethargy = \ln(E_{i+1}) - \ln(E_i) = \ln\left(\frac{E_{i+1}}{E_i}\right)$$

Using a logarithmic abscissa to plot wide-range energy spectra provides a more detailed view on their low-energy components. The advantage of log-lin lethargy plots resides in the fact that the areas under the curve are proportional to the corresponding fluences.

Originally, most neutron transport calculations for shielding design were based on analytical, semi-empirical methods. The simplest and most common method, called the line-of-sight model or point kernel model [55,92], is applicable to a point-like source and considers an exponential attenuation of the dose equivalent by the shield:

$$H(r, d, \theta) = H_0(\theta)\frac{e^{-d/\lambda(\theta)}}{r^2}$$

where r is the distance to the source, d is the traversed thickness along the line of sight (line that connects the source to the reference point), θ is the angle between the line of sight and the proton beam direction, $H_0(\theta)$ is a source term and **$\lambda(\theta)$** is the **attenuation length**. Both the source term and the attenuation length depend on the shape of the local spectrum.

For a monoenergetic neutron source, theoretical calculations (see figure **I-23**) predict that the attenuation length in concrete is approximately constant for initial neutron energies of 1 MeV – 10 MeV, but increases as a function of the energy between ~20 MeV and ~400 MeV due to the increasing occurrence of intranuclear cascades [93].
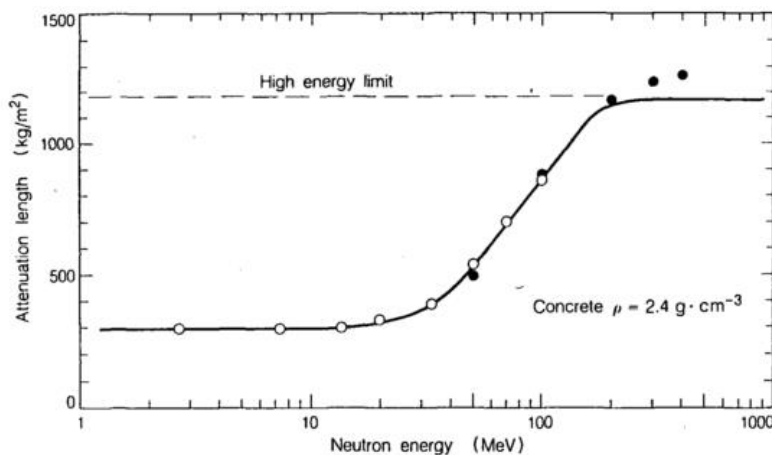
Figure I-23 – Theoretical predictions of the attenuation length of monoenergetic neutrons in a concrete as a function of the neutron energy [93].

In practice, the source spectra in a proton therapy facility are not monoenergetic. As a consequence, the attenuation of the dose equivalent can only be considered as exponential over limited shielding thicknesses. The spectrum shape, and thus the attenuation length, change indeed with increasing depth until the equilibrium spectrum shape is attained.

The analytical methods are easy to use and have the advantage of rapidly providing an estimate of the dose rates behind the shield. On the other hand, many aspects of the neutron transport physics are simplified and the models are limited to simple planar geometries. Moreover, the attenuation lengths involved in the calculations depend on the material and dimensions of the target, as well as on the composition and density of the concrete. For geometries as complex as a proton therapy room, these limitations often result in large errors on the calculated doses outside the room. In some cases, these errors can be larger than two orders of magnitude [94,95].

Today, thanks to generally improving computer performances, the shielding design of proton therapy facilities are almost always based on Monte Carlo simulations, which are better adapted for treating complex geometries and generally allow modelling the neutron transport physics in a more accurate way than analytical models [81,95].

I-5 The Monte Carlo method

I-5.1 General principle

Monte Carlo simulations can be used to stochastically solve complex radiation transport problems [96–99]. In this case, the simulation consists in a sort of numerical experiment in which a pseudo-random sequence of numbers is used to sequentially simulate many possible "particle histories". A history starts with the emission of a primary particle from a source of which the characteristics are defined by the user. All the interactions undergone by this particle inside the user-defined geometry are then simulated one by one, after which the same is done for each generated secondary particle as well. Each particle of the history is tracked until (a) it is absorbed in an interaction, (b) its kinetic energy drops below the predefined cut-off value, or (c) it exits the geometrical domain of interest. The pseudo-random numbers are used to sample from probability distributions which characterise for example:

- the initial position and velocity of the particle emitted by the source;

- the distance covered in straight line between two interactions (a probability distribution that depends on the total interaction cross-section of the material);

- which isotope the particle interacts with (distribution based on the elementary composition of the material and the total interaction cross-sections of the involved isotopes);

- which type of interaction the particle undergoes (according to the cross-sections of the different possible interactions for the selected isotope);

- the outcome of the interaction, *i.e.* the characteristics of the secondary particles (based on double-differential particle production cross-sections).

Cross-sections are typically either extracted from evaluated data stored in tabular form (see section **I-5.3**) or calculated from nuclear reaction models (see section **I-5.4**).

Where desired, a macroscopic physical quantity of interest can be calculated such as, for instance, the fluence averaged over a surface or volume. The contributions to this quantity should be scored for a large number N of histories, so as to obtain the required statistical convergence of these scores. In a well sampled problem, the relative statistical uncertainty on the average result should in principle decrease as $N^{-1/2}$ [98].

Examples of Monte Carlo radiation transport codes that can be used for simulations related to proton/hadron therapy are:

- MCNPX (Monte Carlo N-Particles eXtended) [100]. This code has also recently been merged with the MCNP5 code capabilities to form MCNP6 [101].

- GEANT4 (GEometry ANd Tracking) [102,103] and the GATE platform (GEANT4 Application for Tomographic Emission) [104].

- FLUKA (FLUktuierende KAskade) [105–107].

- PHITS (Particles and Heavy Ions Transport code System) [108].

I-5.2 The MCNPX code

In this thesis work, radiation transport simulations were carried out with MCNPX 2.7.0 [100,109]. MCNPX is one of the most used radiation transport codes, including for the shielding design of particle accelerators. The code can simulate 34 different particle types, including for instance protons, neutrons, photons, electrons, deuterons, tritons, ^{3}He, α particles and carbon ions. The covered energy domain corresponds roughly to 0 – 100 TeV.

An MCNPX simulation is based on a user-created input file that describes all the parameters of the problem. The geometry is specified by means of reference surfaces and so-called "cells" which are volumes delimited by these surfaces. The predefined commands that can be used in an MCNPX input file are called "cards" and the estimators of the investigated physical quantities are referred to as "tallies".

Seven types of standard tallies are available in MCNPX [98,100]. In this thesis work, we will frequently refer to the F4:n tally, which can be used to calculate the volume-averaged neutron fluence in a cell of volume V. This quantity can be expressed as follows:

$$\Phi_V = \frac{1}{V} \int \iiint \Psi(\bar{r}, v, \widehat{\Omega}, t) \, dv \, d\Omega \, dt \; dV$$

where $\Psi(\bar{r}, \widehat{\Omega}, t)$, expressed in cm^{-2}.s^{-1}, is the angular neutron flux at time t corresponding to neutrons moving with a velocity v along the direction vector $\widehat{\Omega}$ through point P, which is determined by the position vector $\bar{r}$.

If $n(\bar{r}, \widehat{\Omega}, t)$, expressed in cm^{-3}, is the density of neutrons moving at velocity v along $\widehat{\Omega}$ through point P at time t, then one can also write: $\Psi(\bar{r}, v, \widehat{\Omega}, t) = n(\bar{r}, v, \widehat{\Omega}, t) \, v$.

Let us call $N(\bar{r}, v, t)$ the density of neutrons in point P at time t, which is obtained by integrating $n(\bar{r}, v, \widehat{\Omega}, t)$ over all possible directions $\widehat{\Omega}$. The average neutron fluence in volume V can then be rewritten as:

$$\Phi_V = \frac{1}{V} \iiint N(\bar{r}, v, t) \, v \, dt \, dv \, dV$$

Since the product $v \, dt$ represents a differential unit of track length ds, we can actually think of the product $N(\bar{r}, v, t) \, v \, dt$ as a density of track lengths. If the collisions inside V are negligible compared to the number of tracks crossing this volume (often a reasonable assumption), we can assume that Φ_V can be reliably estimated by summing the track lengths T_i of all neutrons crossing V. The F4:N tally therefore calculates Φ_V as follows:

$$\Phi_V = \frac{1}{N} \sum_{i=1}^{m} W_i \frac{T_i}{V}$$

where T_i is the track length of particle i inside V, W_i is the weight of this particle and N is the number of simulated histories. By default, the weight of a particle is equal to 1 unless a variance reduction technique is applied (see section **I-5.5**). As for most tallies in MCNPX, the result of an F4:n tally is by default normalized per source-emitted particle, *i.e.* per simulated history.

I-5.3 Evaluated cross-section data in MCNPX

The tabulated cross-section data used by MCNPX to simulate proton and neutron interactions for projectile energies up to 150 MeV (or 20 MeV, depending on the target isotope and the selected library) are *evaluated* nuclear data. Such data are based on both experimental data and nuclear reaction models. Accurate experimental data are seldom available for all important reaction channels and usually concern a limited amount of projectile energies. Nuclear data evaluation groups, such as for example the Cross Section Evaluation Working Group (CSEWG) [110], make compilations of available cross-section measurements and use nuclear reaction models for interpolating and extrapolating from these data, or for determining which

values should be discarded when facing discrepant experimental data [111]. The CSEWG releases the so-called ENDF/B evaluations ('Evaluated Nuclear Data File') [112], which are often relied on by MCNPX users.

Evaluated cross-section data for protons and neutrons below 20 MeV are generally considered as well-established since long. They are based on relatively large sets of experimental data and their accuracy is satisfactory e.g. for the main requirements of nuclear power applications.

At energies above 20 MeV, experimental proton and neutron cross-section data are quite scarce. In spite of this, evaluated cross-section libraries for protons and neutrons in the range of 20 MeV – 150 MeV were progressively developed from the late 1980s onwards, notably in the context of the U.S. Accelerator Production of Tritium (APT) program [113]. The APT program led to the creation of the **la150** proton and neutron libraries for MCNPX. The development of the evaluated cross-section data for the la150 libraries relied extensively on nuclear reaction calculations performed with the GNASH code. This code was originally created at Los Alamos in the 1970s [114], and further improved during the 1980s [115] and 1990s [116,117]. It includes, amongst others, a pre-equilibrium exciton model and an evaporation model based on the Feshbach-Hauser theory, which were used in the calculations of the la150 libraries [113,118,119]. The code was used for calculating particle emission cross-sections, including their angular distributions and energy spectra. To provide the necessary input data to the GNASH code, optical model calculations were carried out with the ECIS code [120]. The parameters of the potential in the optical model were adjusted in order to reproduce the experimental data available for total, elastic, non-elastic and inelastic (direct reaction) cross-sections, as well as the elastic scattering angular distributions. The transmission coefficients intervening in the pre-equilibrium and equilibrium calculations were also determined with ECIS. Other parameters involved in the GNASH calculations, e.g. parameters describing the nuclear level density, were adjusted to optimize the agreement with the experimental data as well [119,121]. The data of the la150 libraries was eventually integrated in the ENDF/B-VI.6 and following evaluations. The latest version of the ENDF/B evaluation available in MCNPX 2.7.0 is called ENDF/B-VII.0 [122].

I-5.4 Physics models in MCNPX

For energies above the upper limit of the evaluated cross-section tables (150 MeV or 20 MeV) and below a few GeV, MCNPX simulates proton and neutron interactions by means of implemented physics models. For the pre-equilibrium phase, the user can select an intranuclear cascade model and/or an exciton pre-equilibrium model. Once the excited nucleus is statistically equilibrated, its further decay is modelled with an evaporation model, except for light nuclei which are fragmented through the Fermi break-up model (as implemented by Brenner *et al.* [123]). For heavy nuclei, a fission model may also be invoked.

I-5.4.1 Intranuclear cascade models

The **Bertini model** is the oldest intranuclear cascade model available in MCNPX. It was developed in the 1960s by H.W. Bertini at the Oak Ridge National Laboratory [66,67]. The model was designed for nucleon-nucleus and pion-nucleus interactions with projectile energies up to 3.5 GeV and 2.5 GeV, respectively. It relies on a space-like approach (see section **I-3.1.1.3**) and uses a 3-step radial function for the description of the nucleus density, *i.e.* the nucleus contains three areas of constant density which are separated by concentric spheres. Although its further development was stopped in the 1980s [124], the Bertini model has been widely used until today for transport calculations in the intermediate energy range.

The **Isabel model** was developed in the 1970s – 1980s by Y. Yariv and Z. Fraenkel at the Weizmann Institute in Israel [70,71]. The implementation of the model in MCNPX applies to nucleon-nucleus interactions as well as nucleus-nucleus interactions with projectiles such as deuterons, tritons, ^{3}He and α [125]. The model is considered valid for projectile energies up to 1 GeV/nucleon. Its description of the nucleus density is by default based on a 16-step radial function. It is a time-like model (see section **I-3.1.1.3**) and requires a significantly longer running time per collision than the Bertini model.

The original idea of the **CEM model** ('Cascade Exciton Model') was proposed in the 1980s by Gudima *et al.* from the Joint Institute for Nuclear Research (JINR) in Dubna, Russia [68]. The model was improved at the JINR until the end of the 1990s. Since then, it has been under continuous development by S.G. Mashnik's team at the Los Alamos National Laboratory [69,126]. The developments have been mainly focussed on improvements for spallation reactions [127], involved for instance in the APT program [113] and in accelerator-driven nuclear reactors. The version of the model included in MCNPX 2.7.0 is named CEM03.01 [128]. The CEM model is not an alone-standing intranuclear cascade model; it also contains an exciton model (see section **I-5.4.2**) and an evaporation-fission model (see section **I-5.4.3**), which are invoked after the intranuclear cascade. The Fermi break-up model is integrated as well, and is used at any stage of the reaction if A < 13, where A is the number of nucleons in the excited nucleus. The calculation of the intranuclear cascade is based on the standard Dubna IntraNuclear Cascade model [129] and uses a space-like approach. It is designed for nucleon-nucleus and pion-nucleus interactions with energies up to 5 GeV and 2.5 GeV, respectively. For light nuclei like carbon the recommended use is actually limited to 1 GeV [69]. The description of the nucleus density is based on a 7-step radial function. The model also includes a nucleon coalescence model which considers the possibility of cluster formation during the intranuclear cascade. Light clusters up to α are possible ejectiles at this stage, as are nucleons and pions.

The **INCL model** ('IntraNuclear Cascade Liège') was created in 1980 by J. Cugnon *et al.* from the University of Liège, in Belgium [72]. It was initially developed for collisions between heavy ions in the GeV range. In the following decade, it was however adapted for nucleon-nucleus and pion-nucleus interactions in the range of 100 MeV – 2 GeV [130,131]. Similarly to Isabel, INCL uses a time-like approach. The nucleus density is modelled by means of a continuous Woods-Saxon distribution [127]. In INCL4.2 [132], the version of the model available in MCNPX 2.7.0, the allowed projectiles are nucleons, pions, deuterons, tritons, ^{3}He and α, with energies up to 2 GeV. The emission of light clusters during the cascade is however not yet implemented.

I-5.4.2 Exciton models

The **Multi-stage Pre-equilibrium Model (MPM)**, developed by Prael *et al.* [133] at the Los Alamos National Laboratory, can be used after the intranuclear cascade models Bertini, ISABEL and INCL4. With the MPM, the excited nucleus may emit a nucleon or a light cluster (up to ^{4}He) at each intermediate state, which is characterised by a certain "pair-hole" configuration. When no emission occurs, the pair-hole configuration evolves through an internal rearrangement that increases the number of excitons. The MPM terminates upon reaching the equilibrium exciton number.

The **Modified Exciton Model (MEM)**, included in the CEM03 package, was developed at the Joint Institute for Nuclear Research, in Dubna. In contrast to the MPM, it allows transitions that reduce the number of excitons [134].

I-5.4.3 Evaporation-fission models

In MCNPX, two evaporation models can be selected after the Bertini, ISABEL and INCL4 models, or after the MPM: the Dresner model or the ABLA model. Both are based on the compound nucleus decay theory of Weisskopf-Ewing [56].

The **Dresner model** [135] was developed at the Oak Ridge National Laboratory (ORNL). Although 19 different particles can be emitted by the excited nucleus in the original model, the implementation in MCNPX is limited to the emission of nucleons and light clusters up to ^{4}He [125]. This evaporation model must be used in association with a separate high-energy fission model for heavy nuclei: either the Rutherford Appleton Laboratory (RAL) fission model [136] or the ORNL fission model [137]. The former applies to atomic numbers Z ≥ 71, the latter to Z ≥ 91 [100].

The **ABLA model**, originally based on a part of the abrasion-ablation theory for heavy ions [138,139], was essentially developed at the *Gesellschaft für Schwerionenforschung* (GSI) by K.-H. Schmidt's team [140]. It is usually coupled to the INCL4 model. The version of ABLA implemented in MCNPX 2.7.0 only allows for the

emission of nucleons and α (unlike the new ABLA07 model [141] which considers also deuterons, tritons, ^{3}He and intermediate mass fragments as ejectiles). This version of ABLA however includes its own semi-empirical fission model.

The **Generalized Evaporation Model (GEM)**, included in the CEM03 package, was developed by S. Furihata from the Mitsubishi Research Institute of Tokyo [142]. It is also based on the Weisskopf-Ewing approach. The model considers 66 types of ejectiles ranging from nucleons to ^{28}Mg. A fission model, based on the RAL model, is also included.

I-5.4.4 Default physics models settings

With the default options of MCNPX 2.7.0 [100], a first part of the pre-equilibrium phase is treated with the Bertini intranuclear cascade model and a second part with the MPM. The transition from one model to the other occurs when all nucleons have energies below a cut-off value corresponding to ~7 MeV above the Fermi energy [64,125]. For the default equilibrium decay, the following models are invoked depending on the number of protons Z and the total number of nucleons A in the intermediate state:

- the Fermi break-up model, if A ≤ 13, or if 14 ≤ A ≤ 20 and the excitation energy E* < 44 MeV;
- the Dresner evaporation model, if A > 20, or if A > 13 and E* > 44 MeV;
- the RAL fission model, which competes with the evaporation model if Z ≥ 71.

I-5.5 Variance reduction

Analog Monte Carlo simulations, which follow the general principle outlined in section **I-5.1,** are simply based on natural event probabilities and only use unit particle weights. Sometimes, however, obtaining the statistical convergence of a particular tally in an analog Monte Carlo simulation requires an unreasonably long computer time. This is typically true for shielding simulations of proton therapy facilities, because the neutron H*(10) gets attenuated by a factor of $10^3 - 10^6$ throughout the shield. For a history initiated by a high-energy proton inside the vault, the probability of registering a neutron track inside a tally cell located somewhere outside the shielding is thus extremely small. The statistical convergence of such a tally is very difficult to obtain without using a variance reduction technique, designed to artificially follow "interesting" particles more often than "uninteresting ones". An "interesting" particle is one that contributes significantly to the tally. To avoid biasing the average tally result when using such a technique, the scores need to be multiplied by a particle weight: for example, if a particle is made w times as likely to follow a certain random walk, the corresponding score to the tally will be multiplied by $1/w$ [98].

Four classes of variance reduction techniques can be used with MCNPX: truncation methods, population control methods, modified sampling methods and partially deterministic methods. An overview of these methods can be found in [98]. In this work, the variance reduction technique applied within the shielding simulations is the "geometry splitting and Russian roulette" method, which belongs to the category of population control methods.

Geometry splitting and Russian roulette can be used to maintain the particle population that migrates towards tally regions more or less constant, and to kill particles that are heading in an unimportant direction. The geometry is subdivided in cells, to each of which an importance I_i is assigned by the user. When a particle of weight w moves from a cell of importance I_i into an adjacent cell of importance I_{i+1}, the following recipe is applied [98]:

- If $I_i < I_{i+1}$: **particle splitting** takes place, with two possible scenarios:
  1) the ratio I_{i+1}/I_i is an integer $n \geq 2$: the particle is split into n identical particles of weight w/n.
  2) the ratio I_{i+1}/I_i is not an integer: the splitting is done probabilistically so that the expectation value of the number of splits is equal to this importance ratio. If we call n the largest integer smaller than I_{i+1}/I_i, there is a probability $p = I_{i+1}/I_i - n$ that the particle gets split into $n+1$ particles of weight $w/(n+1)$ and a probability $1 - p$ of splitting it into n particles of weight w/n.

- If $I_i > I_{i+1}$: **Russian roulette** is played. There is a probability of I_{i+1}/I_i that the transport of the particle continues (with a weight of $w \times I_{i+1}/I_i$) and a probability of $1 - I_{i+1}/I_i$ that the particle gets "killed".

Further information on this variance reduction technique can be found in [98] and [143].

I-6 Neutron measurement techniques

I-6.1 The extended-range rem meter WENDI-2

Rem meters [144] typically consist of a thermal neutron detector surrounded by a moderator assembly, often principally made of polyethylene. Neutrons up to ~10 MeV have a relatively high probability of interacting through elastic scattering with the hydrogen (or carbon) nuclei of polyethylene. Moreover, thanks to the light weight of the recoiling nucleus – hydrogen, especially –, the incident neutron can transfer a large amount of kinetic energy during one interaction. The slowing down of the neutrons is thus very efficient, which is necessary because the sensitivity of the central detector quickly decreases as a function of the neutron energy.

The response of a rem meter can be expressed as:

$$R = C \int_0^{E_{max}} r(E) \ \Phi(E) \ dE$$

where

$\Phi(E)$ is the neutron fluence as a function of the neutron energy;

$r(E)$ is the absolute response function of the rem meter. If the central detector is for instance a gas proportional counter, the absolute response is expressed in counts per unit fluence. The function $r(E)$ gives the absolute response of the rem meter to monoenergetic neutron beams, as a function of their energy.

C is the H*(10) calibration factor, which allows to convert the absolute response into a dose response expressed in Sv. It is often determined by means of reference radioactive neutron sources of ^{252}Cf or AmBe [145].

A rem meter is designed so that its dose response function $Cr(E)$ approximately matches the official fluence-to-H*(10) conversion coefficients over a large energy range (at least 10 orders of magnitude). Active rem meters, which contain a gas proportional counter, are very convenient and widely used since the 1970s for the routine neutron ambient monitoring in many sectors, e.g. around particle accelerators [99,146], around nuclear reactors [147], in nuclear waste management facilities, etc.

The response function of conventional rem meters however strongly decreases for neutrons above ~10 MeV [148]. In neutron fields which contain a relatively important fraction of high-energy neutrons, for example outside the shielding of high-energy charged particle beams, the measurements of a conventional rem meter can significantly underestimate the real neutron H*(10) rates [149]. Since the 1990s, a new generation of extended-range rem meters has therefore been developed, based on the original design of the 'LINUS' by Birattari *et al.* [150,151]. The concept relies on the insertion of a heavy metal layer of 1 – 2 cm in thickness (e.g. Pb or W) inside the hydrogenous moderator. Neutrons above ~10 MeV can undergo nuclear interactions inside the heavy metal layer in which secondary neutrons of lower energy (evaporation neutrons) are produced. These secondary neutrons are subsequently slowed down by the inner layer of hydrogenous moderator and effectively detected in the central detector. Thanks to this heavy metal insert, the measuring range of a rem meter is extended up to energies on the order of the GeV.

The majority of the neutron measurements presented in this thesis were performed with a WENDI-2, an extended-range rem meter designed by Olsher *et al.* [152] and currently commercialised by Thermo Scientific [153]. The good sensitivity of the WENDI-2 to high-energy neutrons is due to the tungsten layer embedded in the polyethylene shell (see figure **I-24**). The central detector is a cylindrical proportional

counter filled with ^{3}He gas. It detects thermal neutrons through the ionisation of the gas induced by protons and tritons produced in ^{3}He(n,p)^{3}H reactions.
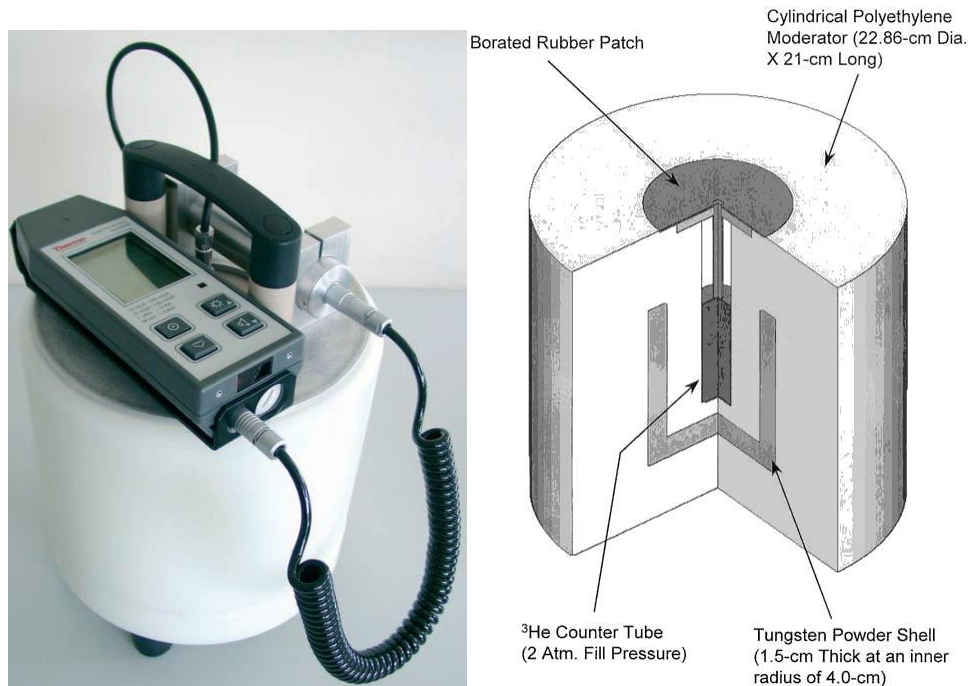
Figure I-24 – Picture of a WENDI-2 connected to a FH40-G survey meter [154] *and cutaway view of the WENDI-2* [152]*.*

All WENDI-2 measurements reported in this thesis were carried out with the same device: model FHT 762, drawing number 42540/85, serial number 344 [155]. A FH40-G digital survey meter [156] (also shown in figure **I-24**) was connected to the WENDI-2 to operate it and to display its response.

I-6.2 Bonner Sphere Spectrometry

Neutron spectrometry consists in measuring a neutron fluence spectrum. In Chapter VI of this thesis, neutron spectrometry measurements performed with a Bonner Sphere Spectrometer (BSS) will be presented. A BSS consists of a collection of moderating spheres, with different sizes and/or inner structures, used around a thermal neutron detector [157]. Most of the spheres are made primarily of polyethylene (see figure **I-25**), but some of them may also contain for instance cadmium or heavy metals. To measure a neutron spectrum in one position, consecutive measurements should be made with each single sphere, which acts like an 'integral' device similar to a rem meter. Due to their different diameters (or inner structures), the spheres have different response functions and can thus provide different energy-integrated responses in the same neutron field. The neutron fluence spectrum can then be determined from the set of readings via an unfolding procedure [158]. The range of the measured spectrum typically spans from thermal energies up to ~10 MeV, with a conventional BSS, and up to several hundreds of MeV if at least one of the spheres contains a heavy metal insert [159].
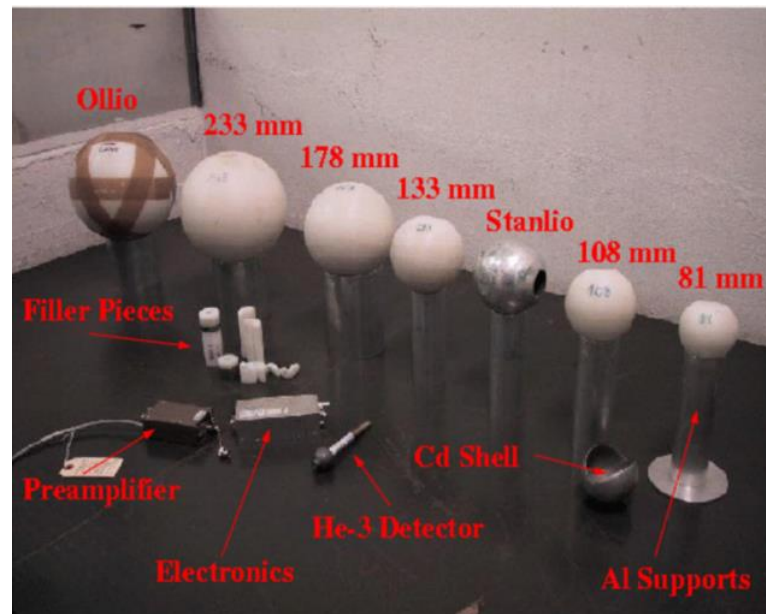
Figure I-25 – Picture of the CERN BSS [160]*.*

I-6.3 Microdosimetry with a Tissue-Equivalent Proportional Counter

As explained by A.J. Waker in [161], microdosimetry with a Tissue-Equivalent Proportional Counter (TEPC) studies the energy deposition spectra of (secondary) charged particles in low pressure proportional counters that simulate microscopic sites of tissue. A TEPC allows measuring the absorbed dose (section **I-1.3.2**) as well as the spectral distribution of the absorbed dose in terms of LET (section **I-1.3.4**). Such measurements are highly interesting for radiobiology, but can also be used in radiation protection to measure the dose equivalent *H* (section **I-4.2.1**). Some TEPC dose equivalent measurements will be presented in Chapter VI.

The wall of a TEPC consists of a material of equivalent energy-absorbing properties as human tissue. Photons or neutrons will mainly interact with this wall, and produce secondary charged particles that induce ionisations inside the gas. The latter is also tissue-equivalent, meaning that the mass stopping power of a charged particle inside the detector is the same as in human tissue. A microscopic tissue site can then be mimicked by adjusting the gas pressure so that the product of the gas density by the cavity diameter equals the product of the tissue density by the micrometric tissue site diameter.

The electric field established between the wall (cathode) and the central anode is such that the detector functions as a proportional counter. Each initial charged particle triggers a voltage pulse of which the amplitude is proportional to the number

of ionisations created by this particle along its path through the gas. The signal thus reflects the energy imparted by the charged particle to a micrometric tissue site.

Microdosimetric spectra are usually represented as spectra of the **lineal energy _y_**, defined as the energy imparted by a charged particle divided by the mean chord length of the simulated tissue site [162]. The mean chord length is the average length of all chords, _i.e._ all straight lines joining two points on the border of the micrometric site. For a spherical site, the mean chord length is equal to 4/3 of the sphere radius. Since for a micrometric site the lineal energy is by definition approximately equal to the LET, the microdosimetric spectra are also commonly considered as LET spectra.

The spectral distribution of the absorbed dose in terms of LET – or, more precisely, the lineal energy – can be derived from the lineal energy spectra. This requires multiplying the number of counts in each interval by the corresponding average lineal energy (and by a constant equal to the ratio of the mean chord length to the mass of the gas). The integral under the curve of the resulting distribution thus provides the measured absorbed dose. Folding this distribution with the quality factor function _Q(L)_ (section **I-4.2.1**) gives us the equivalent dose _H_.

I-7 Experimental validation of shielding calculations

There are relatively few published data regarding comparisons between Monte Carlo shielding simulations and neutron measurements performed in proton therapy facilities (behind the shielding). At the onset of this PhD project, the most recent comparison was – to our knowledge – the one by Newhauser _et al._ [94], published as much as ten years earlier. In their experiment, a 235 MeV proton beam was delivered to a thick brass target in a gantry treatment room of the proton therapy centre at the Massachusetts General Hospital (MGH). Neutron H*(10) measurements were performed in several positions inside the access maze and outside the treatment room. The measurements were in the first place compared to H*(10) calculations obtained through analytical models originally used for the shielding design. A few results were also compared to those of an MCNPX simulation in which the geometry of the shielding was realistically modelled. Both the analytical and Monte Carlo predictions overestimated the measurements in positions outside the shielding. The two methods were thus considered as leading to a conservative shielding design. The agreement achieved with the Monte Carlo simulation was however much better than with the analytical calculations. Outside the shielding, the analytical calculations yielded overestimates by one to two orders of magnitude, whereas the authors reported an overestimate by a factor of 2.4 for the MCNPX simulation. At the entrance of the maze, an overestimate by a factor of 4 was obtained with the analytical model, against an overestimation factor of 1.2 in the MCNPX simulation. The latter was based on the la150 cross-section libraries for proton and neutron interactions up to

150 MeV and on the Bertini intranuclear cascade model for higher-energy interactions. The defined concrete composition was not specified in the article. No details were given either on the use of any variance reduction technique. The statistical uncertainties were nevertheless mentioned to be within 10% for the simulated H*(10) rates. The neutron measurements were acquired with a conventional rem meter (Model 2241, Ludlum Instruments). In positions outside the treatment room, the readings probably significantly underestimated the true neutron H*(10), due to the decreased sensitivity of the detector above ~10 MeV. The statistical uncertainties on the measurements were also relatively large (25%).

Previous studies, conducted inside other proton therapy facilities with different neutron detectors, also showed an overestimate of the shielding calculations with respect to the measurements. Let us mention in this case J.V. Siebers's PhD thesis from 1990 [163] and a paper by A. Mazal *et al.* from 1997 [164].

J.V. Siebers [163] presented dose equivalent measurements performed with a TEPC at the Loma Linda Proton Therapy facility (California, USA). The experiment used a 230 MeV proton beam impinging on a thick iron target, positioned in the shielding study area. Measurements were acquired at different depths inside the surrounding shielding walls (inside PVC pipes), along four different angles with respect to the proton beam direction: 0°, 22°, 45° and 90°.

First, Siebers compared the measurements with existing half-stochastic half-analytical calculations used in the shielding design of the facility [165,166]. In this case, the neutron production in the target were simulated with the Monte Carlo code HETC [167] (based on the Bertini model), whereas the subsequent attenuation of the neutrons was analytically calculated with the ANISN code [168] assuming a spherical shield geometry. The overestimate of the calculated dose equivalent with respect to the measurement was found to increase as a function of the depth in the shield. Depending on the considered angle, the overestimate reached a factor of 4 – 10 at 2 m depth. When fitting the data measured beyond 60 cm depth with a decreasing exponential curve, overestimates in the calculations were actually observed both on the source term (intercept at 0 m depth) and the attenuation length (exponential slope). Depending on the considered angle, overestimates on the source term ranged up to a factor of 6 and those on the attenuation length up to a factor of 1.2 – 1.4. The concrete composition used in the calculations contained however 4 – 5 times less hydrogen atoms per unit volume than the actual composition analysed by X-ray fluorescence spectrometry. The assumed concrete density was, on the other hand, ~20% larger than the measured density.

Secondly, Siebers carried out Monte Carlo simulations with the LAHET Code System (LCS) [169], a partial forerunner of MCNPX. The code provided an implementation of the Bertini intranuclear cascade, a multistage pre-equilibrium model, the Dresner evaporation model and the Fermi break-up model (for light

nuclei). The la150 libraries of evaluated nuclear data were however not yet available. Also, a simplified spherical model was used instead of a realistic representation of the shielding geometry. On the other hand, the concrete composition and density were based on the abovementioned experimental data. Altogether, a relatively better agreement with the measurements was obtained with these simulations, compared to the previous calculations. At 2 m depth, the results overestimated the measurements by a factor of 3 – 6 depending on the considered angle.

Mazal *et al.* [164] conducted a similar experiment for 201 MeV protons impinging on a thick aluminium target. The measurements were carried out in the experimental area of the Orsay proton therapy facility (France). A bunker was built with several blocks of concrete, of which the elemental composition was not specified but the density was estimated to 2.2 g/cm^3. The total thickness of the concrete was changed from 0 m to 3 m in several steps. At each step, neutron measurements were performed at several angles with respect to the proton beam (0°, 22.5°, 45°, 67.5° and 90°). Different types of detectors were used, including an extended-range rem meter based on the LINUS design [151]. The data of the extended-range meter acquired beyond 1 m of concrete were fitted with an exponential function. The corresponding attenuation lengths were compared to calculated data from Alsmiller *et al.* [170], obtained by combining Monte Carlo HETC calculations for the neutron production and analytical ANISN calculations for the transport through the concrete. The calculated attenuation lengths were larger than the measured ones by a factor of 1.1 – 1.3.

In the early 2000s, Siebers's shielding simulations with LAHET for the 230 MeV protons incident on a thick iron target were repeated by Tayama *et al.* [171], using MCNPX with the la150 libraries. The agreement with the measurements was much improved, most probably thanks to the use of the evaluated cross-section data for proton and neutron energies up to 150 MeV. At 2 m depth, the overestimates of the simulated dose equivalents remained nevertheless as large as a factor of 2 – 3. For the exponential attenuation beyond 1 m depth, the source terms and the attenuation lengths agreed with the measured values within factors of 2 and 1.35, respectively.

Evidently, the neutron attenuation through the concrete shields of proton therapy facilities is a complex problem that depends on many parameters. The initial neutron spectrum, at the entrance of the shield, is of course one of them. Accurately simulating these neutron spectra is in fact not trivial, partly due to the complex configuration and equipment of the treatment rooms. Examples of simulation-to-measurement comparisons for positions located inside treatment rooms can be found in [46,172–176]. Amongst these, the three most recent comparisons (dating from 2011 – 2014) include measurements acquired with wide-energy-range neutron detectors. The treatment room walls were also taken into account in the Monte Carlo simulations. All simulations were performed with MCNPX using the la150 libraries and the Bertini model.

- The experiment of Hohmann *et al.* [175] was conducted in the gantry treatment room of the Paul Scherrer Institute in Villingen, Switzerland. A water phantom was irradiated with 200 MeV protons delivered in active mode, *i.e.* without the use of a scatterer inside the nozzle. WENDI-2 measurements were acquired at various angles between 0° and 90° with respect to the proton beam direction. The simulation-to-measurement ratios were in the range of 0.95 – 1.3. Additional measurements were also performed with a conventional rem meter (LB 6411, Berthold Technologies) at angles of 0° – 30°, where the spectra are characterised by large fractions of high-energy neutrons. The LB6411 measurements were lower than the WENDI-2 measurements by factors of 1.6 – 2.6.

- In her PhD thesis [46], Rima Sayah presented a similar study carried out in the gantry treatment room of the Orsay proton therapy facility. In this case, however, a water phantom was irradiated in the Double Scattering mode, using an initial proton energy of 178 MeV. She reported measurements performed with a WENDI-2 and a TEPC at angles of 50° – 125° with respect to the proton beam axis. The measurements agreed with each other within at most a factor of 1.25, but the MCNPX simulation overestimated them by factors of 1.6 – 2.4. The absence of the gantry structure in the simulated geometry was indicated as one of the possible causes for the observed discrepancies.

- Hereafter, Farah *et al.* [176] also published such a study for the fixed-beam eye line of Orsay, using an initial proton energy of 75 MeV. This treatment room did not possess a gantry. The beam was delivered through a passive technique using several scatterers and collimators. Five measurement positions were considered at angles of 0° – 120° with respect to the delivered proton beam. The WENDI-2 and TEPC measurements agreed with each other within factors of 1.1 – 1.3. The neutron H*(10) rates simulated with MCNPX agreed with the WENDI-2 measurements within factors of 1.0 – 1.4.

It thus seems that the neutron H*(10) inside treatment rooms can be simulated with relatively good accuracy when using MCNPX with the la150 libraries and the Bertini model. Nevertheless, the difficulty to achieve satisfactory accuracy seems to depend a lot on the lay-out of the treatment room, and perhaps especially on the specific structure of the gantry (if present). The considered irradiation modalities, including the initial proton energy and the beam delivery technique, might also influence the achievable accuracy.

Finally, in the context of carbon ion therapy, a successful benchmark exercise, conducted   under well-controlled conditions at GSI, was published in 2009 by members of the Coordinated Network for Radiation Dosimetry (CONRAD) [149,177,178]. The experiment was carried out in an experimental area instead of the hadron therapy room, but mimicked the typical secondary neutron production and shielding attenuation of carbon ion therapy facilities. The study is in part relevant for

the radiation protection inside proton therapy centres as well, because the neutron spectra outside the shielding have similar shapes in both types of facilities. Carbon ions of 400 MeV/nucleon, suitable for the treatment of deep-seated tumours, were delivered onto a thick carbon target. The walls of the surrounding concrete bunker had thicknesses between 160 cm and 480 cm. Neutron measurements were performed with different types of detectors in six positions outside the bunker. A good agreement in general was obtained between dose equivalent measurements of TEPCs and ambient dose equivalents measured with extended-range rem meters (including a WENDI-2) and extended-range BSSs. The measurements of conventional rem meters were however lower than those of the wide-energy-range detectors by a factor of ~1.7. The results of four different Monte Carlo simulations, carried out by three independent groups, were compared to the average ambient dose equivalents derived from the BSS measurements. Two groups each performed a "one-step" FLUKA simulation of the neutron production and subsequent attenuation through the shielding. The results of the two groups agreed well with each other for some positions, but for others discrepancies of a factor of 1.3 – 1.7 were observed (not attributable to the stated statistical uncertainties). It is not clear which parameters caused these differences. Apparently, the two groups used the same version of FLUKA (2006) and the same realistically represented shielding geometry. The simulation-to-measurement ratios were in the range of 0.8 – 1.3 in one case, and 0.8 – 1.5 in the other. Another group performed calculations with FLUKA in two steps, with separate runs for the neutron production in the target and the transport through the shielding. The FLUKA output for the neutron production in the target was also used in the definition of a neutron source of an MCNPX simulation. In the latter, a simplified rotationally symmetrical geometry was however used for the shielding. The simulation-to-measurement ratios obtained in the "two-step" FLUKA and FLUKA/MCNPX simulations were also in the range of 0.8 – 1.3. In this study, a good accuracy of the Monte Carlo simulations was thus achieved. The accuracy is better than in the abovementioned studies on the neutron shielding in proton therapy facilities [94,163,164]. Several favourable aspects should be underlined in this context [177]:

- The simulated double-differential distributions (in angle and energy) of the secondary neutrons produced by the carbon ions could be successfully benchmarked against experimental data existing in literature.

- The configuration inside the bunker was relatively simple to model, with a single experimental beam line but no treatment nozzle and no gantry structure.

- The elemental composition and density of the concrete could be determined by chemical analysis. Earlier comparisons [179,180], from the time when this information was not yet available, in fact reported simulation-to-measurement ratios of ~2 outside the shielding.

I-8 Goals of the thesis work

Monte Carlo simulations used for the shielding design of proton therapy facilities depend on many parameters, several of which tend to be difficult to control in a precise way. The exact average concrete composition of the future building is for instance rarely known in advance. Often, only a minimum density is selected beforehand and imposed on the concrete provider. The cross-sections for the interactions of protons and neutrons with matter also have limited precisions, especially in the case of projectile energies above ~20 MeV. Where possible, it is preferable to use a library of evaluated cross-section data. Above the upper limit of the evaluated data tables (e.g. 150 MeV for the la150 libraries in MCNPX), theoretical physics models however need to be invoked. Different models have been developed over the past decades but none of them truly stands out as the most accurate in general. Experimental validation data are unfortunately scarcely available at high energies. It is in fact up to the user to assess which physics options ought to be the most suitable to the considered application. Furthermore, the geometry of the treatment rooms or the accelerator room is rather complex, especially since the equipment may have a significant influence on the distribution of the neutron fluxes. Due to time constraints, only a limited amount of detail can be represented in the modelled geometry. Informed physical insight is required to identify the most important elements to model. Moreover, correctly modelling the proton beam losses, for example inside the accelerator, is not necessarily straightforward either.

As a consequence, a conservative approach is preferably adopted in the Monte Carlo simulations. In a conservative simulation, the neutron doses calculated outside the shielding are in principle overestimated, so that a safety margin will be implicitly included in the shielding design. A typical conservative choice consists for instance in defining a concrete density that is slightly lower than the minimum density requested to the concrete provider. Another one consists in selecting the physics models that lead to the highest calculated neutron doses. The simulations will also be based on the highest delivered proton energy, because the average number of secondary neutrons produced per proton increases with the energy of the proton beam.

Despite the conservative choices, it remains important to assess the overall conservative nature of the original shielding design simulations for existing proton therapy facilities. The simulation method should indeed be validated experimentally by means of comparisons with on-site neutron measurements performed outside the shielding. As highlighted in the previous section, the scientific literature contains few comparisons of this type. Moreover, amongst the studies published before 2012, we only found one that focusses on measurement positions around an actual treatment room [94] (instead of an experimental area). In this case, the measurements were however acquired with a conventional rem meter and probably underestimated the true H*(10) rates.

Therefore, a central part of this thesis work was dedicated to the acquisition of accurate neutron H*(10) measurements around the treatment rooms and the accelerator room of an existing proton therapy facility. These measurements were then compared to Monte Carlo simulations based on the same parameter choices as the original shielding design simulations. The main objective was to evaluate the degree of conservativeness of the applied simulation method, *i.e.* to verify whether the simulated neutron doses outside the shielding were indeed overestimated and if so, to which extent.

For the measurements, it was preferable to use a neutron detector that possesses a good sensitivity over the entire width of the neutron spectra, which ranged from thermal energies up to 230 MeV. The literature review actually indicated that conventional rem meters, which have a poor sensitivity for high-energy neutrons (E > 10 MeV), might underestimate the neutron H*(10) by a factor of ~2 in some positions inside proton or carbon ion therapy facilities (see section **I-7**). The WENDI-2, as an extended-range rem meter, was selected as a suitable detector because of its wide energy range and its practical use.

A first part of this work focussed on the characterisation of the WENDI-2 response according to the energy of the detected neutrons. The level of accuracy achieved in H*(10) measurements indeed depends on the local energy spectrum and the corresponding adequacy of the detector response function and calibration. As a reminder, the dose response function of a detector provides its response (in Sv) to an irradiation by neutrons of a single energy, as a function of this energy. The dose response function is the product of the calibration factor and the absolute response function. An ideal detector of which the dose response function perfectly reproduces the fluence-to-H*(10) conversion coefficients at all energies does unfortunately not exist. As a consequence, if the energy distribution of the local neutron field is very different from that of the calibration field, the reading of a detector may significantly deviate from the true H*(10) rate (depending on the local spectrum shape).

The standard calibration of a WENDI-2 is based on a ^{252}Cf field, which is characterised by a bell-shaped energy spectrum in the range of ~0.1 MeV – 10 MeV. The shapes of the neutron spectra inside a proton therapy facility are quite different, in particular behind the shielding walls (see section **I-4.3**). It should thus be verified which accuracy can be expected when measuring H*(10) with a WENDI-2 in such neutron fields. At the start of this project, there were no specific studies in literature that treated this problem in detail for WENDI-2 measurements performed inside proton therapy facilities. Jägerhofer *et al.* [181] had nevertheless suggested that a measurement uncertainty of 20% should probably be considered when using the WENDI-2 (with the standard ^{252}Cf calibration) behind the shielding of primary proton beams of ~250 MeV. They had inferred this from an experiment conducted at the Research Centre for Nuclear Physics of Osaka, with a quasi-monoenergetic neutron beam of 246 MeV and different shielding thicknesses of iron. Other engaging results

had also been reported in the CONRAD experiment at GSI [149,177,178]. Based on comparisons with Bonner Sphere Spectrometry results, the study indicated that the WENDI-2 should provide relatively accurate H*(10) measurements outside the shielding of carbon ion therapy beams. Depending on the considered position, the WENDI-2 measurements agreed indeed within 15% – 40% with the H*(10) values obtained via extended-range Bonner Sphere Spectrometry.

So far, it seems that the best way to evaluate the accuracy of a WENDI-2 measurement consists in measuring the local neutron spectrum through an adapted spectrometry technique, like in the CONRAD experiment. The WENDI-2 measurement can then be compared to an H*(10) evaluation obtained by folding the measured spectrum with the fluence-to-H*(10) conversion coefficients. In the last part of this thesis (Chapter VI), this method was actually applied for a couple of measurement positions, by means of extended-range Bonner Sphere Spectrometry. However, for the majority of the WENDI-2 measurements such an experimental validation could not be done, because we did not have access to suitable spectrometry equipment at that time. Also, Bonner Sphere Spectrometry is very time-consuming since more than half a dozen of irradiations (one per sphere) have to be performed to acquire the spectrum in a single position. With a given set of Bonner Spheres, only a few spectrum acquisitions can therefore be obtained during an 8-hour shift at the proton therapy facility.

As an alternative to the validation by means of neutron spectrometry, the project was first oriented towards the study of the WENDI-2 response function (Chapter II). The underlying goal was to fold the neutron spectra obtained in the Monte Carlo simulations of the proton therapy facility with this response function (Chapter III). In this way, the results of the shielding simulations would be directly comparable to the WENDI-2 measurements (Chapter IV).

For the characterisation of the detector response function, one generally relies on Monte Carlo simulations representing the irradiation of the detector by monoenergetic neutron beams of different energies. The simulated response function will be in principle affected by uncertainties related to, for example, the modelled geometry, the material definitions and the interaction cross-sections (selected from evaluated data tables or calculated from physics models). It is therefore important to also perform validation measurements of the response function by means of well-characterised neutron fields.

In **Chapter II**, we will present simulations of the WENDI-2 response function carried out with MCNPX 2.7.0. The results will be compared to those of other authors, calculated with different Monte Carlo codes. In a second part of the chapter, validation measurements in the range of approximately 0.1 MeV – 10 MeV, carried out with radionuclide sources of ^{252}Cf and AmBe, will be presented as well. These will be confronted to validation data from literature concerning irradiations with

monoenergetic neutron beams. The third and last part of the chapter revolves around the experimental validation of the response function at high energies (above 20 MeV). In this energy range, monoenergetic beams cannot be produced. One has to rely on quasi-monoenergetic beams, of which the spectrum is characterised by a well-marked high-energy peak and a low-energy tail extending down to 0 MeV. Due to the limited availability of quasi-monoenergetic neutron beams of high metrological quality, very few data have been published for the experimental validation of the WENDI-2 response function above 20 MeV. To our knowledge, the only published measurements are those by Olsher *et al.* [182]. These measurements were acquired with quasi-monoenergetic neutron beams at the Theodor Svedberg Laboratory (TSL), in Uppsala (Sweden). Compared to the response function simulated by Olsher *et al.* using MCNPX 2.1.5 [152], the measurements are actually lower by a factor of 2.1 in the range of 40 MeV – 150 MeV, and 1.6 at 173 MeV. Since the causes of these discrepancies were not explained, we decided to conduct a similar experiment at the TSL, to see whether the results of Olsher *et al.* would be reproducible. Section **II-4** provides a full account of this experiment, including amongst others a detailed description of the neutron fluence monitoring method.

Chapter III focusses on the MCNPX simulations of the neutron fields inside the proton therapy centre of Essen, the facility in which we performed our WENDI-2 measurements. Four case-studies will be presented: the cyclotron room, a gantry room operated in PBS, a gantry room operated in DS and the fixed-beam treatment room. The methodology followed in the MCNPX simulations will be described in detail. It relies on the same conservative hypotheses as those of the original shielding design simulations for this facility. For every position in which a WENDI-2 measurement was performed at Essen, the simulated neutron spectrum will be shown. The knowledge gathered in Chapter II about the WENDI-2 response function will be used to calculate the corresponding energy-integrated WENDI-2 responses, which can be directly compared to the measurements. We will also provide an evaluation of the uncertainties on the energy-integrated responses with respect to the uncertainties on the evaluation of the WENDI-2 response function. Finally, the simulated responses will be compared to simulated H*(10) rates, obtained by folding the neutron spectra with the fluence-to-H*(10) conversion coefficients. This comparison will give us a theoretical prediction of the accuracy of the WENDI-2 measurements in terms of H*(10) in the considered positions.

In **Chapter IV**, we will describe the experimental set-up and the results of the WENDI-2 measurements carried out at Essen. The measurements will be compared to the simulated WENDI-2 responses from Chapter III. In this way, we will assess the expected conservative nature of these simulations concerning the neutron fluxes outside the shielding.

In the shielding simulations of Chapter III, the main conservative hypotheses concern the density of the concrete as well as the physics models selected in MCNPX

for the interactions of protons and neutrons above 150 MeV. In **Chapter V**, we will explore how the results of the shielding simulations could vary if other physics models were selected, or if a different elemental composition and density was used in the material definition of concrete. A simplified spherical geometry of the shielding will be used in these studies.

In **Chapter VI**, we will present additional measurements acquired inside and around the fixed-beam treatment room, using an extended-range BSS, a conventional rem meter LB 6411 and a TEPC. The H*(10) values obtained from the BSS spectra will be used to assess the accuracy of the WENDI-2 measurements (from Chapter IV) and that of the other detectors. Furthermore, the BSS spectra will be compared to the spectra obtained in the MCNPX simulation of Chapter III. We will try to quantify the potentially conservative impact of the selected physics models on the simulation results. A comparison will also be made with MCNPX results that are based on the least conservative physics models identified in Chapter V. Finally, we will also attempt to use the measured spectrum that has the largest fraction of high-energy neutrons to validate the simulated WENDI-2 response function at high energies (as a consistency check for the results of Chapter II).

CHAPTER II
Response function of the WENDI-2

II-1 Introduction

The goal of this chapter is to characterise the WENDI-2 response function, *i.e.* to study how the WENDI-2 responds to monoenergetic neutron beams as a function of the energy of those neutrons. The motivation for this study has been outlined in section **I-8**.

This chapter consists of three main parts:

- The first part is dedicated to a theoretical study of the response function by means of Monte Carlo simulations performed with MCNPX 2.7.0 [100]. These simulation results are compared to similar results from other authors [152,183,184], obtained with different Monte Carlo codes.

- The second part focusses on the experimental validation of the simulated response function in the range of ~0.1 MeV – 10 MeV. The validation relies on measurements performed with radionuclide sources of ^{252}Cf and AmBe in the Laboratory for Nuclear Calibrations of the SCK-CEN (Mol, Belgium). The measurements were performed following the recommendations of the ISO 8529 norm [145,185,186]. The results were also confronted to a series of monoenergetic neutron beam measurements published by Olsher *et al.* [152].

- The third part revolves around the experimental validation of the WENDI-2 response function at energies between ~20 MeV and ~175 MeV. Calibration neutron fields in this energy range are typically produced by means of cyclotron-accelerated protons or deuterons reacting with a light element target (Li or Be). Truly monoenergetic neutron beams cannot be produced because the high energy of the charged projectile generally exceeds the threshold for multi-body break-up reactions. This creates a continuous low-energy tail in the neutron spectrum, which is therefore referred to as "quasi-monoenergetic". The presence of this low-energy tail constitutes a major complication for the high-energy calibration of extended-range rem meters like the WENDI-2, which have a good sensitivity to both the peak and tail neutrons. In fact, no international standard comparable to the ISO 8529 norm currently exists for this type of high-energy calibrations [187]. In this work, WENDI-2 measurements were performed in high-energy quasi-monoenergetic neutron beams at the Theodor Svedberg Laboratory (Uppsala, Sweden). The results are compared to similar measurements of Olsher *et al.* [182], which were acquired in the same facility in a slightly different manner (see section **II-4.2.4**).

II-2 Simulation of the WENDI-2 response function

II-2.1 Methodology

II-2.1.1 Main principle

The WENDI-2 absolute response function, expressed in counts per unit neutron fluence, was evaluated with MCNPX 2.7.0 [100] for 80 neutron energies between 10^{-9} MeV and 250 MeV. The value of the absolute response function at a given energy was calculated as the ratio of the results from two different simulations:

- In the first simulation, the structure of the detector was modelled (see Figure **II-1 (a)**). Details on the geometric model will be given in the following section. This simulation calculated the average number of counts generated in the helium tube per source-emitted neutron.

- In the second simulation, only air was considered and the volume-averaged neutron fluence per source-emitted neutron was calculated within a reference volume. Following the convention adopted by other authors [152,183,184], the reference volume corresponds to the sensitive volume of the helium tube defined in the first simulation. In this simulation, however, this cylindrical volume is filled with air instead of helium (see Figure **II-1 (b)**).
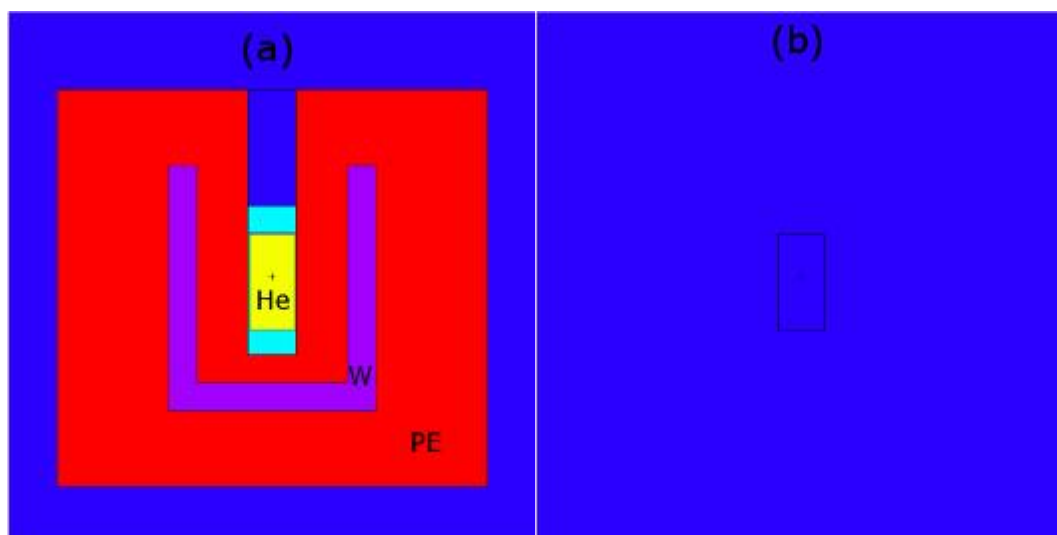
Figure II-1 - Geometry of the MCNPX simulations used to calculate (a) the counts generated in the WENDI-2, and (b) the average neutron fluence within the reference volume.

II-2.1.2 Definition of the neutron source

The response function was simulated for lateral irradiations of the WENDI-2. The reason hereof is that, in the measurements reported in this thesis, the main neutron flux reached the detector from lateral angles. (Directional response measurements with radionuclide sources can also be found in [152]).

Two different geometric configurations of the monoenergetic neutron source were compared for the simulation of the WENDI-2 response function:

- In the first version, an isotropic point source located at 50 cm from the centre of the detector was considered, following the work of Olsher *et al.* [152] and that of Vanaudenhove *et al.* [184]. To speed up the calculation, the isotropic emission was actually limited to a cone circumscribed to the detector, having a half aperture angle α of 17.25°. This variance reduction method was also applied by Vanaudenhove *et al.* [184].

- In the second version, a rectangular parallel beam that encompasses the whole volume of the detector, was used as in the work of Jägerhofer *et al.* [183]. The neutron emission originated from a 23 x 24 cm² rectangle at 50 cm from the centre of the detector.

II-2.1.3 Modelling of the WENDI-2

The counter tube at the centre of the WENDI-2 is a cylindrical ^{3}He-filled proportional counter Type 252180 manufactured by LND, Inc (New York). The active volume was modelled as a ^{3}He cell with a diameter of 2.438 cm and a height of 5.13 cm, following the specifications in [188]. The ^{3}He density was set to 0.333 kg/m^3, correspondingly to the gas pressure of 2 atm indicated in [188]. For the 0.5 cm thick tube hull, a generic elementary composition of stainless steel was defined with 74% Fe, 18% Cr and 8% Ni in mass, and a density of 8 g/cm^3. The borated rubber patch, which closes off the air volume above the counter tube, was not represented in the simulations, because of its negligible influence during side irradiations of the detector.

The central counter tube is surrounded by a thick polyethylene moderator with an embedded layer of tungsten powder. The outer diameter of the WENDI-2 is of 22.86 cm and its height of 21 cm. The assumption was made that the polyethylene has a medium density of 0.94 g/cm^3 [189,190]. The tungsten shell was defined with an inner radius of 4.0 cm and a thickness of 1.5 cm [152]. Its density was set to 10.624 g/cm^3, according to R.H. Olsher's estimate for the effective density of the tungsten powder [184]. An overview of the material definitions used in the simulations is given in table **II-1**.

Table II-1 - Material definitions in the MCNPX simulation of the WENDI-2 counts. The upper limit in energy of the cross-section data tables applies to both the neutron and the proton data.

Material	Isotope or element	Atom fraction	Neutron library	Upper limit (MeV)	Proton library
Polyethylene 0.94 g/cm^3	^{1}H	0.666667	la150n & s(α,β)	150 4.10^{-6}	endf70prot
	^{nat}C	0.333333	la150n	150	/
Tungsten powder 10.624 g/cm^3	^{184}W	0.306203	la150n	150	endf70prot
	^{186}W	0.281056	la150n	150	endf70prot
	^{182}W	0.267745	la150n	150	endf70prot
	^{183}W	0.144996	la150n	150	endf70prot
Stainless steel 8 g/cm^3	^{56}Fe	0.671469	la150n	150	endf70prot
	^{54}Fe	0.044354	la150n	150	endf70prot
	^{57}Fe	0.015234	la150n	150	endf70prot
	^{58}Fe	0.001996	endf70b	20	/
	^{52}Cr	0.160062	la150n	150	endf70prot
	^{53}Cr	0.017967	la150n	150	endf70prot
	^{50}Cr	0.008661	la150n	150	endf70prot
	^{54}Cr	0.004369	la150n	150	endf70prot
	^{58}Ni	0.051998	la150n	150	endf70prot
	^{60}Ni	0.019365	la150n	150	endf70prot
	^{62}Ni	0.002599	la150n	150	endf70prot
	^{61}Ni	0.000826	la150n	150	endf70prot
	^{64}Ni	0.000640	la150n	150	endf70prot
Helium 3.33 · 10^{-3} g/cm^3	^{3}He	1	endf70a	20	endf70prot
Air 1.205 · 10^{-3} g/cm^3	^{14}N	0.784431	la150n	150	endf70prot
	^{16}O	0.210748	la150n	150	endf70prot
	^{nat}Ar	0.004671	rmccsa	20	/
	^{nat}C	0.000150	la150n	150	/

II-2.1.4 Calculation of the WENDI-2 counts

The ^{3}He(n,p)^{3}H reactions constitute the main count generating mechanism in the WENDI-2. In our simulations, the average number of (n,p) reactions per source-emitted neutron was obtained by folding the average neutron fluence in the ^{3}He volume with the ^{3}He(n,p)^{3}H cross-section from the ENDF/B-VII.0 evaluation [122] (table 2003.70c [100]), multiplied hereafter by the atomic density of the gas and the volume of the gas cell. To that end, a tally multiplier card (FM4 -1 1 103) and a segment divisor card (SD4 1) were associated to a F4:n tally defined in the helium cell [100].

With this method, each (n,p) reaction was assumed to generate one count, meaning that any count losses due to the wall effect were neglected. The wall effect corresponds to the situation in which one or both of the reaction products of an (n,p) reaction escape the gas volume without having deposited together enough energy to trigger a count. In the WENDI-2, the minimum energy deposition required for this is of 50 keV, due to the lower discriminator of the detector electronics which is set to

1 mV [152]. Jägerhofer *et al.* used the Monte Carlo code FLUKA to simulate the spectrum of the energy depositions in the gas and estimated herefrom that only 1.1% of the (n,p) reactions do not trigger counts (on average, for all incident neutron energies considered) [183]. Therefore, even if our simulation method does not account for the wall effect, it was judged sufficiently satisfactory for our purposes.

The neutron cross-sections available for ^{3}He in the ENDF/B-VII.0 evaluation [122] are shown in figure **II-2**. In the total generated WENDI-2 counts, the contribution of neutron absorbing reactions other than (n,p) is evidently negligible at energies below a few MeV. Above the reaction threshold of 5 MeV, the (n,d) reaction becomes possible, but the number of these reactions, which was evaluated in a similar manner as the number of (n,p) reactions, was found to be negligible compared to the latter (< 0.01%, at all energies).
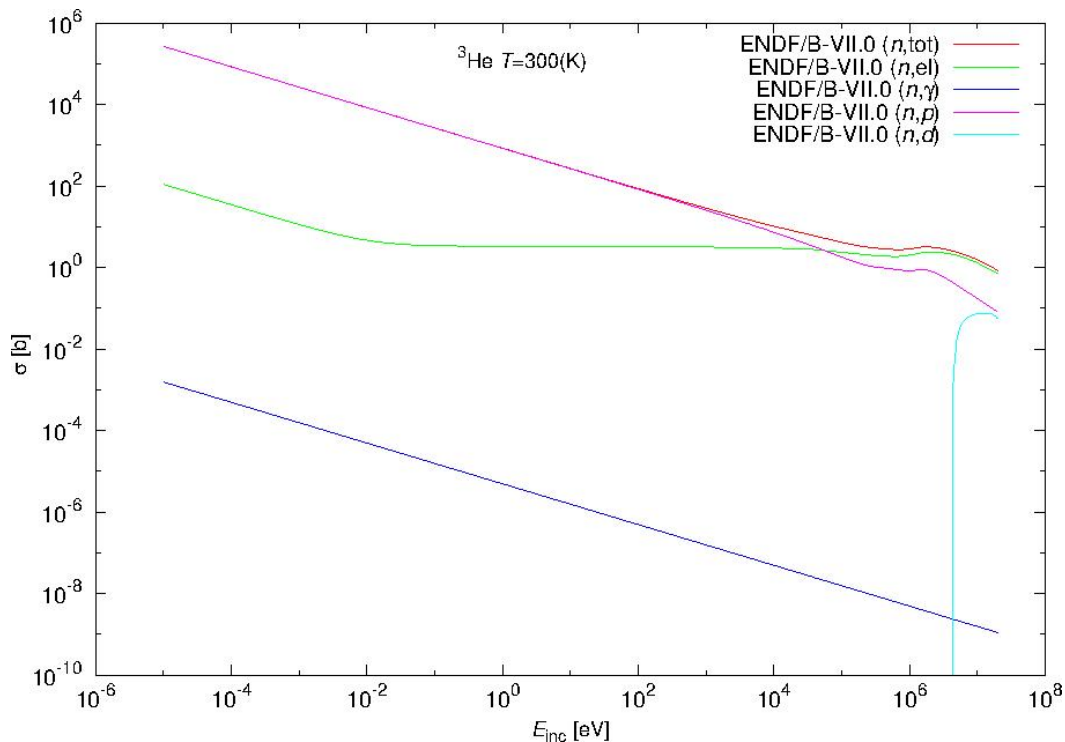
Figure II-2 - Neutron cross-sections for ^{3}He from the ENDF/B-VII.0 evaluation (figure from [191]*). The cross-section of the (n,p) reaction is shown in pink, that of the (n,d) reaction in cyan.*

Some of the charged particles – protons, mainly – that are produced by neutron interactions inside the solid materials of the detector may also cross the helium volume and occasionally deposit enough energy therein to trigger counts. This contribution, which is believed to be small in the considered energy range (below 250 MeV), was not taken into account in our calculation of the absolute response function of the WENDI-2. The response function calculations referenced in [152,183,184] did not include this contribution either. Olsher *et al.* calculated nevertheless that, at the incident neutron energy of 500 MeV, this contribution from protons, deuterons, tritons, ^{3}He ions, charged pions and muons represents only ~2.5% of the total counts (and ~3% at 5 GeV) [152].

Pions can only be produced in the intranuclear cascade above the threshold of ~280 MeV for an incident neutron (or proton) [65]. Therefore, the decay of neutral pions into highly energetic photons and the possible subsequent photon-induced nuclear reactions did not need to be considered over the studied energy range. It thus sufficed to only track neutrons and protons for the simulation of the intranuclear cascades.

II-2.1.5 Evaluated cross-section data and physics models

Neutron interaction cross-sections from the la150n library [113,119], defined up to 150 MeV, were used wherever possible, namely for all isotopes/elements except ^{3}He, ^{58}Fe and Ar (see table **II-1**). In the same manner, the available data from the endf70prot library [192] was used for the proton cross-sections (see table **II-1**). Most of the data included in the endf70prot library is given up to 150 MeV since it originates directly from the la150h library [113,119].

By default, MCNPX treats neutron scattering by using a free-gas approximation for the target nuclei. Below neutron energies of a few eV, this approximation is no longer valid in liquids and solids because the energy transfers in scattering become similar to different types of excitation energies of condensed matter. In such case, the binding of the target nucleus has an important effect on the scattering cross-section and on the angular and energy distributions of the scattered neutrons. To account for these effects in the scattering on hydrogen nuclei inside polyethylene, the $S(\alpha,\beta)$ poly.01t table from the tmccs library (ENDF/B-V evaluation) [100], was used below 4 eV.

Initially, neutron and proton interactions for which no evaluated cross-section data was available (at projectile energies above 150 MeV, essentially), were simulated using the default physics models of MCNPX 2.7.0. These encompass the Bertini intranuclear cascade model, the multistage pre-equilibrium exciton model and the Dresner evaporation model (or the Fermi break-up model for light nuclei).

In a second phase, the sensitivity of the calculated response function to the selected physics models was assessed. All possible combinations of intranuclear cascade and evaporation models available in MCNPX 2.7.0 were tested. These combinations are summarized in table **II-2**. The CEM03 model (version .02) differs from the other intranuclear cascade models in the sense that it is a self-contained package which includes its own pre-equilibrium and evaporation models, and which does not offer any user-adaptable options [100]. For the other models, only default parameters were used. Thus, after using the Bertini, Isabel or INCL4 model, the multistage pre-equilibrium exciton model was invoked, followed by [100]:

- the Fermi break-up model, if the atomic mass number A ≤ 13, or if 14 ≤ A ≤ 20 and the excitation energy E* < 44 MeV, or

- the selected evaporation model, in the other cases.

With the CEM03 model, the Fermi break-up model is used at any stage of the reaction as soon as A < 13.

Table II-2 – Possible combinations of the models available in MCNPX 2.7.0 for the intranuclear cascade and the evaporation.

Intranuclear cascade	Evaporation
Bertini	Dresner (ATC80)
Bertini	ABLA
Isabel	Dresner (ATC80)
Isabel	ABLA
INCL4	Dresner (ATC80)
INCL4	ABLA
CEM03	

II-2.2 Results

II-2.2.1 Absolute response function

II-2.2.1.1 With the default physics models of MCNPX 2.7.0

Figure **II-3** shows the simulation results for the average number of WENDI-2 counts generated per source-emitted neutron, as a function of the energy of the source neutrons. The corresponding absolute response function is calculated by normalizing these results with respect to the reference neutron fluence in air (per source-emitted neutron), for which the simulation results are shown in Figure **II-4**. The neutron fluence in air depends very little on the neutron energy. The small decrease in the fluence for decreasing neutron energies is related to the fact that the air outscatter between the source and the reference volume is more important for lower neutron energies. However, the effect is very small in this case thanks to the short distance between the source and the reference volume. For the rectangular parallel beam, the simulated average fluence at high energy (where the air outscatter is negligible) corresponds, as expected, to the inverse area of the source: 1/(23.0 cm . 24.0 cm) = 0.00181 cm^{-2}. In the case of the point source, emitting neutrons isotropically in a cone circumscribed to the detector, the average fluence per source-emitted neutron at high-energy is equal to 0.00142 cm^{-2}. This corresponds to the inverse of the area $S = \Omega.d^2$, where $\Omega = 0.282$ sr is the solid angle of the source emission and $d = 50$ cm the distance from the source to the centre of the reference volume.
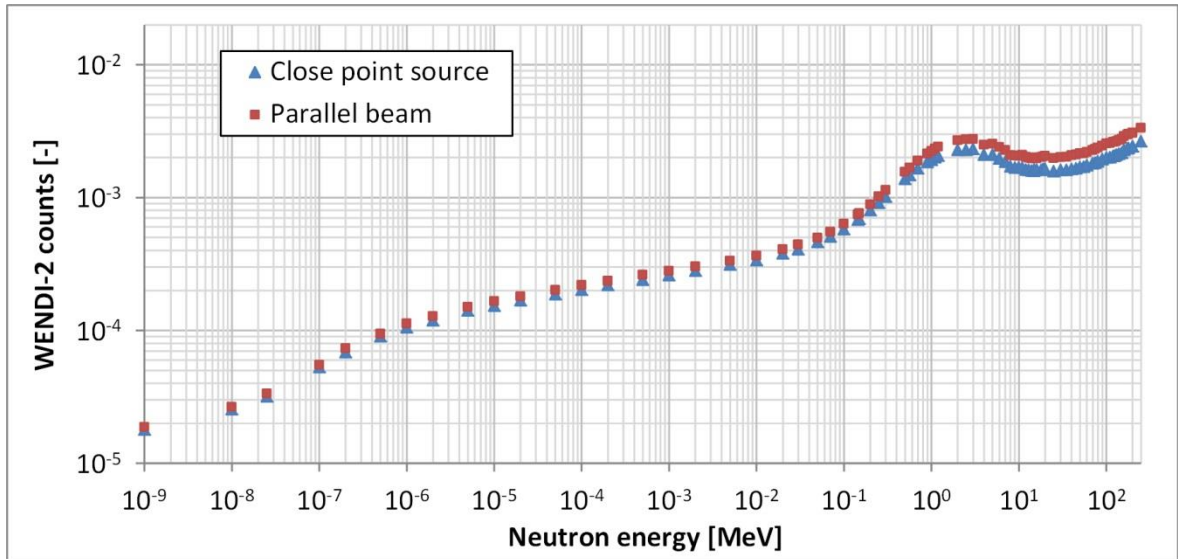
Figure II-3 – Simulated number of WENDI-2 counts per source-emitted neutron, for the close point source and for the rectangular parallel beam. The relative statistical MCNPX uncertainties are well below 1%.
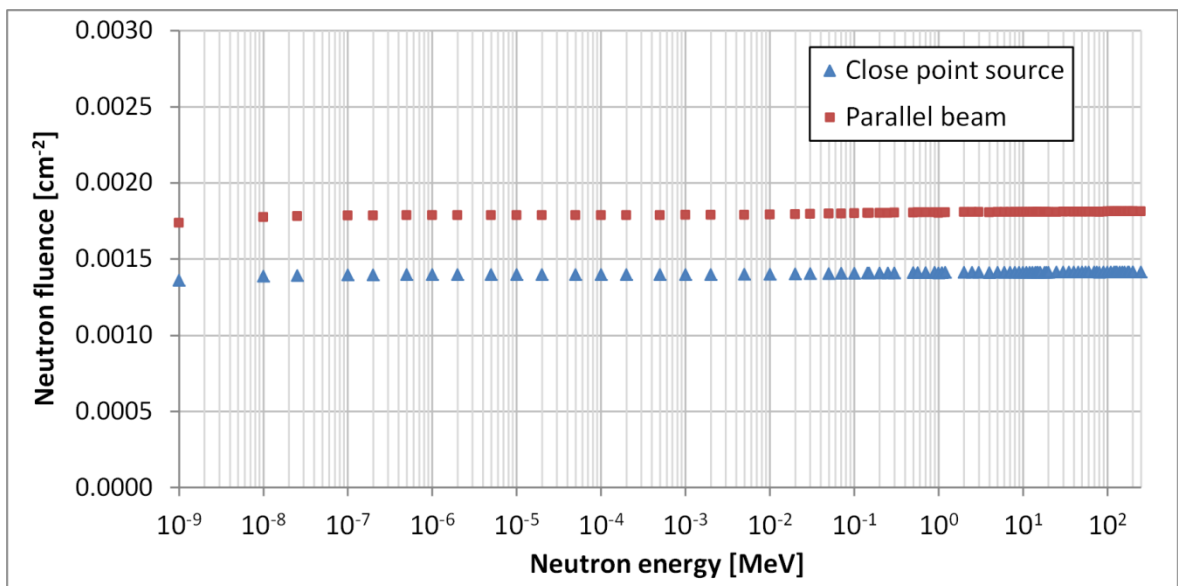
Figure II-4 –Simulated free-in-air neutron fluence per source-emitted neutron, for the close point source and for the rectangular parallel beam. The relative statistical MCNPX uncertainties are well below 1%.
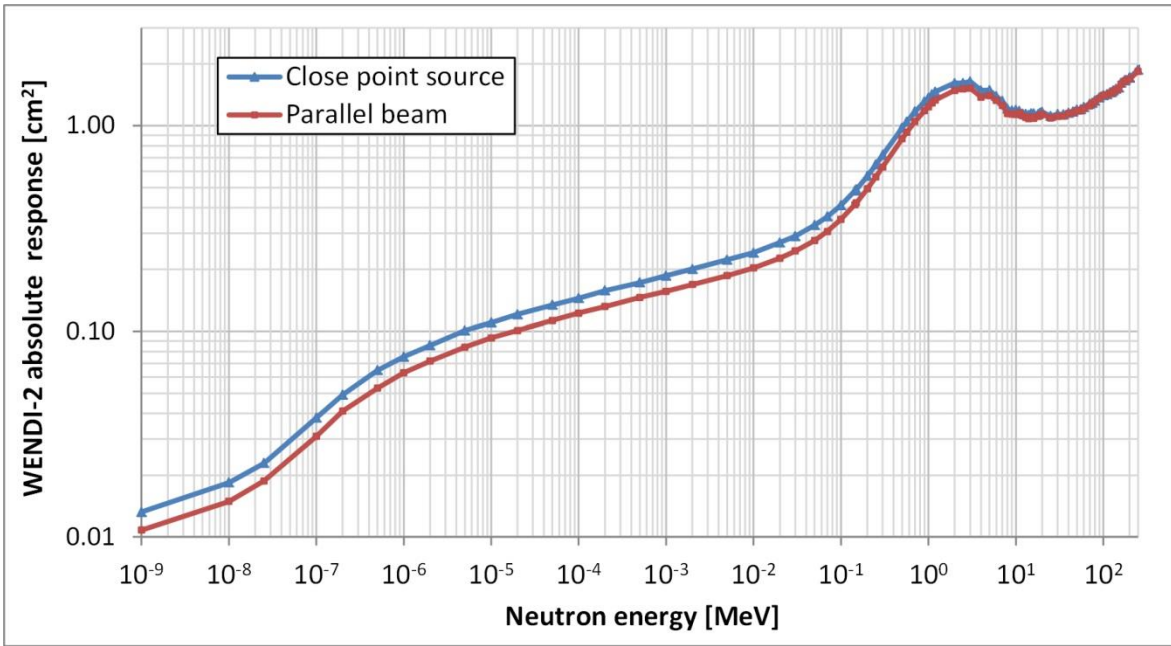
Figure II-5 - Absolute response function of the WENDI-2, simulated with the close point source and with the rectangular parallel beam. Neutron interactions above 150 MeV were calculated with the default physics models of MCNPX 2.7.0 (Bertini & Dresner). The relative statistical uncertainties are smaller than 1%. The lines connecting the points are only a guide for the eye.
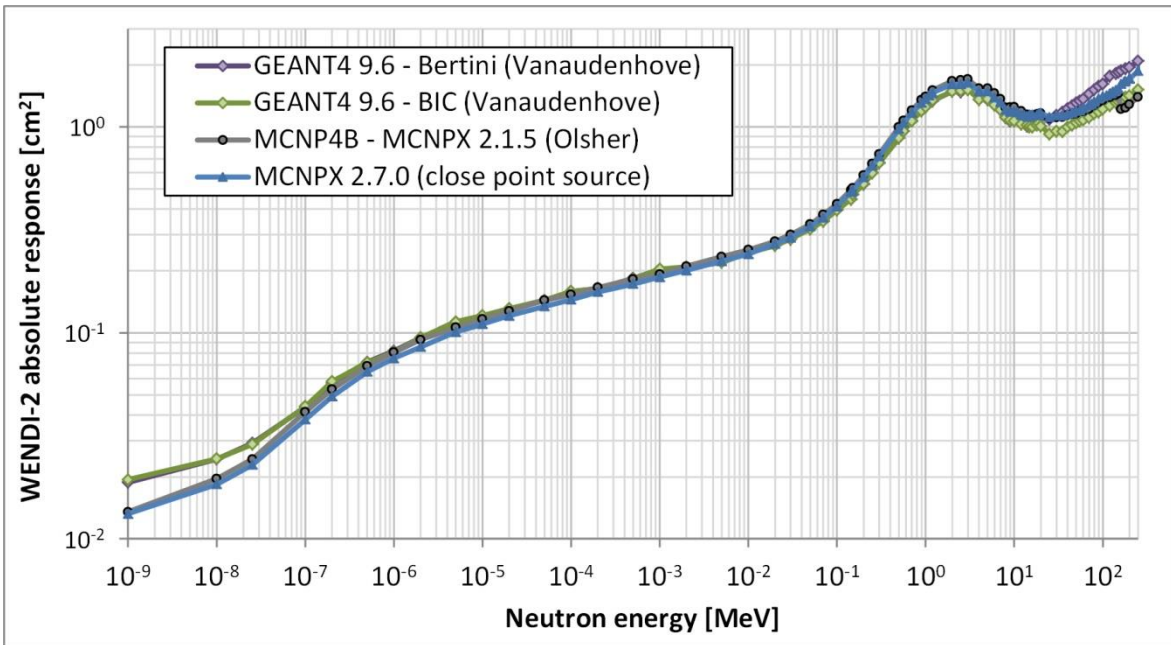
Figure II-6 - Absolute response function of the WENDI-2 for a close point source (simulated with MCNPX 2.7.0 using the Bertini & Dresner models): comparison with the results obtained by Olsher et al. using MNCP4B and MCNPX 2.1.5 [152] and by Vanaudenhove et al. using GEANT4 9.6 with (a) the Bertini model and (b) the BIC model [184]. The two curves of Vanaudenhove et al. are identical below 20 MeV because they rely on the same evaluated cross-section data.
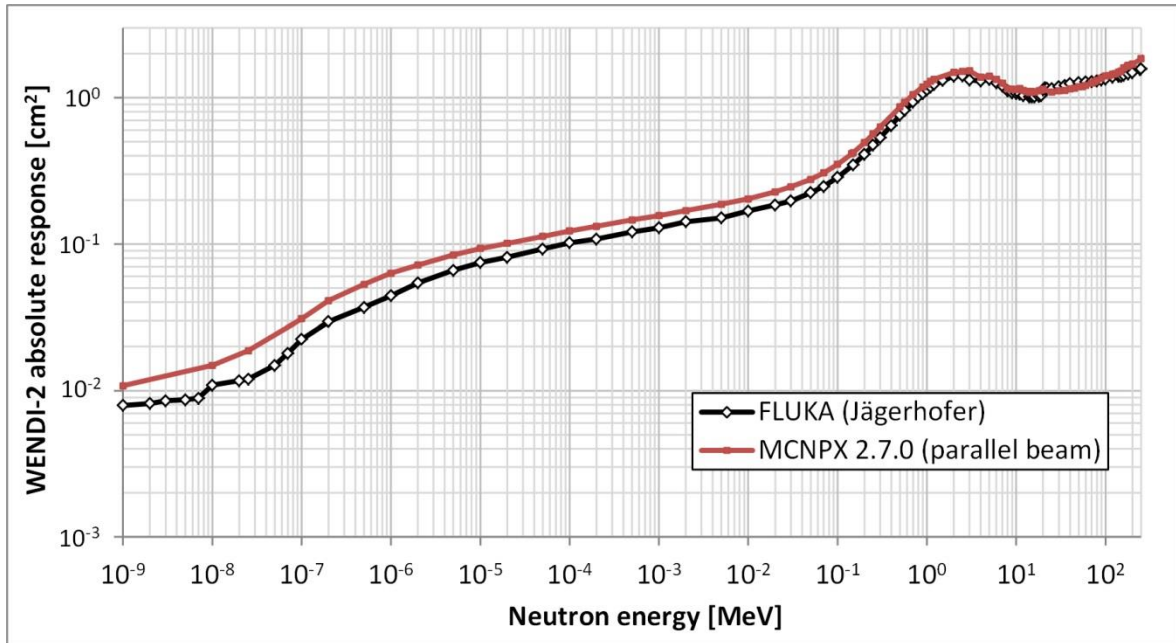
Figure II-7 - Absolute response function of the WENDI-2 for a rectangular parallel beam (simulated with MCNPX 2.7.0 using the Bertini & Dresner models): comparison with the results obtained by Jägerhofer et al. using FLUKA [183].

The calculated absolute response functions corresponding to the close point source and to the rectangular parallel beam are compared in Figure **II-5**. With respect to the parallel beam irradiation, the use of the close point source increases the absolute response function by ~20% for thermal neutrons, and by ~5-15% for neutrons between 0.5 MeV and 10 MeV (evaporation neutrons). The influence of the source configuration thus decreases with increasing energies, and becomes entirely negligible above ~70 MeV. High-energy neutrons tend to travel more in straight line through matter than low-energy neutrons, which undergo more scattering. At high energies, the parallel beam therefore leads to a larger number of counts than the close point source (see Figure **II-3**). In the absolute response, this increase at high energies is however compensated by a similar increase in the neutron fluence in air (see Figure **II-4**).

Our absolute response function simulated with the close point source configuration is compared in Figure **II-6** to the results of other authors who used that same source definition:

- Olsher *et al.* [152]: used previous versions of MCNPX, namely MCNP4B below 20 MeV and MCNPX 2.1.5 above 20 MeV. Like in our work, their simulations relied on evaluated data for the S(α,β) thermal treatment of hydrogen in polyethylene (below 4 eV) and on the la150 libraries (up to 150 MeV). A good agreement of our response function with theirs was obtained below 150 MeV. Their response function differs from ours by less than 10% in the thermal region, and less than 5% at other energies up to 150 MeV. The small differences

can be due to little variations in the geometric model or material definitions. For neutron interactions above 150 MeV, Olsher *et al.* used the first implementation of the CEM model (CEM95). It led to a discontinuity in the response function around 150 MeV which, to our knowledge, is not physically justified. Between 150 MeV and 250 MeV, the response function of Olsher *et al.* is ~25% smaller than ours, which must be mainly due to the use of different hadronic models. Our response function, which is based on the Bertini & Dresner models, does not have a marked discontinuity around 150 MeV.

- Vanaudenhove *et al.* [184]: used the Monte Carlo code GEANT4 9.6. For the scattering of neutrons by hydrogen nuclei of polyethylene, their simulations invoked evaluated S(α,β) thermal scattering data from the class G4NeutronHPThermalScattering below 4 ev. This data was based on the ENDF/B-VI.2 evaluation (a more recent evaluation than the one used in the poly.01t table of MCNPX). At thermal energies, the response function of Vanaudenhove *et al.* is 20-40% larger than ours. For neutron interactions up to 20 MeV, Vanaudenhove *et al.* used cross-section data from the G4NDL 4.2 library, which is based on the ENDF/B-VII.0 evaluation [122]. In this energy range, their response function agrees within 10% with ours. Above 20 MeV, evaluated cross-section libraries were not available in GEANT4 9.6 and hadronic non-elastic models had to be selected. Two different intranuclear cascade models of GEANT4 9.6 were compared in this case: the Bertini model [66,67,193] and the Binary Intranuclear Cascade Model (BIC) [194,195]. In both cases, the simulated intranuclear cascade is followed by the Griffin exciton pre-equilibrium model [61,196] and the Weisskopf evaporation model [56,197] (or the Fermi break-up model [58,198], for light nuclei). Between 20 MeV and 250 MeV, the use of the GEANT4 Bertini model led to a response function which is up to ~20% larger than our function based on the la150n library and the Bertini model of MCNPX. The response function based on the GEANT4 BIC model, on the other hand, is ~10-20% smaller than our response function over that same energy range.

For a lateral irradiation by a parallel beam, our simulated response function is compared in figure **II-7** to the corresponding results of Jägerhofer *et al.* [183], who used the Monte Carlo code FLUKA [106]. For the interactions of neutrons up to 20 MeV, FLUKA uses a cross-section library which is divided in 260 energy groups and provides group-to-group transfer probabilities [199]. This library is continuously updated according to the most recent evaluations (including ENDF/B evaluations) and contains specific data for hydrogen in its bound state within polyethylene [199]. However, Jägerhofer *et al.* did not indicate in their paper [183] which version of FLUKA (and which cross-section data) they used. Compared to our parallel beam response function, theirs is ~25–35% smaller at thermal energies and only ~3-13% smaller in the range of 0.5 MeV – 20 MeV. Between 20 MeV and 250 MeV, the hadron interactions in FLUKA are modelled through the Generalised Intra-Nuclear Cascade

(GINC) model [65,200], the Blann exciton pre-equilibrium model [65,201–204] and the Weisskopf evaporation model (as adapted by Ferrari & Sala) [56,65,205] (or, for light nuclei, the Fermi break-up model [58,65]). The response function of Jägerhofer *et al.* differs from ours by less than 10% in the range of 20 MeV – 150 MeV, while it is 10-15% smaller than ours in the range of 150 MeV – 250 MeV.

Without distinguishing between the two different source configurations, the largest observed discrepancies between all different results here compared, are of:

- a factor of 3.0 at thermal energies (GEANT4 *vs.* FLUKA),
- a factor of 1.3 in the range of 0.5 MeV – 20 MeV (MCNP4B *vs.* FLUKA),
- a factor of 1.5 in the range of 20 MeV – 250 MeV (GEANT4 Bertini *vs.* MCNPX 2.1.5).

II-2.2.1.2 Influence of the selected physics models in MCNPX 2.7.0

Figure **II-8** shows how the simulated WENDI-2 response function varies in the range of 150 MeV – 250 MeV according to the intranuclear cascade and evaporation models selected within MCNPX 2.7.0. Without varying the evaporation model, the intranuclear cascade models Bertini and Isabel seem to produce nearly identical results, whereas INCL4 yields 6-7% smaller results in general. Comparing the evaporation models (without varying the intranuclear cascade model), the results are 8-9% smaller when using ABLA instead of Dresner.
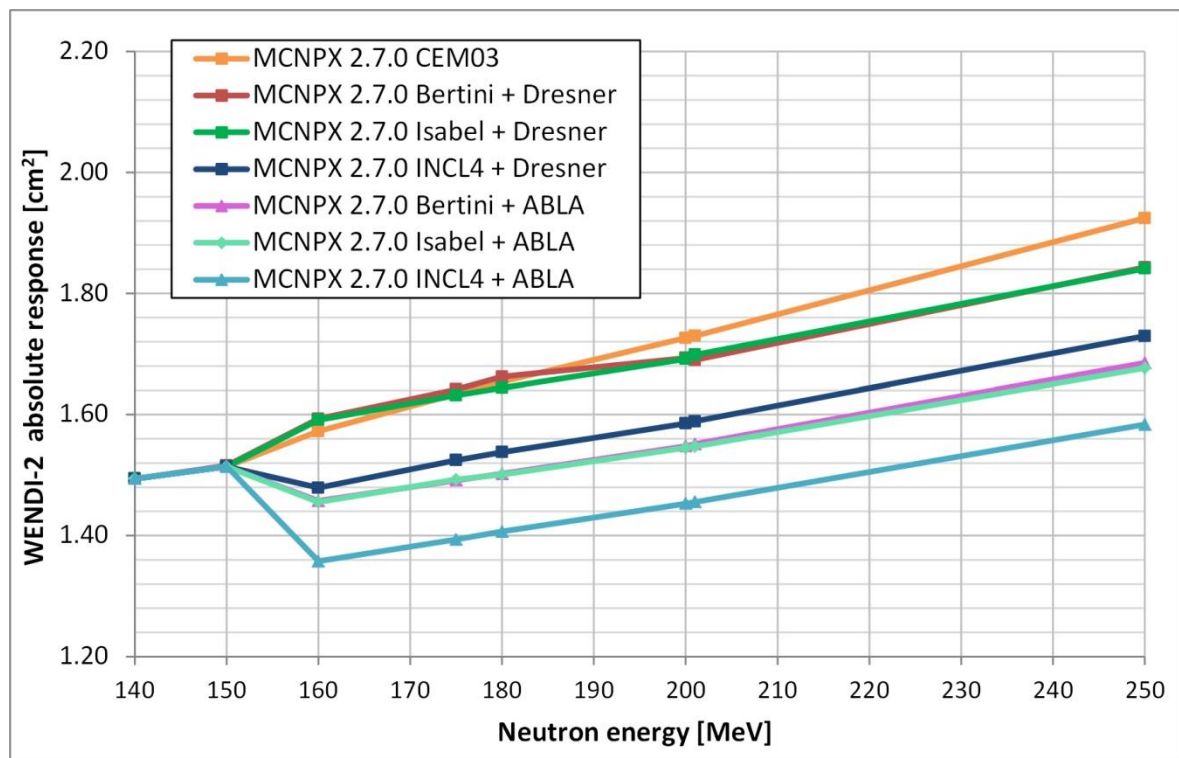
Figure II-8 – Absolute WENDI-2 response function, as simulated above 150 MeV using the seven possible combinations of hadronic models in MCNPX 2.7.0.

The choice of the selected hadronic models within MCNPX 2.7.0 has thus a relatively limited impact on the simulated WENDI-2 response function between 150 MeV and 250 MeV. Compared to the 'default' response function based on the Bertini & Dresner models, the largest positive discrepancies were obtained with the CEM03 model (+4% at 250 MeV) and the largest negative discrepancies with the INCL4 & ABLA models (-15% around 160-180 MeV). These differences are smaller than those observed with the results of Vanaudenhove *et al.* and Olsher *et al.* (see figure **II-9**).
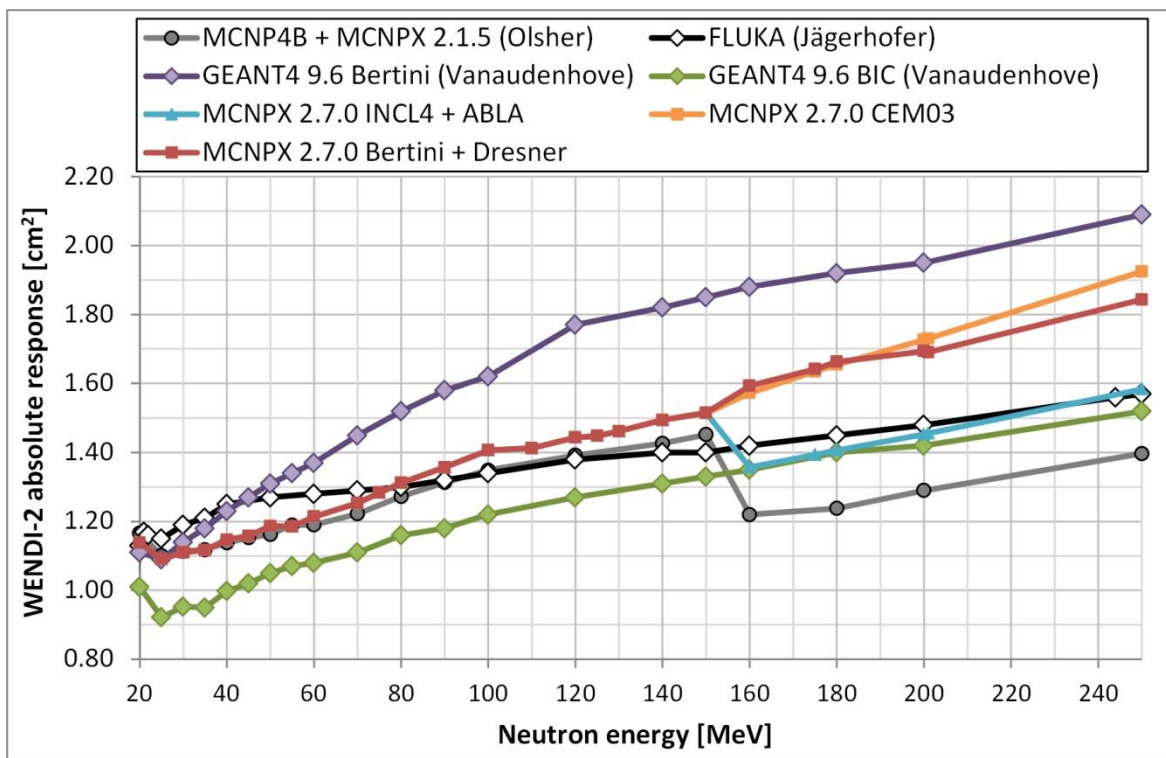
Figure II-9 – Absolute WENDI-2 response function simulated with MCNPX 2.7.0 using the Bertini & Dresner models (in red), the CEM03 model (in orange), and the INCL4 & ABLA models (in blue), compared to the results of Olsher et al. [152], Jägerhofer et al. [183] and Vanaudenhove et al. [184].

II-2.2.2 Dose response function

The built-in calibration factor of the WENDI-2 allows converting the number of counts into a dose expressed in Sv. According to the datasheet provided by the manufacturer for our detector [155], this calibration factor corresponds to 1.14 (μSv/h)/(counts/s), which is equal to $3.17 \cdot 10^{-10}$ Sv/count. To obtain the dose response function of our WENDI-2, our simulated absolute response function was multiplied by this calibration factor. These results, for a parallel beam irradiation, are

shown in figure **II-10** together with the fluence-to-H*(10) conversion coefficients from ICRP Publication 74 [87]. The ratio of the dose response function to the fluence-to-H*(10) coefficients, which is called the relative dose response function, is also given in figure **II-11**, along with the results from other authors [152,183,184] (considering the same calibration factor).
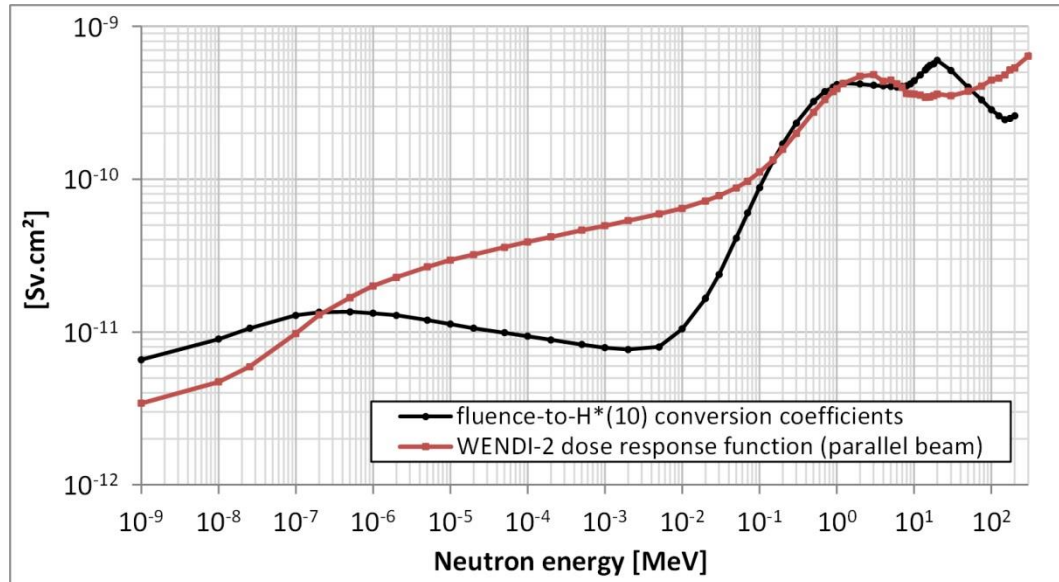
Figure II-10 - Dose response function of the WENDI-2 for a lateral irradiation by a parallel beam, compared to the fluence-to-H(10) conversion coefficients from ICRP Publication 74 [87].*
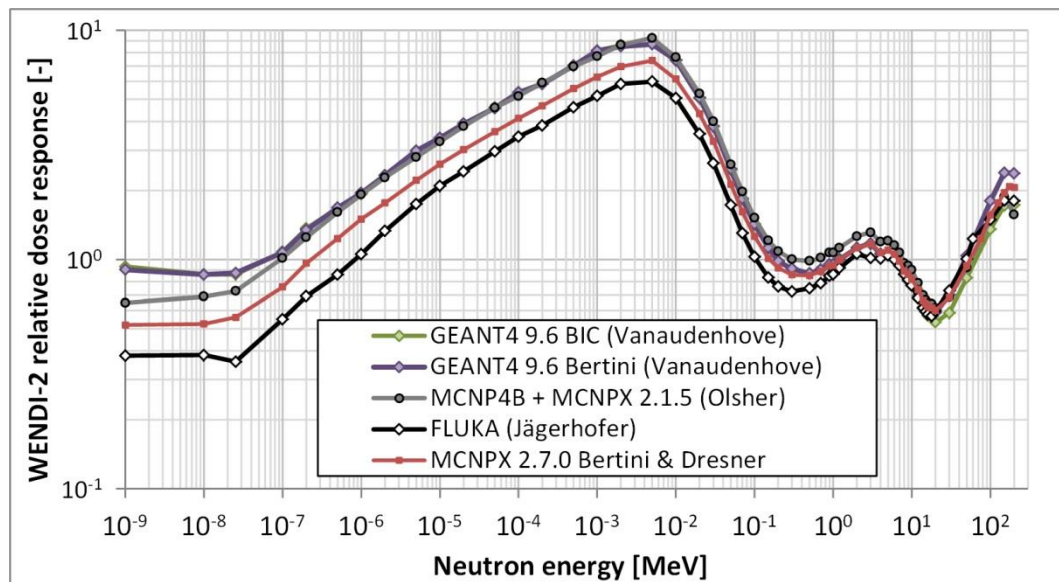
Figure II-11 - Relative dose response function of the WENDI-2, as simulated with MCNPX 2.7.0 using the Bertini & Dresner models, and as calculated by Olsher et al. [152], Jägerhofer et al. [183] and Vanaudenhove et al. [184], considering a calibration factor of 3.17 · 10-10 Sv/count.

The WENDI-2 was calibrated by Thermo Scientific using a bare ^{252}Cf source. Therefore, in the emission range of such a neutron source (~0.1 MeV – 10 MeV), the obtained dose response function matches as expected quite closely with the fluence-to-H*(10) conversion coefficients. At high energies (10 MeV – 250 MeV) and at thermal energies, the dose response function differs from the ICRP 74 coefficients by at most a factor of 2. The agreement is less satisfactory at intermediate energies (1 eV – 0.1 MeV), where the dose response function overestimates the ICRP 74 coefficients by up to a factor of ~7.

Except for neutrons in the range of 0.1 MeV – 10 MeV, relatively large discrepancies thus exist between the predicted WENDI-2 dose response function and the ideal behaviour required to measure H*(10) accurately in any neutron field. Fortunately, intermediate neutrons do not represent a large fraction of the typical neutron spectra encountered behind the shielding of proton therapy rooms (see section **III-3**). In such neutron fields, the WENDI-2 response will be in fact largely determined by the neutrons of the evaporation peak and the cascade peak. The response function in these energy regions is indeed more than ten times larger than for thermal neutrons. In principle, the response to the evaporation neutrons (0.1 MeV – 10 MeV) ought to be quite accurate. The accuracy of the WENDI-2 measurements will thus depend for a great deal on the capacity to accurately measure the contribution of the high-energy neutrons. Judging from the simulated dose response function, that contribution has the potential to be relatively accurate too, thanks to a compensating effect between the underestimated response to neutrons of ~10 – 50 MeV and the overestimated response above ~50 MeV.

The validity of the simulated response function needs however to be verified experimentally. In the context of this thesis work, the experimental validation seems especially important for the evaporation neutrons and the high-energy neutrons up to ~230 MeV. The following parts of this chapter are therefore dedicated to validation measurements in these energy regions.

II-3 Validation measurements using radionuclide source of ^{252}Cf and AmBe

II-3.1 Methodology

II-3.1.1 Experiment

WENDI-2 measurements were performed with radionuclide sources of ^{252}Cf and AmBe at the Laboratory for Nuclear Calibration (LNC) of the SCK-CEN, in Mol, Belgium. The SCK-CEN staff provided us with the up-to-date reference H*(10) rates delivered by the sources. The calibration of these sources is traceable to primary standards from the National Physical Laboratory in the United Kingdom.

The measurements were performed inside the LNC bunker represented in the figures **II-12** and **II-13**. The neutrons sources were stored in pits below the floor and lifted up by a cable into the bunker when irradiations had to be performed.

In a first series of measurements, the bare ^{252}Cf source labelled as 'CF3' was used. As indicated in the figure **II-12**, the WENDI-2 was placed at three different distances from this source: 0.69 m (position 1), 1.00 m (position 2) and 2.00 m (position 3). In a second series, measurements were acquired at two different distances from the AmBe source: 1.00 m (position 4) and 2.00 m (position 5). For all measurements, the position of the detector was adjusted using a horizontal laser at source height as well as a vertical plumb line. The geometric centre of the detector was considered to be the reference point for the measurements.
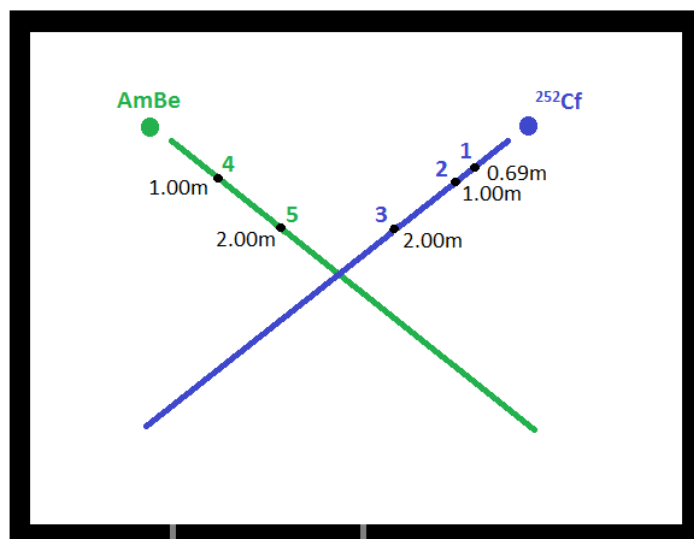
Figure II-12 - Measurement positions with respect to the radionuclide sources in the LNC bunker.
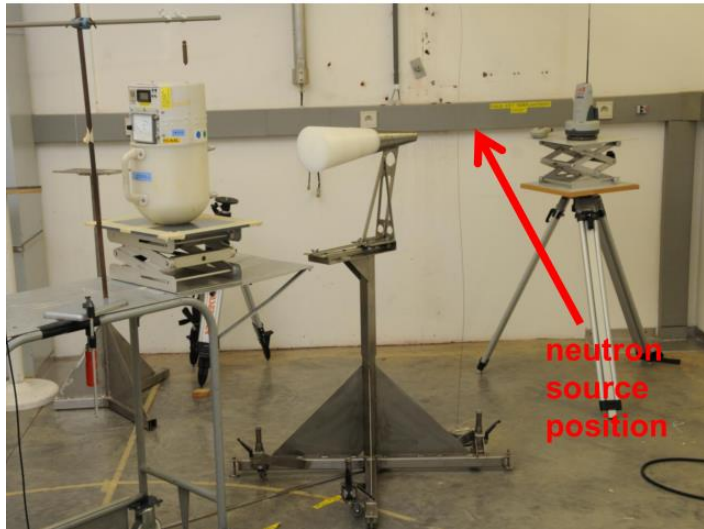
Figure II-13 - Picture of a rem meter calibration procedure performed with the shadow cone technique in the LNC bunker (courtesy of SCK-CEN).

Without any uplifted radionuclide sources inside the bunker, only 12 counts were registered with the WENDI-2 within 200 s, which corresponds to a neutron background of (68 ± 24) nSv/h. This background was negligible compared to the dose rates delivered by the uplifted radioactive sources (see table **II-3**). Dead-time losses were also considered to be negligible in all measurements, since the measured dose rates were well within the range of WENDI-2 specified by the manufacturer (1 nSv/h – 100 mSv/h [154]) .

Table II-3 - Reference H(10) rates at the measuring positions (date: 15/10/2013).*

Position	Source	Source-to-detector distance [cm]	Reference H*(10) rate [µSv/h]
1	^{252}Cf	69.0	1084 ± 48
2	^{252}Cf	100.0	516 ± 22
3	^{252}Cf	200.0	129 ± 6
4	AmBe	100.0	128 ± 7
5	AmBe	200.0	32 ± 2

The response of the WENDI-2 was determined according to recommendations of the ISO 8529 norm [185]. Among other things, this norm specifies how the detector readings should be corrected for extraneous effects related to neutron scattering by the air and the walls, floor and ceiling of the calibration room. The calibration factor of a detector should indeed be an intrinsic property that does not depend on the used calibration facility and experimental technique.

Four different methods to correct for scatter effects are proposed in the ISO 8529 norm [185]. The method applied in this case was the "shadow cone technique", which is routinely used at the SCK-CEN. This technique relies on the experimental determination of the so-called inscattered components of the detector reading. Inscattered components are due to neutrons which reach the detector from an indirect angle after having been scattered by the air and/or the room surfaces. To measure this contribution, a specifically designed shadow cone is placed between the source and the detector to prevent the detection of neutrons coming directly from the source. The contribution from direct neutrons is then obtained by subtracting this shadow cone measurement from the regular measurement performed without the cone. Finally, a correction should also be applied for the outscatter of direct neutrons by the air between the source and the detector. If l represents the centre-to-centre distance from the source to the detector, the response $R(l)$ of the detector is thus obtained through the following equation [185,206]:

$$R(l) = (R_{tot}(l) - R_{insc}(l))\, e^{\overline{\Sigma} l} \quad \textbf{(II.1)}$$

where

$R_{tot}(l)$ is the detector reading measured without the shadow cone,

$R_{insc}(l)$ is the detector reading measured with the shadow cone,

$e^{\overline{\Sigma} l}$ is the air outscatter correction factor for direct neutrons, with $\overline{\Sigma}$ = 1055 $\cdot$ 10^{-7} cm^{-1} for a bare ^{252}Cf source [185] and $\overline{\Sigma}$ = 890 $\cdot$ 10^{-7} cm^{-1} for a bare AmBe source [185].

The equation (**II.1**) is only valid as long as the source-to-detector distance l is at least two times larger than the radius of the detector [185,206]. This condition ensures a negligible geometry correction for the finite size of the source and the detector.

The ISO 8529 criteria on the design and the use of a shadow cone [185] were met in the experiment at the SCK-CEN. The used shadow cone, which is shown in figure **II-13**, was made of an iron front part, of 20 cm in length, and a 5% boron-doped polyethylene rear part, of 30 cm in length. Shadow cone measurements were only carried out for the measurement positions 3, 4 and 5. For the positions 1 and 2, the corrected response was determined using the factors in table **II-4**, which the SCK-CEN staff obtained from previous shadow cone measurements with another WENDI-2 probe. The ISO 8529 norm states indeed that once the shadow cone measurements have been carried out for one particular instrument type, they need not be repeated each time an identical device is calibrated in the same conditions [185].

Table II-4 – Pre-established correction factors for WENDI-2 calibration measurements with the ^{252}Cf source 'CF3' at the SCK-CEN. These factors were derived by the SCK-CEN staff from shadow cone measurements with another WENDI-2 (serial number: 10420; 11/09/2013).

Position	Distance to the ^{252}Cf source 'CF3' [cm]	Correction factor for WENDI-2 calibration measurements
1	69.0	0.841 ± 0.025
2	100.0	0.745 ± 0.022
3	200.0	0.509 ± 0.015

II-3.1.2 Simulated WENDI-2 responses and H*(10) rates

Simulations were performed using MCNPX 2.7.0 in which a point source emits neutrons isotropically with an energy distribution based on the group source strength values given in the ISO 8529-1 (table A.2 for the ^{252}Cf source and table A.4 for the AmBe source) [145]. The corresponding neutron spectra are shown on lethargy plots in the figures **II-14** and **II-15**. The fluence-average energy of the emitted neutrons is of 2.13 MeV for ^{252}Cf and 4.16 MeV for AmBe, respectively.

For each measurement, a simulation was made in which a reference air-filled cell, with the dimensions of the active ^{3}He volume of the WENDI-2, was defined at the appropriate distance in air from the point source. An F4:n tally in association with DE-DF cards [100] was applied to the reference air cell. This allowed simulating the WENDI-2 response by folding the volume-averaged fluence spectrum with the detector response function (multiplied by $3.17 \cdot 10^{-10}$ Sv/count, the built-in calibration factor [155]). This calculation was done for different versions of the response function, which are shown in the figure **II-16**:

- our response function obtained with MCNPX 2.7.0 considering a point source at 50 cm from the geometric centre of the detector,
- our response function obtained with MCNPX 2.7.0 for a parallel beam,
- the results of Olsher *et al.* obtained with MCNP4B [152],
- the results of Jägerhofer *et al.* obtained with FLUKA [183],
- the results of Vanaudenhove *et al.* obtained with GEANT4 9.6 [184],
- the experimental data obtained by Olsher *et al.* at the *Physikalisch-Technische Bundesanstalt* (PTB), with monoenergetic neutron beams of energies from 0.144 MeV to 19 MeV (and, at energies below 0.144 MeV, the abovementioned simulation results of Olsher *et al.*).

In the air cell used to compute the WENDI-2 response, the neutron H*(10) rate was also calculated, by means of the fluence-to-H*(10) conversion coefficients of the ICRP Publication 74 [87].
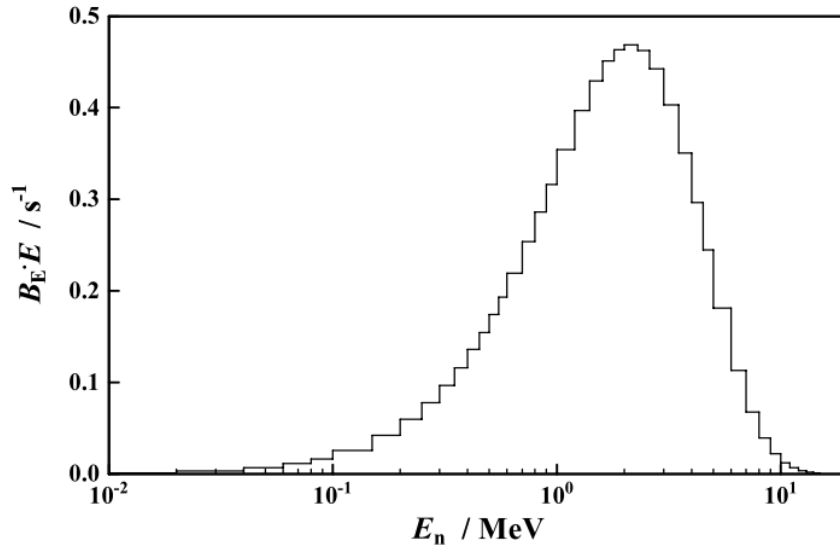
Figure II-14 - Neutron emission spectrum of a bare ^{252}Cf source, normalized to a total source strength of 1 neutron/s [145]*.*
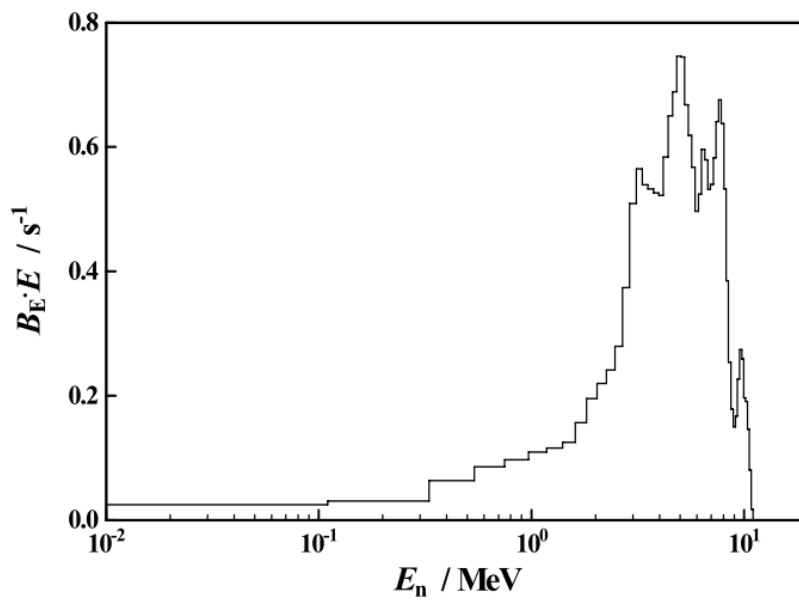
Figure II-15 - Neutron emission spectrum of a bare AmBe source, normalized to a total source strength of 1 neutron/s [145]*.*
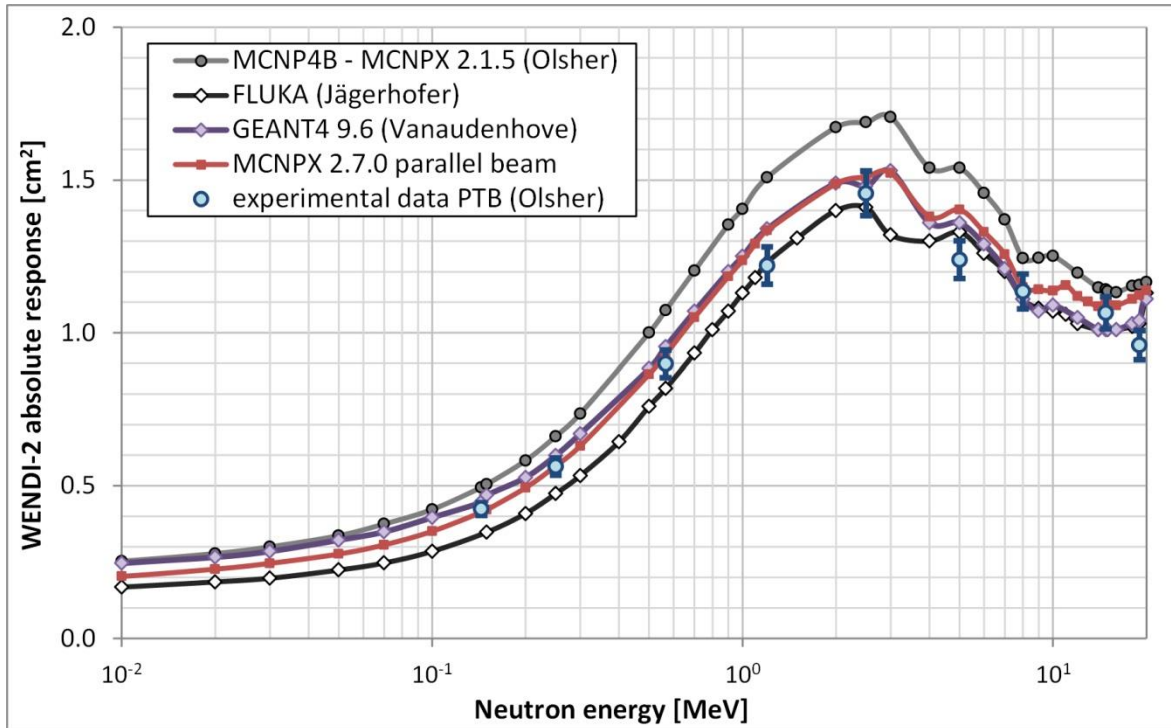
Figure II-16 – Simulated WENDI-2 response functions (from this work and from [152,183,184]*) & experimental responses obtained by Olsher et al. at the PTB with monoenergetic neutron beams* [152]*.*

For the comparison with the measurements and the reference H*(10) rates, a normalization factor equivalent to the neutron source strength (in neutrons/s) needed to be applied to the simulation results, because the latter are given per source-neutron. To this end, the SCK-CEN staff provided us with the reference values of the neutron flux at 1.00 m distance from the source, in the direction of the measurement positions (see table **II-5**). Therefore, a neutron fluence tally F4:n, applied to a reference air cell at 1.00 m from the source, was added to our simulations. The normalization factor was subsequently calculated as the ratio of the reference neutron flux to the corresponding simulated neutron fluence per source-neutron.

Table II-5 – Reference neutron flux at 1.00 m from the source, along the axis of the measurement positions.

Source	Reference neutron flux [cm^{-2}.s^{-1}]
^{252}Cf (label 'CF3')	373.46 ± 13.99
AmBe	90.69 ± 5.11

II-3.2 Results

II-3.2.1 Measurement results

The results of the WENDI-2 measurements performed with and without the shadow cone are summarized in the table **II-6**. This table also gives the WENDI-2 responses corrected for all scatter effects. These were determined according to the equation (**II.1**) for all positions except those at 0.69 m and 1.00 m from the ^{252}Cf source. In these two cases, the measurement performed without shadow cone was multiplied by the global correction factor given in table **II-4**. The overall 1σ uncertainty associated to the corrected WENDI-2 responses (3.1%) includes:

- the uncertainty on the inscattered response component measured with the shadow cone technique (3% according to the ISO 8529, based on "experience gathered over many years" [185]) ,
- the uncertainty on the linear air-attenuation coefficient $\bar{\Sigma}$ (1.5%, according to the ISO 8529 [185]),
- the Poisson counting uncertainties (0.4% - 0.8%),
- the uncertainty on the source-to-detector distance l (<0.1%).

It can be noted about the measurements at 2 m from the ^{252}Cf source that the ratio of the corrected response to the measurement without shadow cone equals 0.519 ± 0.016, which is compatible within one standard uncertainty with the corresponding ratio determined by the SCK-CEN with another WENDI-2 (0.509 ± 0.015; see table **II-4**).

Table II-6 - WENDI-2 measurements with and without shadow cone, and scatter-corrected WENDI-2 responses (air outscatter correction factor $e^{\bar{\Sigma}l}$ included).

Source	Source-to-detector distance [cm]	WENDI-2 measurement without shadow cone [µSv/h]	WENDI-2 measurement with shadow cone [µSv/h]	Corrected WENDI-2 response [µSv/h]
^{252}Cf	69.0	1230 ± 5	/	1034 ± 31
^{252}Cf	100.0	652 ± 4	/	486 ± 15
^{252}Cf	200.0	232 ± 1	114 ± 3	121 ± 4
AmBe	100.0	167 ± 1	53.3 ± 1.7	115 ± 4
AmBe	200.0	62.5 ± 0.5	32.4 ± 1.0	31 ± 1

II-3.2.2 Simulation results

The results of the source strength normalization factors are given in table **II-7**. Correspondingly to the uncertainties on the reference neutron fluxes provided by the SCK-CEN, the normalization factors have a relative standard uncertainty of 3.7% and 5.6% for the ^{252}Cf and AmBe sources, respectively.

Table II-7 – Simulated neutron fluence per source-emitted neutron at 1 m from the source, and the corresponding source strength normalization factor.

Source	Reference neutron flux at 1 m [cm^{-2}.s^{-1}]	Simulated neutron fluence at 1 m [cm^{-2}]	Normalization factor [s^{-1}]
^{252}Cf	373.46 ± 13.99	(8.041 ± 0.007) · 10^{-6}	(4.645 ± 0.174) · 10^{7}
AmBe	90.69 ± 5.11	(8.020 ± 0.009) · 10^{-6}	(1.131 ± 0.064) · 10^{7}

The simulation results for the neutron H*(10) rates and the WENDI-2 responses are summarized in the tables **II-8** and **II-9**, for the ^{252}Cf and the AmBe irradiations, respectively. The standard uncertainty associated to the results includes the uncertainty on the source strength normalization factor (see table **II-7**) and, in the case of the response based on the measurements of Olsher *et al.*, the experimental uncertainty of 5% [152]. The statistical MCNPX uncertainties were negligible.

Table II-8 - Simulation results relative to the irradiations with the ^{252}Cf source.

Distance to ^{252}Cf source [cm]	69.0	100.0	200.0
Neutron H*(10) [μSv/h]	1080 ± 41	515 ± 19	128 ± 5
Response MCNPX 2.7.0 (resp. fct. close point source) [μSv/h]	1221 ± 46	582 ± 22	145 ± 5
Response MCNPX 2.7.0 (resp. fct. parallel beam) [μSv/h]	1121 ± 42	535 ± 20	133 ± 5
Response MCNP4B (resp. fct. of Olsher *et al.* [152]) [μSv/h]	1263 ± 47	602 ± 23	150 ± 6
Response FLUKA (resp. fct. of Jägerhofer *et al.* [183]) [μSv/h]	1028 ± 39	490 ± 18	122 ± 5
Response GEANT4 9.6 (resp. fct. of Vanaudenhove *et al.* [184]) [μSv/h]	1122 ± 42	535 ± 20	133 ± 5
Response Monoenergetic measurements of Olsher *et al.* at PTB [152] [μSv/h]	1046 ± 65	499 ± 31	124 ± 8

Table II-9 - Simulation results relative to the irradiations with the AmBe source.

Distance to AmBe source [cm]	100.0	200.0
Neutron H*(10) [µSv/h]	128 ± 7	31.8 ± 1.8
Response MCNPX 2.7.0 (resp. fct. close point source) [µSv/h]	143 ± 8	35.5 ± 2.0
Response MCNPX 2.7.0 (resp. fct. parallel beam) [µSv/h]	133 ± 8	33.1 ± 1.9
Response MCNP4B (resp. fct. of Olsher *et al.* [152]) [µSv/h]	148 ± 8	36.8 ± 2.1
Response FLUKA (resp. fct. of Jägerhofer *et al.* [183]) [µSv/h]	123 ± 7	30.7 ± 1.7
Response GEANT4 9.6 (resp. fct. of Vanaudenhove *et al.* [184]) [µSv/h]	131 ± 7	32.6 ± 1.8
Response Monoenergetic measurements of Olsher *et al.* at PTB [152] [µSv/h]	124 ± 9	30.8 ± 2.3

II-3.2.3 Discussion

As shown in the figures **II-17** and **II-18**, the simulated H*(10) rates are in excellent agreement with the corresponding reference rates in all cases. It proves that the source strength normalization factors were calculated accurately.
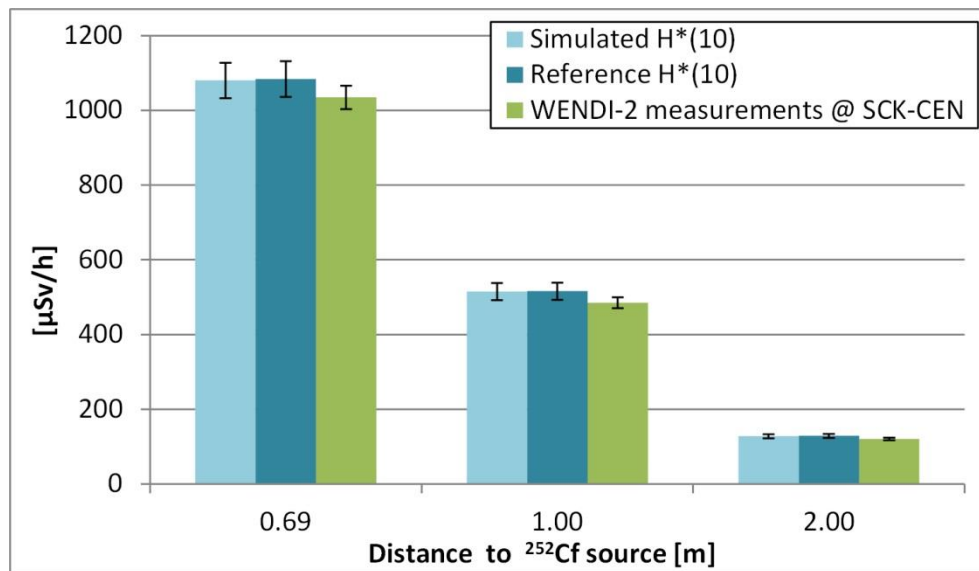
Figure II-17 – Comparison of the simulated H(10) rate and the corrected WENDI-2 response with the reference H*(10) rate, for different distances to the ²⁵²Cf source.*

For the [252]Cf irradiations (see figure **II-17**), the measured WENDI-2 responses deviate from the reference H*(10) rates by -4.5% to -6.6%. In each position, the two quantities agree with each other within one standard uncertainty (1σ). In this aspect, our measurements thus validate the built-in calibration factor determined by the manufacturer of the WENDI-2 [155].

In the AmBe field (see figure **II-18**), deviations of -10% and -3.9% were obtained for the measured WENDI-2 responses with respect to the reference H*(10) rates. It corresponds to an agreement within 2σ and 1σ for the measurements at 1 m and 2 m from the source, respectively.

The results tend to confirm that the WENDI-2 can provide accurate measurements for the contribution to H*(10) due to neutrons in the range of 0.1 MeV – 10 MeV.
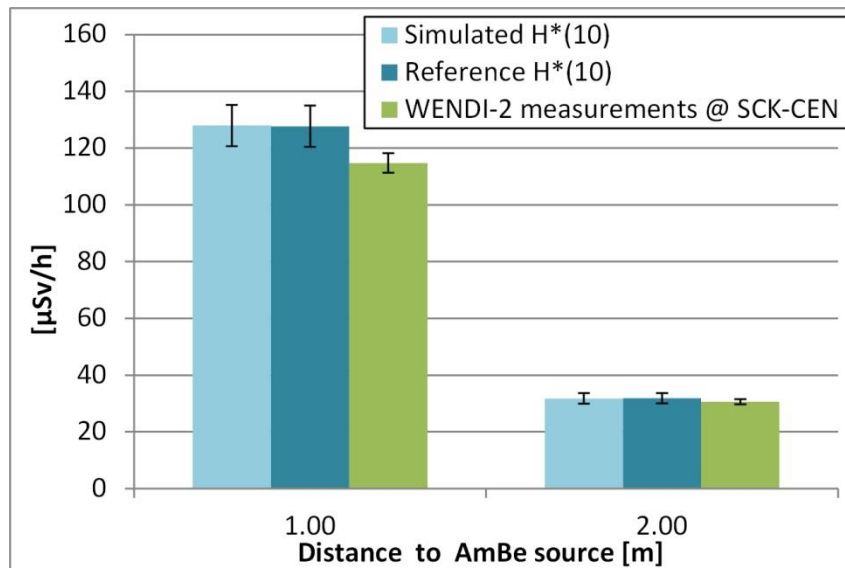
Figure II-18 - Comparison of the simulated H(10) rate and the corrected WENDI-2 measurement with the reference H*(10) rate, for different distances to the AmBe source.*

The simulated WENDI-2 responses, based on the different versions of the response function (see figure **II-16**), are compared to the measured WENDI-2 responses in the figure **II-19** and **II-20**. The experimental validation of Olsher *et al.* performed with monoenergetic neutron beam measurements at the TSL is confirmed by our measurements, which agree with the corresponding energy-integrated responses within 1σ. Amongst the response functions calculated with a Monte Carlo code, the version of Jägerhofer *et al.* [183], obtained with FLUKA, provided the best agreement with our measurements (agreement within 1σ). The worst agreement was obtained with the response function of Olsher *et al.* [152] simulated with MCNP4B (agreement within 3σ; deviations of 20-30 % with respect to the measured response).
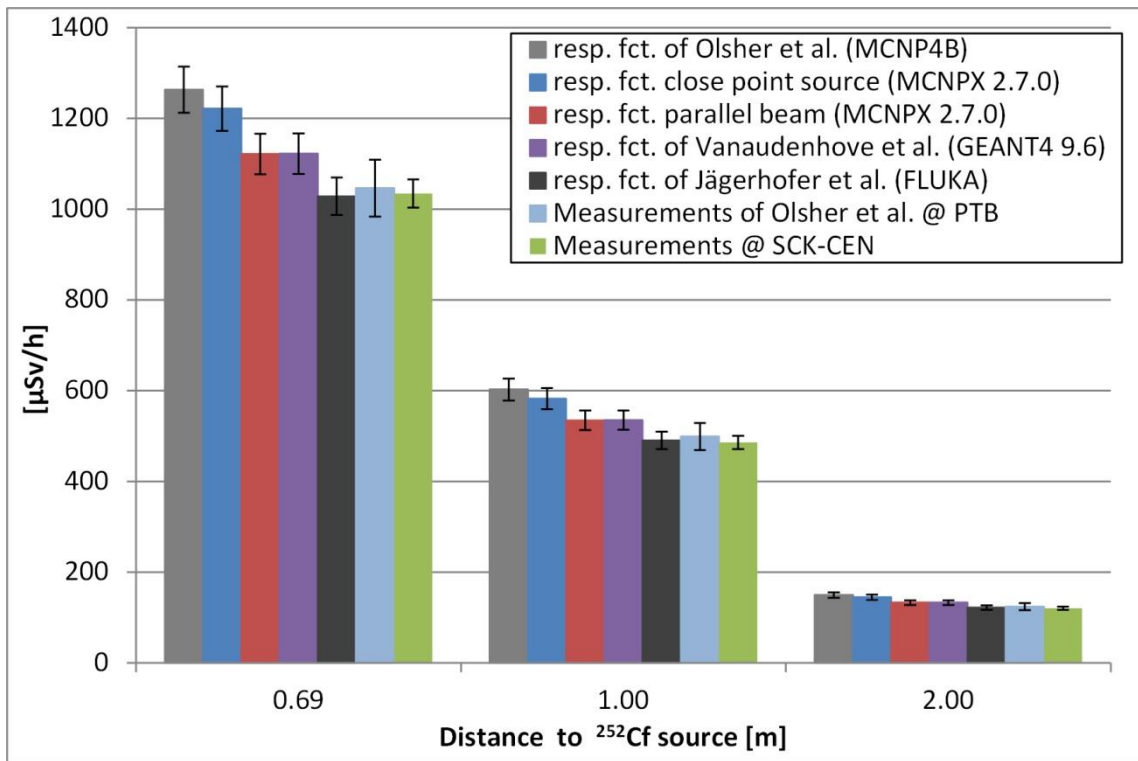
Figure II-19 – Comparison for the [252]Cf irradiations of the measured WENDI-2 responses with the simulated responses based on different versions of the response function, obtained either by simulation (this work and [152,183,184]) or from monoenergetic neutron measurements [152].
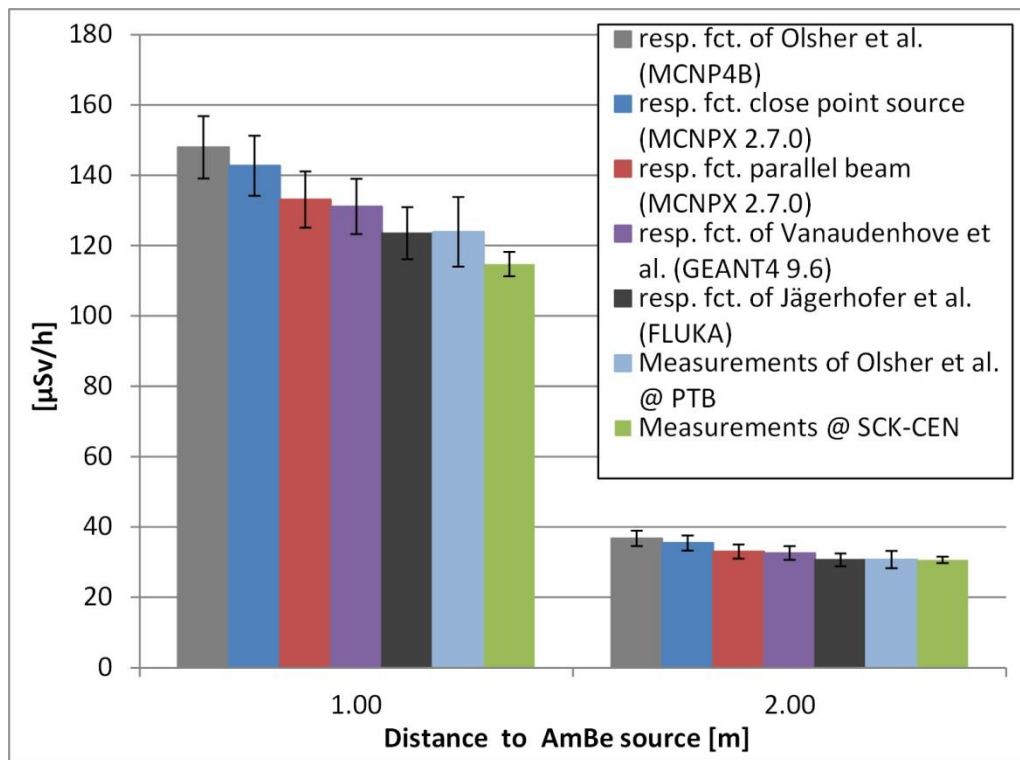
Figure II-20 – Comparison for the AmBe irradiations of the measured WENDI-2 responses with the simulated responses based on different versions of the response function, obtained either by simulation (this work and [152,183,184]) or from monoenergetic neutron measurements [152].

II-4 Validation measurements in high-energy quasi-monoenergetic neutron beams

II-4.1 Methods and procedures

II-4.1.1 QMN beam irradiations

Irradiations of the WENDI-2 were performed in high-energy QMN beams at the Theodor Svedberg Laboratory (TSL), in Uppsala, Sweden. A beam of cyclotron-accelerated protons was directed at a thin lithium target enriched to 99.98% in ^{7}Li, in order to produce QMN beams through the ^{7}Li(p,xn) reaction. To avoid the contamination of the QMN beam with protons, a magnet downstream the target deflected the exiting proton beam towards a water-cooled graphite beam dump.

The neutron beam was shaped by a cylindrical iron collimator block (100 cm long) with a 10.2 cm diameter aperture. This allowed creating a uniform field of 25 cm in diameter at the Actual User Position (AUP). The AUP was located at 9.50 m of the target, inside the experimental area referred to as the 'Blue Hall'. This area is shielded from the target by 60 – 120 cm thick concrete blocks, as shown on the map in figure **II-21**. Additional information on the QMN facility can be found in [207,208].

Runs were conducted at three different proton energies:

- The minimum available proton energy (~25 MeV), producing a QMN beam with a peak near 22 MeV. This energy was selected as a kind of benchmark point for the experiment since the WENDI-2 response function is already well characterised between ~0.1 MeV and ~20 MeV thanks to, amongst others, the experimental data acquired by Olsher *et al.* at the PTB [152].

- The maximum available proton energy (~180 MeV), producing a QMN beam with a peak around 175 MeV.

- An intermediate proton energy of ~100 MeV, producing a QMN beam with a peak around 95 MeV. Apart from providing an intermediate point between the minimum and maximum energies, this energy is also of interest because it approximately corresponds to the centre of the high-energy peak in the neutron spectra typically encountered in proton therapy facilities when delivering protons of ~230 MeV.

The exact proton energies, which were measured by the TSL staff, are given in Table **II-10**, along with the corresponding thickness of the used Li target.

Table II-10 - Measured proton energies and Li target thicknesses of the three QMN runs

Date of the run	13/06/2014	17-18/06/2014	18-19/06/2014
Measured proton energy [MeV]	177.8 ± 1.0	96.3 ± 0.4	24.60 ± 0.05
Target thickness [mm]	23.5	8.5	2.0
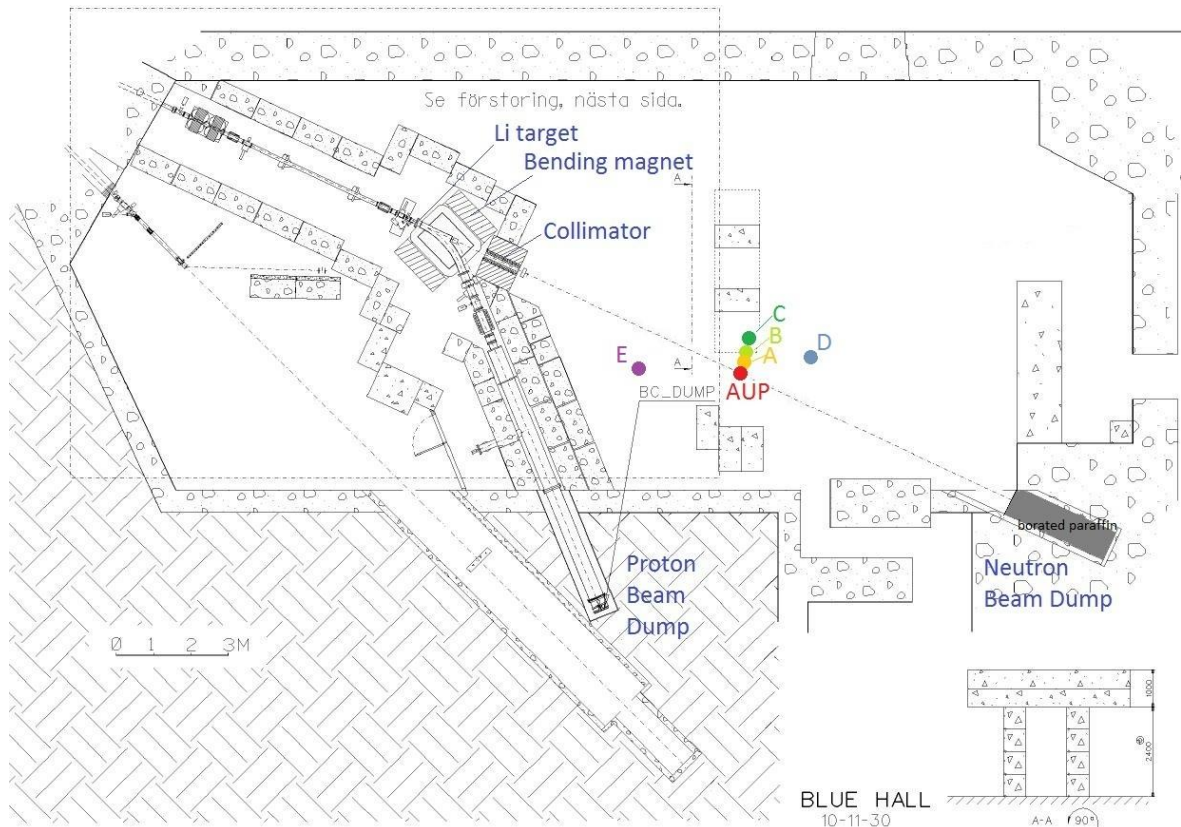
Figure II-21 - Map of the Blue Hall at the TSL (courtesy of the TSL). Measurement positions are indicated by coloured dots: the positions AUP (Actual User Position) is centred on the beam axis, whereas the positions A, B, C, D and E lie out of the beam.

WENDI-2 measurements were performed in the first place at the AUP, which is the reference position for the measurement of the delivered neutron fluence. The diameter of the plateau in the neutron beam profile at the AUP was of 25 cm in order to irradiate uniformly the entire volume of the WENDI-2 (which, as a reminder, has a diameter of 22.86 cm and a height of 21 cm).

At the AUP, the geometric centre of the WENDI-2 was aligned with the fixed horizontal laser indicating the beam axis. For each run, the measurement uncertainty related to the detector positioning was also assessed by redoing the positioning procedure in between two irradiation series.

Complementary measurements were made with the WENDI-2 in other positions than the AUP, including several outside of the QMN beam. The measurement positions are described in Table **II-11** and shown in Figure **II-21**.

- The lateral extent of the QMN beam at the AUP was roughly assessed by successively displacing the WENDI-2 by 15 cm, 30 cm, 50 cm and 88.5 cm perpendicularly to the beam axis (see positions HO, A, B and C, respectively).

- Measurements were also performed in two positions (D and E) located at more than 1 m from the beam axis. These measurements give indications on the room-scattered neutron flux and the neutron leakage through the target shielding. They were used to make a rough estimate of the contribution of low-energy neutrons (E < 0.1 MeV) to the WENDI-2 response at the AUP, a contribution which was not directly measured in this experiment. Based on this estimate (see section **II-4.2.1**) and on consistent low-energy fluence measurements from [207], it was assumed reasonable in a first approach to neglect the contribution of neutrons with less than 0.1 MeV in the data analysis.

Table II-11 – Overview of the measurement positions in the Blue Hall

Position	Description
AUP	Actual User Position: reference position at 9.50 m from the Li target.
HO	Not shown in Figure 1; located between AUP and A, at 15 cm from AUP. About half of the detector volume stood in the beam penumbra.
A	At 30 cm from AUP.
B	At 50 cm from AUP.
C	At 88.5 cm from AUP.
D	At 11 m from the Li target (measured along the neutron beam axis) and at 1m20 from the neutron beam axis.
E	At 7 m from the Li target (measured along the neutron beam axis) and at 1 m from the neutron beam axis.

II-4.1.2 Operation of the WENDI-2

Before starting the irradiations, the neutron background was measured during 5 minutes with the WENDI-2 positioned at the AUP. The average measured dose rate did not exceed 2 nSv/h, wherefore the neutron background was considered to be negligible. The Blue Hall is in fact an underground facility.

During the irradiations, the WENDI-2 was operated in counter mode, which means that the detector counted the triggered impulses during a preselected measuring time. The accumulating number of counts was displayed by the FH-40 monitor during the counting. Immediately at the end of the measuring time, the display switched to the "average dose rate", calculated by the FH-40 as the number of counts divided by the preselected measuring time and multiplied by the built-in

calibration factor (0.317 nSv/c [155]). Since there was no guarantee that the measuring time would systematically be equal to the irradiation time, it was preferable to record the total number of counts instead of the average dose rate calculated by FH-40. Knowing that the neutron background was negligible, the preselected measuring time was therefore chosen to be a bit longer than the estimated irradiation time so that (1) the counting could be started just before turning the beam on and (2) the counting continued a little while after the irradiation had ended, leaving time to write down the total number of counts before the display switched to the average dose rate.

The beam was automatically switched off as soon as the peak fluence preset in the TSL "BORN" software was delivered. This peak fluence was set so as to ensure good counting statistics (> 2000 counts) for the peak fluence monitoring system, which is described in section **II-4.1.3**. This setting also ensured excellent counting statistics for the WENDI-2 measurements, with more than 10^5 counts at the AUP and more than 10^4 counts in out-of-beam positions.

At the beginning of each run, the proton beam intensity was increased in steps until reaching a suitable neutron flux that allowed delivering the requested fluence within 3 – 5 min. In the runs with the 24.6 MeV and 93.1 MeV protons, the neutron flux was continuous since the cyclotron was operated in Continuous Wave (CW) mode. In the run with the 177.8 MeV protons, however, the cyclotron functioned in Frequency Modulated (FM) mode and produced beam pulses of 600 μs at a frequency of 160 Hz, which corresponds to a duty cycle of 9.6%.

Since the helium tube inside the WENDI-2 is a proportional counter, its dead-time losses were estimated following the basic model of Feller for a non-paralyzable detector (Type I model) [209]. This model is based on the idea of a fixed dead-time, during which any occurring event is lost, and after which the detector fully recovers. The true count rate n can then be estimated from the observed count rate m and the dead-time τ with the following formula [209]:

$$n = \frac{m}{1 - m\tau}$$

A dead-time τ of 1.8 μs was assumed for the WENDI-2 according to the datasheet of the manufacturer [155]. The observed count rate m was determined by dividing the WENDI-2 counts by the irradiation time deduced from the fluence monitoring logs that the TSL staff provided after the experiment. In the two runs operated in CW mode, the dead-time losses were found to be negligible (< 1%) in all positions. For the run in FM mode (177.8 MeV protons), the logged irradiation time was multiplied by the duty cycle of 9.6 % to provide a conservative estimate of the true neutron irradiation time. Under this assumption, the true count rate n was estimated to be 4.9 % larger than the observed count rate m for the irradiations at the AUP. Dead-time losses in other positions were negligible.
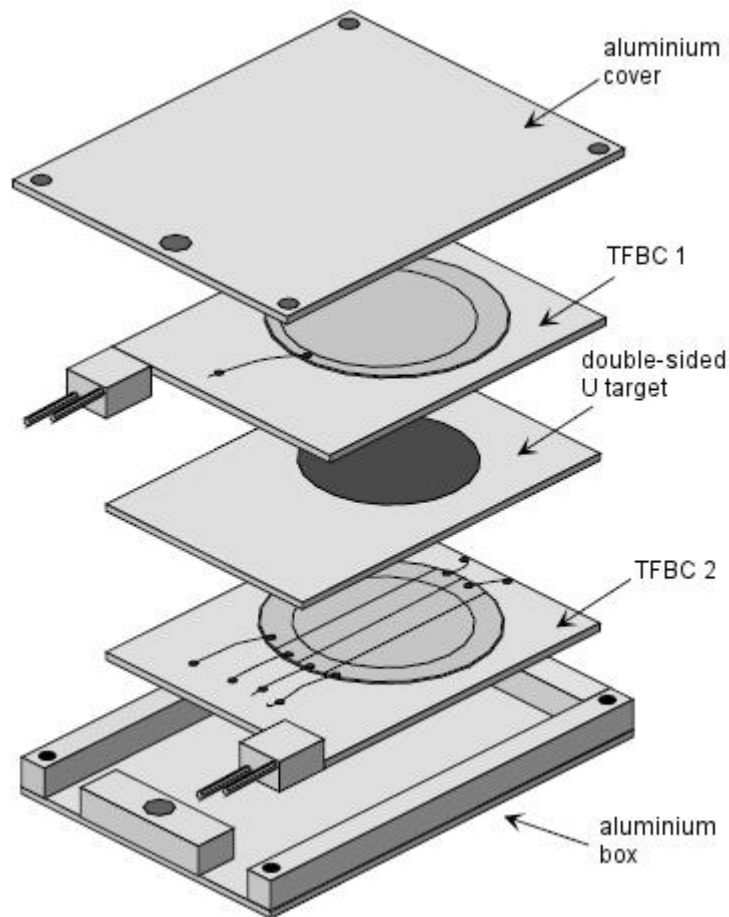
Figure II-22 – Exploded view of the TFBC monitor (adapted from [210]*)*

II-4.1.3 Neutron fluence measurements

The measurements of the neutron fluence at the AUP were carried out entirely by the TSL staff. The cornerstone of the fluence monitoring system at the TSL is a monitor based on two Thin-Film Breakdown Counters (TFBCs). The TFBCs [211–214] are Metal-Oxide-Semiconductor capacitors to which a low voltage of ~100 V is applied. They consist of a very thin SiO_2 dielectric film sandwiched between a low-resistivity n-type silicon wafer and a very thin metal electrode. As shown in the schematic view in figure **II-22**, the TFBCs are placed on both sides of a thin natural uranium target, in which the neutron beam induces fast fissions of ^{238}U nuclei. The produced fission fragments are detected in the TFBCs thanks to their track of ionizations which causes an electrical breakdown of the capacitor. Most of the time, these breakdowns do not cause lasting short-circuits because they create a tiny hole in the insulator and the thin metal electrode by evaporation. As such, the TFBCs in regular use at the TSL generally have a lifetime of a few years [215]. Important advantages of the TFBCs are their good timing capabilities and their insensitivity to electrons, light ions, gammas and neutrons.

The TFBC monitor was absolutely calibrated by the TSL staff to measure the fluence of the neutrons in the high-energy peak of the QMN spectrum (the 'peak fluence'). A detailed explanation of the calibration method is given in [215]. It relies on previous measurements in which the thin natU target inside the TFBC monitor was replaced by a similar target containing a mixture of natU and 252Cf, with a known surface density of spontaneous fission activity. To avoid dismantling the TFBC monitor at every calibration, a relationship was established between this absolute calibration and the response to an external Pu-Be radioactive neutron source. Hence, at the beginning of a new QMN run, the TSL staff performs a measurement with a Pu-Be source. This allows to determine the sensitivity s_{peak}, defined as the ratio of the number of TFBC monitor counts to the peak fluence, using the following formula derived in [215]:

$$s_{peak} = \frac{\sigma_{ff}(E_{peak})N_{PuBe}}{k_{low}k_{anis}B}k_{180}$$

where

$\sigma_{ff}(E_{peak})$ is the fission cross-section of 238U at the neutron peak energy (experimental data from [216])

N_{PuBe} is the count rate of the TFBC monitor in the irradiation with the Pu-Be source,

k_{low} is the ratio of the number of 238U fission events induced by peak neutrons to the total number of 238U fission events (experimental data from [215]),

k_{anis} is a correction for the angular anisotropy in the emission of the fission fragments (experimental data from the similar proton-induced fission of 238U, see references cited in [217]),

k_{180} is a correction for the difference in efficiency between the 'forward' TFBC and the 'backward' TFBC (experimental data from [215]),

$B = 8.017 \cdot 10^{-21}$ ($\pm 5\%$) is the constant that establishes the relationship with the natU+252Cf calibration [215].

The factor k_{low} was determined from data acquired during the experiment described in [217], in which the Time-Of-Flight (TOF) technique was applied with the use of a TFBC coupled to a 238U fission sample. The TOF spectra of fission events were decomposed into a component due to peak neutrons and a component due to tail neutrons by means of a "simple empirical algorithm" [217]. No details about this decomposition method are given in [217], but [215] mentions a "graphical procedure" with an estimated uncertainty of 5-7% related to the time structure of the cyclotron micropulse, the time resolution of the detector and the counting statistics. An explicit explanation of how this uncertainty was estimated is not given. The report points out, though, that most of the k_{low} values measured at the same neutron peak energies (2 - 6 values per energy) agree with each other within these uncertainties [215].

Because the TFBC monitor has a relatively low sensitivity, the online fluence monitoring at the TSL is usually performed with the Ionization Chamber Monitor (ICM) [210], used as a relative monitor calibrated against the TFBC monitor. This allows to gain one to two orders of magnitude in sensitivity [210]. The ICM is essentially a fission chamber with a stack of eleven electrodes: five cathodes and six anodes positioned in alternation. Each cathode is coated on both sides with U_3O_8 and the chamber is filled by a gas mixture of 90% Ar – 10% CF_4 at atmospheric pressure. As in the TFBC monitor, the neutrons are detected through a two stage process. In the first stage, ^{238}U fission fragments are produced in the U_3O_8 coating. In the second stage, the fission fragments are detected through the ionizations they produce in the gas and the subsequent drift of the free electrons towards the anode.

In our experiment, the ICM was located upstream the AUP, at ~3.3 m from the Li target. Before each run, the TSL staff positioned the TFBC at the AUP in order to determine the calibration factor P_{ICM}, by which the ICM counts N_{ICM} need be multiplied to obtain the peak fluence Φ_{peak} delivered at the AUP. This calibration factor was simply calculated as follows:

$$P_{ICM} = \frac{\Phi_{peak}}{N_{ICM}} = \frac{N_{TFBC}}{N_{ICM}s_{peak}}$$

The P_{ICM} factors of the three runs are given in Table **II-12**. The TSL staff estimated the overall relative uncertainty associated to P_{ICM} to 10%. The full uncertainty analysis behind this estimate was not given, but the most important contributions probably arise from the factors k_{low} (5-7%) and B (5%), as well as the ^{238}U fission cross-section (5% at 173 MeV, 4% at 93 MeV and 2% at 21.8 MeV [216]). A relative uncertainty of 2.7% was associated to the count rate N_{PuBe} (Prokofiev, A.V., private communication).

A negligible statistical uncertainty on the number of ICM counts was reached during the WENDI-2 irradiations. Following the evaluation made by the TSL staff, an overall uncertainty of 10% was thus considered on the peak fluence delivered at the AUP.

Table II-12 – Values of the ICM calibration factor for the three QMN runs

Measured proton energy [MeV]	177.8	96.3	24.60
P_{ICM} [cm^{-2}]	72.0	58.3	112

Unlike the peak fluence, the fluence of neutrons in the low-energy tail could not be measured with the available means. This aspect constitutes a large limitation to the experiment because, depending on the peak energy, the measured peak fluence Φ_{peak} only represents at most ~50% of Φ_{total}, and the WENDI-2 has a good sensitivity to a large part of the low-energy tail (above 0.1 MeV). Determining the WENDI-2

response thus requires dividing the number of WENDI-2 counts by the total neutron fluence Φ_{total}.

Unfortunately, the ideal monitor that would be capable of measuring Φ_{total} directly does not exist. Therefore, the fraction of peak neutrons k_{peak} needs to be determined through a precise characterisation of the neutron fluence spectrum down to the thermal energies, or at least down to 0.1 MeV in a first approach. Once k_{peak} is known with good accuracy, Φ_{total} can be determined from the measurement of Φ_{peak} by dividing it by k_{peak}.

Accurately characterising the QMN spectra is however not a straightforward task. In the absence of adequate neutron spectrometry equipment, k_{peak} had to be estimated from neutron spectrum calculations or from previously published experimental spectra. Four different versions of the spectra were taken into account in this work, in order to assess the influence of the assumed spectrum shape on k_{peak} and the associated WENDI-2 response. The following sections describe how these spectra were obtained.

II-4.1.4 Spectra simulated with MCNPX 2.7.0 (default models)

Simulations were run with MCNPX 2.7.0 in order to calculate the QMN spectrum at the AUP for the three different beams. A simple geometry was defined in which a monoenergetic source produces a narrow proton beam impinging on a thin ^{7}Li target in air. The proton energy and the thickness of the target were set to the values given in table **II-10**. Because on a first basis it was considered reasonable to neglect the low-energy room-scattering component in the neutron spectra (see section **II-4.2.1**), the walls of the Blue Hall were not included in the geometry.

In the officially distributed version of MCNPX 2.7.0, the only available evaluated cross-section data for protons interacting with ^{7}Li are those from table 3007.70h [100] of the *endf70prot* library [192]. This table is limited to a maximum proton energy of 10 MeV and was thus not useful to our simulations. As a work-around, the default intranuclear cascade model (Bertini) was used, in conjunction with the multi-stage pre-equilibrium exciton model and the Fermi break-up model, to simulate the interactions of the high-energy protons with the ^{7}Li target. It should be noted here, however, that intranuclear cascade models are believed to be less reliable below 150 MeV and that pre-equilibrium models are relatively poor if applied to light target nuclei such as ^{7}Li. Therefore, only moderate expectations were held regarding the validity of the neutron spectra obtained with these models.

Below 150 MeV, neutron interactions with ^{7}Li and air were based on evaluated cross-section data from the *endf70* library [218], which includes the data of the *la150* library. The Bertini intranuclear cascade model, the pre-equilibrium model and the Dresner evaporation model (or the Fermi break-up model for the lighter nuclei) were used for neutron interactions above 150 MeV.

In the experiment, the protons exiting the target were removed from the neutron beam by electromagnetic deflection. Since MCNPX does not allow simulating magnetic fields, the protons in the simulation were killed after exiting the target. This was done by defining immediately behind the ^{7}Li target an air cell with a proton importance set to zero.

The neutron spectrum was calculated at 9.50 m downstream the target as the energy distribution of the fluence averaged over the volume of a cell (Tally type F4 + E card [100]). The tally cell was a cylindrical air volume with a radius of 11 cm (perpendicular to the beam) and a thickness of 2.5 cm along the beam axis. The thickness corresponds to the diameter of the He tube in the WENDI-2, which is generally taken as the reference volume for fluence calculations (see section **II-2.1.1**). In the transverse direction, however, the tally cell was made almost as large as the entire WENDI-2 detector in order to obtain better statistics when reaching the maximum allowed number of histories per simulation. With the executable of MCNPX 2.7.0 for Linux, the number of histories per simulation is indeed limited to 2 147 483 647, the maximum positive value of the 32-bit signed integer. In this case, it was difficult to obtain a good sampling of the low-energy tail despite the relatively coarse energy binning. The assumption was made that the enlargement of the studied solid angle, which corresponds to a half aperture angle of 0.7°, would not affect the shape of the average neutron spectrum in a significant way.

Despite the coarse energy binning and the enlargement of the tally cell, it was not possible to reach sufficient statistics in the bins of the low-energy tail with the maximum allowed number of histories per simulation. The relative uncertainties calculated by MCNPX were between 10% and 20% for most of the tail bins, which according to the MCNPX manual means that the results may be questionable [100]. To increase the overall statistics, twenty-five separate simulations were run, each of which used a different series of pseudorandom numbers. The modified parameter of the pseudorandom number generation was the random number stride S, which is the number of pseudorandom numbers allocated to each single history. Since this parameter also influences the initial random number of the first history [98], it can easily be used to generate a simulation in which all histories are different from those of the simulation based on the default random number stride. For each new simulation, the value of the random number stride was simply increased by one, starting from the default value of 152 197. The maximum allowed number of histories was run in each simulation. The average of the twenty-five simulated spectra was taken to produce the final spectrum and the statistical uncertainties calculated by MCNPX in each simulation were combined according to the method described in [219]. To assess the accuracy of the uncertainties calculated by MCNPX, Type-A standard uncertainties were also computed using only the spectrum values, as twenty-five independent observations obtained under the same simulation conditions. Since the calculated Type-A standard uncertainties [220] were found to be

compatible with the combined MCNPX uncertainties, the simulation results were considered to be reliable from the statistical point of view.

The simulated spectra for the three different QMN beams will be shown and discussed in section **II-4.2.2**.

II-4.1.5 Spectra simulated with MCNPX 2.7.0 (3007.00h table)

At the end of the 1990s, Mashnik *et al.* attempted to produce evaluated ^{7}Li(p,n) cross-section data which could potentially be included in the *la150h* library of MCNPX. Experimental data for protons in the range of 10 – 150 MeV were used to evaluate the ^{7}Li(p,n_0) and ^{7}Li(p,n_1) direct reactions, which populate the ground state and the first excited state of ^{7}Be, respectively. The available measured data for the angular distributions of the n_0 and n_1 neutrons were fitted with Legendre polynomials as described in [221]. The GNASH code [116], which relies on the evaporation model of Hauser-Feshbach and a pre-equilibrium exciton model, was used to calculate the remaining reaction flux, including reactions to higher excited beryllium states and break-up reactions (see [221] for details). The GNASH output for the n_0 and n_1 neutron emission cross-sections was not used in the evaluation.

At projectile energies lower than 150 MeV, the compound nucleus decay theory, on which the GNASH code is based, is assumed to be generally more reliable for nuclear reaction calculations than intranuclear cascade models such as e.g. the Bertini model. Intranuclear cascade models are indeed based on the assumption that the projectile-nucleus interactions can be approximately described as free collisions of the projectile with individual nucleons. This assumption only holds for sufficiently energetic projectiles that have a wavelength of the order of the internucleonic distance ($\sim 10^{-13}$ cm).

Although the nuclear models of the GNASH code are better adapted to the 10 – 150 MeV range, they are not ideal either in the case of light target nuclei such as ^{7}Li. This is due to the fact that statistical pre-equilibrium and evaporation models are based on a level density formalism, which in general does not work well for widely spaced levels as encountered in light nuclei. Therefore, some weaknesses are inevitably expected in the evaluated ^{7}Li(p,n) data of Mashnik *et al.* [221]*.*

Moreover, Mashnik *et al.* also mention in [221] that their evaluation may be particularly problematic for simulations with protons of more than 30 MeV, due to less accurate Legendre fits of the n_0 and n_1 neutron emission data.

Eventually, the evaluated ^{7}Li(p,n) data was not included in the official *la150h* library of MCNPX 2.7.0, perhaps because of the abovementioned problems. The data is nevertheless still available for downloading on the MCNPX Data Library Access webpage (https://mcnpx.lanl.gov/data.html), as a standard Type-1 formatted table labelled as "3007.00h" (version of 27th September 2000).

More recently, an experimental validation of the evaluated [7]Li(p,n) data for proton energies between 20 MeV and 40 MeV has also been published by S.G. Mashnik and J.S. Bull [222]. This work shows a relatively satisfactory agreement of the simulated spectra with the zero-degree neutron spectrum measurements of Uwamino *et al.* [223]. These TOF measurements were performed with a NE213 liquid scintillator placed at about 12 m of a 2-mm thick Li target (backed with a 12-mm thick graphite beam stopper). Figure **II-23** shows that the zero-degree QMN spectrum produced with 25 MeV protons was much better reproduced using the 3007.00h data table, than using the Bertini or CEM03.03 intranuclear cascade models.

Based on these encouraging results, it was deemed worthwhile to rerun our MCNPX simulation for the 24.6 MeV proton beam (see section **II-4.1.4**), using the 3007.00h data table instead of the default physics models for proton interactions. The same table was also tested in the simulation with the 96.3 MeV proton beam, but without high expectations given the warnings of Mashnik *et al.* concerning the use of this data at high energies. The table was in any case of no use for the simulation with the 177.8 MeV protons since it is limited to a maximum energy of 150 MeV. The results of these simulations based on the 3007.00h data will be shown and discussed in Section **II-4.2.2**.
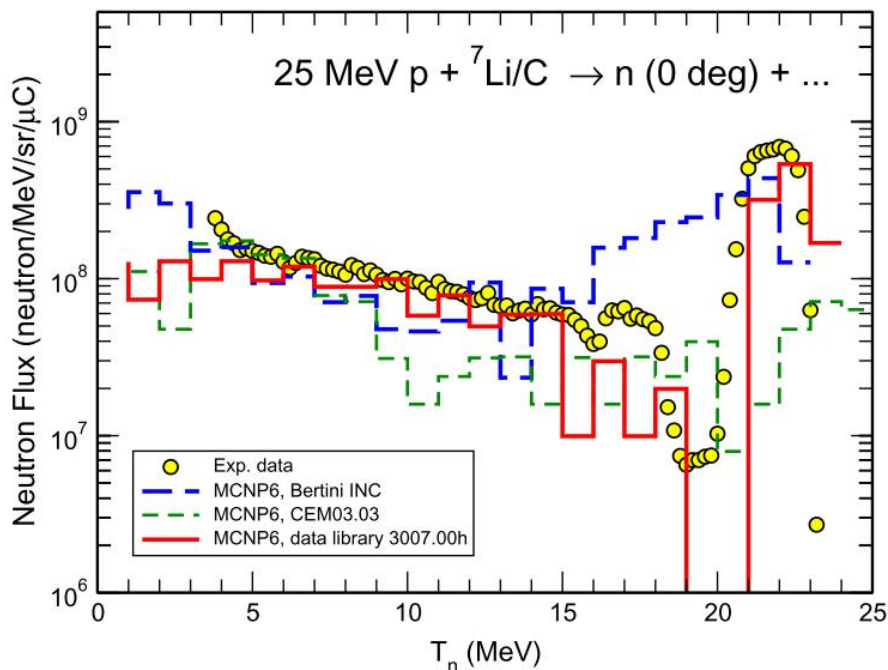
Figure II-23 – Comparison of MCNP6 results of Mashnik & Bull [222] *for the neutron spectrum from a [7]Li target bombarded with protons of 25 MeV to the experimental data by Uwamino et al.* [223] *(figure from* [222]*).*

II-4.1.6 Spectra calculated by the TSL

The third set of spectra used in the analysis was calculated by members of the TSL. Figure **II-24** shows these spectra on a lethargy plot, in which the areas under the curves are proportional to the corresponding energy-integrated fluences.

The shape of the high-energy peak (in terms of fluence per unit energy) was assumed to be rectangular, with a width equal to the proton energy loss in the target. This energy loss was calculated based on the measured energy of the impinging protons and the thickness of the Li target, using the SRIM software [224] (SRIM stands for 'Stopping Range of Ions in Matter'). Subsequently, the Q-value of the ^{7}Li(p, n)^{7}Be reaction and one half of the calculated proton energy loss were subtracted from the measured energy of the impinging protons in order to determine the centre of the peak. Concerning the Q-value, it should be noted that two reaction paths contribute significantly to the high-energy peak: the ground state reaction ^{7}Li(p,n$_0$) ($Q_{g.s.}$=-1.64 MeV) and the first excited state reaction ^{7}Li(p,n$_1$) (E^*=0.43 MeV, Q_1=-2.07 MeV). For simplicity, the hypothesis was made that these two reaction paths are equiprobable and the Q-value was taken equal to the average value of -1.855 MeV. The calculated values for the centre of the peak and the peak width are summarized for the three runs in Table **II-13**.
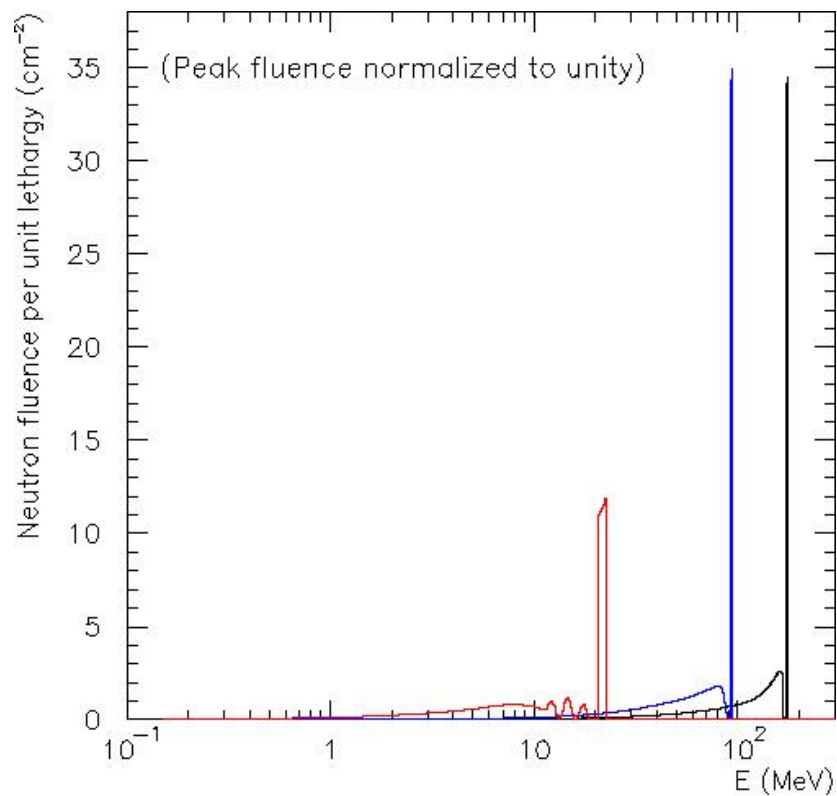
Figure II-24 – QMN spectra as calculated by the TSL staff

Table II-13 – Calculated peak centre and peak width for the three QMN runs

Proton energy [MeV]	177.8	96.3	24.6
Average energy of peak neutrons [MeV]	173.4	93.1	21.8
Neutron peak width [MeV]	5.0	2.6	1.9

The low-energy continuum of the 21.8 MeV QMN beam was calculated by the members of the TSL from the ready parameters in an ENDF-formatted file compiled at the Los Alamos National Laboratory in July 1999 (Prokofiev, A.V., private communication). This data is most likely an earlier version of the ENDF data on which the latest 3007.00h table is based [221] (see section **II-4.1.5**).

For the 93.1 MeV and 173.4 MeV QMN beams, the continuum was calculated according to semi-empirical systematics developed by Prokofiev *et al.* for protons energies of 50 – 200 MeV [225]. These systematics are partially based on an original idea of Baba *et al.* [226] to calculate the low-energy tail by means of G. Olhsen's phase-space distribution for a three-body break-up process [227], applied to the ^{7}Li(p,n^{3}He)α reaction. According to Baba *et al.*, this method worked well within the proton energy range of 40 – 90 MeV. Prokofiev *et al.* extended the applicability of the method up to 200 MeV by multiplying the phase-space distribution with an empirically parametrized function of the neutron energy [225], following an idea of S. Neumann [228]. Compared to MCNPX results based on the 3007.00h table (for proton energies above 40 – 50 MeV), the semi-empirical systematics lead to overall peak-to-tail ratios which are in much better agreement with experimental data [225].

II-4.1.7 Experimental spectra from literature

The fourth set of spectra used in our analysis was obtained experimentally at the TSL in the 2000s [207,208]. The conditions in which the three QMN beams of interest were produced were very similar to those of our own experiment. Yet, in the case of the two highest energies, slightly larger proton energies were used (~1.0 MeV - 1.5 MeV larger, see Table **II-14** below *vs.* Table **II-10** on **p. 79**).

Table II-14 – Measured proton energies and Li target thickness in the PRT measurements [207,208]

Proton beam energy [MeV]	179.3 ± 0.8	97.9 ± 0.3	24.68 ± 0.04
Target thickness [mm]	23.5	8.5	2.0
Average energy of peak neutrons [MeV]	175	95	21.8

The QMN spectra were measured using a conventional "Proton Recoil Telescope" (PRT) technique, involving n-p elastic scattering on a polyethylene target. This target was placed at the centre of the so-called "Medley" set-up (see [229] for a full description). A ΔE-ΔE-E telescope, placed at an angle of 20° relative to the neutron beam, was used to detect recoil protons from n-p elastic scattering on H nuclei, as well as protons, deuterons, ^{3}H nuclei, ^{3}He nuclei and α particles from n + C reactions. This telescope, which is schematized in Figure **II-25**, also allowed identifying these different types of charged particles. It essentially consisted of:

- a fully depleted silicon surface barrier detector of 50-60 μm in thickness, recording the energy loss ΔE_1;

- another fully depleted silicon surface barrier detector, with a thickness of either 400-500 μm (if used with QMN beams of 22 MeV - 95 MeV [207,229]) or ~1000 μm (if used with 175 MeV QMN beams [208,230]), measuring the energy loss ΔE_2;

- a CsI(Tl) scintillation crystal coupled to photodiodes. The thickness of the crystal was large enough to ensure the absorption of the total energy of the most energetic charged particles involved. This detector thus measured the remaining energy E of the detected charged particle.
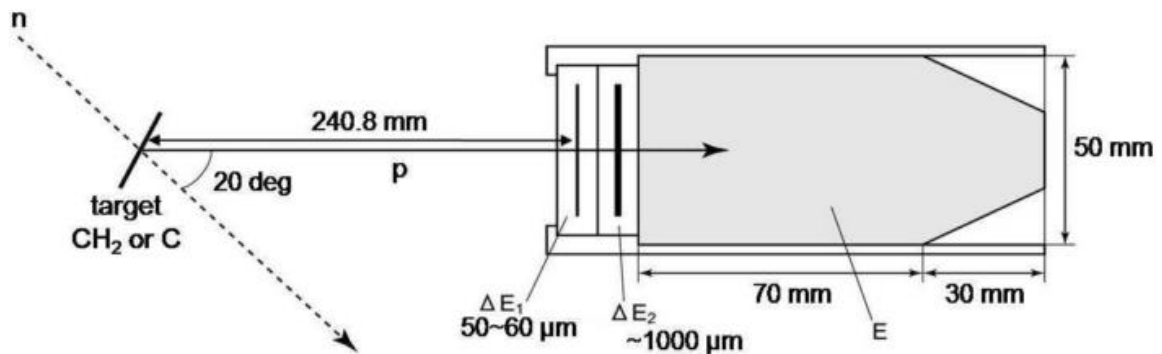
Figure II-25 – Sketch of the ΔE-ΔE-E telescope [208]

The ΔE-ΔE-E telescope was calibrated according to the method described in [229]. The proton events were selected by means of a particle identification procedure based on scatter plots of ΔE_1 *vs.* ΔE_2 and ΔE_2 *vs.* E (details given in [229]). Proton events due to n + C reactions could be subtracted thanks to data obtained in the same manner using a graphite target instead of a polyethylene target. Background events were removed as well, based on acquisitions performed without a reaction target. Hereafter, the recoil proton spectrum was corrected for the non-negligible energy loss and absorption within the thick polyethylene target, using the TCORR code [231].

The neutron spectrum was then derived from the net recoil proton spectrum in the following way:

- using the kinematics of elastic scattering, the one-to-one relationship between the energy E_p of the recoil proton at 20° and the energy E_n of the incident neutron at 0° was established.

- For a given neutron energy E_n, information on the probability that the recoil proton is emitted at an angle of 20° (*vs.* at any other angle) was also required. Therefore, reference data for the differential cross-section $d\sigma_{np}/d\Omega$ of n-p elastic scattering was taken from the online database of the SAID Partial-Wave Analysis Program (http://gwdac.phys.gwu.edu). Each bin value of the neutron spectrum $\Phi(E_n)$ was calculated from its corresponding bin value of the recoil proton spectrum $S_{np}(E_p)$ with the following formula:

$$\Phi(E_n) = \frac{S_{np}(E_p)}{\frac{d\sigma_{np}}{d\Omega}(E_n)\bigg|_{20°} \Delta\Omega \; N_p}$$

where $\Delta\Omega$ is the solid angle of detection and N_p the number of target hydrogen atoms.

The experimental spectra that were used in our analysis are shown on a lethargy plot in Figure **II-26**. The 22 MeV and 95 MeV QMN spectra were taken from [207] (in which the statistical uncertainties are not given). The low-energy tail was measured down to 4.5 MeV for the 25 MeV QMN beam, and down to 10 MeV for the 95 MeV QMN beam. We extended these tails down to 0.1 MeV, using a linear function of the fluence per unit lethargy which has a zero at 0.1 MeV. The 175 MeV QMN spectrum was taken from [208]. It was measured down to 2 MeV and did not require a low-energy extension in the context of our analysis.
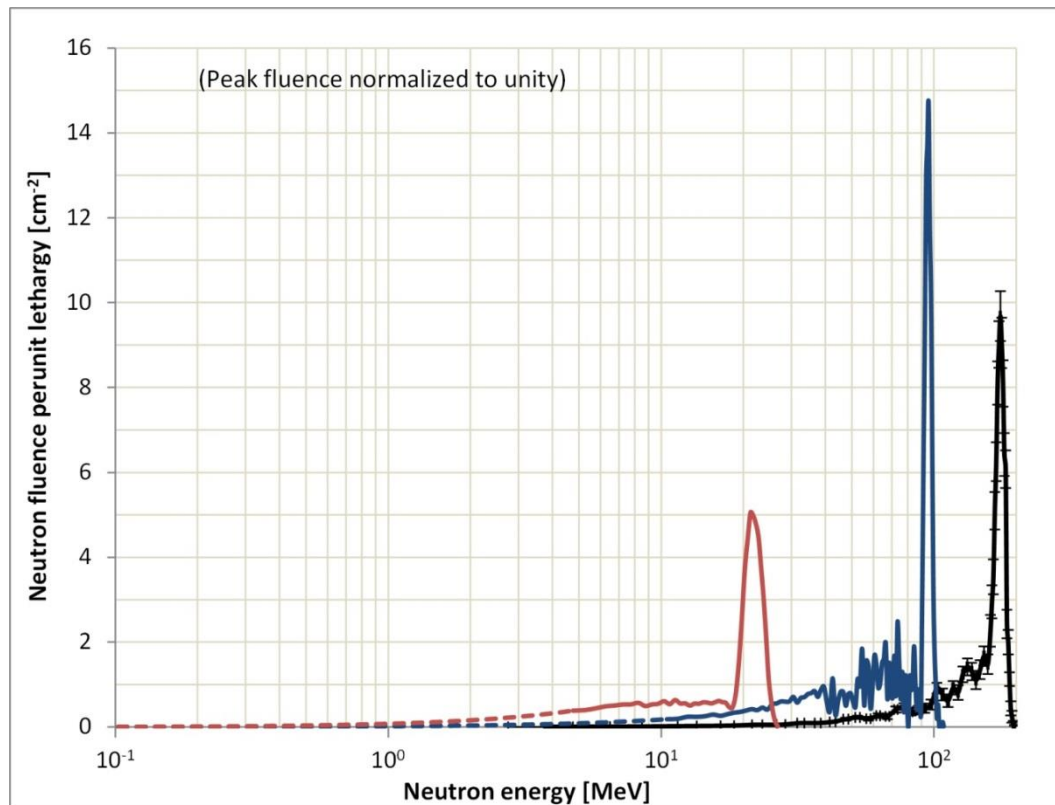
Figure II-26 – Experimental QMN spectra of 25 MeV and 95 MeV from [207] *(with their calculated low-energy extensions in dashed lines), and the experimental QMN spectrum of 175 MeV from* [208] *(with its statistical 1σ uncertainties)*

II-4.1.8 Comparison with the simulated WENDI-2 responses

The four series of QMN spectrum evaluations described in the preceding sections were used for two purposes. The first one was to estimate the k_{peak} factor, *i.e.* the ratio of the peak fluence to the total fluence, which is necessary for determining the measured WENDI-2 response to the QMN beam. The measured WENDI-2 response is indeed obtained by dividing the number of WENDI-2 counts by the total fluence, *i.e.* the ratio of the measured peak fluence to the k_{peak} factor.

The second purpose of the QMN spectrum evaluations was to fold them with the different available versions of the WENDI-2 response function, in order to assess which of these functions tends to produce the best match with the WENDI-2 measurements.

Folding the QMN spectra with the WENDI-2 response functions was done using MCNPX simulations, in which a neutron source emits a parallel QMN beam that uniformly irradiates the air cell of reference (having the same volume as the He tube of the WENDI-2). To this air cell, the Tally type F4 was applied in combination with

DE – DF cards [100], which defined the response function to be folded with the neutron fluence.

The response functions that were used are shown in Figure **II-27**. A common section for all response functions was defined between 0.144 MeV and 19 MeV, using the experimental data acquired by Olsher *et al.* [152]. This allowed focusing entirely on the impact that the high-energy part of the response function (above 20 MeV) has on the energy-integrated response. Our version of the response function, obtained using MCNPX 2.7.0 with the Bertini and Dresner models, was compared to other published versions obtained with MCNP4B & MCNPX 2.1.5 [152], FLUKA [183], and GEANT4 9.6 (with the Bertini model and with the BIC model) [184]. A response function was also defined based on the experimental values at high energies that Olsher *et al.* acquired at the TSL in the 2000s [182].
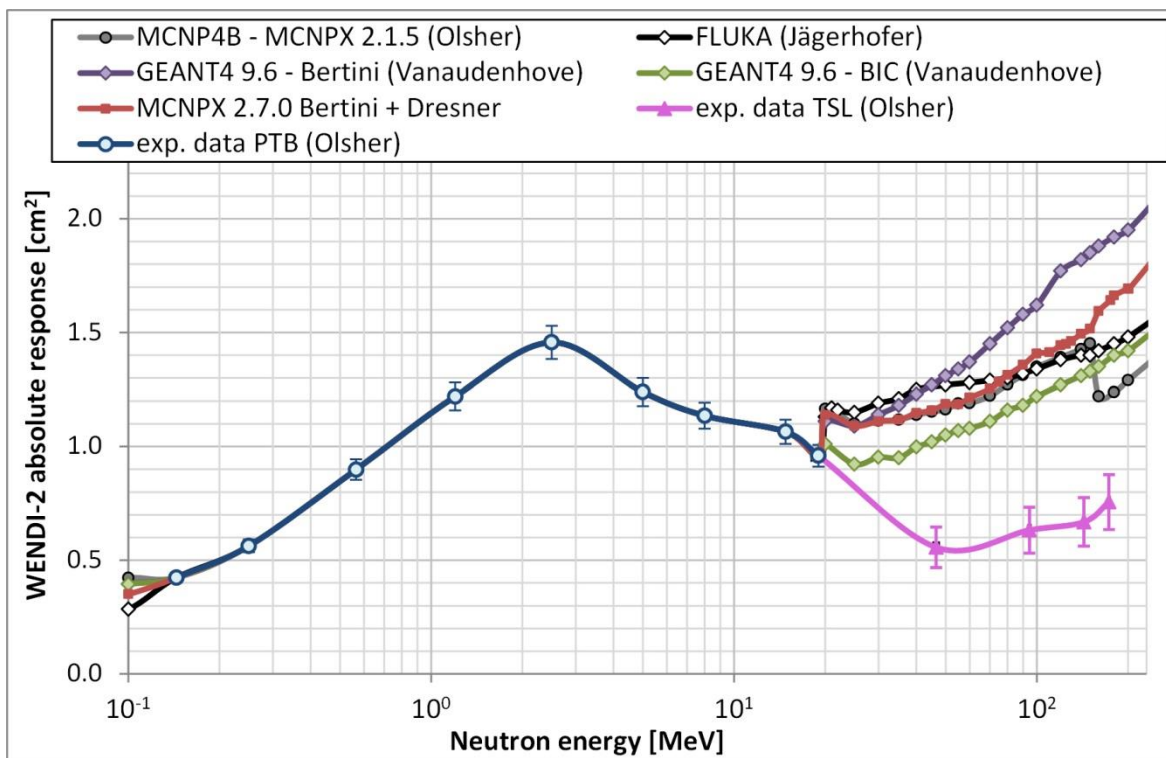
Figure II-27 – Response functions which were used to simulate the WENDI-2 response to the QMN beams. The connections between the points are only a guide for the eye; a log-log interpolation was automatically calculated by the MCNXP code.

II-4.2 Results

II-4.2.1 WENDI-2 and peak fluence measurements

The data collected with the WENDI-2 positioned at the AUP are given in the tables **II-15**, **II-17** and **II-19**, for the QMN beams of 21.8 MeV, 93.1 MeV and 173.4 MeV, respectively. At each energy, the irradiations were repeated several times (6 – 15 times) and the measurements show a good reproducibility. The relative type-A standard uncertainty on the average of the WENDI-2 counts was of 0.4% - 0.8 %. It was smaller than 0.1% for the average of the ICM counts. The P_{ICM} factor, which converts the ICM counts into the peak fluence, was assumed to have a relative standard uncertainty of 10%, following the estimate of the TSL members (see section **II-4.1.3**). Variations in the detector response due to the repositioning of the WENDI-2 at the AUP were of 0.4% - 0.5%. Based on these contributions, the relative combined standard uncertainty on the average WENDI-2 counts per unit peak fluence was estimated to 10%.

Tables **II-16** (21.8 MeV), **II-18** (93.1 MeV) and **II-20** (173.4 MeV), show the average WENDI-2 counts per unit peak fluence measured in positions out of the QMN beam or in its penumbra. With a lateral displacement of 30 cm with respect to the AUP (see position A), the WENDI-2 stood as expected entirely out of the beam plateau, yet still partially in the penumbra. Its response corresponded to 3-4 % of the response at the AUP. At distances of more than 50 cm from the beam axis, the WENDI-2 response varied between ~0.5% and ~2.5% of its corresponding AUP value. A decreasing trend was observed as the distance to the Li target increased (see positions E – C – D), which might reflect a contribution of the neutron leakage through the shielding of the target area. The neutron spectrum in these positions was expected to be largely dominated by low-energy room-scattered neutrons (mostly thermal neutrons), with perhaps a more significant contribution of cascade and evaporation neutrons in positions that are closer to the target area. It was assumed, based on the out-of-beam measurements, that the contribution to the WENDI-2 response at the AUP due to low-energy neutrons (E < 0.1 MeV) was negligible. The assumption also seems consistent with the measurements at the AUP reported in [207], in which the TFBC monitor containing a ^{235}U target was temporarily shielded by a sheet of cadmium (that acts as a strong absorber of neutrons below ~0.5 MeV). From these measurements, Prokofiev *et al.* estimated the low-energy fluence to ~0.5 – 2% of the peak fluence, *i.e.* less than 1% of the total fluence. Taking also into account the lower sensitivity of the WENDI-2 in this energy region, the contribution of low-energy neutrons to the WENDI-2 response should then indeed be smaller than 1%.

Table II-15 – Measurements in the 21.8 MeV QMN beam, with the WENDI-2 at the AUP

Position of WENDI-2	WENDI-2 counts	Irradiation time [s]	Dead-time corrected WENDI-2 counts	ICM counts
AUP	455.10^3	195	457.10^3	2132
	451.10^3	190	453.10^3	2135
	479.10^3	199	481.10^3	2145
	485.10^3	198	487.10^3	2139
	472.10^3	196	474.10^3	2129
	444.10^3	188	446.10^3	2141
	464.10^3	197	466.10^3	2143
	441.10^3	185	443.10^3	2158
	465.10^3	196	467.10^3	2142
	441.10^3	187	443.10^3	2159
	470.10^3	199	472.10^3	2146
	455.10^3	191	457.10^3	2151
	470.10^3	199	472.10^3	2144
	461.10^3	193	463.10^3	2142
	474.10^3	199	476.10^3	2145
Average			**$(464 \pm 4).10^3$**	**2143 ± 2**
P_{ICM} (cm^{-2})			112 ± 11	
Average WENDI-2 counts/peak fluence (cm^2)			**1.93 ± 0.19**	
Position of WENDI-2	WENDI-2 counts	Irradiation time [s]	Dead-time corrected WENDI-2 counts	ICM counts
AUP (repositioning)	479.10^3	205	481.10^3	2155
	466.10^3	198	468.10^3	2157
	461.10^3	196	463.10^3	2161
	549.10^3	194	461.10^3	2150
Average			**$(468 \pm 5).10^3$**	**2156 ± 7**
P_{ICM} (cm^{-2})			112 ± 11	
Average WENDI-2 counts/peak fluence (cm^2)			**1.94 ± 0.19**	

Table II-16 – Penumbra and out-of-beam measurements in the 21.8 MeV QMN beam

Position of WENDI-2	Distance to Li target (m)	Lateral displacement from beam axis (m)	Average WENDI-2 counts/peak fluence (cm^2)
HO	9.5	0.15	1.3 ± 0.1
A	9.5	0.30	0.067 ± 0.007
B	9.5	0.50	0.030 ± 0.003
C	9.5	0.885	0.023 ± 0.002
D	11.0	1.2	0.015 ± 0.002
E	7.0	1.0	0.039 ± 0.004

Table II-17 – Measurements in the 93.1 MeV QMN beam, with the WENDI-2 at the AUP

Position of WENDI-2	WENDI-2 counts	Irradiation time [s]	Dead-time corrected WENDI-2 counts	ICM counts
AUP	727.10^3	209	732.10^3	5156
	735.10^3	210	740.10^3	5154
	736.10^3	216	741.10^3	5132
	739.10^3	212	744.10^3	5127
	734.10^3	214	736.10^3	5124
	751.10^3	217	756.10^3	5157
	721.10^3	218	725.10^3	5140
	731.10^3	212	736.10^3	5135
	733.10^3	211	738.10^3	5128
	719.10^3	215	723.10^3	5115
	Average		**$(737 \pm 3).10^3$**	**5137 ± 5**
	P_{ICM} (cm^{-2})		58.3 ± 5.8	
	Average WENDI-2 counts /peak fluence (cm²)		**2.46 ± 0.25**	
Position of WENDI-2	WENDI-2 counts	Irradiation time [s]	Dead-time corrected WENDI-2 counts	ICM counts
AUP (repositioning)	737.10^3	226	741.10^3	5144
	736.10^3	220	740.10^3	5142
	Average		**$(741 \pm 3).10^3$**	**5143 ± 6**
	P_{ICM} (cm^{-2})		58.3 ± 5.8	
	Average WENDI-2 counts /peak fluence (cm²)		**2.47 ± 0.25**	

Table II-18 – Penumbra and out-of-beam measurements in the 93.1 MeV QMN beam

Position of WENDI-2	Distance to Li target (m)	Lateral displacement from beam axis (m)	Average WENDI-2 counts/peak fluence (cm²)
HO	9.5	0.15	1.5 ± 0.2
A	9.5	0.30	0.093 ± 0.009
B	9.5	0.50	0.038 ± 0.004
C	9.5	0.885	0.019 ± 0.002
D	11.0	1.2	0.012 ± 0.001
E	7.0	1.0	0.028 ± 0.003

Table II-19 – Measurements in the 173.4 MeV QMN beam, with the WENDI-2 at the AUP

Position of WENDI-2	WENDI-2 counts	Irradiation time [s]	Dead-time corrected WENDI-2 counts	ICM counts
AUP	712.10^3	287	747.10^3	4194
	714.10^3	289	749.10^3	4182
	692.10^3	283	725.10^3	4185
	706.10^3	284	741.10^3	4182
	715.10^3	289	750.10^3	4176
	710.10^3	286	745.10^3	4195
	Average		**$(743 \pm 4) .10^3$**	**4186 ± 3**
	P_{ICM} (cm^{-2})		72.0 ± 7.2	
	Average WENDI-2 counts /peak fluence (cm^2)		**2.46 ± 0.25**	
Position of WENDI-2	WENDI-2 counts	Irradiation time [s]	Dead-time corrected WENDI-2 counts	ICM counts
AUP (repositioning)	686.10^3	276	720.10^3	4186
	706.10^3	282	741.10^3	4184
	723.10^3	290	758.10^3	4198
	Average		**$(740 \pm 11) .10^3$**	**4189 ± 4**
	P_{ICM} (cm^{-2})		72.0 ± 7.2	
	Average WENDI-2 counts /peak fluence (cm^2)		**2.45 ± 0.25**	

Table II-20 – Penumbra and out-of-beam measurements in the 173.4 MeV QMN beam

Position of WENDI-2	Distance to Li target (m)	Lateral displacement from beam axis (m)	Average WENDI-2 counts/peak fluence (cm^2)
A	9.5	0.30	0.095 ± 0.010
B	9.5	0.50	0.060 ± 0.006
C	9.5	0.885	0.038 ± 0.004
D	11.0	1.2	0.023 ± 0.002
E	7.0	1.0	0.058 ± 0.006

II-4.2.2 QMN spectrum evaluations

A good knowledge of the shape of the QMN spectrum is necessary in order to accurately determine k_{peak}, the ratio of the measured peak fluence to the total fluence. Without an accurate estimate of k_{peak}, and thus of the total delivered fluence, the measured WENDI-2 response cannot be determined properly. Four methods to characterise the QMN spectra (see sections **II-4.1.4 – II-4.1.7**) were examined in this work. The spectra calculated by the TSL staff and the spectra measured through PRT spectrometry [207][208] have already been shown on **p. 89** and **p. 93**, respectively. Here, the results of our two MCNPX simulations, based on the Bertini model and the 3007.00h table, are shown in the figures **II-28** and **II-29**, respectively. These spectra are presented on lethargy plots in order to give a meaningful visual appreciation of the relative neutron energies.
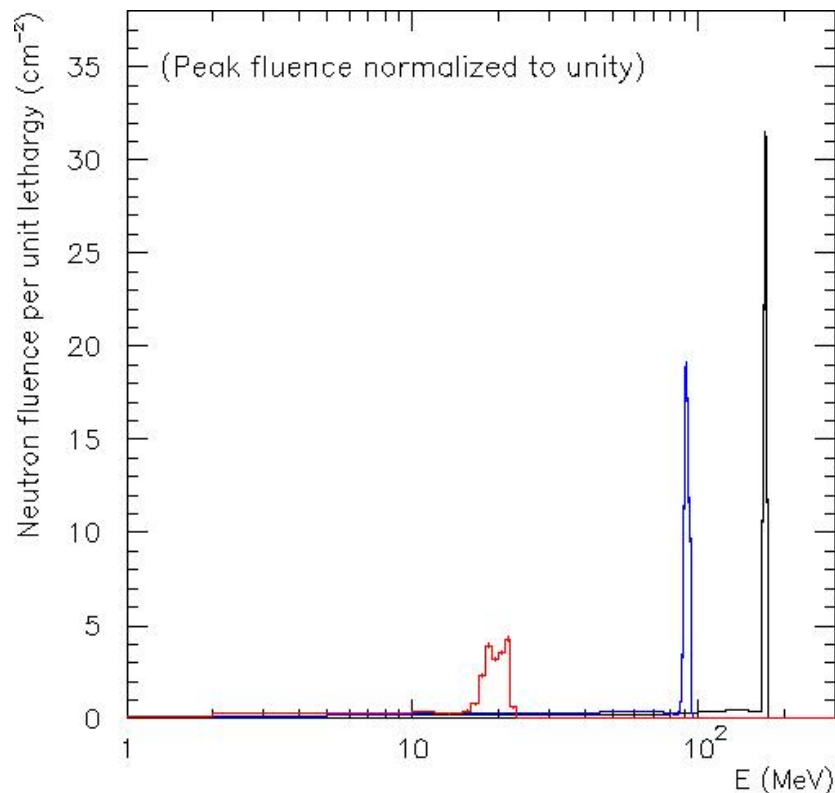
Figure II-28 – Lethargy plot of the QMN spectra simulated with MCNPX using the Bertini model (with proton energies of 24.6 MeV, 96.3 MeV and 177.8 MeV).
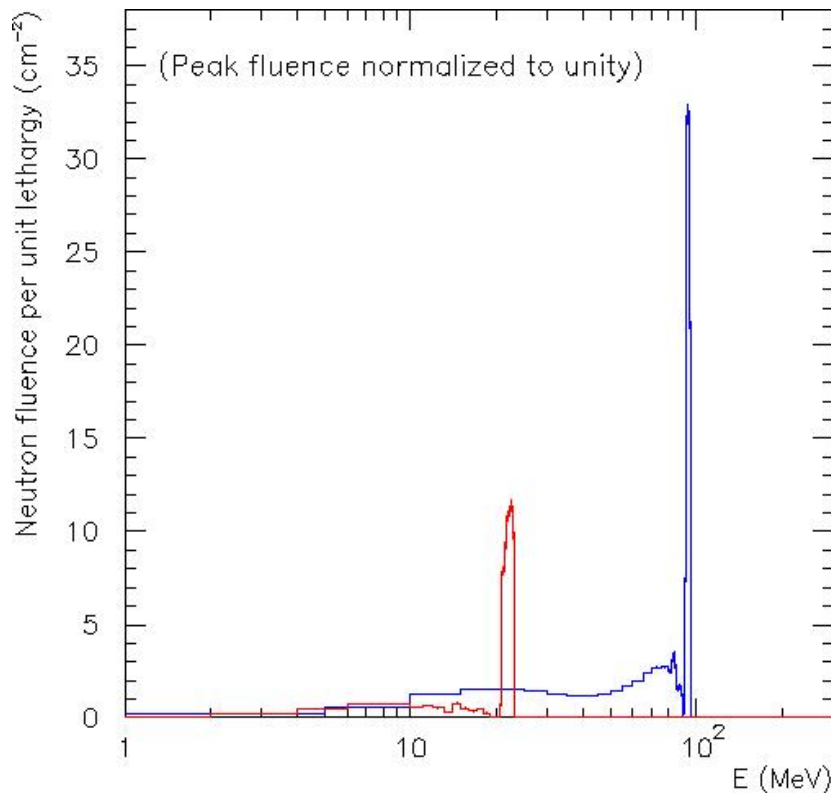
Figure II-29 – Lethargy plot of the QMN spectra simulated with MCNPX using the 3007.00h data (with proton energies of 24.6 MeV and 96.3 MeV).

Next, the four different spectrum evaluations are compared with each other, for each QMN beam separately, in the figures **II-30**, **II-31** and **II-32**. These are linear-logarithmic plots of the neutron fluence per unit energy, which provide a more detailed view of the high-energy end of the spectra. The peak fluences are normalized to unity, because the experimental data in [207,208] are given with this normalization (and not as absolute fluences per unit proton). A summary of the main characteristics of the four evaluations, including the average peak energy, the peak Full-Width at Half Maximum (FWHM) and the k_{peak} value, is given in table **II-21**.

The comparison shows that the spectral resolution of the PRT spectrometry was relatively poor. The FWHMs of the high-energy peak in the experimental spectra are indeed 2 – 3 times larger than the theoretical widths corresponding to the maximum proton energy loss in the Li target (see the spectra calculated by the TSL staff). It was not attempted to correct these spectra through an unfolding procedure, because the knowledge on the energy dependence of the resolution was considered insufficient. As such, the influence of the poor spectral resolution on the k_{peak} value is difficult to quantify precisely. In the case of the 21.8 MeV and 93.1 MeV QMN beams, the k_{peak} value is also influenced by the way in which the spectra were extrapolated at low energies. The non-extrapolated spectra of the 21.8 MeV and 93.1 MeV QMN beams had k_{peak} values that were larger by 21% and 5%, respectively. Let us then assume that these percentages constitute an upper estimate for the relative uncertainty on k_{peak} due to the extrapolation method.
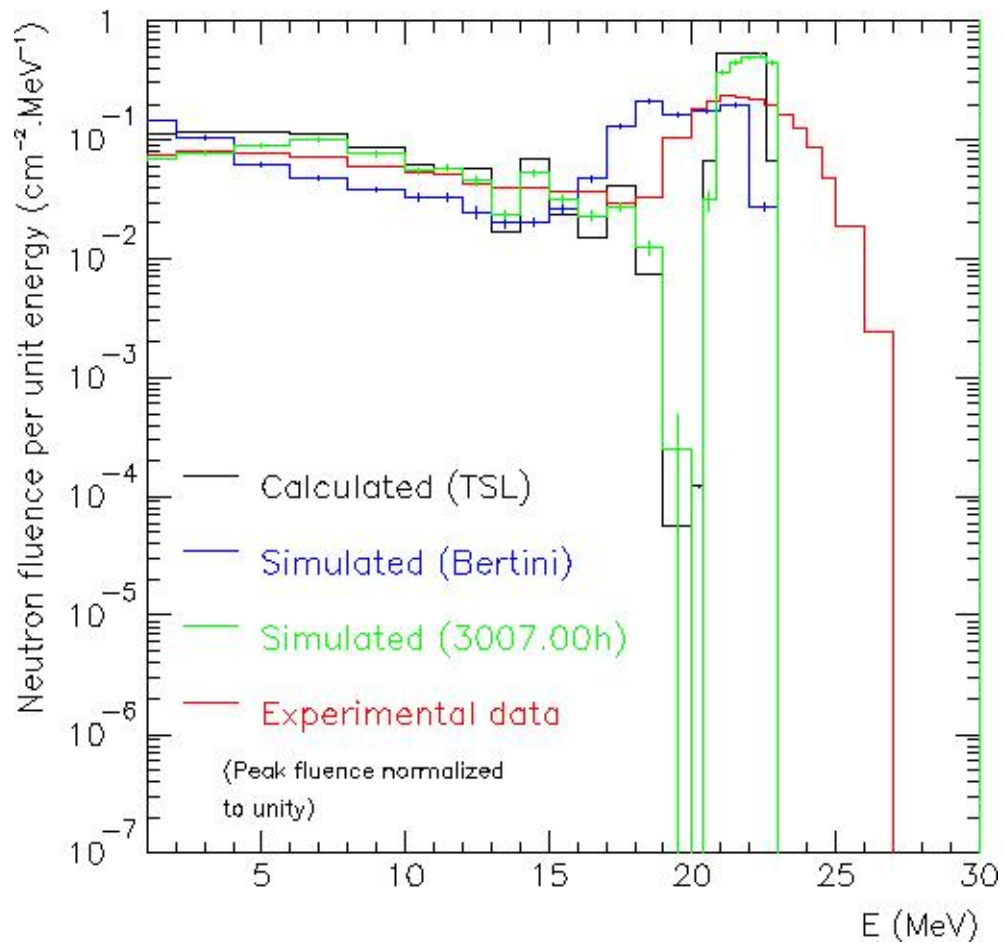
Figure II-30 – Evaluations of the QMN spectrum produced by 24.6 MeV protons on a 2 mm thick Li target, as calculated by the TSL members and as simulated with MCNPX using the Bertini model and the 3007.00h data, respectively. Comparison with the spectrum measured through PRT spectrometry for a proton energy of 24.68 MeV (±0.04 MeV) and the same target thickness [207]. The peak fluences are normalized to unity.
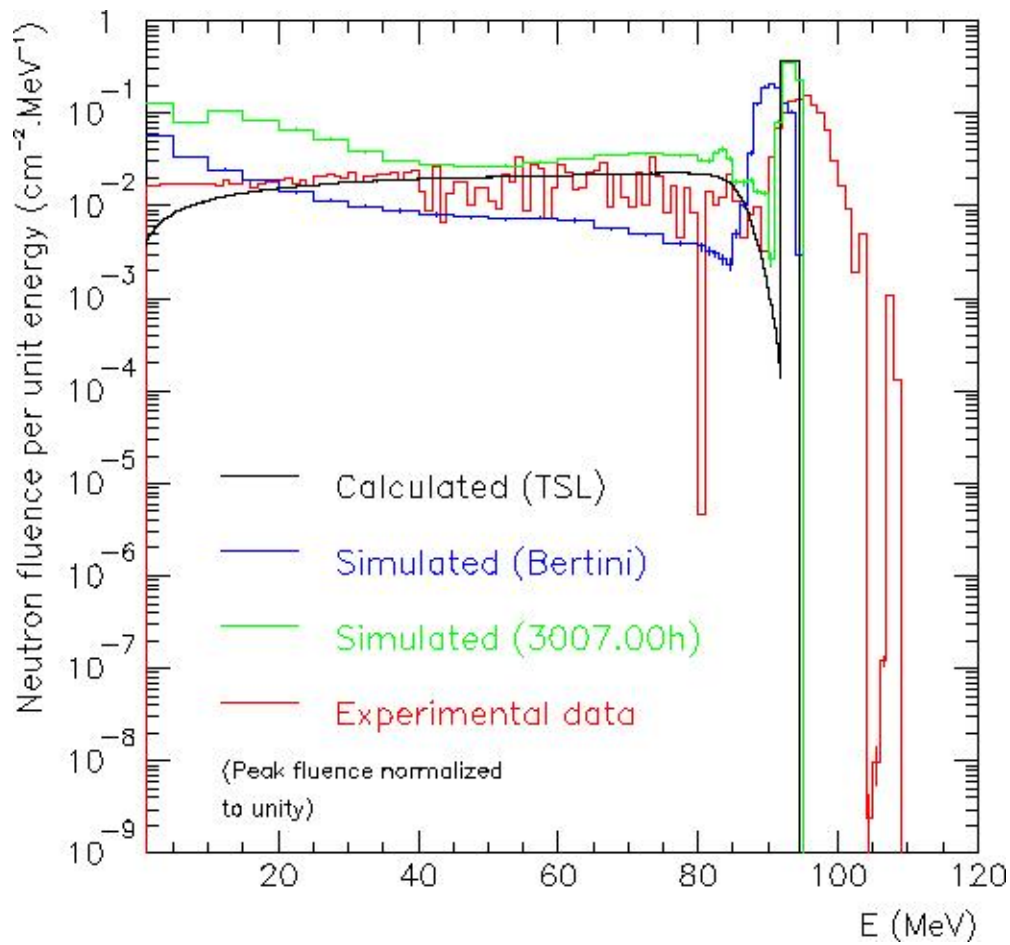
Figure II-31 – Evaluations of the QMN spectrum produced by 96.3 MeV protons on a 8.5 mm thick Li target, as calculated by the TSL members and as simulated with MCNPX using the Bertini model and the 3007.00h data, respectively. Comparison with the spectrum measured through PRT spectrometry for a slightly higher proton energy of 97.9 MeV (±0.3 MeV) and the same target thickness [208]. *The peak fluences are normalized to unity.*
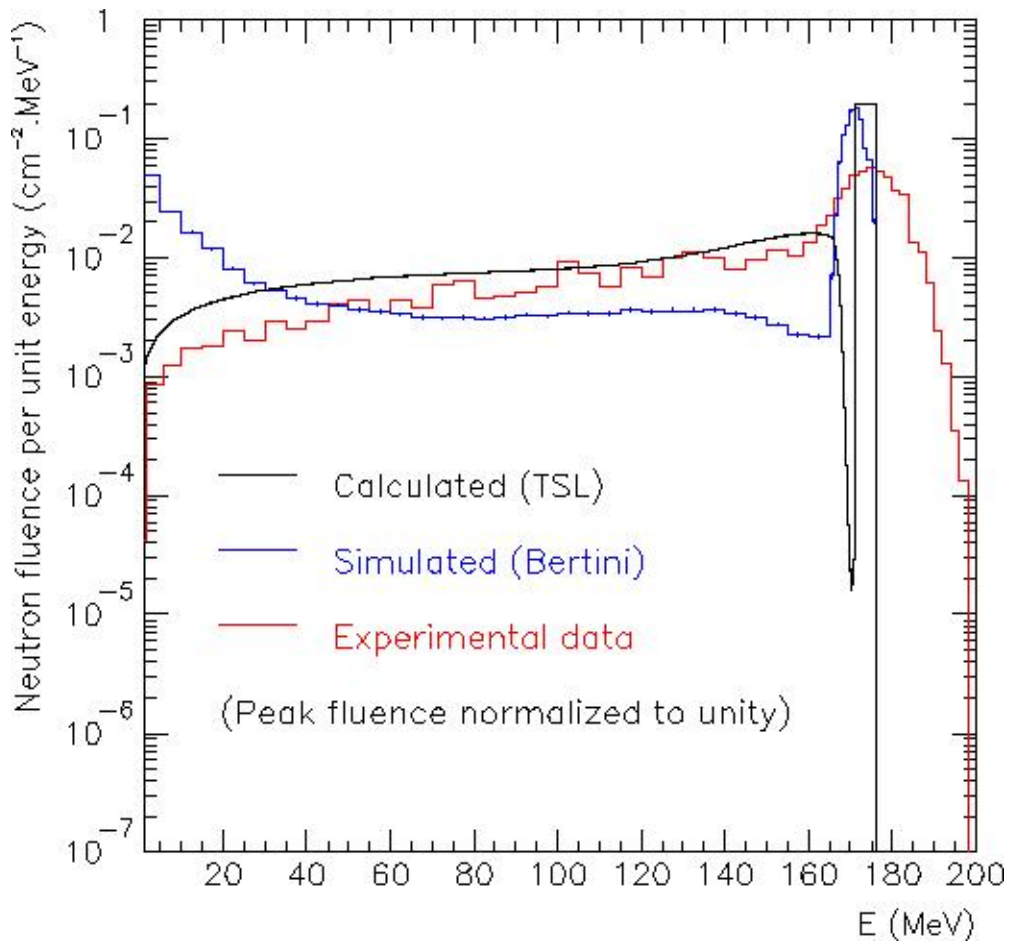
Figure II-32 – Evaluations of the QMN spectrum produced by 177.8 MeV protons on a 23.5 mm thick Li target, as calculated by the TSL members and as simulated with MCNPX using the Bertini model. Comparison with the spectrum measured through PRT spectrometry for a slightly higher proton energy of 179.3 MeV (±0.8 MeV) and the same target thickness. The peak fluences are normalized to unity.

Table II-21 – Characteristics of the four QMN spectrum evaluations

	MCNPX Bertini	MCNPX 3007.00h	TSL calculation	Experimental spectrum
E_p [MeV]	24.6			24.68
Li target thickness [mm]	2.0			2.0
Average peak energy [MeV]	19	22	21.8	21.8
Peak FWHM [MeV]	5	2	1.9	4.5
k_{peak}	0.529	0.465	0.413	0.48
E_p [MeV]	96.3			97.9
Li target thickness [mm]	8.5			8.5
Average peak energy [MeV]	90.8	93.5	93.1	95
Peak FWHM [MeV]	6	3	2.6	6
k_{peak}	0.462	0.183	0.391	0.40
E_p [MeV]	177.8	-	177.8	179.3
Li target thickness [mm]	23.5	-	23.5	23.5
Average peak energy [MeV]	171	-	173.4	175
Peak FWHM [MeV]	6	-	5.0	18
k_{peak}	0.489	-	0.421	0.53

Concerning the 'default' MCNPX simulations, it appears that the Bertini model fails to satisfactorily predict the studied QMN spectra, even at the proton energy of 177.8 MeV. In the three cases, the average energy of the high-energy peak is too low and the peak width too large, given the maximum energy losses in the Li target. An improvement with increasing proton energies is nevertheless noticeable in the prediction of the high energy peak. This is however not the case for the low-energy tail. There is a clear underestimate compared to the experimental spectra on a large part of the continuum above a certain energy (~4 MeV/25 MeV/50 MeV), whereas below that energy, the simulated continua seem to be overestimated. In spite of these issues, the resulting k_{peak} value might be relatively realistic in the case of the 173.4 MeV QMN beam (0.489, compared to 0.53 for the experimental spectrum). For the two lower energy QMN beams, the k_{peak} values predicted by the Bertini model are ~10 - 15% larger than those of the extrapolated experimental spectra.

The MCNPX simulations based on the 3007.00h data (see Figures **II-30** and **II-31**) reproduce the shape of the high-energy peak more realistically than the Bertini-based simulations, especially at the lowest energy. At both QMN energies (21.8 MeV and 93.1 MeV), the centre and the width of the high-energy peak reasonably match those of the theoretical peak calculated by the TSL staff. The peak-to-tail ratio,

however, seems to be reproduced correctly only in the case of the 21.8 MeV QMN beam. The low-energy tail in Figure **II-30** indeed approximates the experimental continuum relatively well, whereas an overall overestimate of the continuum is visible in Figure **II-31** (93.1 MeV). For the 21.8 MeV QMN beam, the MCNPX simulation based on the 3007.00h data thus seems to provide a rather realistic spectrum representation. The obtained k_{peak} factor is only 3% smaller than that of the extrapolated experimental spectrum (0.465 *vs.* 0.48). In the case of the 93.1 MeV QMN beam, the k_{peak} factor of the 3007.00h-based spectrum is however much underestimated (0.183 *vs.* 0.40).

Our results for the 93.1 MeV QMN beam confirm the discrepancies that Prokofiev *et al.* observed when using the 3007.00h data (referred to as the "la150 library" in their work [225]). The semi-empirical systematics that they developed to remedy this problem [225], and which were used here in the spectrum calculated by the TSL staff, indeed provide a better match for the experimental continuum in Figure **II-31** (93.1 MeV). The k_{peak} value is in this case just ~2% smaller than that of the extrapolated experimental spectrum (0.391 *vs.* 0.40). For the 173.4 MeV QMN beam, the semi-empirical systematics obviously agree much better with the experimental continuum than the Bertini-based MNCPX prediction (see Figure **II-32**), but the agreement is apparently a little less satisfying than for the 93.1 MeV QMN beam. This translates as a 20% smaller k_{peak} value compared to the experimental spectrum (0.421 *vs.* 0.53).

For the 21.8 MeV QMN beam, the spectrum calculated by the TSL staff is as expected very similar to our 3007.00h-based spectrum (see Figure **II-30**), since the results are based on nearly the same evaluated nuclear data. The k_{peak} value of the calculated spectrum is about 14% smaller than that of the extrapolated experimental spectrum (0.413 *vs.* 0.48).

II-4.2.3 Simulated WENDI-2 responses

For each QMN spectrum evaluation, the WENDI-2 response was calculated using the different versions of the response function shown in Figure **II-27** on **p. 94**. The results for the QMN beams of 21.8 MeV, 93.1 MeV and 173.4 MeV are shown in the Figures **II-33**, **II-34** and **II-35**, respectively.

These results show that, for a given QMN beam, the simulated WENDI-2 response does not depend strongly on the choice of the spectrum evaluation. This can be related to the fact that, regardless of the tested function, the value of the absolute response function at the peak energy is not extremely different from the values at the energies mainly represented in the low-energy tail. For the 21.8 MeV QMN beam, for instance, the WENDI-2 response varies by maximum 2-3% due to the selected spectrum shape (for a given version of the response function). For the 93.1 MeV QMN beam, these variations do not exceed 2-4% for most response functions. They are a

bit larger for the two functions which tend to "stick out" from the others at higher energies, namely the response function calculated with GEANT4 using the Bertini model (variations of maximum 9%) and the response function based on Olsher's experimental data (maximum 25%). The same trend is seen in the results for the 173.4 MeV QMN beam. The maximum variations related to the choice of the spectrum shape are of 4-6% for all response functions except for the GEANT4 Bertini version (11%) and the experimental version (16%).

Following the same logic, the WENDI-2 responses to the QMN beams are in most cases not very different from their corresponding monoenergetic response (variations of less than 10%). The largest observed differences are:

- a variation of +12% with the GEANT4 BIC response and the Bertini spectrum, for the 21.8 MeV QMN beam,
- a variation of +32% with Olsher's experimental response and the 3007.00h spectrum, for the 93.1 MeV QMN beam, and
- a variation of -16% with the GEANT4 Bertini response and the Bertini spectrum, for the 173.4 MeV beam.

As such, the spread between the responses obtained from different response functions remains quite large with the QMN beams of 93.1 MeV and 173.4 MeV. The maximum spread reaches up to a factor of 2.1 and 2.5, respectively (see GEANT4 Bertini *vs.* Olsher's experimental data). With the 21.8 MeV QMN beam, however, nearly the entire low-energy tail lies below 19 MeV, *i.e.* in the common section of the used response functions. In this case, the maximum spread between the QMN responses does not exceed 8%.
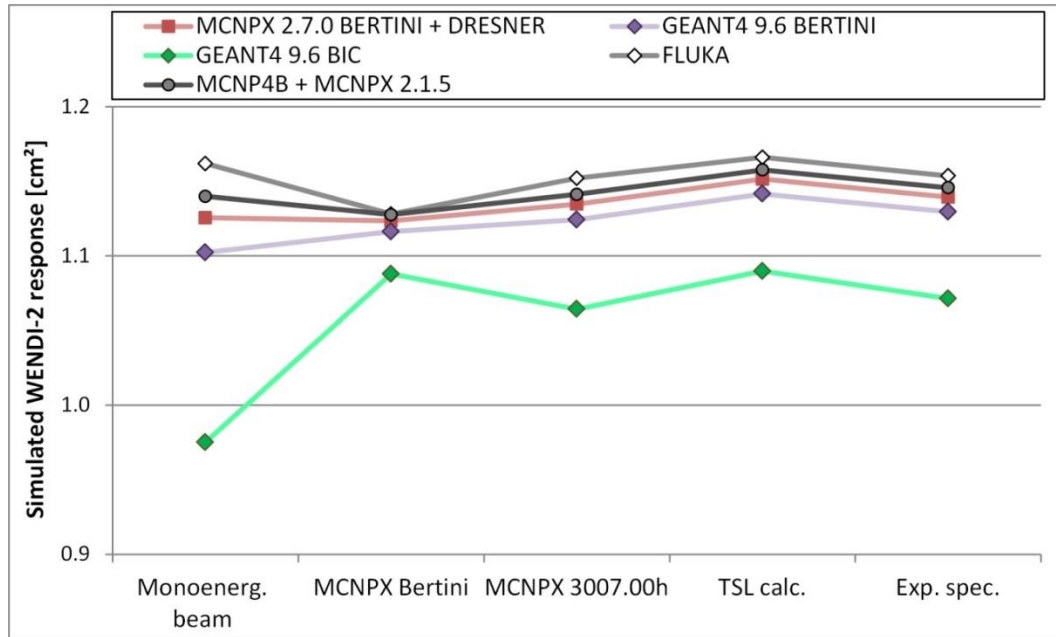
Figure II-33 – Simulated WENDI-2 response to a monoenergetic beam of 21.8 MeV vs. four evaluations of the corresponding QMN spectrum (from left to right: with MCNPX using the Bertini model, with MCNPX using the 3007.00h data, calculated by the TSL, and measured with the PRT technique [207]*). Five different versions of the WENDI-2 response function were used (see Figure II-27). The response function based on Olsher's experimental data acquired at the TSL is not considered for the 21.8 MeV QMN beam, because these experimental values were only given above 46 MeV. The lines connecting the points are just a guide for the eye.*
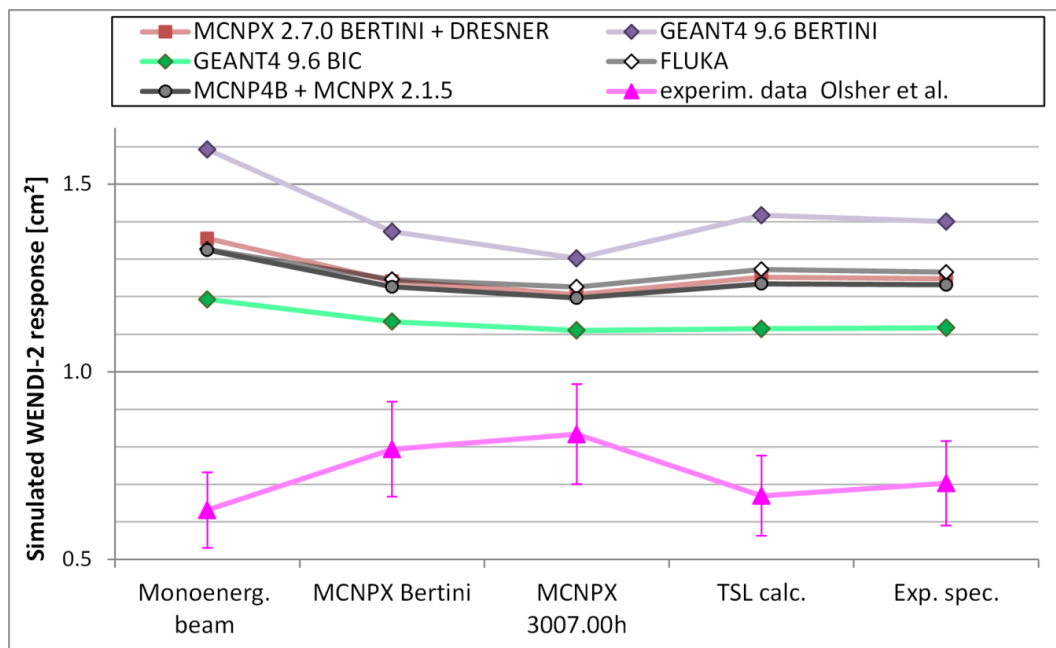
Figure II-34 – Simulated WENDI-2 response to a monoenergetic beam of 93.1 MeV vs. four evaluations of the corresponding QMN spectrum (from left to right: with MCNPX using the Bertini model, with MCNPX using the 3007.00h data, calculated by the TSL, and measured with the PRT technique [207]*). For each case, the WENDI-2 response was evaluated according to six versions of the response (see Figure II-27). The lines connecting the points are just a guide for the eye.*
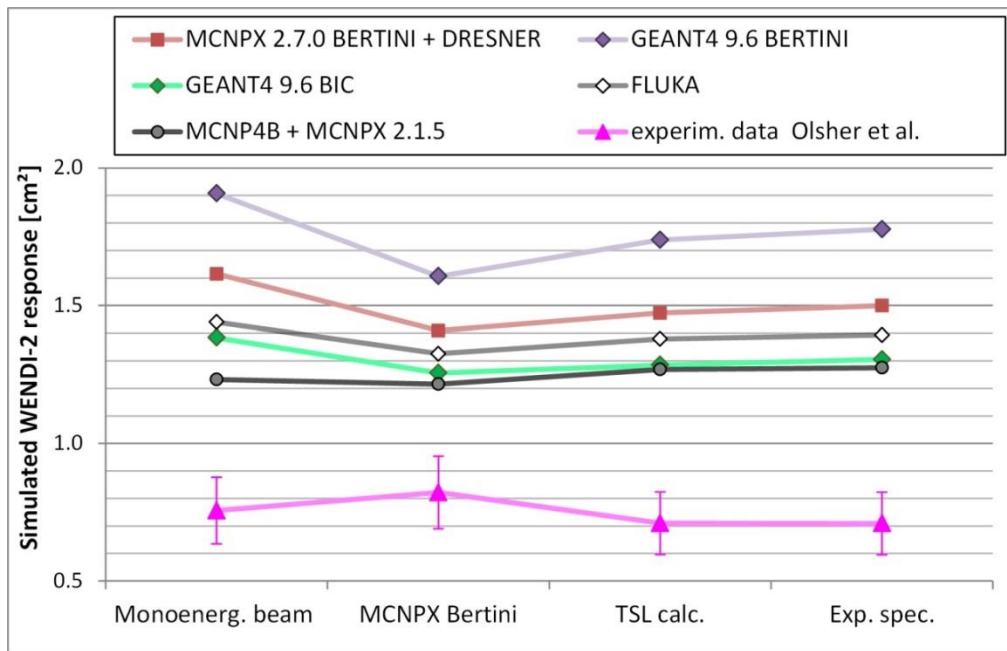
Figure II-35 – Simulated WENDI-2 response to a monoenergetic beam of 173.4 MeV vs. three evaluations of the corresponding QMN spectrum (from left to right: simulated with MCNPX using the Bertini model, calculated by the TSL, and measured with the PRT technique [207]*). For each case, the WENDI-2 response was evaluated according to six versions of the response (see Figure II-27). The lines connecting the points are just a guide for the eye.*

II-4.2.4 Comparison with measured WENDI-2 responses

Due to the direct proportionality existing between k_{peak} and the measured WENDI-2 response, the latter is much more sensitive to the assumed spectrum shape than the simulated WENDI-2 responses discussed in the previous section. This is illustrated in the figures **II-36**, **II-37** and **II-38**, which compare the measured and simulated WENDI-2 responses for each considered QMN spectrum evaluation. The error bars on the measured WENDI-2 responses correspond to the 1σ uncertainty on the measured peak fluence (10%, see sections **II-4.1.3** and **II-4.2.1**).

For the 21.8 MeV QMN beam, the k_{peak} value varies by up to 28% depending on the considered neutron spectrum. Due to the limitations of the available experimental spectrum, it is not possible to determine k_{peak} with a better precision in this case. Nevertheless, the results show a general trend in which the measured WENDI-2 response tends to be smaller than the simulated responses, and Vanaudenhove's function based on the GEANT4 BIC model yields the better agreement with these measurements (see figure **II-36**). The latter seems relatively reasonable because, around 20 MeV, this function provides the least abrupt transition with the experimental data acquired by Olsher *et al.* up to 19 MeV (see Figure **II-27** on **p. 94**). To our knowledge, no existing physical process ought to cause a brusque increase in the response function between 19 and 20 MeV.
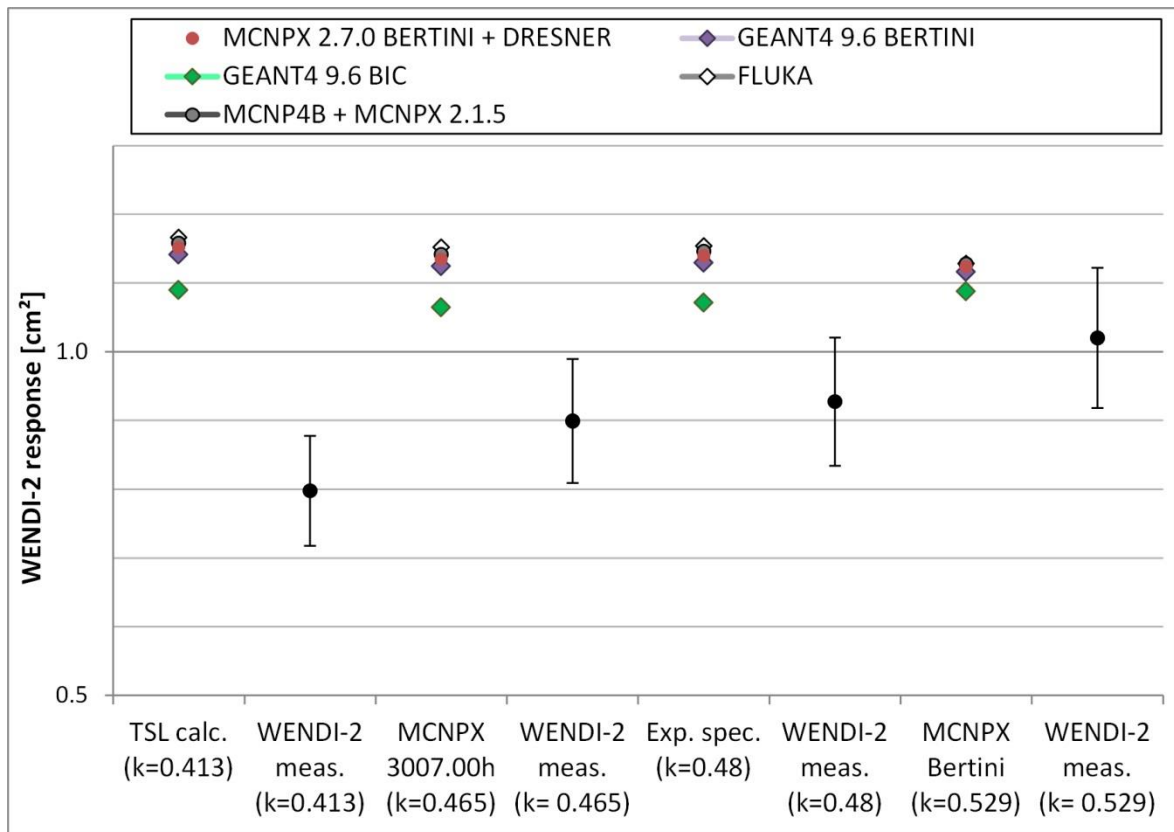
Figure II-36 – Simulated vs. measured WENDI-2 response for the 21.8 MeV QMN beam, considering four different evaluations of the corresponding QMN spectrum (from left to right: calculated by the TSL, simulated with MCNPX using the 3007.00h data, measured with the PRT technique [207], and simulated with MCNPX using the Bertini model). The plain black dots represent the WENDI -2 measurements.

Concerning the 93.1 MeV QMN beam, the k_{peak} value of the spectrum simulated using the 3007.00h data has seemed much underestimated, in comparison to that of the experimental spectrum (0.183 *vs.* 0.40, see section **II-4.2.2**). As a matter of fact, the measured WENDI-2 response based on this k_{peak} value also seems unrealistically low, with respect to both the simulated response functions and the high-energy QMN measurements of Olsher *et al.* (see Figure **II-37**). By contrast, the spectrum evaluation based on the Bertini model of MCNPX leads to a measured response that agrees within 1σ with nearly all simulated response functions (except the one based on the Bertini model of GEANT4 9.6). In this case, however, the spectrum shape is not very realistic either and we cannot exclude that the k_{peak} value might be a bit overestimated (see section **II-4.2.2**). A more accurate measured response is probably obtained when using the k_{peak} value of the spectrum calculated by the TSL staff (0.391) or the extrapolated experimental spectrum (0.40). In these two cases, the measured response agrees within 2σ with the BIC-based simulated response, as well as with the QMN measurements of Olsher *et al.*
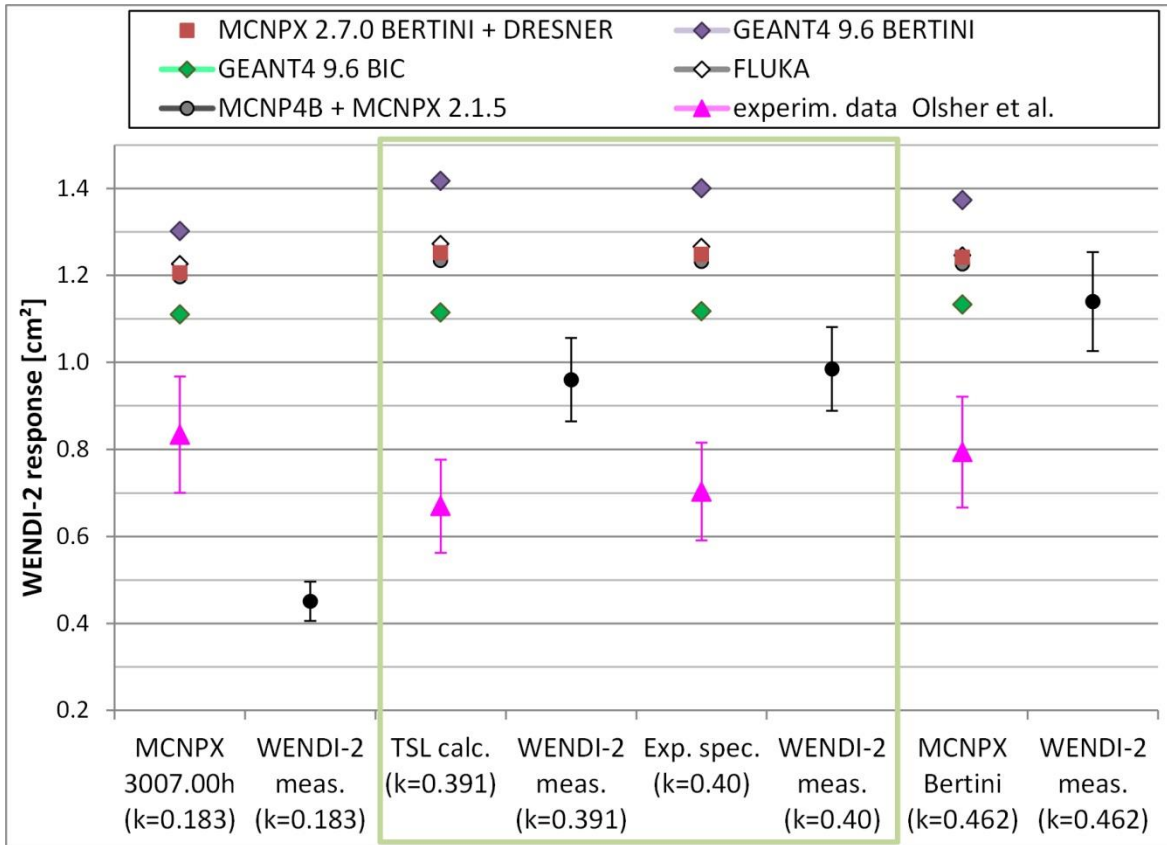
Figure II-37 – Simulated vs. measured WENDI-2 response for the 93.1 MeV QMN beam, considering four different evaluations of the corresponding QMN spectrum (from left to right: simulated with MCNPX using the 3007.00h data, calculated by the TSL, measured with the PRT technique [207], and simulated with MCNPX using the Bertini model). The plain black dots represent the WENDI -2 measurements.

As for the 173.4 MeV QMN beam, the true k_{peak} value potentially lies somewhere in between that of the spectrum calculated by the TSL (0.421) and that of the (particularly poorly resolved) experimental spectrum (0.53). A more precise evaluation of k_{peak} could not be determined. Nevertheless, for any of the considered spectrum evaluations, our measurements are in better agreement with the simulated response functions than the measurements of Olsher *et al.* (see Figure **II-38**). The response functions calculated with MCNP4B/MCNPX 2.1.5 and the BIC model of GEANT4 9.6 yield the best agreement, with energy-integrated responses lying within one to two standard uncertainties of the measured response. These two simulated responses are very similar in this case because of the discontinuity near 150 MeV in the MCNP4B/MCNPX 2.1.5 response function (see Figure **II-27** on **p. 94**): the larger response to continuum neutrons (compared to the BIC response function) is compensated by a smaller response above 150 MeV. Finally, it should be noted that our measurements are also compatible with those of Olsher *et al.* within two (to three) standard uncertainties.
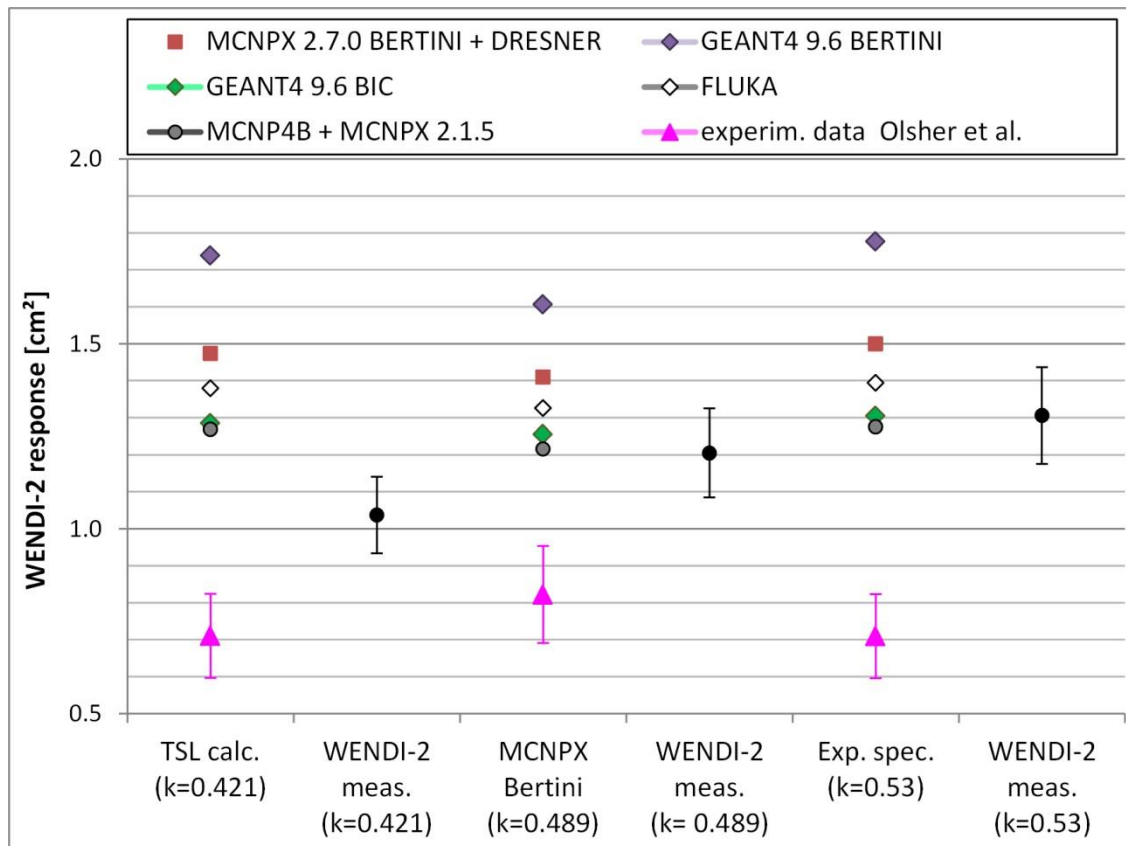
Figure II-38 – Simulated vs. measured WENDI-2 response for the 173.4 MeV QMN beam, considering three different evaluations of the corresponding QMN spectrum (from left to right: calculated by the TSL, simulated with MCNPX using the Bertini model ,and measured with the PRT technique [207]*). The plain black dots represent the WENDI -2 measurements.*

Olsher *et al.*, unlike us, used polyethylene filters to harden the QMN spectra, by preferentially attenuating the neutron fluence below 20 MeV [182]. The optimum polyethylene thickness for each QMN beam was determined through MCNPX simulations, in which the source spectrum was based on the semi-empirical systematics of Prokofiev *et al.* The optimum filter thicknesses ranged from 30 cm (for the 46.5 MeV QMN beam) up to 50 cm (for the 173 MeV QMN beam). According to the MCNPX simulations, the use of these filters allowed increasing the peak fluence fraction (k_{peak}) from ~0.4 to ~0.6 for each QMN beam [182]. This publication does not mention, however, whether the estimated k_{peak} factors were actually used to correct the measured neutron fluences. No description of the fluence measurements is in fact provided in the paper. It is likely, though, that the fluence measurements also relied on the TFBC monitor, which was already operational at the TSL in the 2000s. Nevertheless, without a full knowledge of the methodology followed by Olsher *et al.*, it is difficult to assess whether any specific systematic errors are largely responsible for the differences observed between their measurements and our own.

Also, an accurate validation of the high-energy response function would actually require correcting the measured QMN response for the contribution of low-energy neutrons, in order to determine the true monoenergetic response at the

energy of the QMN peak. In the publication of Olsher *et al.* [182], the WENDI-2 measurements were presented on a graph as monoenergetic responses at the peak energies, but the text does not mention any correction for the contribution of tail neutrons. Possibly, the correction was simply considered to be negligible. Looking back on our simulation results in section **II-4.2.3**, in particular those of the BIC-based WENDI-2 response, it actually seems plausible that the required correction would be relatively small (<10%), at least for the two high-energy QMN beams. However, it was not possible to estimate these corrections by means of measurements performed within the facility of the TSL. Moreover, trying to calculate them would not yield precise results because the calculation requires the knowledge of both the spectrum and the response function over the entire low-energy tail (including at energies above 19 MeV in the case of high-energy QMN beams).

The large measuring uncertainties thus prevent us from precisely determining the values of the high-energy response function at the peak energies. Nevertheless, our measurements indicate that this function might be intermediate to the measurements of Olsher *et al.* and the response function simulated with the BIC model of GEANT4 9.6 by Vanaudenhove *et al.* In this aspect, our results confirm that the sensitivity of the WENDI-2 in the range of 20 MeV – 175 MeV is very similar in magnitude to its sensitivity between ∼0.5 MeV and 20 MeV (see figure **II-27** on p. **94**).

II-5 Conclusion

The absolute response function of the WENDI-2 was simulated using MCNPX 2.7.0 for energies from 10^{-9} MeV to 250 MeV. Two different neutron source configurations were compared for the lateral irradiation of the detector: an isotropic point source located at 50 cm from the detector centre and a uniform rectangular parallel beam. The differences due to the considered source configuration were found to decrease with increasing neutron energies, starting from ∼20% at thermal energies and becoming fully negligible above ∼70 MeV. In both cases, evaluated cross-section data from the la150n library were used to compute neutron interactions up to 150 MeV. At higher energies, hadronic models had to be used to simulate the intranuclear cascade, pre-equilibrium and evaporation stages of the nuclear reactions. The different nuclear reaction models available in the code were compared but yielded relatively similar results between 150 MeV and 250 MeV (differences of ∼20% at most). In general, our results were found to be intermediate to those obtained by other authors with different Monte Carlo codes. The intercomparison of their results showed differences of up to ∼300% at thermal energies, ∼30% in the range of 0.5 MeV – 20 MeV, and ∼50% between 20 MeV and 250 MeV.

The dose response function of the WENDI-2, obtained by multiplying the absolute response function with the built-in calibration factor, was compared to the fluence-to-H*(10) conversion coefficients of the ICRP Publication 74. The latter represent the behaviour of an ideal detector, capable of measuring H*(10) accurately in any kind of neutron spectrum. Relatively large discrepancies between the response function and the fluence-to-H*(10) conversion coefficients were observed in some energy regions (intermediate neutrons in particular). In spite of these discrepancies, the WENDI-2 seems to have a good potential for providing accurate H*(10) measurements behind shielding walls in proton therapy facilities. The WENDI-2 response to such neutron fields is indeed expected to be largely due to evaporation and high-energy neutrons. An accurate response to evaporation neutrons is in principle ensured by the ^{252}Cf calibration of the WENDI-2. As for the high-energy neutrons, the theoretical dose response function in the range of 10 MeV – 250 MeV seems relatively well-balanced with respect to the fluence-to-H*(10) coefficients.

To validate the simulated response function in the energy range of evaporation neutrons (0.1 MeV – 10 MeV), measurements were performed with ^{252}Cf and AmBe sources. These measurements were found compatible within one standard uncertainty with the monoenergetic beam measurements of Olsher *et al.* at energies between 0.144 MeV and 19 MeV. Since the measured WENDI-2 responses to the ^{252}Cf field were within one standard uncertainty of the reference H*(10) rates, our measurements also validated the built-in calibration factor determined by the manufacturer. The responses based on our simulated response functions, obtained with MCNPX 2.7.0, agreed with the measurements within two to three standard uncertainties. Amongst the different response functions compared in this work, the best agreement with the measurements was obtained with the function simulated by Jägerhofer *et al.* using FLUKA (agreement within one standard uncertainty).

At energies between 20 MeV and 250 MeV, validating experimentally the response function of an extended-range rem meter like the WENDI-2 remains a challenging task. The core difficulty lies in the fact that the calibration fields always contain a fraction of lower-energy neutrons yielding a significant contribution to the detector response. As a consequence, the delivered neutron fluence needs to be measured accurately over the entire neutron spectrum and the shape of the spectrum has to be well characterised. The lower-energy contribution should be evaluated with good precision so that it can be subtracted from the measurement. No international standard has yet been established for such procedure. In this work, WENDI-2 measurements were performed in high-energy QMN beams at the TSL in Uppsala. The used beams had peak energies of 21.8 MeV, 93.1 MeV and 173.4 MeV. Only the peak fluence could be measured, with a relative uncertainty estimated to 10%. The total fluence had to be derived from the measured peak fluence by dividing it by the fraction of peak neutrons k_{peak}. The latter was however affected by a rather large uncertainty (of probably ~20-30%), due to the difficulty to obtain a precise characterisation of the neutron spectra. The experimental spectra available in

literature, obtained through proton recoil spectrometry, suffer from a poor spectral resolution and their lower energy threshold is of a few MeV at best. The latter is particularly limiting for the QMN beam with the lowest peak energy (21.8 MeV). Also, the experimental spectra for the two high-energy QMN beams were not acquired for exactly the same peak energies as in our experiment (differences of 1.0-1.5 MeV). The capabilities of MCNPX 2.7.0 to simulate these spectra were also found disappointing, except perhaps when using the evaluated cross-section table 3007.00h in the case of the 21.8 MeV QMN beam. For ^{7}Li(p,n) reactions induced by protons in the range of 40 MeV – 175 MeV, there seems to be a lack of appropriate evaluated cross-section data and the existing statistical nuclear reaction models, which are based on a level density formalism, are ill-adapted. The semi-empirical systematics developed by Prokofiev *et al.* seem to provide a reasonable alternative for these spectrum calculations, but they still need to be confronted to spectral measurements of higher quality. Due to the uncertainties in the spectrum shape, a precise validation of the high-energy response function of the WENDI-2 could not be achieved. Nevertheless, our results suggest that the response function near the peak energies of 93.1 MeV and 173.4 MeV might be intermediate to the results of Vanaudenhove *et al.* simulated with the BIC model of GEANT4 9.6 and the earlier QMN measurements by Olsher *et al.* They thus confirm that the sensitivity of the WENDI-2 in the range of 20 MeV – 175 MeV must be comparable to its sensitivity in the range of ~0.5 MeV – 20 MeV.

Further progress in the experimental characterisation of the WENDI-2 response function at energies between 20 MeV and 250 MeV can perhaps be achieved by means of QMN irradiations at the Research Centre for Nuclear Physics (RCNP) in Osaka, Japan. Very recently [232,233], characterised QMN beams with peak energies of 76 MeV, 96 MeV, 134 MeV, 197 MeV and 244 MeV have become available in this facility. The spectra of these QMN beams have been measured down to 3 MeV through the time-of-flight method, with a very good precision thanks to among others the great length of the experimental tunnel (~100m). Moreover, Iwamoto *et al.* have proposed a promising method for the calibration of high-energy neutron dosimeters in which the contribution of the low-energy tail can be evaluated experimentally [233]. The method relies on the capacity to move the ^{7}Li target within the swinger magnet in order to select various neutron emission angles between 0° and 30°. At angles of 20°-30°, the shape of the low-energy continuum in the neutron spectrum is strikingly similar to that of the 0° spectrum, while its high-energy peak is very small (nearly indistinguishable from the continuum). At each beam energy, Iwamoto *et al.* have determined for the spectrum at 25° the normalization factor k that equalizes its continuum to that of the spectrum at 0°. They suggest that the mono-energetic response of a high-energy neutron dosimeter at the peak energy could be evaluated by measuring the detector response to the beam at 25°, multiplying it by k and subtracting this contribution from the detector response to the beam at 0°.

CHAPTER III
MCNPX simulations of secondary neutrons in the proton therapy facility of Essen

III-1 Introduction

This chapter presents Monte Carlo simulations carried out with MCNPX 2.7.0 to compute the neutron fluxes and their energy spectrum in several positions inside and around four rooms of the proton therapy facility at Essen. The simulations were carried out following the same methodology as in the MCNPX simulations on which the shielding design for this facility was based (design by F. Stichelbaut, IBA, [79]). This methodology is based on several conservative hypotheses, which will be explained in this chapter.

Later, in Chapter IV, it will be our goal to verify the conservative nature of these MCNPX simulations, by comparing the simulated results of this chapter to on-site neutron dose measurements performed with a WENDI-2 at Essen. In this chapter, the simulated neutron spectra will therefore be used to compute the operational quantity H*(10). The WENDI-2, like most ambient neutron dosimeters in use today, was indeed designed to measure H*(10). However, as we have shown in Chapter II, its response function does not perfectly follow the ideal behaviour represented by the fluence-to-H*(10) conversion coefficients. Thus, in neutron fields that differ strongly from the ^{252}Cf calibration field, one should in principle verify the degree of accuracy with which the WENDI-2 can measure H*(10). This constitutes another goal of this chapter. The knowledge on the WENDI-2 response function gathered in Chapter II will be used to theoretically predict the WENDI-2 responses at the positions of interest inside the proton therapy facility and these predictions will be compared to the simulated H*(10).

Four case-studies will be presented here:

- an irradiation of the proton beam stop inside the cyclotron room,
- a simple Pencil Beam Scanning (PBS) irradiation inside a gantry treatment room,
- a simple Double Scattering (DS) irradiation inside a gantry treatment room, and
- a simple Uniform Scanning (US) irradiation inside the fixed-beam treatment room.
  (See section **I-2.1.2** for a brief introduction to the principles of the PBS, DS and US irradiation modes).

Comparable simulation results obtained with GEANT4 for the three first case-studies can also be found in Thibault Vanaudenhove's PhD thesis [184], and in [234].

III-2 Methodology

III-2.1 Modelled geometries and particle sources

III-2.1.1 Cyclotron room

The C230 cyclotron, the Energy Selection System (ESS), the adjacent shielding walls and the access maze were modelled according to the plans of the Essen facility. An overview of the modelled geometry is shown in figure **III-1**. A detailed view of the modelled cyclotron and ESS is also given in figure **III-2**.

The magnet yoke and poles of the cyclotron were represented in iron and its electromagnetic coil in copper. According to data provided by IBA, it is assumed that only 40% of the accelerated protons are extracted from the cyclotron. The other 60% do not follow the ideal acceleration trajectory and end up interacting with solid constituents of the cyclotron, which causes a significant production of secondary neutrons. The distribution of the proton losses inside the cyclotron is however difficult to quantify. Most of these losses are thought to occur on the copper septum of the extraction channel as well as, to a lesser extent, on the copper counter-dees [79] (see figure **III-3** below and figures 4.11 and 4.12 in T. Vanaudenhove's thesis [184]). The assumption was made that 40% of the accelerated protons are lost on the septum (see 'P2' arrow in figure **III-1**) and 10% on each of the two pairs of counter-dees (see 'P3' and 'P4' arrows in figure **III-1**). As a conservative approximation, the losses were considered as localized in a point on the extraction radius, where the protons have already reached their maximum energy of ~230 MeV. The angular neutron emission spectra were calculated beforehand, in a simulation representing a 230 MeV proton beam impinging on a thick copper cylinder (using MCNPX 2.5.0, with the la150n library and the default physics models [235]). The calculated spectra were then integrated in the definition of the neutron sources 'P2', 'P3' and 'P4' in the cyclotron room simulations.

The cyclotron-extracted proton beam (40%) was considered to be fully stopped on the nickel beam stop located on the degrader wheel of the ESS. This configuration, in which the beam is being produced but not (yet) delivered to a treatment room, obviously causes the largest production of secondary neutrons in the maze. Apart from the nickel beam stop, high Z materials of the ESS quadrupoles and dipoles (iron & copper pieces) were also modelled because they constitute important neutron scattering elements which significantly influence the neutron flux distribution in the room.
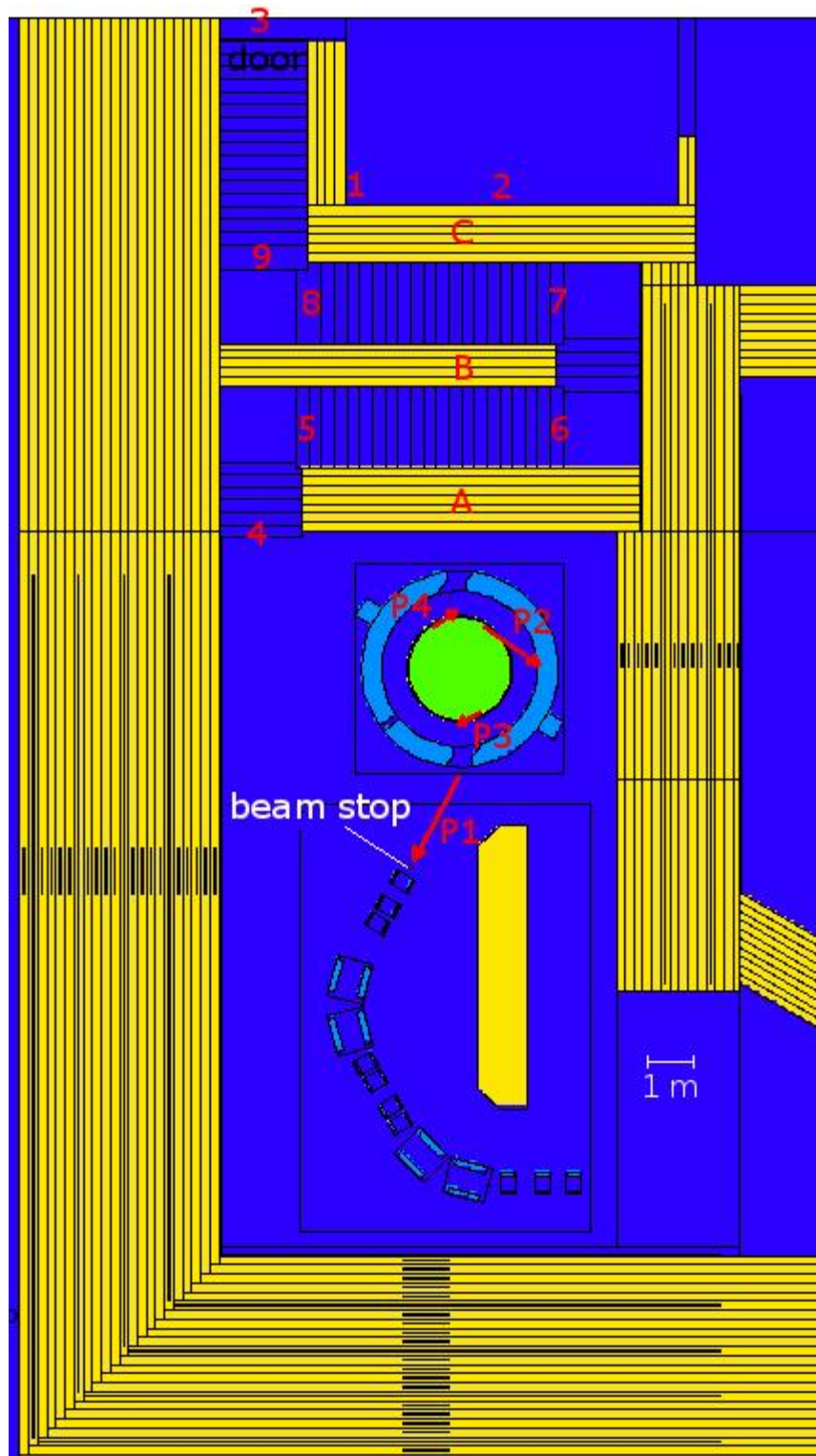
Figure III-1 - Modelled geometry of the cyclotron room (horizontal cut at height of the cyclotron median plane, 1.25 m above the floor). The concrete walls are represented in yellow, the cyclotron vacuum in green. The proton losses inside the cyclotron are represented by the 'P2', 'P3' and 'P4' arrows. A long red arrow also represents the cyclotron-extracted proton beam impinging on the beam stop of the degrader wheel. The red numbers in the maze (4 - 9) and outside the cyclotron room (1 - 3) indicate the WENDI-2 measurement positions. In the positions 1-3, the detector stood directly on the floor. In the positions 4-9, the detector stood on a trolley at ~1 m above the floor.
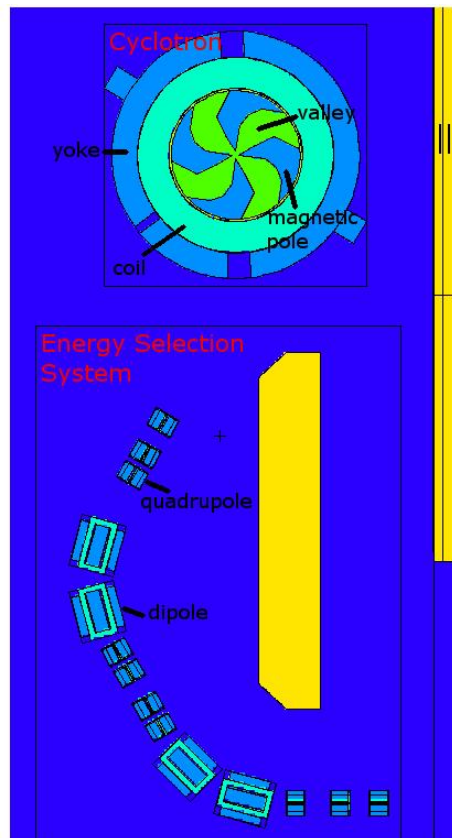
Figure III-2 - Detailed view of the modelled cyclotron and ESS (horizontal cut at 8 cm below the cyclotron median plane).
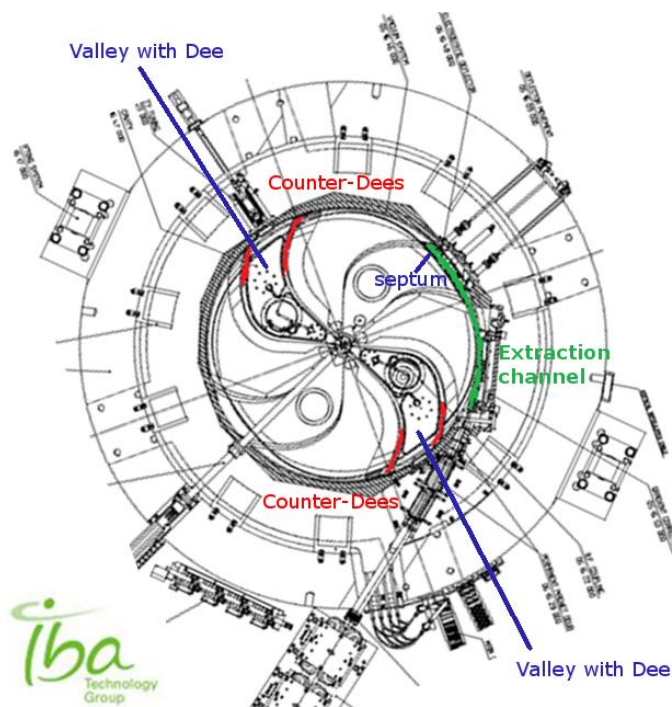
Figure III-3 - Positions of the counter-Dees and the extraction channel inside the cyclotron (courtesy of IBA).

III-2.1.2 Gantry room operated in PBS

The shielding walls and access maze of a standard gantry treatment room of the Essen facility were modelled with MCNPX 2.7.0 as shown in figure **III-4**. The gantry was assumed to be positioned at the worst angle from the radiation protection point of view (270°), *i.e.* the proton beam was shot horizontally in the direction of the patient-accessible area of the adjacent gantry room.
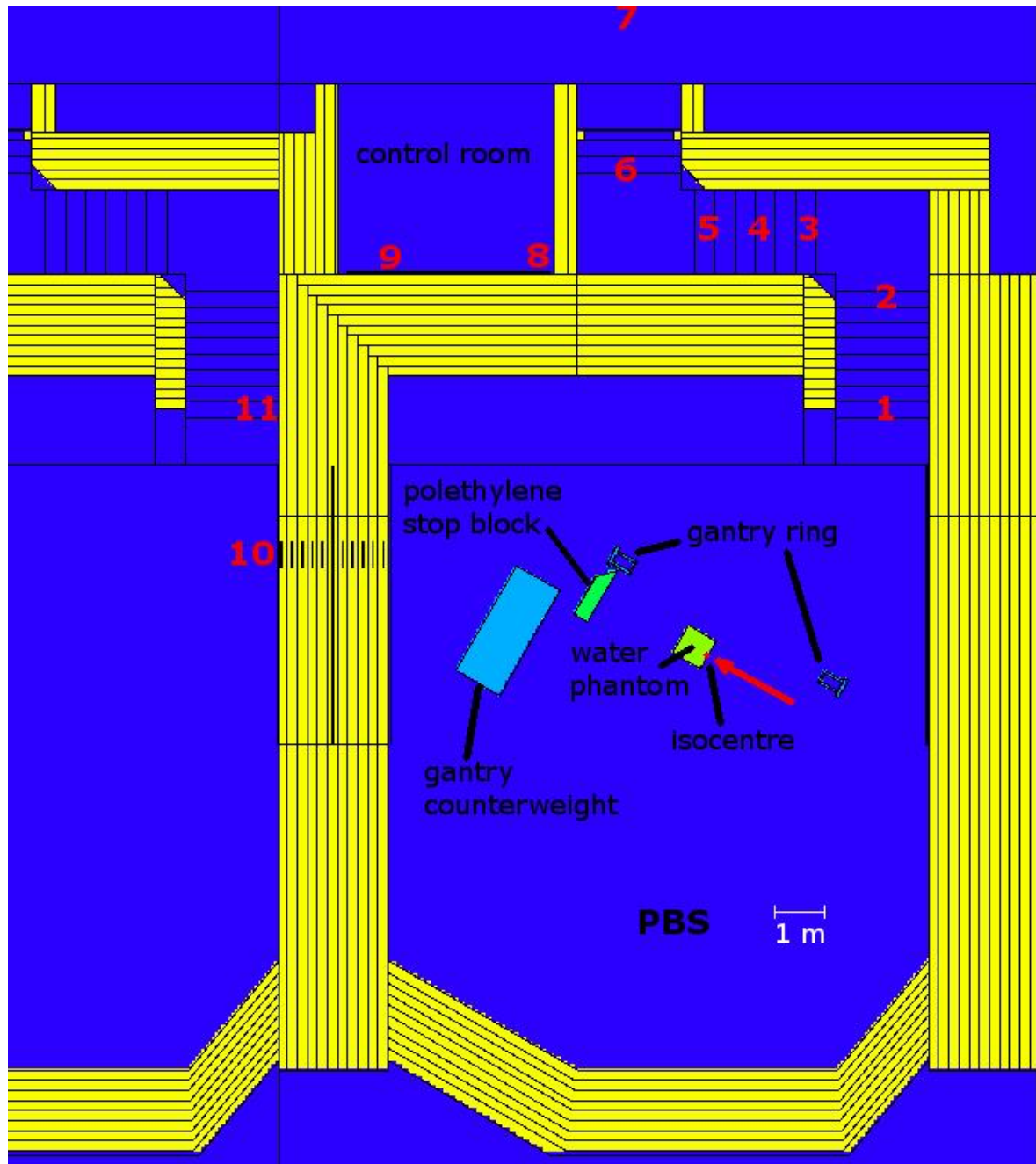
Figure III-4 - Modelled geometry of the gantry room operated in PBS. The concrete walls are represented in yellow, the water phantom in green. The red numbers in the maze (1 – 6) and outside the treatment room (7 – 11) indicate the WENDI-2 measurement positions. In positions 1 -7, the detector stood at ~25 cm above the floor. In positions 8 -11, the detector stood at ~1 m above the floor. Proton beam height: 1.25 m.

A water phantom was irradiated with a simple PBS configuration, consisting in a single beam spot with a fixed initial proton energy of 226.7 MeV. This proton beam has a range of 32.2 cm in water. In order to simulate the pencil beam, a Gaussian intensity profile with a standard deviation of 3 mm was defined for the proton source in front of the water phantom. The phantom was modelled as a water volume of 64 x 64 x 40 cm^3. The proton beam was directed towards the gantry isocentre and had a perpendicular incidence onto the vertical entrance plane of the water phantom. The isocentre lied at 16 cm below the water surface in this entrance plane.

The gantry structure, which is quite complex, was not modelled entirely. Initially, only two massive elements located downstream from the proton beam were represented in the model: the high-density (HD) polyethylene beam stop and the steel counterweight (see figure **III-5**). Preliminary results for this model simulated with MCNPX 2.5.0 were already presented in [184] and [234]. Later, the front ring of the gantry (see figure **III-5**) was added to the model, to see whether it would significantly influence the simulation result for position 9 in the control room (see figure **III-4**).

Figure III-5 - Schematic view of the gantry installed at the Essen facility (courtesy of IBA).

III-2.1.3 Gantry room operated in DS

A simple DS irradiation of a water phantom, without beam current modulation and without rotation of the Range Modulator wheel, was modelled as well. The corresponding beam shaping elements of the treatment nozzle were added to the geometry of the gantry treatment room (see figure **III-6**).
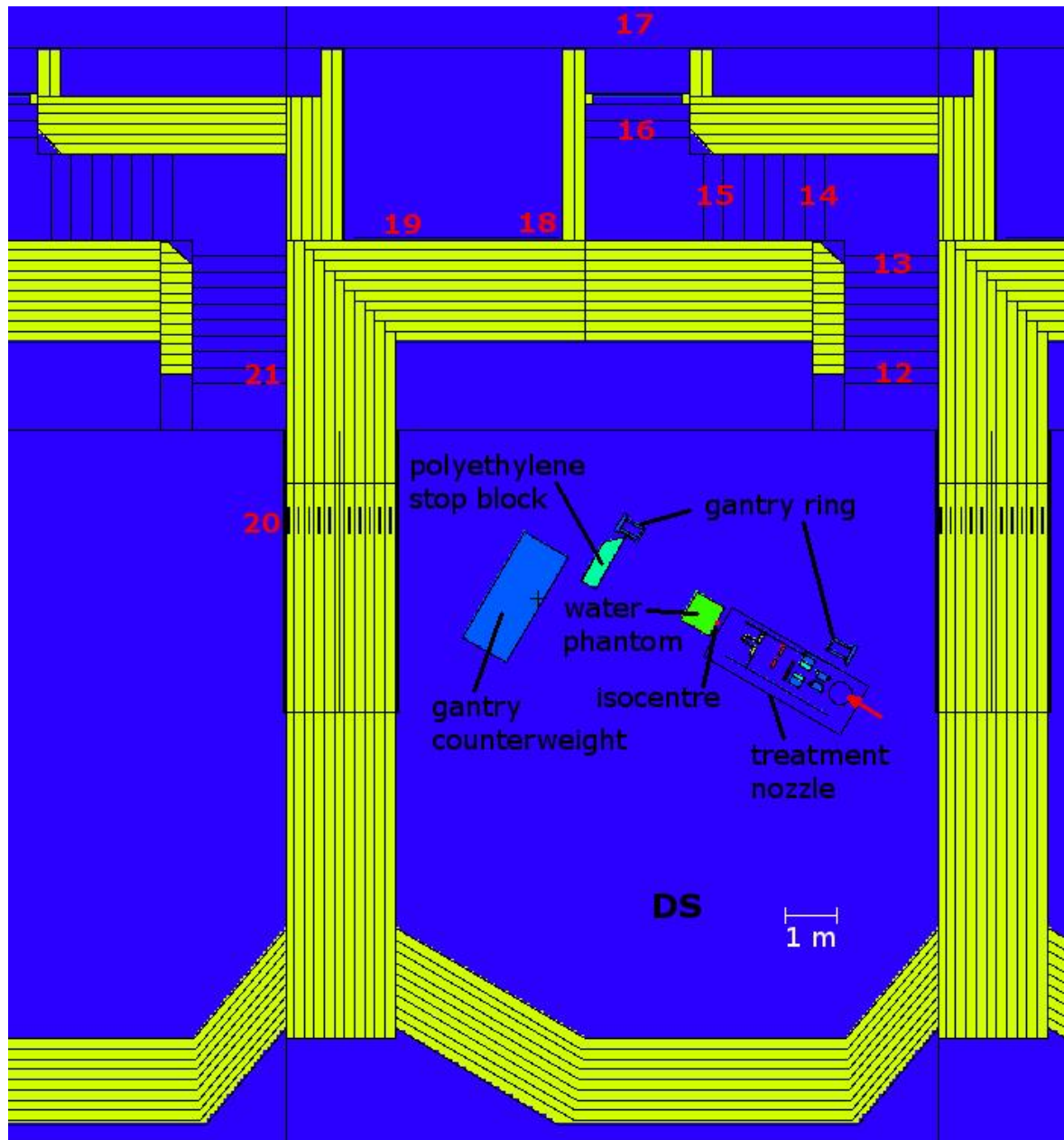
Figure III-6 - Modelled geometry of the gantry room operated in DS. The concrete walls are represented in yellow, the water phantom in green. The red numbers in the maze (12 –1 6) and outside the treatment room (17 – 21) indicate the WENDI-2 measurement positions. The detector stood at ~25 cm above the floor in positions 12-17, ~1 m above the floor in positions 18-19, and directly on the floor in positions 20-21. Proton beam height: 1.25 m.

A close-up of the modelled treatment nozzle is shown in figure **III-7**. The selected DS configuration produced a 16 cm diameter proton field at the isocentre, with a range of 28.2 cm in water. The following settings were used:

- Proton energy at the entrance of the treatment nozzle: 227.5 MeV.

- First Scatterer: tantalum, 1.351 mm thick.

- Range Modulator: Track #2 on Wheel #3. The wheel was held still so that only the first step of track #2 was irradiated. This step, covering the angles from 26.09° to 140.64° on the wheel, consists of 1 mm aluminium and 2.74 mm lead.

- Second Scatterer: Lens #3, consisting of a contoured piece of Lexan with a contoured lead topping. The thickness of both layers is a function of the radius.

- The opening of the collimating jaws along the X- and Y-axes was set to 10.6 cm. The X- and Y-axes are the horizontal and vertical axes, respectively, which are perpendicular to the proton beam axis. The X-axis jaws are made of nickel; the Y-axis jaws of brass. The pieces are 57 mm thick.

- Snout: retractable type #100-A, made of brass. Position: completely drawn in.

- Aperture: brass, with an internal diameter of 117 mm.
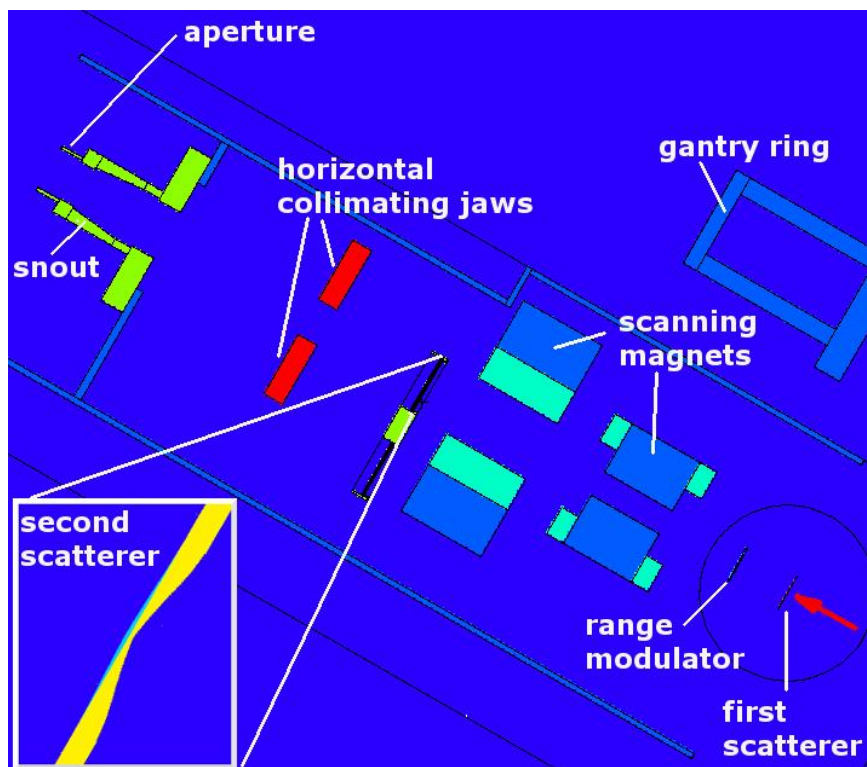
Figure III-7 – Modelled geometry of the DS treatment nozzle
(horizontal cut through the beam axis).

The scanning magnets inside the nozzle, which are not active during the DS delivery mode, were modelled because of their important neutron scattering/attenuating power (iron & copper pieces).

The phantom was modelled as a water volume of 64 x 64 x 45 cm^3, positioned with its vertical entrance plane perpendicular to the proton beam axis (see figure **III-6**). The gantry isocentre lied in this entrance plane, at 15 cm below the water surface. The proton source was defined in the same way as in the PBS simulation, except that it was positioned in front of the First Scatterer.

III-2.1.4 Fixed-beam treatment room

The fixed-beam treatment room of the Essen facility was modelled as shown in Figure **III-8**. This room possesses two separate beamlines: one for fixed-beam irradiations (in US mode, for example) and one dedicated to eye treatments. In this case, the beam was delivered to a water phantom through the fixed-beam treatment nozzle, which was operated in a simple US configuration.

The phantom was modelled as a 64 x 64 x 45 cm^3 water volume. It was positioned in such way that the beam isocentre lied in its vertical entrance plane, which was perpendicular to the beam direction. The dimensions of the proton field at the entrance of the phantom were of 19 cm x 22 cm. This was obtained only by means of active scanning, *i.e.* no beam scatterer was used inside the nozzle. The particle source in the simulation was therefore defined right in front of the water phantom, as a rectangular planar source of 19 cm x 22 cm, producing a parallel and uniform proton beam. It was assumed that this source definition provides a sufficiently good approximation of the true US field, which is actually not perfectly uniform (as will be shown in section **IV-2.4**). The proton energy at the entrance of the phantom was of 226.7 MeV. No scatterer and no energy modulation were used.

The fixed-beam treatment nozzle and the eye line were not modelled because it was assumed that they would have a negligible impact on the simulated neutron fields in the positions of interest (indicated with red labels in figure **III-8**). In fact, none of these structures intersect the straight lines that connect the water phantom to the considered measurement positions.
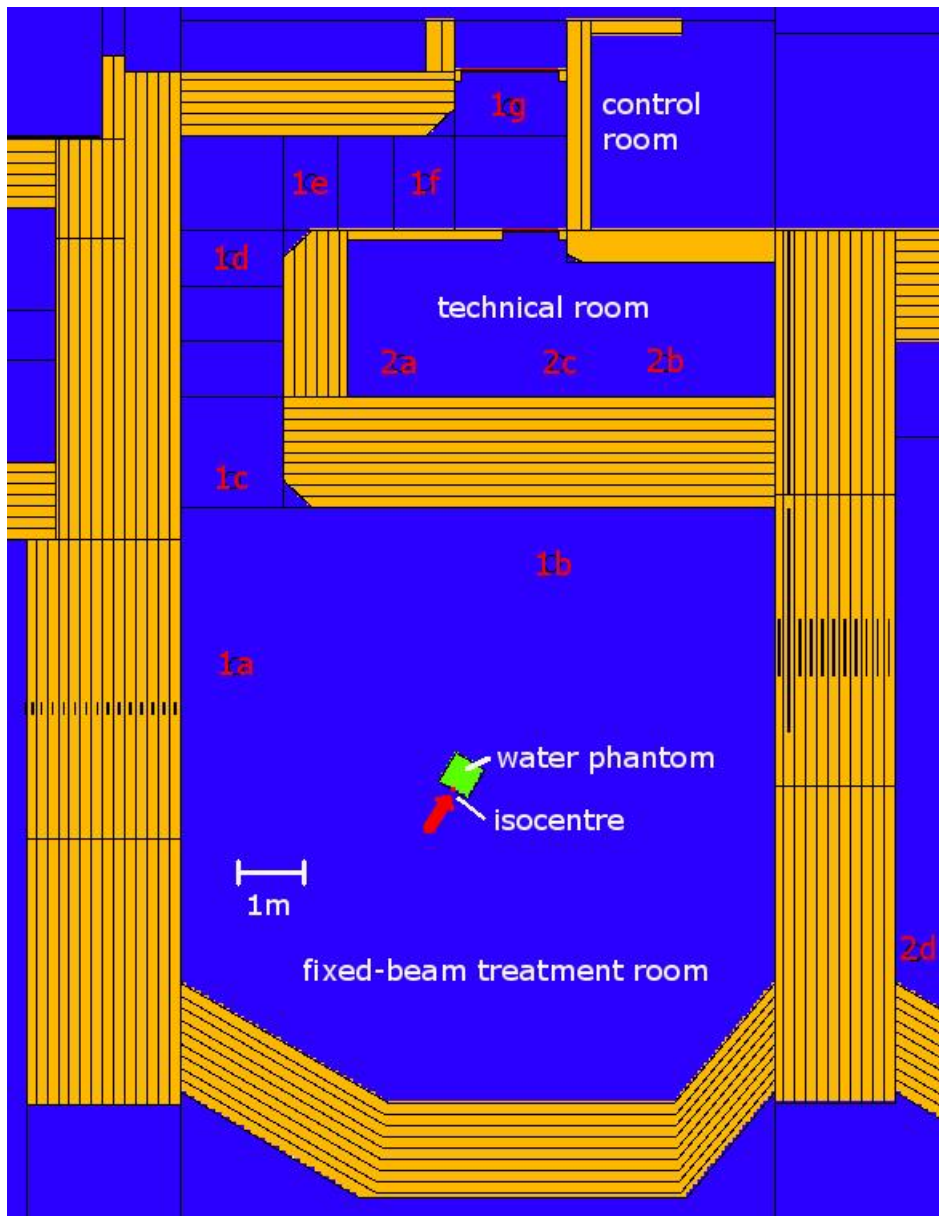
Figure III-8 - Modelled geometry of the fixed-beam treatment room. The concrete walls are represented in orange, the water phantom in green. The indicated isocentre is that of the fixed-beam treatment line. The red labels indicate the measurement positions (all situated at ~150 cm above the floor, except for 2d located right on the floor).

III-2.2 Neutron H*(10) and WENDI-2 responses

As explained in section **I-4.2**, ambient dosimeters commonly used today were designed to measure the operational quantity H*(10). Therefore, when one wishes to compare the results of a Monte Carlo simulation to on-site measurements performed with a neutron ambient dosimeter (our goal in Chapter IV), the neutron H*(10) rates at the positions of interest should in principle be computed in this simulation. This can be done for instance by folding the simulated neutron spectra with the appropriate fluence-to-H*(10) conversion coefficients (see section **I-4.2.2**).

However, ideal dosimeters which measure H*(10) accurately in just any type of neutron spectrum do not exist. In Chapter II, we have shown that the WENDI-2 (with its ^{252}Cf calibration) is no exception to this assertion, because in some energy regions discrepancies by up to a factor of ~7 seem to exist between the WENDI-2 dose response function and the fluence-to-H*(10) conversion coefficients (see section **II-2.2.2**). Nevertheless, there are reasons to believe that for the typical neutron spectra encountered in proton therapy facilities the WENDI-2 response function is relatively well-balanced with respect to the fluence-to-H*(10) conversion coefficients. One of the goals of this chapter is therefore to verify theoretically whether the WENDI-2 can measure H*(10) accurately in all the measurement positions indicated in the figures **III-1**, **III-4, III-6** and **III-8**. This can be done by folding the simulated neutron spectra with the WENDI-2 dose response function, and comparing the results to the simulated H*(10) rates.

Predicting the true WENDI-2 response requires an accurate and precise knowledge of the WENDI-2 response function. In Chapter II, several simulated versions of this response function, obtained with different Monte Carlo codes, have been compared amongst each other, as well as with a few validation measurements. From these comparisons, it appeared that in some energy regions the uncertainties on the response function are relatively large, especially at high energies (20 MeV – 250 MeV) and at thermal energies. To take these uncertainties into account, a systematic study was carried out in which the simulated neutron spectra at the measurement positions were folded with each of the following versions of the WENDI-2 response function (see Chapter II):

- our response function simulated with MCNPX 2.7.0, using the Bertini & Dresner models for neutron interactions above 150 MeV (case of the parallel beam irradiation),
- the results of Jägerhofer *et al.* obtained with FLUKA [183],
- the results of Vanaudenhove *et al.* obtained with GEANT4 9.6, using the Bertini model for neutron interactions above 20 MeV [184],
- the results of Vanaudenhove *et al.* obtained with GEANT4 9.6, using the BIC model for neutron interactions above 20 MeV [184],
- the simulation results of Olsher *et al.* obtained with MCNP4B [152] (from thermal energies up to 0.144 MeV), and the experimental data acquired above 46 MeV by Olsher *et al.* with QMN beams at the TSL [182].

These absolute response functions were multiplied by the built-in calibration constant of the WENDI-2 (3.17 x 10^{-4} μSv/c [155]). The resulting dose response functions are shown in figure **III-9**, together with the fluence-to-H*(10) conversion coefficients. Between 0.144 MeV and 19 MeV, however, the values of all simulated response functions were replaced by a common section based on the experimental data acquired by Olsher *et al.* with monoenergetic neutron beams at the PTB [152]. As a reminder, these measurements agreed within less than 3σ with the five

abovementioned simulated response functions and were also compatible within 1σ with our measurements performed with ²⁵²Cf and AmBe sources (see Chapter II). For this reason, these measurements were considered sufficiently accurate to be taken as a reference in this energy range. A relative uncertainty of 5%, corresponding to the experimental uncertainty estimated by Olsher *et al.* [152], was taken into account on the contribution of 0.1 MeV – 19 MeV neutrons to the simulated WENDI-2 response (σ_{exp}).
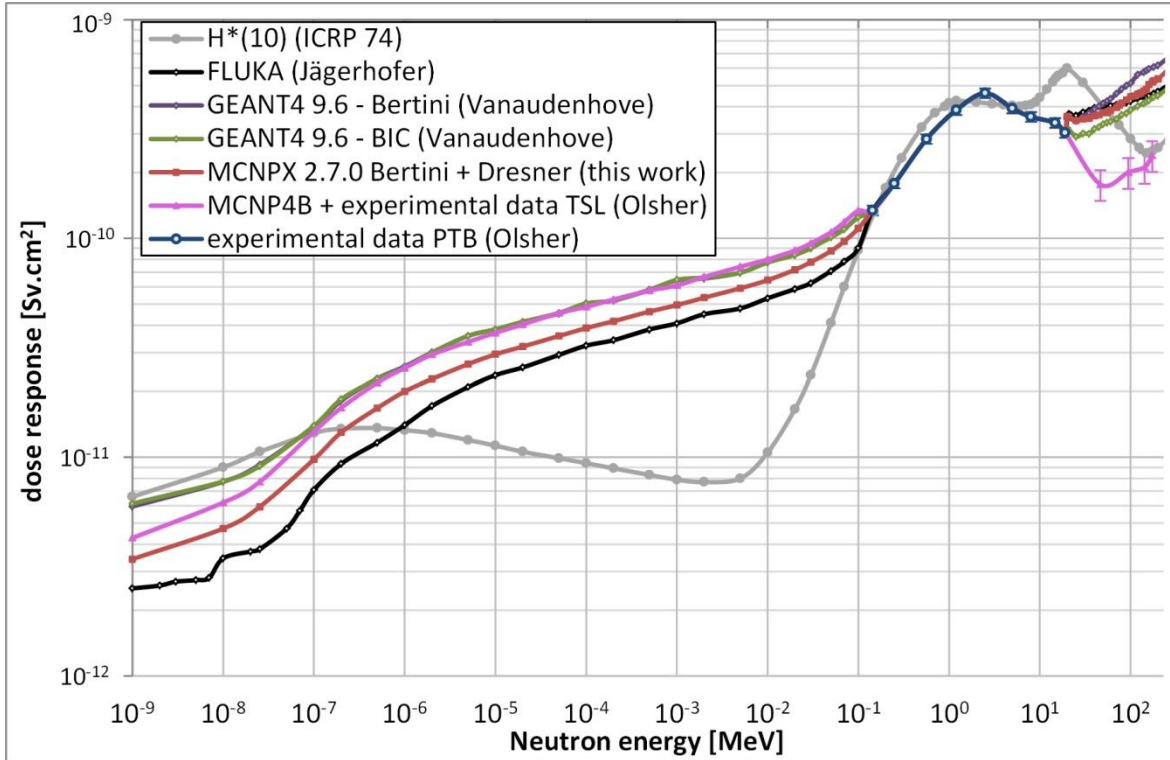
Figure III-9 – Five versions of the dose response function used to simulate the WENDI-2 response at the measurement positions inside the proton therapy facility. The fluence-to-H*(10) conversion coefficients of ICRP Publication 74 are also shown. The connections between the points are only a guide for the eye; a log-log interpolation was calculated by MCNPX.

The reference value for the simulated WENDI-2 response at a given measurement position was calculated as the average $R_{sim,avg}$ of the five energy-integrated responses $R_{sim,i}$ obtained with the abovementioned response functions. A symmetric uncertainty $\sigma_{resp.fct.}$, representing the uncertainties on the response function below 0.144 MeV and above 19 MeV, was then estimated as:

$$\sigma_{resp.fct.} = \frac{1}{3} \max_{1 \leq i \leq 5} \left| R_{sim,i} - R_{sim,avg} \right|.$$

The total uncertainty σ_{tot} on $R_{sim,avg}$, which combines the average statistical MCNPX uncertainty σ_{stat} and the uncertainties on the entire WENDI-2 response function, was calculated as:

$$\sigma_{tot} = \sqrt{\sigma_{stat}^2 + \sigma_{exp}^2 + \sigma_{resp.fct.}^2} \, .$$

From a practical point of view, the neutron spectra at the measurement positions (see figures **III-1**, **III-4, III-6** and **III-8**) were calculated inside air spheres of 25 cm in diameter, using an F4:n neutron fluence tally in association with an E card [100]. In addition, DE-DF cards [100] were used to calculate the neutron H*(10) by folding these neutron spectra with the conversion coefficients of the ICRP Publication 74 [87]. Other sets of DE-DF cards were also used to fold the neutron spectra with the abovementioned versions of the WENDI-2 dose response function. By adding an E card [100] to the tallies of the neutron H*(10) and the WENDI-2 responses, the energy spectra for these quantities were calculated as well.

III-2.3 Material compositions & evaluated cross-section data

The compositions of the materials defined in our MCNPX simulations are summarized in Table **III-1**. The concrete that constitutes the Essen facility is an ordinary type of concrete, but no quantitative information on its average elemental composition was available. Like the original shielding design simulations, our simulations were based on the standard 'Portland' composition [236]. This composition was defined by the National Institute of Standards and Technology (NIST), U.S.A. The choice of the density, 2.30 g/cm^3, is in principle a conservative one, because the concrete provider was asked to ensure a minimum density of 2.35 g/cm^3 for the construction of this facility (private communication, F. Stichelbaut, IBA).

Since the maximum energy of the simulated particles ($\sim$230 MeV) was lower than the pion production threshold ($\sim$280 MeV), it sufficed to only track protons and neutrons in the simulations (following the same argument as in section **II-2.1.4**).

For neutron interactions, evaluated cross-section data from the endf70 library were used [100,192,218]. The library is based on the ENDF/B-VII.0 evaluation [122], in which the data of the earlier la150n library [113,119] was officially integrated. For most isotopes of interest here, the library thus contains data for neutron energies up to 150 MeV (see table **III-1**). For proton interactions, the cross-section data from the endf70prot library [100,192] was used anywhere possible.

Where no evaluated cross-section data was available in MCNPX 2.7.0 at high energies, the default physics models were used: the Bertini intranuclear cascade model, followed by the multi-stage pre-equilibrium model, and the Dresner evaporation model (or the Fermi break-up model for light nuclei, see details in section **II-2.1.5**) [100]. Selecting the default physics models was however a well-considered decision because the Bertini model yields the highest simulated neutron doses at forward angles in this type of simulations (as will be shown in Chapter **V**). The Bertini model thus constitutes the most conservative choice in these case-studies.

Table III-1 - Material definitions in the MCNPX simulation of the proton therapy rooms. The given upper energy limit of the cross-section data tables applies to the neutron data. The upper limit for the data from the proton library 'endf70prot' is 150 MeV.

Material	Isotope or element	Atom fraction	Neutron library	Upper limit (MeV)	Proton library
NIST Portland concrete 2.30 g/cm^3	^{16}O	0.562562	endf70a	150	endf70prot
	^{28}Si	0.188905	endf70a	150	endf70prot
	^{29}Si	0.009277	endf70a	150	endf70prot
	^{30}Si	0.005927	endf70a	150	endf70prot
	^{1}H	0.168742	la150n	150	endf70prot
	^{27}Al	0.021350	endf70a	150	endf70prot
	^{40}Ca	0.018152	endf70a	200	endf70prot
	^{44}Ca	0.000355	endf70a	200	/
	^{42}Ca	0.000116	endf70a	200	/
	^{48}Ca	0.000029	endf70a	200	/
	^{43}Ca	0.000023	endf70a	200	/
	^{23}Na	0.011836	endf70a	20	/
	^{nat}K	0.005654	actia	20	/
	^{56}Fe	0.004257	endf70b	150	endf70prot
	^{nat}C	0.001416	endf70a	150	/
	^{nat}Mg	0.001399	actia	20	/
Soil 1.4 g/cm^3	^{16}O	0.517766	endf70a	150	endf70prot
	^{1}H	0.254036	la150n	150	endf70prot
	^{28}Si	0.128118	endf70a	150	endf70prot
	^{27}Al	0.061957	endf70a	150	endf70prot
	^{nat}Mg	0.026025	actia	20	/
	^{56}Fe	0.009424	endf70b	150	endf70prot
	^{40}Ca	0.002676	endf70a	200	endf70prot
Air 1.205 · 10^{-3} g/cm^3 (or vacuum 10^{-10} g/cm^3)	^{14}N	0.784431	endf70a	150	endf70prot
	^{16}O	0.210748	endf70a	150	endf70prot
	^{nat}Ar	0.004671	rmccsa	20	/
	^{nat}C	0.000150	endf70a	150	/
Iron 7.87 g/cm^3	^{56}Fe	0.920000	endf70b	150	endf70prot
	^{54}Fe	0.060000	endf70b	150	endf70prot
	^{57}Fe	0.020000	endf70b	150	endf70prot
Copper 8.96 g/cm^3	^{63}Cu	0.690000	endf70b	150	endf70prot
	^{65}Cu	0.310000	endf70b	150	endf70prot
Nickel 8.90 g/cm^3	^{58}Ni	0.680800	endf70b	150	endf70prot
	^{60}Ni	0.262200	endf70b	150	endf70prot
	^{62}Ni	0.036300	endf70b	150	endf70prot
	^{61}Ni	0.011400	endf70b	150	endf70prot
	^{64}Ni	0.009300	endf70b	150	endf70prot
Aluminium 2.70 g/cm^3	^{27}Al	1.000000	endf70a	150	endf70prot
Water 1.0 g/cm^3	^{1}H	0.666667	la150n	150	endf70prot
	^{16}O	0.333333	endf70a	150	endf70prot
HDPE 0.97 g/cm^3	^{1}H	0.666667	la150n	150	endf70prot
	^{nat}C	0.333333	endf70a	150	/
Brass 8.96 g/cm^3	^{63}Cu	0.417439	endf70b	150	endf70prot
	^{65}Cu	0.182066	endf70b	150	endf70prot
	^{nat}Zn	0.390646	endf70b	20	/
	^{208}Pb	0.007298	endf70i	200	endf70prot
	^{206}Pb	0.002551	endf70i	200	endf70prot

Table III-1 (continued)

Material	Isotope or element	Atom fraction	Neutron library	Upper limit (MeV)	Proton library
Lexan 1.2 g/cm^3	^{nat}C	0.484821	endf70a	150	/
	^1H	0.424249	la150n	150	endf70prot
	^{16}O	0.090930	endf70a	150	endf70prot
Lead 11.35 g/cm^3	^{208}Pb	0.524000	endf70i	200	endf70prot
	^{206}Pb	0.241000	endf70i	200	endf70prot
	^{207}Pb	0.221000	endf70i	200	endf70prot
	^{204}Pb	0.014000	endf70i	200	/
Tantalum 16.6 g/cm^3	^{181}Ta	1.000000	endf70i	20	/
Cellulose 0.5 g/cm^3	^1H	0.605812	la150n	150	endf70prot
	^{nat}C	0.203330	endf70a	150	/
	^{16}O	0.190858	endf70a	150	endf70prot

III-2.4 Variance reduction and statistical treatment

To obtain sufficient statistics within a reasonable computing time in positions located outside the treatment rooms or at the end of the access mazes, it was necessary to rely on a variance reduction technique. The population control method named "geometry splitting and Russian roulette", introduced in section **I-6.5**, was applied. The geometry of the shielding walls was divided in several cells of ~20 cm in thickness, perpendicularly to the main direction of the neutron flux. An importance was assigned to each cell in order to maintain the cell populations of neutrons relatively constant between the source region and the tally region. The distribution of these neutron importances was determined using the population ratios of adjacent cells, obtained from a short run in which all cell importances were set to unity. Working outwards, starting from the source region, the importance I_{n+1} of a cell with a population P_{n+1}, was set to $I_{n+1} = I_n . P_n/P_{n+1}$, based on the population P_n and importance I_n of the previous cell. The concrete layer being nearest to the neutron source was assigned the importance $I_1 = 1$. The chosen thickness of the concrete cells allowed keeping the importance ratios below a factor of ~8 at all depths of the concrete walls, as generally recommended when using this variance reduction technique [143,237]. Inside the access maze, geometry splitting was also applied to the air volumes, perpendicularly to the main direction of the diffusing neutron flux.

The distribution of the neutron importances used in each simulation are shown in the figures **III-10** and **III-11** for the cyclotron room, in figures **III-12** the gantry treatment rooms operated in PBS and DS, and in figure **III-13** for the fixed-beam treatment room.

For each simulation, 25 runs with different pseudorandom number sequences were submitted in parallel, to gain more statistics. Generating different pseudorandom number sequences was done by incrementing the random number

stride S following the same method as already outlined in section **II.4.1.4**. The tally results x_i of the 25 runs were combined by computing their weighted average $\bar{x}$ based on the corresponding MCNPX absolute uncertainties σ_i:

$$\bar{x} = \frac{\sum_i \frac{1}{\sigma_i^2} x_i}{\sum_i \frac{1}{\sigma_i^2}}$$

$$\text{with } \sigma_{\bar{x}} = \sqrt{\frac{1}{\sum_i \frac{1}{\sigma_i^2}}}$$

Only results of tallies that had reached a satisfactory statistical convergence were taken into account (x_i with a relative uncertainty $\sigma_i/x_i \leq 0.10$, as advised in the MCNPX manual [100]).

In the positions 1 – 3 outside the cyclotron room, obtaining good statistical convergence of the tallies remained relatively difficult in spite of the applied variance reduction, especially for the simulations in which the considered proton beam was not directed towards the maze region (*i.e.* in all simulations except that with the 'P4' source). After tracking 850 million histories per run in about 4 weeks of computing time, the statistical uncertainties on the doses in the positions 1 – 3 were not necessarily smaller than 10% in each of the 25 runs. A few outliers, affected by MCNPX uncertainties larger than 10%, were left out before combining results.

With the simulations of the gantry room and the fixed-beam room, no particular problems were encountered in the statistical convergence of the tallies. Eventually, all 25 runs had similar tally results and statistical uncertainties ($\leq$ 10%). For the PBS case, as well as for the fixed-beam room, 750 million histories were simulated per run in ~2.5 weeks. In the DS case, 300 million histories were simulated per run in ~3 weeks.
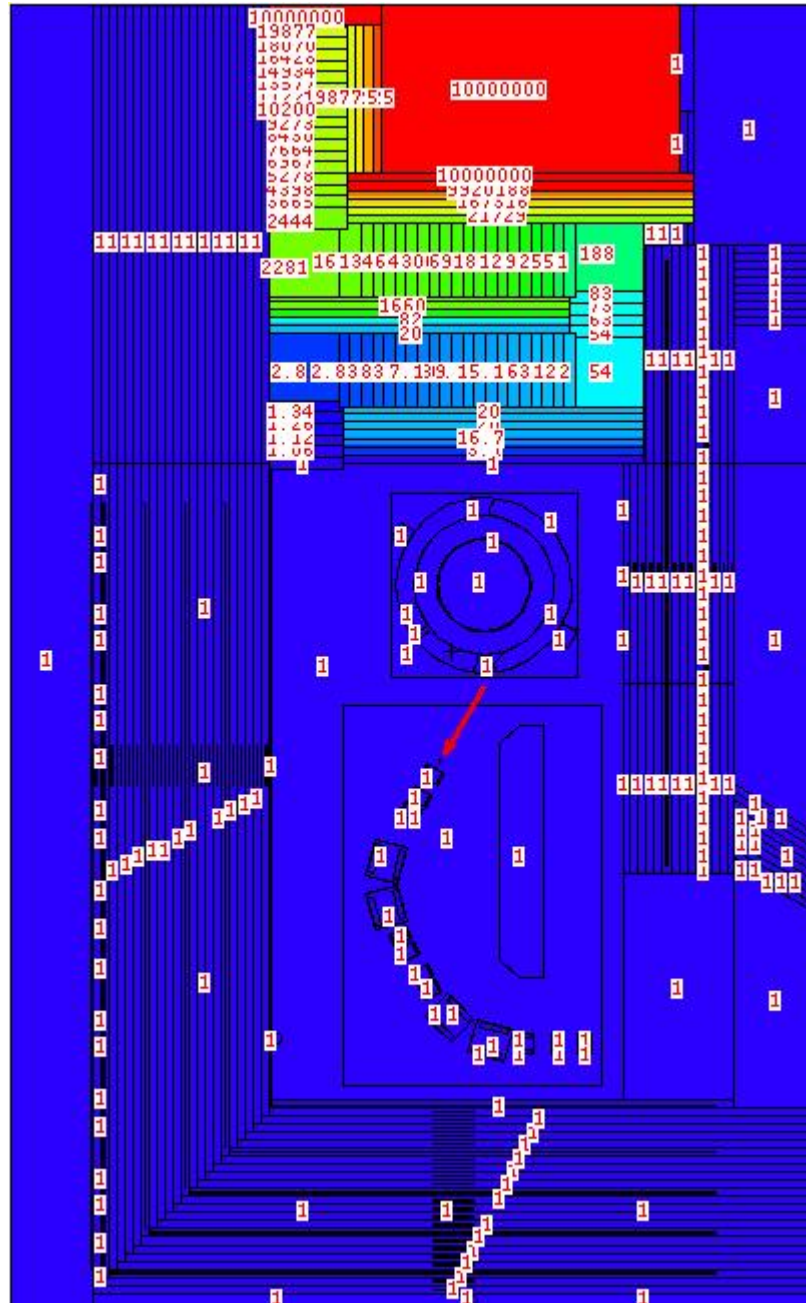
Figure III-10 - Variance reduction for the neutron transport in the simulation of the cyclotron-extracted proton beam impinging on the beam stop in the cyclotron room.
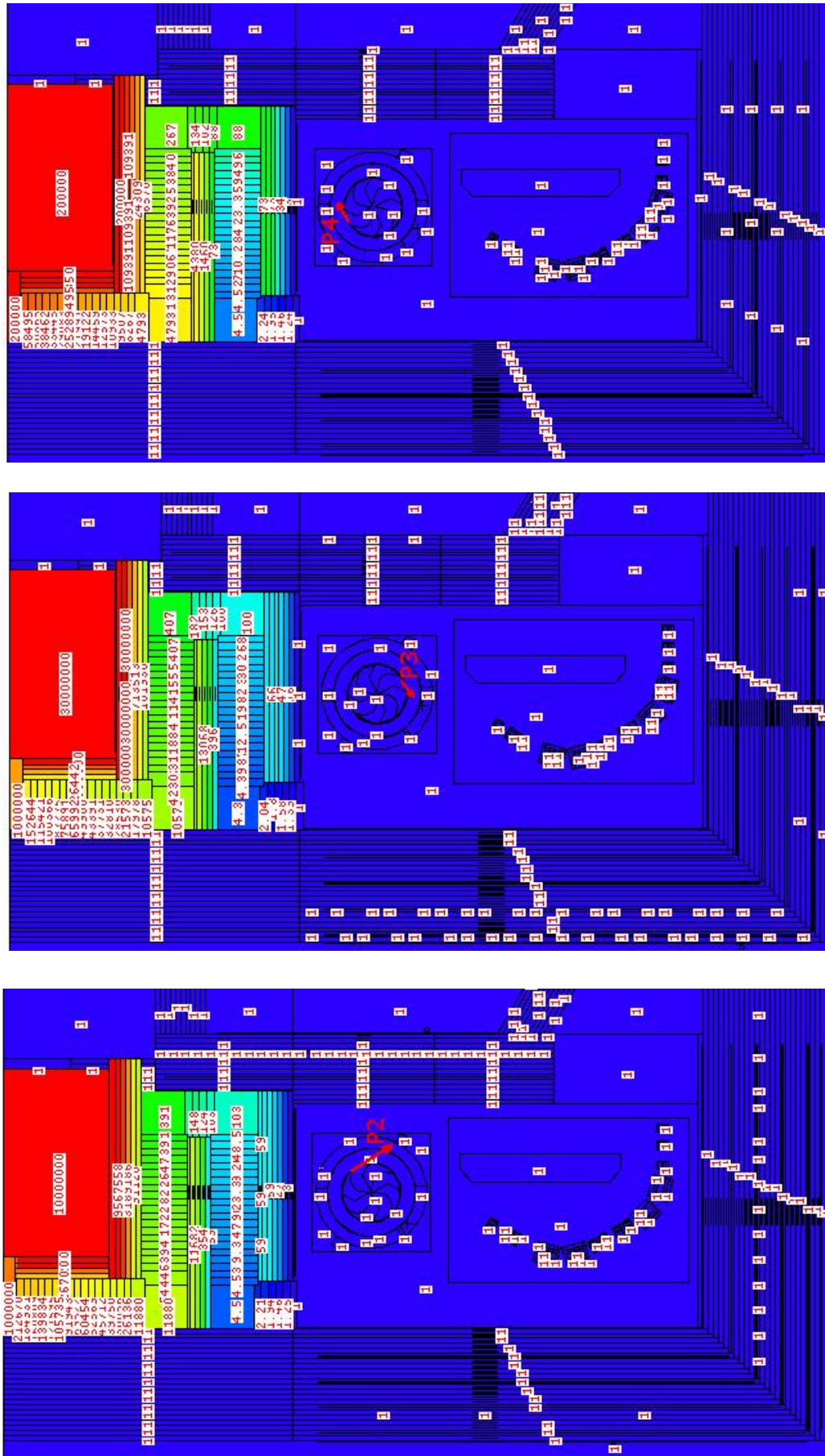
Figure III-11 - Variance reduction for the neutron transport in the simulations of the proton losses inside the cyclotron: on the septum ('P2') and on the counter-dees ('P3' and 'P4').

Figure III-12 - Variance reduction for the neutron transport in the simulations of the gantry room operated in PBS (left) and in DS (right).
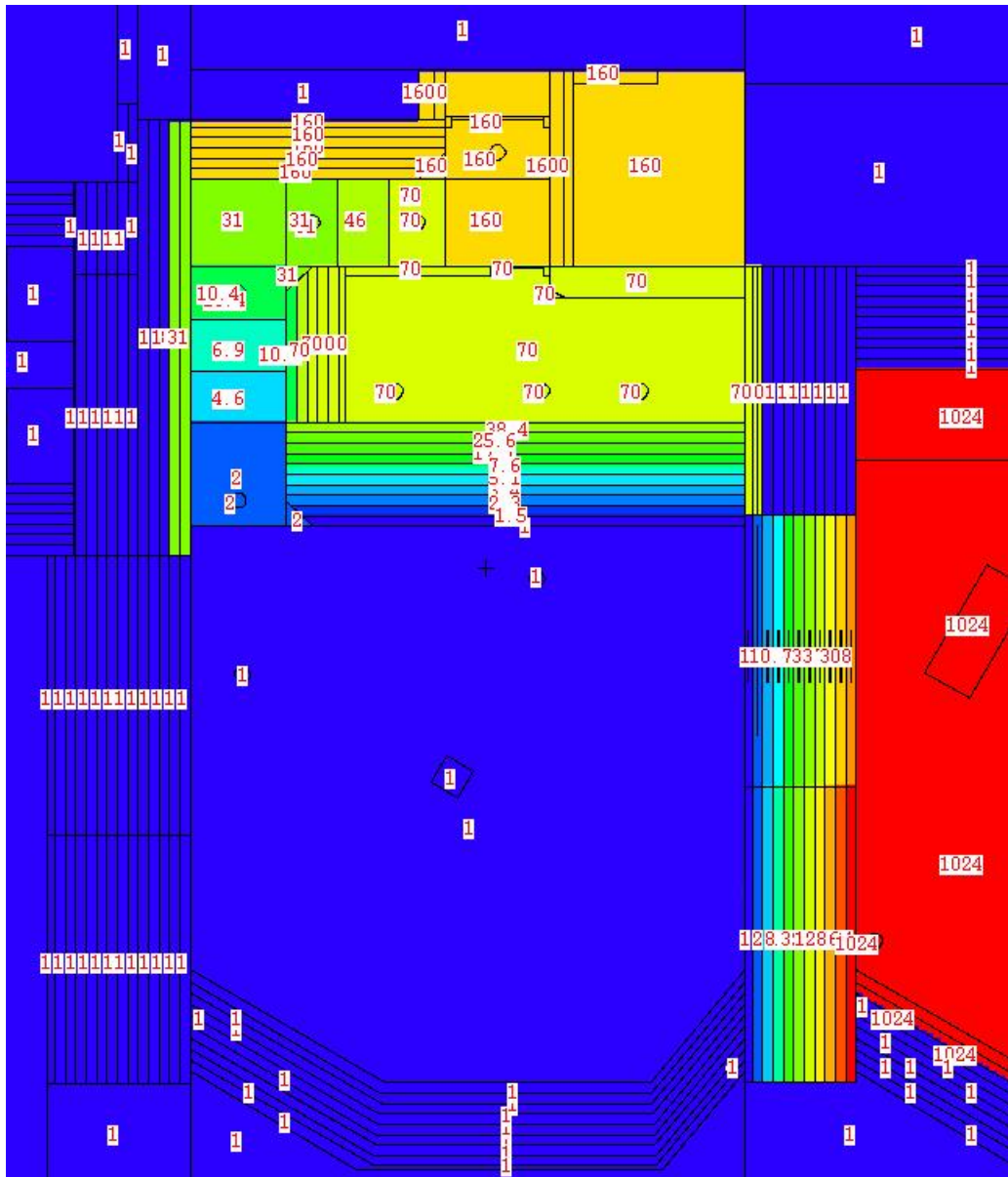
Figure III-13 - Variance reduction for the neutron transport in the simulation of the fixed-beam treatment room.

III-3 Results

III-3.1 Cyclotron room

The results obtained for the neutron H*(10) due to the four different neutron sources in the cyclotron room are listed in table **III-2** and shown in figure **III-14**.

All along the maze (positions 4 – 9) and behind the maze door (position 3), the neutrons produced in the beam stop cause the largest contribution to H*(10). This contribution constitutes more than 80% of the total H*(10), except in the positions 6 (71%) and 7 (56%) where the contribution from the cyclotron losses 'P4' plays a more significant role. These two positions lie in fact at small angles from the direction of the 'P4' proton beam and at almost 180° from the direction of the proton beam impinging on the beam stop (see figure **III-1** on **p. 117**).

Inside the main control room (positions 1 and 2), the 'P4' cyclotron losses are the largest contributor to H*(10). The 'P4' contribution is proportionally larger in position 2 than in position 1, mainly because of the smaller angle of position 2 with respect to the direction of the 'P4' proton beam.

Table III-2 - Neutron H(10) obtained in the cyclotron room simulations. The results are expressed in μSv/(nA.h), where the nA.h refer to the cyclotron-extracted proton charge. The given uncertainties are the MCNPX statistical uncertainties (1σ).*

Position	Beam stop	P2	P3	P4	Total H*(10)
4	(1.277 ± 0.001) $\times 10^3$	(1.379 ± 0.002) $\times 10^2$	(2.945 ± 0.004) $\times 10^1$	(9.008 ± 0.009) $\times 10^1$	(1.534 ± 0.001) $\times 10^3$
5	(2.024 ± 0.004) $\times 10^2$	(1.504 ± 0.004) $\times 10^1$	(4.30 ± 0.01) $\times 10^0$	(8.06 ± 0.02) $\times 10^0$	(2.298 ± 0.004) $\times 10^2$
6	(6.74 ± 0.06) $\times 10^0$	(7.94 ± 0.05) $\times 10^{-1}$	(2.06 ± 0.01) $\times 10^{-1}$	(1.701 ± 0.007) $\times 10^0$	(9.44 ± 0.06) $\times 10^0$
7	(3.53 ± 0.08) $\times 10^{-1}$	(9.6 ± 0.1) $\times 10^{-2}$	(2.54 ± 0.02) $\times 10^{-2}$	(1.62 ± 0.04) $\times 10^{-1}$	(6.36 ± 0.09) $\times 10^{-1}$
8	(8.4 ± 0.2) $\times 10^{-2}$	(4.2 ± 0.2) $\times 10^{-3}$	(1.07 ± 0.05) $\times 10^{-3}$	(8.8 ± 0.2) $\times 10^{-3}$	(9.8 ± 0.2) $\times 10^{-2}$
9	(9.9 ± 0.2) $\times 10^{-2}$	(1.5 ± 0.2) $\times 10^{-3}$	(4.7 ± 0.4) $\times 10^{-4}$	(4.0 ± 0.1) $\times 10^{-3}$	(1.05 ± 0.02) $\times 10^{-1}$
3	(1.09 ± 0.01) $\times 10^{-2}$	(6.5 ± 0.5) $\times 10^{-5}$	(2.1 ± 0.2) $\times 10^{-5}$	(7.2 ± 0.5) $\times 10^{-5}$	(1.11 ± 0.01) $\times 10^{-2}$
1	(9.6 ± 0.2) $\times 10^{-5}$	(1.25 ± 0.05) $\times 10^{-5}$	(2.10 ± 0.09) $\times 10^{-6}$	(2.57 ± 0.03) $\times 10^{-4}$	(3.67 ± 0.03) $\times 10^{-4}$
2	(8.0 ± 0.3) $\times 10^{-6}$	(2.52 ± 0.08) $\times 10^{-5}$	(9.5 ± 0.4) $\times 10^{-7}$	(1.86 ± 0.02) $\times 10^{-3}$	(1.89 ± 0.02) $\times 10^{-3}$
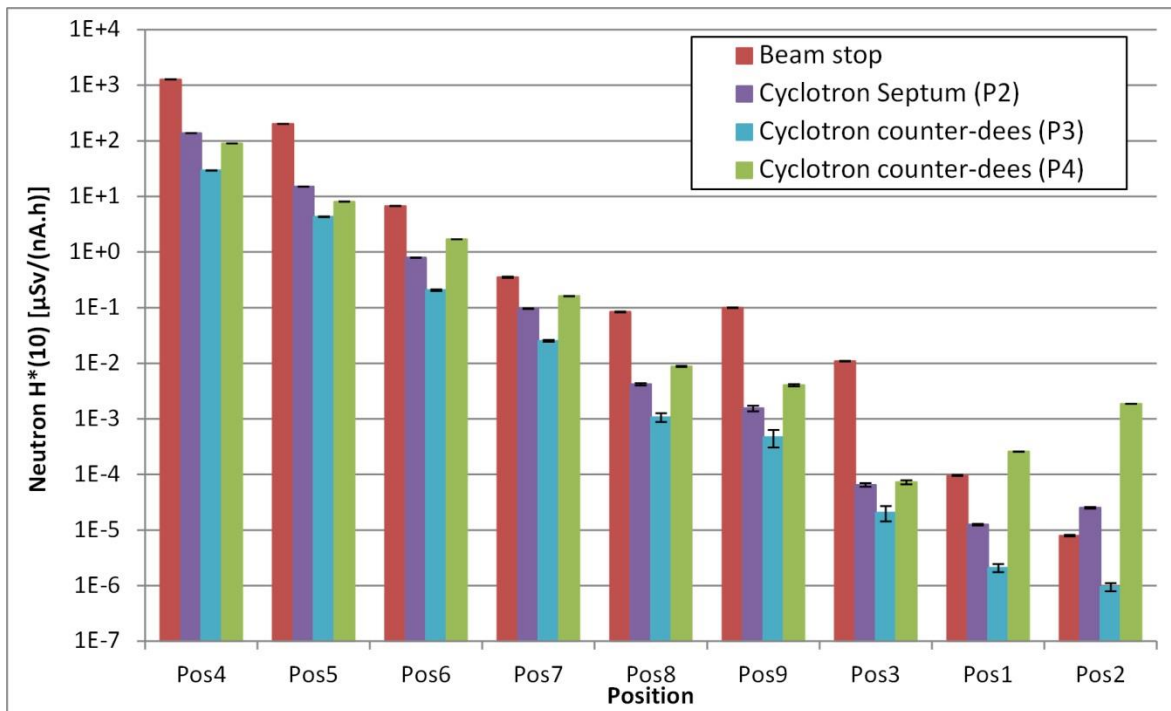
Figure III-14 - Neutron H*(10) obtained with each of the four neutron sources in the cyclotron room simulations.

The simulated energy spectra of the total neutron fluence are presented in the figures **III-15** and **III-16** for the positions inside the maze and outside the cyclotron room, respectively. Similarly, the energy spectra of the total neutron H*(10) are shown in the figures **III-17** and **III-18** (in black). To facilitate the discussion of these results, integrals of the fluence and H*(10) spectra were also calculated over four energy domains, which will be subsequently referred to as:

- 'Thermal neutrons': 10^{-9} MeV $\leq E_n \leq 2 \cdot 10^{-7}$ MeV;
- 'Intermediate neutrons': $2 \cdot 10^{-7}$ MeV $< E_n \leq 0.1$ MeV;
- 'Evaporation neutrons': 0.1 MeV $< E_n \leq 10$ MeV;
- 'High-energy neutrons': 10 MeV $< E_n \leq 230$ MeV (neutrons emitted during the pre-equilibrium and the intranuclear cascade).

Figures **III-19** and **III-20** show the relative contributions of these four categories to the total neutron fluence and H*(10), respectively.

At the entrance of the maze, in position 4, the fraction of high-energy neutrons in the fluence neutron spectrum (see figures **III-15** and **III-19**) is negligible, because none of the considered proton beams are pointing towards that position. The neutron field essentially involves neutrons of thermal and intermediate energies, which have undergone several scattering interactions throughout the room before reaching the entrance of the maze. About 55% of the neutron fluence in position 4 originates from the beam stop. That may seem surprising knowing that the cyclotron sources are actually closer to position 4 than the beam stop. However, the massive structure of

the cyclotron, consisting of iron and copper, significantly attenuates the neutrons produced inside it. Evaporation neutrons only constitute 19% of the simulated fluence in position 4, but due to their larger fluence-to-H*(10) coefficients compared to low-energy neutrons (see Figure **III-9** on p. **126**) they give the largest contribution to the total H*(10) (79%, see figures **III-17** and **III-20**).

Moving along the maze from position 4 towards position 7, the fluence spectra are softening: the evaporation and intermediate components progressively diminish in favour of thermal neutrons (see figures **III-15** and **III-19**). The neutron field in these positions is thus dominated by neutrons that have been moving along the maze path, progressively losing their kinetic energy through scattering interactions. In comparison, the fluence of high-energy neutrons directly transmitted through maze wall 'A' (see figure **III-1** on p. **117**) is negligible. In positions 6 and 7, a tiny contribution around 100 MeV is nevertheless distinguishable in the fluence spectra. It is mainly due to high-energy neutrons emitted by the 'P4' source and transmitted through maze wall 'A'. Because of their high fluence-to-H*(10) conversion coefficients, these few neutrons cause a non-negligible contribution to H*(10), which is clearly visible in the spectra of the total H*(10) in figure **III-17**.

Continuing one's walk towards the exit of the maze, it appears that the maze-scattered fluence component is already fully thermalized in positions 8 and 9 (see figure **III-15**). Yet, small contributions in the evaporation and high-energy regions can be noticed in the fluence spectra, especially in position 9. These are due to a small amount of high-energy neutrons emitted mainly by the beam stop and transmitted directly through maze wall 'B', and perhaps maze wall 'A' as well (see figure **III-1** on p. **117**). As shown in the figures **III-17** and **III-20**, the few evaporation and high-energy neutrons are actually responsible for ~60-80% of the total H*(10). Throughout the last portion of the maze, these energetic neutrons are less strongly attenuated than the thermal component. In position 3 behind the maze door (see figure **III-16**), the fraction of evaporation and high-energy neutrons is therefore larger than in position 9.
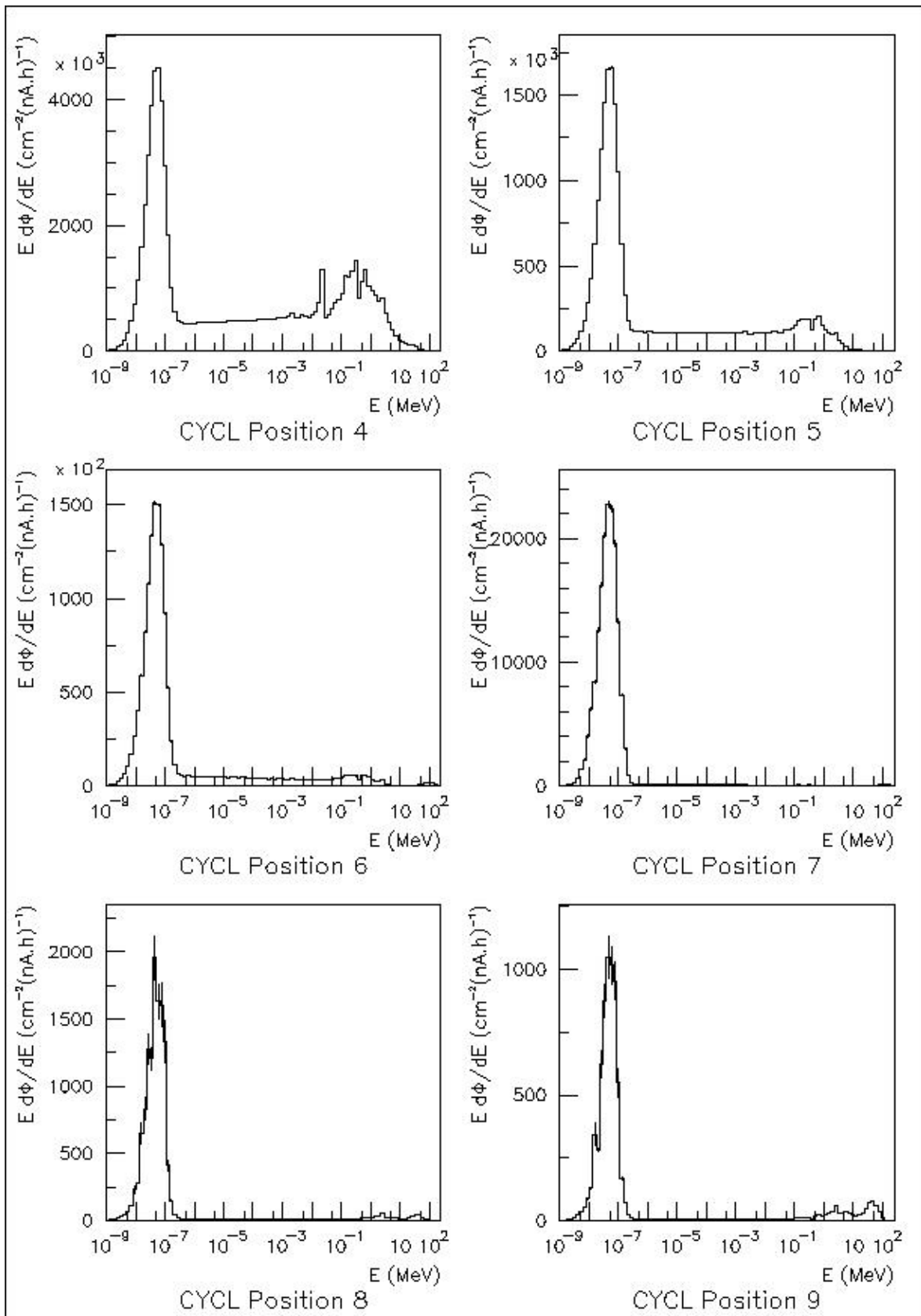
Figure III-15 - Neutron fluence spectra simulated inside the maze of the cyclotron room.
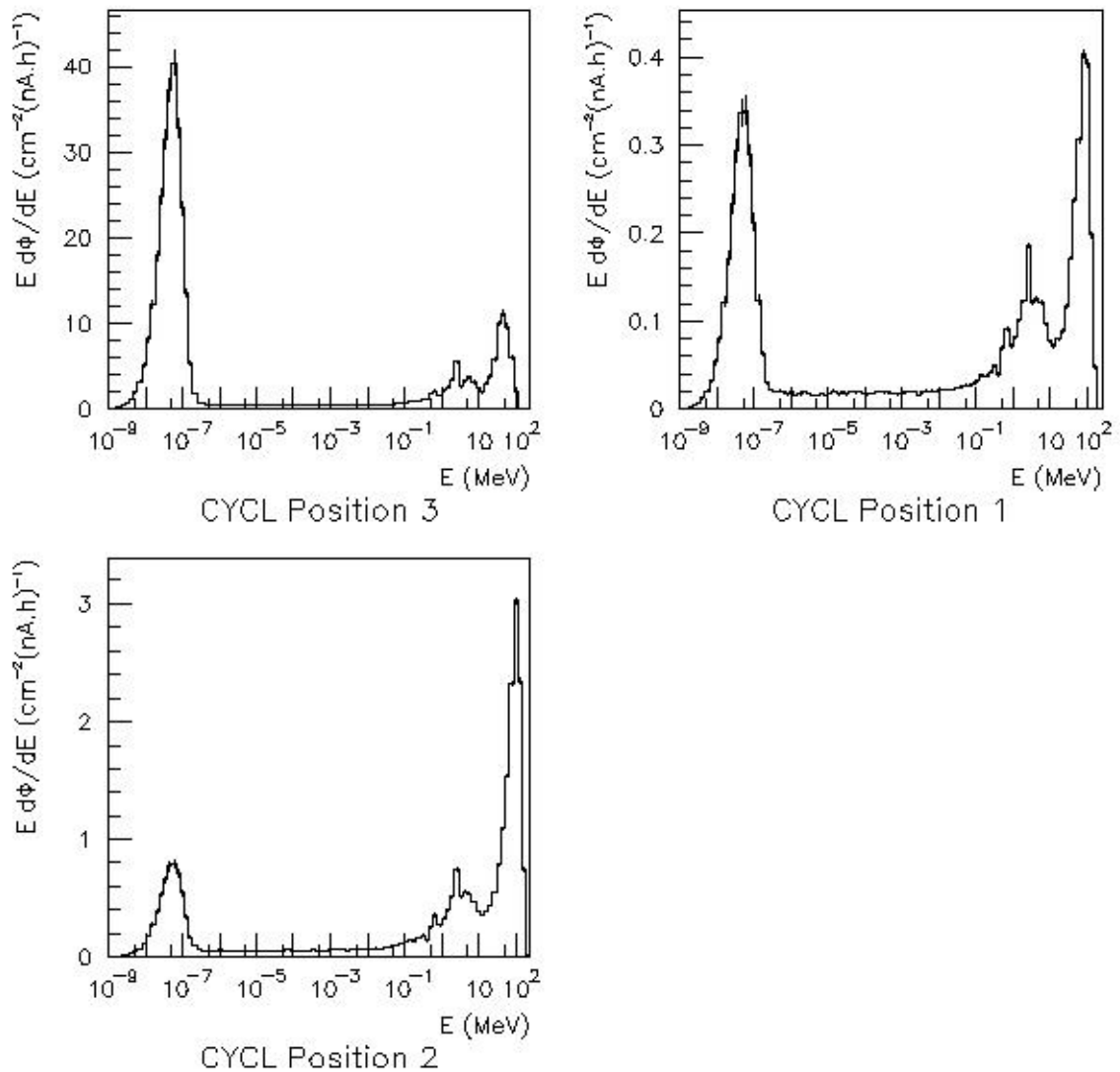
Figure III-16 - Neutron fluence spectra simulated behind the maze door of the cyclotron room (position 3) and inside the main control room (positions 1 and 2).

The neutron fluence spectra in positions 1 and 2, inside the main control room, have the characteristic shape of the shielded neutron fields described in section **I-4.1** (see figure **III-16**). The "cascade" peak represents high-energy neutrons that have barely undergone any interactions and travelled nearly in straight line from the source to the position of interest. As indicated earlier, this peak is mainly populated by the forward-peaked intranuclear cascade emissions of the 'P4' source and is therefore proportionately larger in position 2 than in position 1. The evaporation peak follows the same trend as the cascade peak because it mainly consists of neutrons produced inside maze wall 'C' (see figure **III-1** on p. **117**) by non-elastic interactions of high-energy 'P4' neutrons. The thermal peak corresponds mainly to room-scattered neutrons, also indirectly due to the 'P4' source. Their contribution to the total H*(10) does not exceed a few percent. The latter is almost entirely determined by the high-energy and evaporation neutrons only (see figures **III-18** and **III-20**).
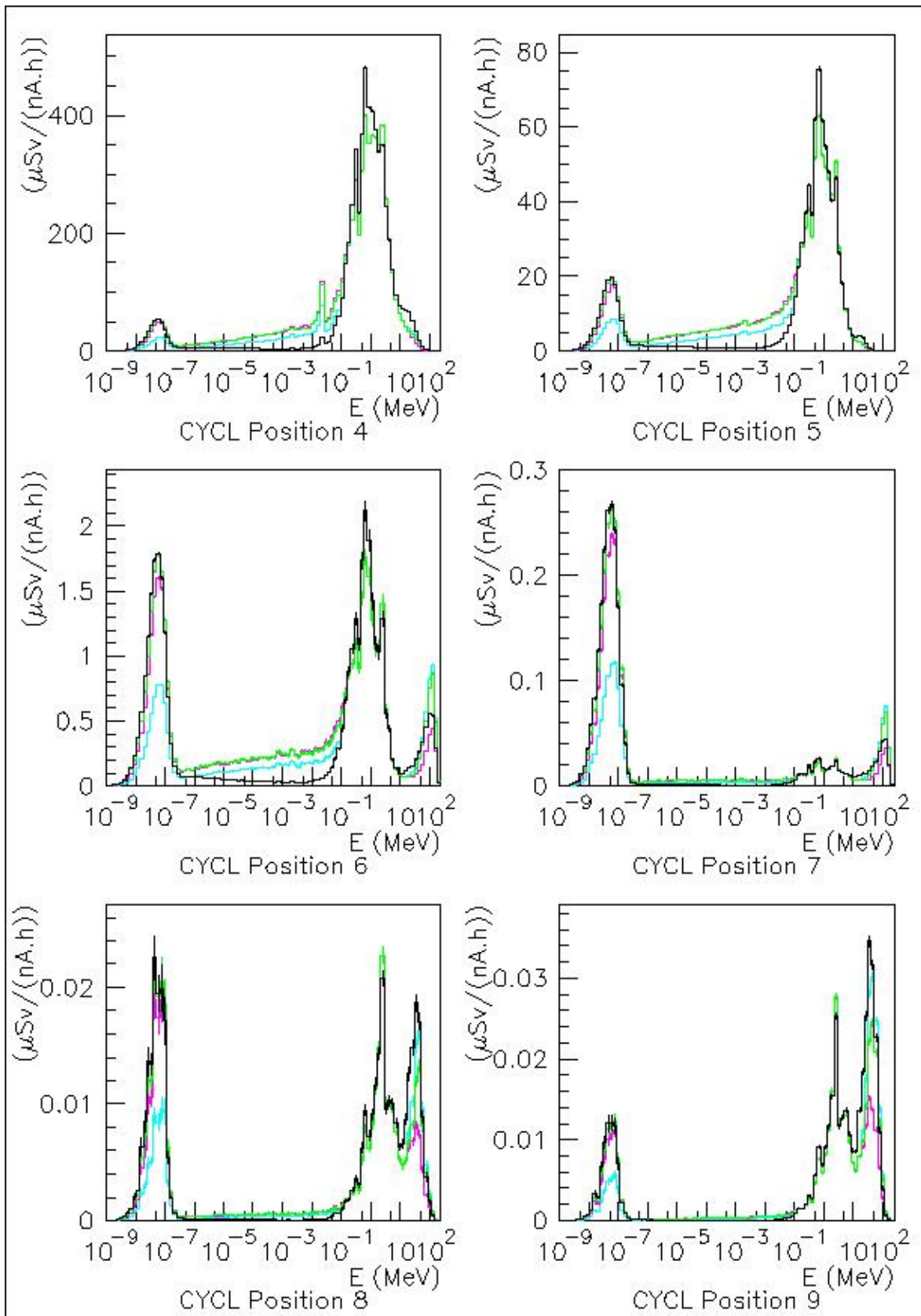
Figure III-17 - For positions inside the maze of the cyclotron room: neutron H*(10) spectra (in black) and WENDI-2 spectra based on the GEANT4 9.6 BIC response function (in green), the FLUKA response function (in cyan) and the response function of Olsher et al. based on experimental data above 46 MeV (in pink).
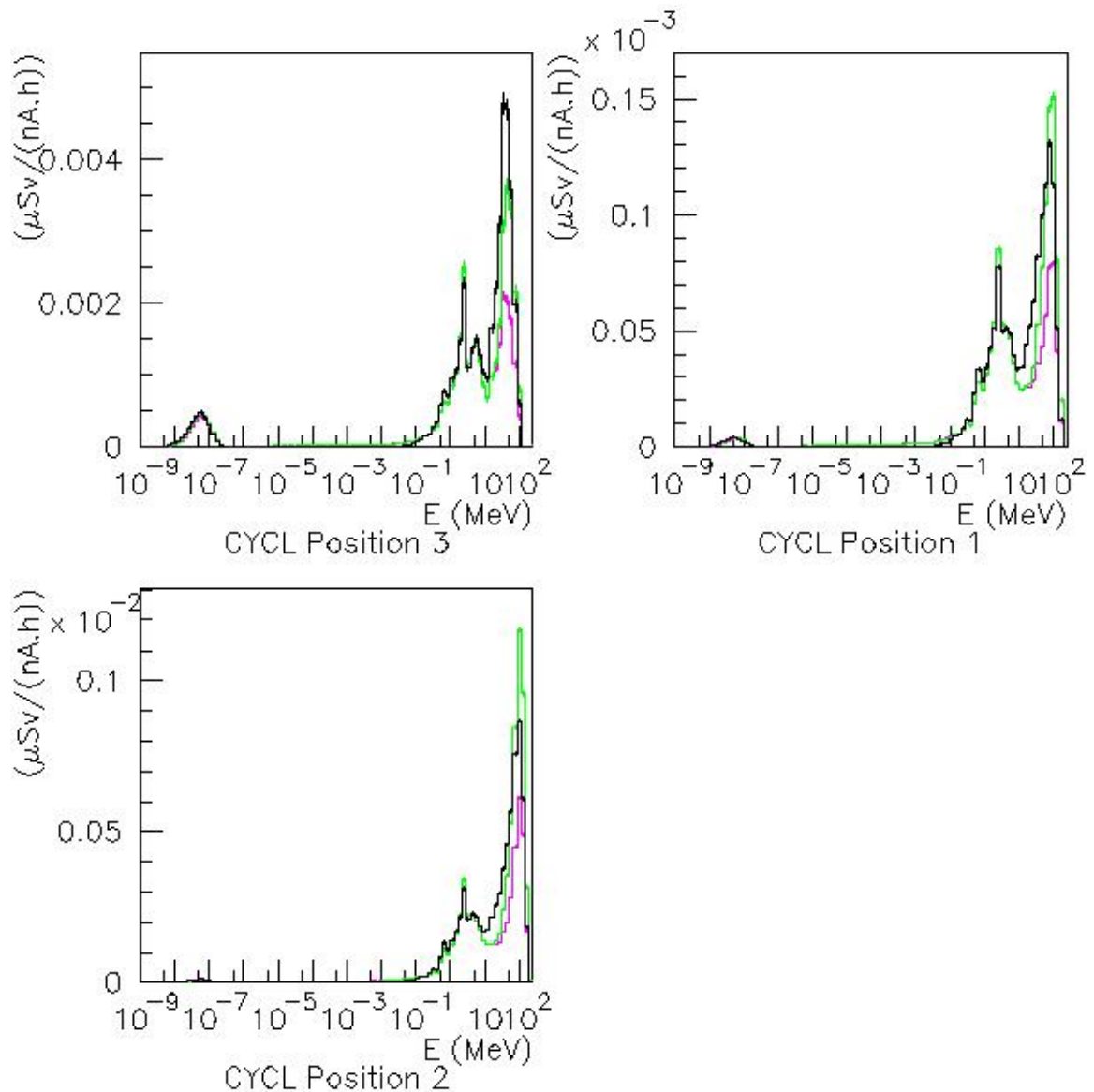
Figure III-18 - For positions inside the maze of the cyclotron room: neutron H*(10) spectra (in black) and WENDI-2 spectra based on the GEANT4 9.6 BIC response function (in green) and the response function of Olsher et al. based on experimental data above 46 MeV (in pink).

In brief, the overview presented in the figures **III-19** and **III-20** shows that:

- In all positions except position 2, the thermal neutrons constitute the largest fraction of the fluence, but do not cause dominant H*(10) contributions, except in the middle of the maze (positions 7 – 8).

- In the first part of the maze (positions 4 – 6), the largest contribution to H*(10) is due to the evaporation neutrons (~45-80%). The contribution from high-energy neutrons is small (< 10%).

- Starting from position 7, behind maze wall 'B', the fluence fraction of high-energy neutrons keeps increasing along the maze and, from position 9 onwards, their contribution to H*(10) outgrows that of the evaporation neutrons (which does not exceed ~35-40% in positions 7 – 9).

- Outside the cyclotron room, the high-energy neutrons represent ∼55-65% of H*(10) and the evaporation neutrons ∼30-40%.
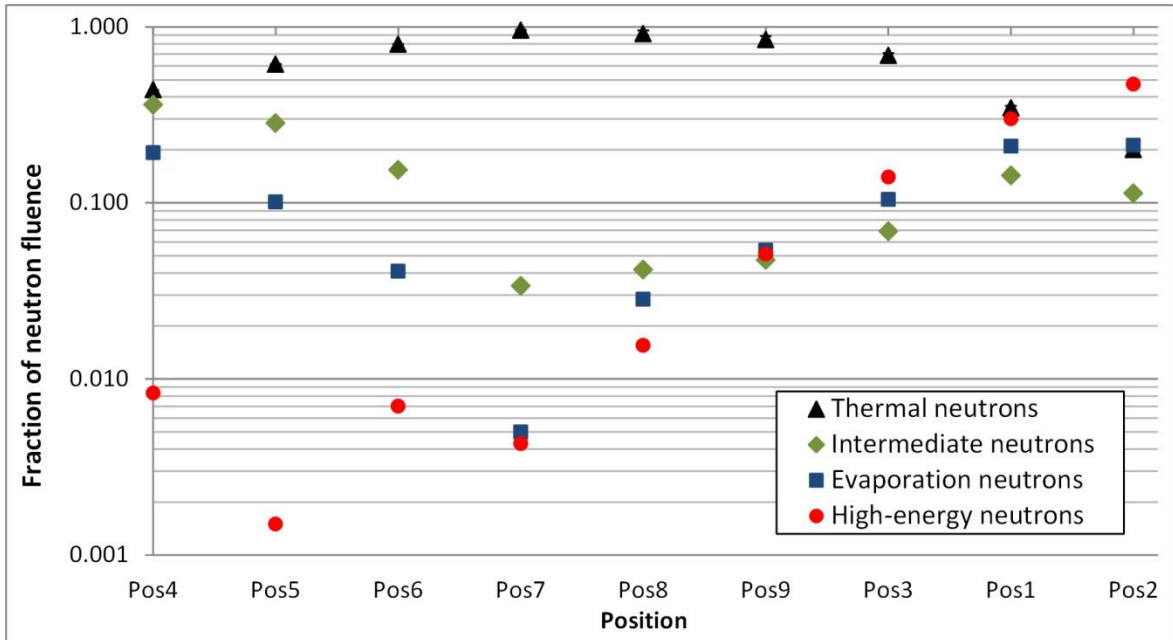
Figure III-19 - Fractions of the simulated neutron fluence that are due to 'thermal', 'intermediate', 'evaporation' and 'high-energy' neutrons, in the positions inside and around the cyclotron room.
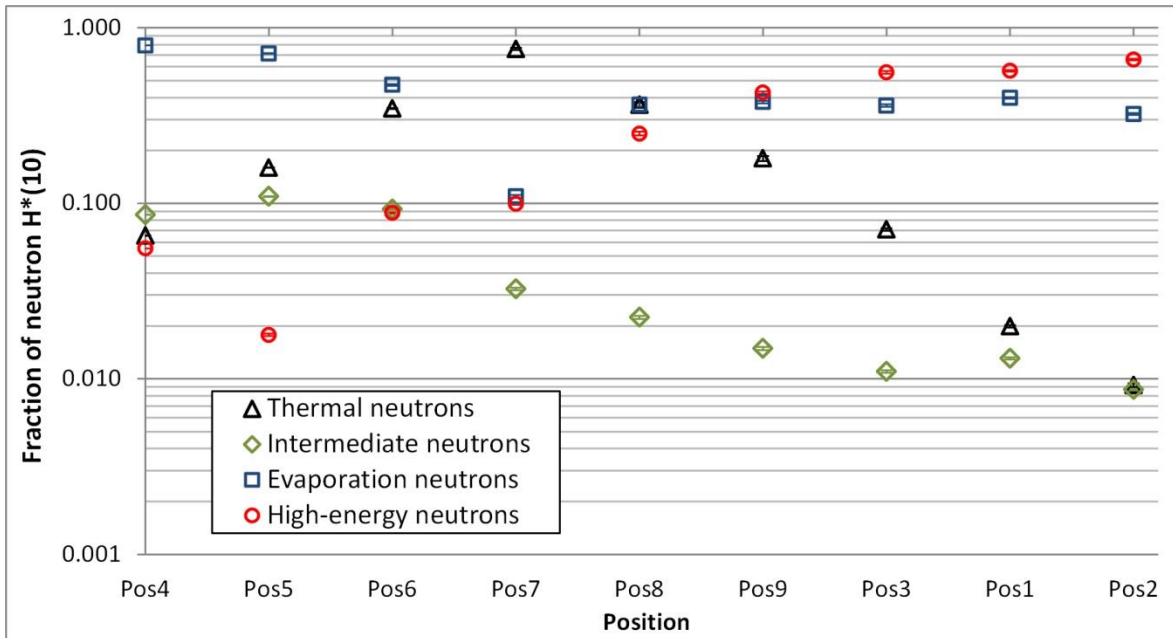
Figure III-20 - Fractions of the simulated neutron H(10) that are due to 'thermal', 'intermediate', 'evaporation' and 'high-energy' neutrons, in the positions inside and around the cyclotron room.*

Apart from the neutron H*(10) spectra, the figures **III-17** and **III-18** also show the spectra for the WENDI-2 responses simulated using the following response functions from figure **III-9** on p. **126**:

- the response function of Vanaudenhove *et al.* simulated with GEANT4 9.6 using the BIC model [184],

- the response function of Olsher *et al.* based on MCNP4B simulations (E < 0.144 MeV) [152] and high-energy QMN measurements [182],

- the response function of Jägerhofer *et al.* simulated with FLUKA (only shown in figure **III-17**).

As a reminder, our measurements performed in high-energy QMN beams at the TSL suggest that the WENDI-2 response function above 20 MeV might have values that are intermediate to the two first functions (see section **II-4**). As for the third function, it differs quite strongly from the two others in the thermal and intermediate energy regions and is therefore interesting for the positions in the maze.

For each of the response functions shown in figure **III-9** (p. **126**), the corresponding energy-integrated responses are given in table **III-3.** The percent deviation of these simulated responses with respect to the simulated H*(10) is shown in figure **III-21**.

Table III-3 - Simulated WENDI-2 responses obtained in the cyclotron room simulations, using the different versions of the response function shown in figure III-9. The results are expressed in µSv/(nA.h), where the nA.h refer to the cyclotron-extracted proton charge. The given uncertainties are the MCNPX statistical uncertainties (1σ).

Position	MCNPX 2.7.0 Bertini & Dresner	GEANT4 9.6 Bertini	GEANT4 9.6 BIC	FLUKA	MCNP4B + HE QMN Olsher et al.
4	(1.642 ± 0.001) x 10^3	(1.731 ± 0.001) x 10^3	(1.726 ± 0.001) x 10^3	(1.530 ± 0.001) x 10^3	(1.717 ± 0.001) x 10^3
5	(2.505 ± 0.004) x 10^2	(2.752 ± 0.004) x 10^2	(2.749 ± 0.004) x 10^2	(2.264 ± 0.004) x 10^2	(2.719 ± 0.004) x 10^2
6	(9.37 ± 0.06) x 10^0	(1.150 ± 0.006) x 10^1	(1.122 ± 0.006) x 10^1	(8.52 ± 0.06) x 10^0	(1.047 ± 0.006) x 10^1
7	(5.38 ± 0.09) x 10^{-1}	(7.00 ± 0.09) x 10^{-1}	(6.76 ± 0.09) x 10^{-1}	(4.00 ± 0.08) x 10^{-1}	(5.92 ± 0.09) x 10^{-1}
8	(8.7 ± 0.2) x 10^{-2}	(9.7 ± 0.2) x 10^{-2}	(9.3 ± 0.2) x 10^{-2}	(7.5 ± 0.2) x 10^{-2}	(8.5 ± 0.2) x 10^{-2}
9	(9.6 ± 0.2) x 10^{-2}	(1.02 ± 0.02) x 10^{-1}	(9.5 ± 0.2) x 10^{-2}	(8.9 ± 0.2) x 10^{-2}	(8.2 ± 0.2) x 10^{-2}
3	(9.8 ± 0.1) x 10^{-3}	(1.06 ± 0.01) x 10^{-2}	(9.6 ± 0.1) x 10^{-3}	(9.9 ± 0.1) x 10^{-3}	(8.0 ± 0.1) x 10^{-3}
1	(3.79 ± 0.04) x 10^{-4}	(4.13 ± 0.04) x 10^{-4}	(3.59 ± 0.04) x 10^{-4}	(3.78 ± 0.04) x 10^{-4}	(2.81 ± 0.03) x 10^{-4}
2	(2.12 ± 0.02) x 10^{-3}	(2.35 ± 0.02) x 10^{-3}	(1.96 ± 0.02) x 10^{-3}	(2.10 ± 0.02) x 10^{-3}	(1.41 ± 0.02) x 10^{-3}

Figure III-21 – Percent deviation of the WENDI-2 response with respect to the neutron H*(10) obtained in the cyclotron room simulations. The WENDI-2 response was calculated using the different versions of the response function shown in figure III-9.The uncertainty bars represent the MCNPX statistical uncertainties (1σ).

In the first part of the maze (positions 4 – 5), all the considered response functions lead to an energy-integrated response that overestimates H*(10), except for the FLUKA response function of Jägerhofer *et al.* due to its lower values at thermal and intermediate energies (see spectra in figure **III-17**). As the neutron spectrum softens towards position 7, the discrepancies between the different versions of the response increases. For a better characterisation of the response in these positions, an experimental validation of the response function with thermal neutron beam irradiations could thus be useful. The results nevertheless indicate that the WENDI-2 should allow to measure H*(10) with tolerable accuracy in positions 4 – 7. In the last part of the maze (positions 8 – 9) and behind the maze door (position 3), the simulation results suggest that the WENDI-2 might perhaps slightly underestimate H*(10), although not by more than ~30%.

In the main control room (positions 1 – 2), the WENDI-2 response is more strongly determined by the sensitivity of the detector to high-energy neutrons. Position 2, which has the largest fraction of high-energy neutrons, shows the largest discrepancies between the different versions of the simulated WENDI-2 response. Assuming that the true response function above 20 MeV would be intermediate to the GEANT4 BIC response and the experimental response of Olsher *et al.* (see measurements in section **II-4**), then the WENDI-2 would provide quite accurate (though slightly underestimating) H*(10) measurements outside the cyclotron room. However, without precise validation measurements of the WENDI-2 response

function between 20 MeV and 230 MeV, it is not possible to predict the WENDI-2 response with such precision at this stage. One can thus only be confident that the WENDI-2 response will lie within at most 30% of H*(10).

Based on the present results, it was chosen not to use H*(10) as a reference quantity for the comparison of our simulation results with real on-site WENDI-2 measurements, which will be the topic of Chapter IV. Instead, the measurements will be compared to the average simulated WENDI-2 response $R_{sim,avg}$ and its estimated total uncertainty σ_{tot} (calculated as explained in section **III-2.2**). These results are given in table **III-4**. For positions outside the cyclotron room, the average values $R_{sim,avg}$ are very similar to the responses obtained with the GEANT4 BIC-based response function. This is however not the case inside the maze. The uncertainties σ_{tot} represent 4 – 11% of $R_{sim,avg}$ depending of the positions. The uncertainties that were considered in the estimation of σ_{tot} are detailed in table **III-5**. The uncertainties on the response function below 0.144 MeV and above 19 MeV give the largest contribution to σ_{tot} in all positions except position 4.

Table III-4 – Average WENDI-2 response $R_{sim,avg}$ and its total uncertainty σ_{tot} in the simulation of the cyclotron room.

Position	$R_{sim,avg}$ [μSv/(nA.h)]	σ_{tot} [μSv/(nA.h)]	$\frac{\sigma_{tot}}{R_{sim,avg}} x\ 100\%$
4	1.67×10^3	0.07×10^3	4%
5	2.60×10^2	0.14×10^2	5%
6	1.02×10^1	0.06×10^1	6%
7	5.8×10^{-1}	0.6×10^{-1}	11%
8	8.7×10^{-2}	0.5×10^{-2}	6%
9	9.3×10^{-2}	0.5×10^{-2}	5%
3	9.6×10^{-3}	0.6×10^{-3}	6%
1	3.6×10^{-4}	0.3×10^{-4}	8%
2	2.0×10^{-3}	0.2×10^{-3}	10%

Table III-5 – Uncertainties on the average WENDI-2 response in the simulation of the cyclotron room: the average MCNPX statistical uncertainty σ_{stat}, the systematic uncertainty σ_{exp} representing 5% of the contribution of 0.144 MeV – 19 MeV neutrons to the simulated WENDI-2 response, and the systematic uncertainty $\sigma_{resp.fct.}$ caused by the uncertainties on the WENDI-2 response function below 0.144 MeV and above 19 MeV.

Position	σ_{stat} [μSv/(nA.h)]	σ_{exp} [μSv/(nA.h)]	$\sigma_{resp.fct.}$ [μSv/(nA.h)]
4	1.0×10^0	5.8×10^1	4.6×10^1
5	3.8×10^{-1}	7.6×10^0	1.1×10^1
6	5.7×10^{-2}	2.1×10^{-1}	5.7×10^{-1}
7	9.2×10^{-3}	3.4×10^{-3}	6.1×10^{-2}
8	2.3×10^{-3}	1.8×10^{-3}	4.2×10^{-3}
9	2.2×10^{-3}	2.1×10^{-3}	3.4×10^{-3}
3	1.3×10^{-4}	2.1×10^{-4}	5.3×10^{-4}
1	3.7×10^{-6}	7.7×10^{-6}	2.7×10^{-5}
2	2.2×10^{-5}	3.3×10^{-5}	1.9×10^{-4}

III-3.2 Gantry room operated in PBS

The neutron fluence spectra simulated for the gantry room operated in PBS are shown in the figures **III-22** and **III-23**. These figures actually compare two versions of the spectra:

- The spectra in red were obtained in an earlier simulation, in which the gantry front ring was not yet included in the geometry;

- The spectra in black are the latest results for the geometry shown in figure **III-4** (gantry front ring included).

For the latest version of the simulation, the neutron H*(10) spectra are also shown, in black, in the figures **III-24** and **III-25**. The fluence and H*(10) fractions of thermal, intermediate, evaporation and high-energy neutrons were calculated in the same way as in the previous section. The results hereof are shown in the figures **III-26** and **III-27**. As for the results for the total neutron H*(10), they are given in table **III-6**, for both versions of the simulation.

From a global perspective, the evolution of the spectra throughout the maze is quite similar to the one observed in the maze of the cyclotron room. The fluence is dominated by the maze-scattered component. From position 1 to 3 (see figure **III-22**), the neutron spectrum softens as this component is being attenuated. At the same time, the contribution of high-energy neutrons transmitted through the maze wall increases because of the decreasing angle with the proton beam direction. This causes the small peak around ~100 MeV which appears in the spectra of positions 5 and 6.

One difference here is that the neutron spectrum at the entrance of the maze contains a larger fraction of neutrons with energies between ~10 MeV and ~50 MeV (see 'PBS Position 1' on figure **III-22** *vs.* 'CYCL Position 4' on figure **III-15**). There is indeed no massive shielding structure such as that of the cyclotron between the water phantom and the entrance of the maze. Moreover, the angle between the proton beam and the entrance of the maze is smaller than for the beam stop contribution in the cyclotron room. The larger fraction of high-energy neutrons results in a much larger contribution to H*(10) in 'PBS Position 1' (figure **III-24**), than in 'CYCL Position 4' (figure **III-17**).

Inside the maze, the presence of the gantry ring leads to a non-negligible fluence increase for neutrons of less than ~1 MeV (see figure **III-22**). Since in iron, elastic scattering is by far the most probable neutron interaction for energies between ~10^{-4} MeV and ~1 MeV, these extra neutrons must have reached the entrance of the maze after undergoing elastic scattering inside the front ring. As one moves towards the door, the influence of the front ring progressively decreases because the maze-scattered component is being attenuated while the wall-transmitted fluence component increases. In terms of H*(10), the front ring causes a

maximum increase of 24% in position 1 and a minimum increase of 7% in position 6 (see table **III-6**).

The most important impact of the gantry front ring is observed in position 9 inside the control room. The total neutron fluence in this position is reduced by about 55% after including the front ring in the simulation. Figure **III-23** shows that the reduction affects the entire width of the spectrum, with a somewhat larger impact on the high-energy peak. It translates as a reduction of H*(10) by a little more than a factor of 2 (see table **III-6**). The other positions located outside the treatment room are not affected by the inclusion of the gantry front ring. This can be understood by the fact that the doses behind the shield are mainly determined by the fluence of high-energy neutrons present in front of the shield, while high-energy neutrons tend to travel almost in straight line through the shield. As shown in figure **III-4**, the front ring crosses the straight line that connects the isocentre to position 9. Due to this, high-energy neutrons produced in the water phantom and emitted towards position 9 have to cross a total average thickness of ~10 cm of iron, which is an efficient attenuator of high-energy neutrons (via inelastic scattering).

Iron is however not a good neutron attenuator at energies below 847 keV, the first excited state of ^{56}Fe. Elastic scattering on such heavy nuclei is indeed an inefficient slowing-down mechanism because of the relatively small energy transfers. In consequence, an iron shield tends to soften the neutron spectra by preferentially attenuating high-energy neutrons. This effect explains why, compared to other outside positions such as 8 and 11 (see figure **III-23**), a lower fraction of high-energy neutrons is encountered in position 10, which is shielded by the thick iron counterweight of the gantry (see figure **III-4**). The same effect is in fact also visible, to a lesser extent, in position 9 when the gantry front ring is introduced in the simulation.
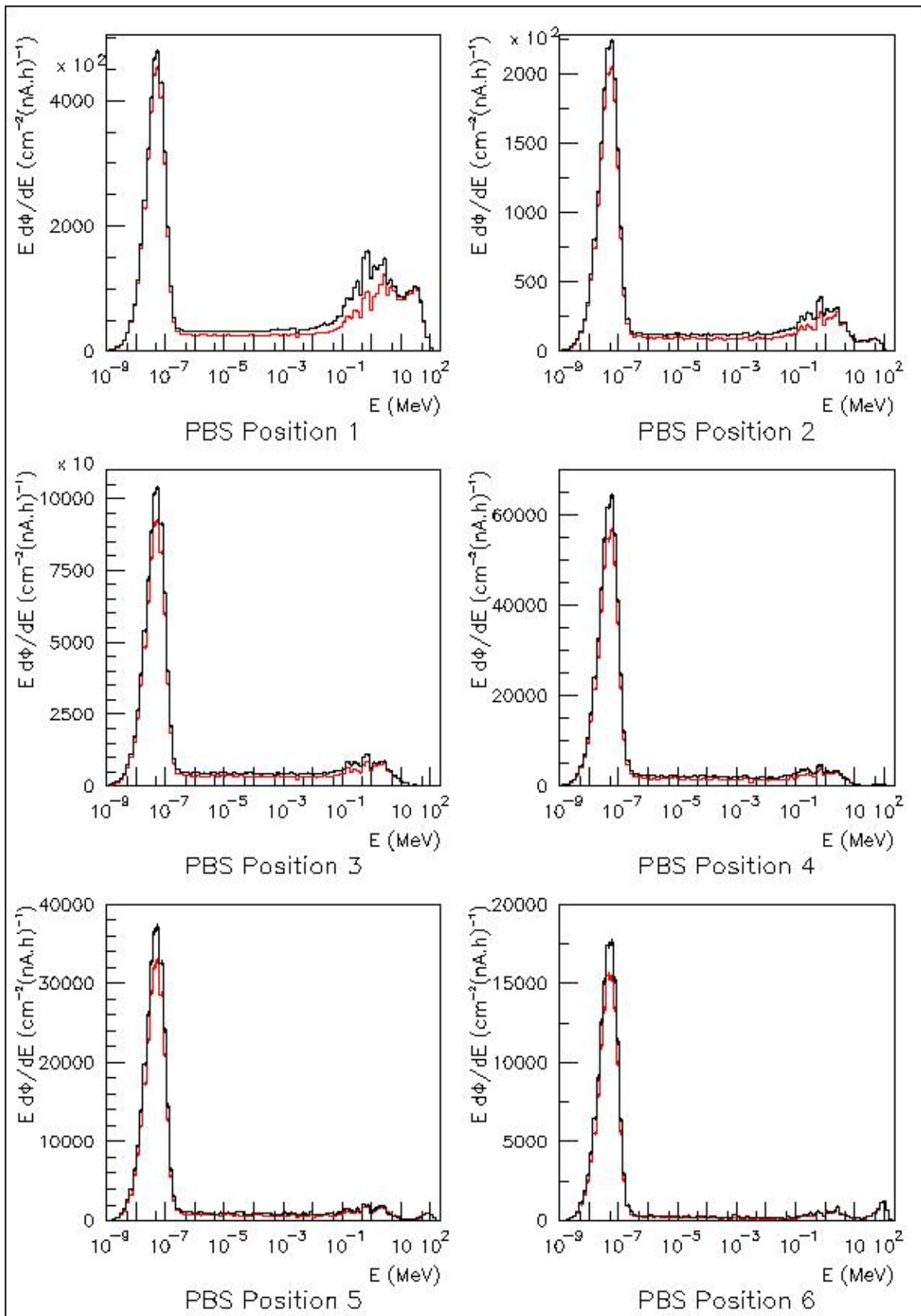
Figure III-22 - Neutron fluence spectra simulated inside the maze of the gantry treatment room operated in PBS. The spectra in red were obtained without the gantry front ring, those in black __with__ the gantry front ring.
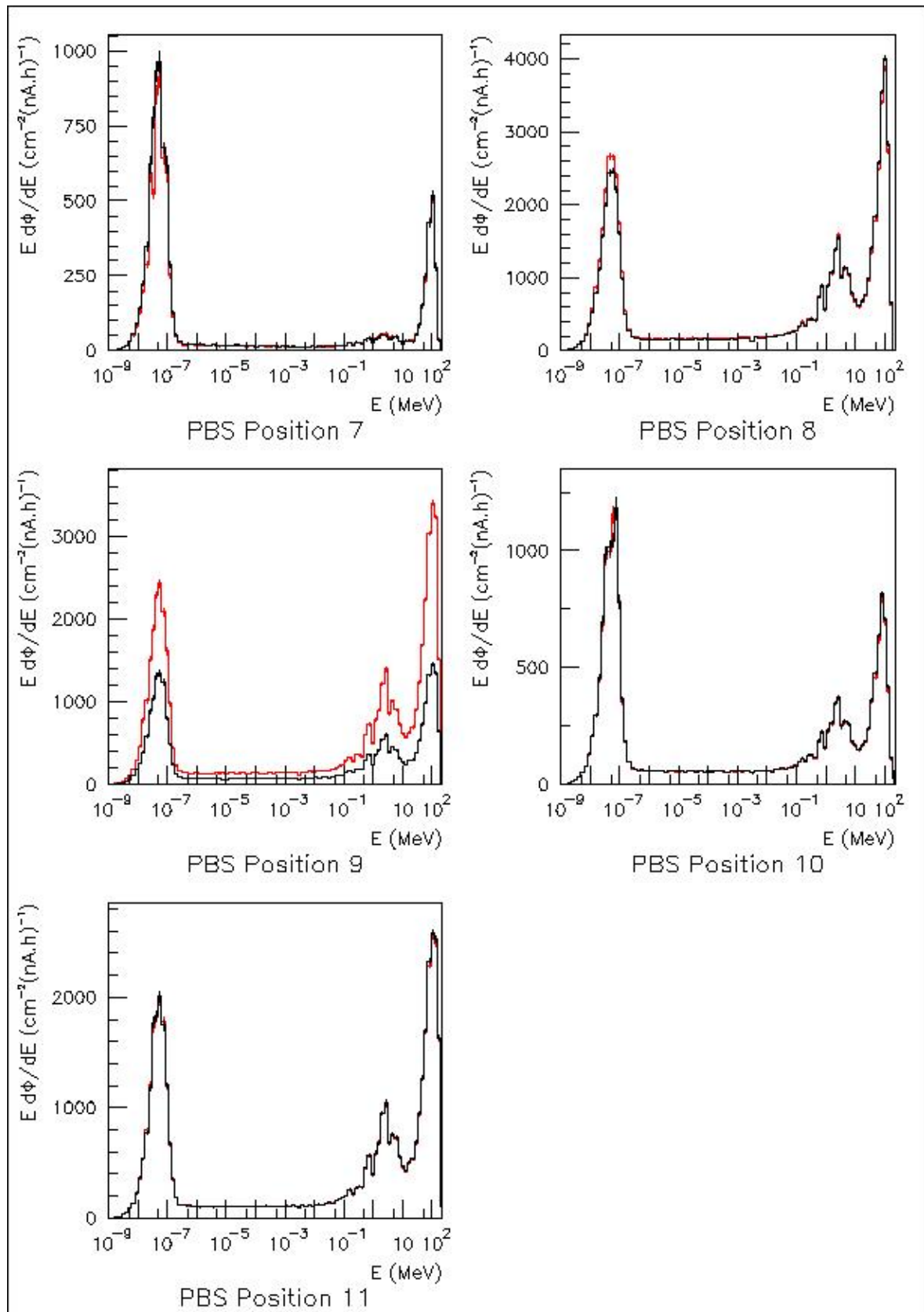
Figure III-23 - Neutron fluence spectra simulated outside the gantry treatment room operated in PBS. The spectra in red were obtained without the gantry front ring, those in black <u>with</u> the gantry front ring.
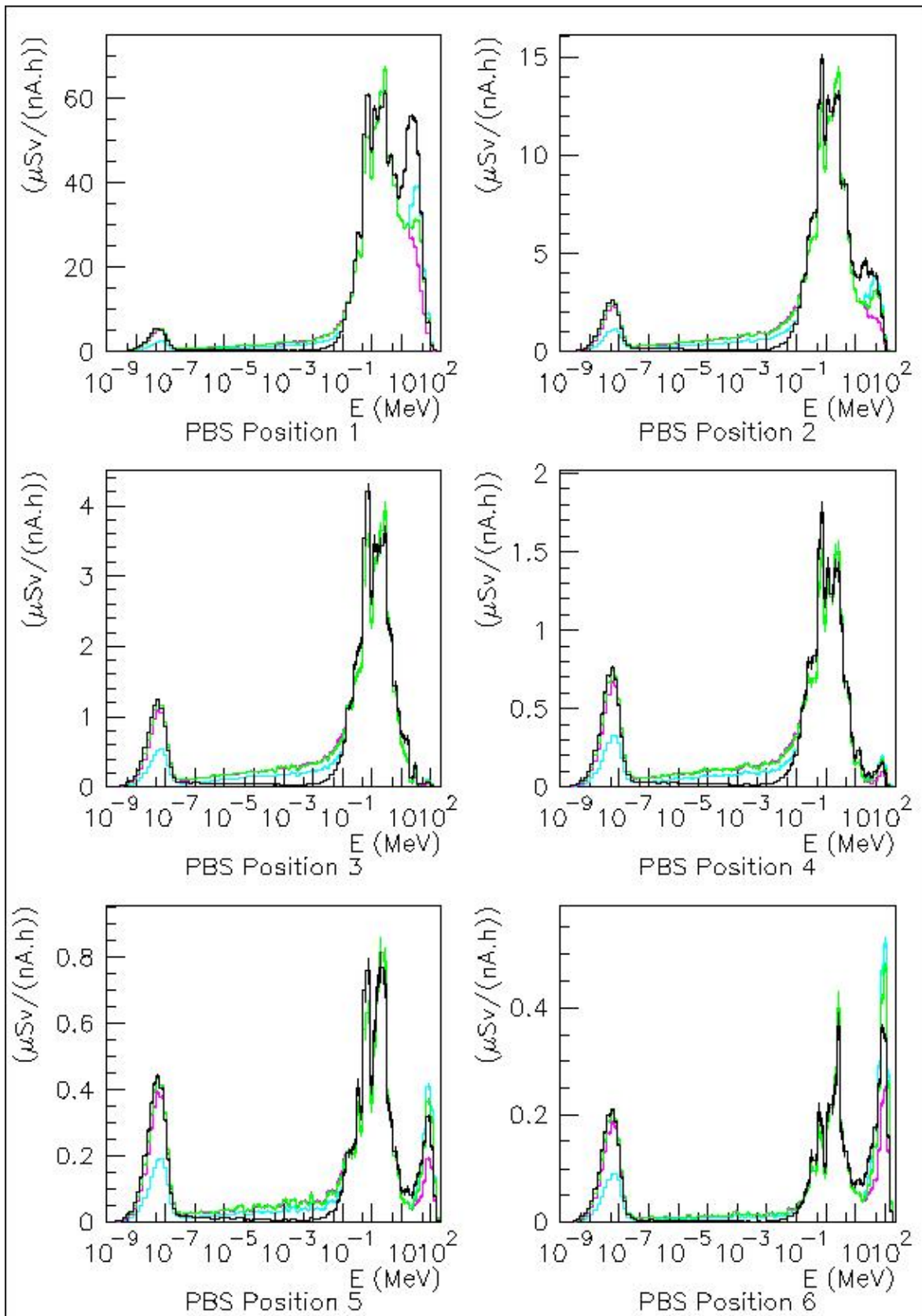
Figure III-24 - For positions inside the maze of the gantry treatment room operated in PBS (with gantry ring): neutron H*(10) spectra (in black) and WENDI-2 spectra based on the GEANT4 9.6 BIC response function (in green), the FLUKA response function (in cyan) and the response function of Olsher et al. based on experimental data above 46 MeV (in pink).
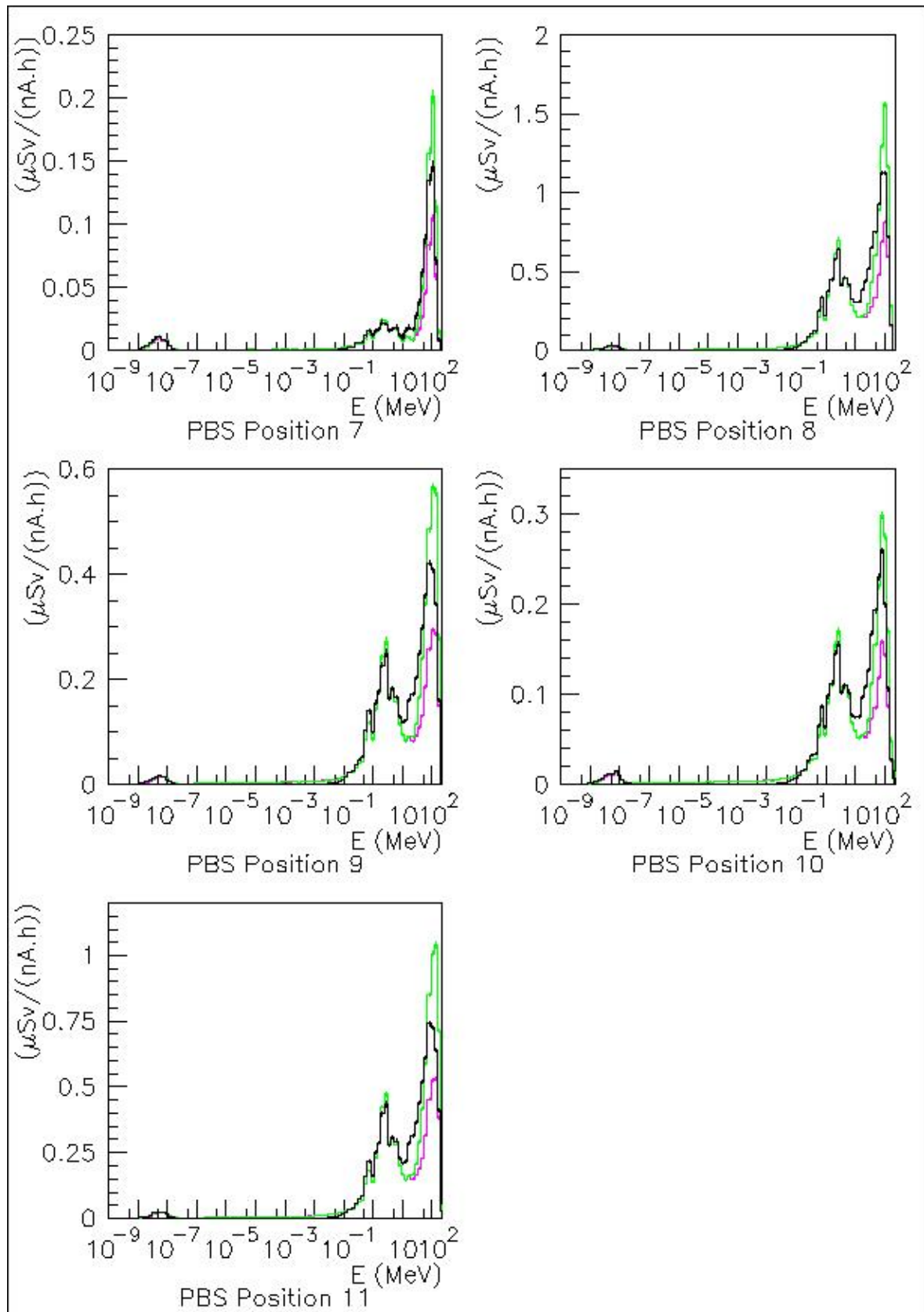
Figure III-25 - For positions outside the gantry treatment room operated in PBS (with gantry ring): neutron H*(10) spectra (in black) and WENDI-2 spectra based on the GEANT4 9.6 BIC response function (in green) and the response function of Olsher et al. based on experimental data above 46 MeV (in pink).
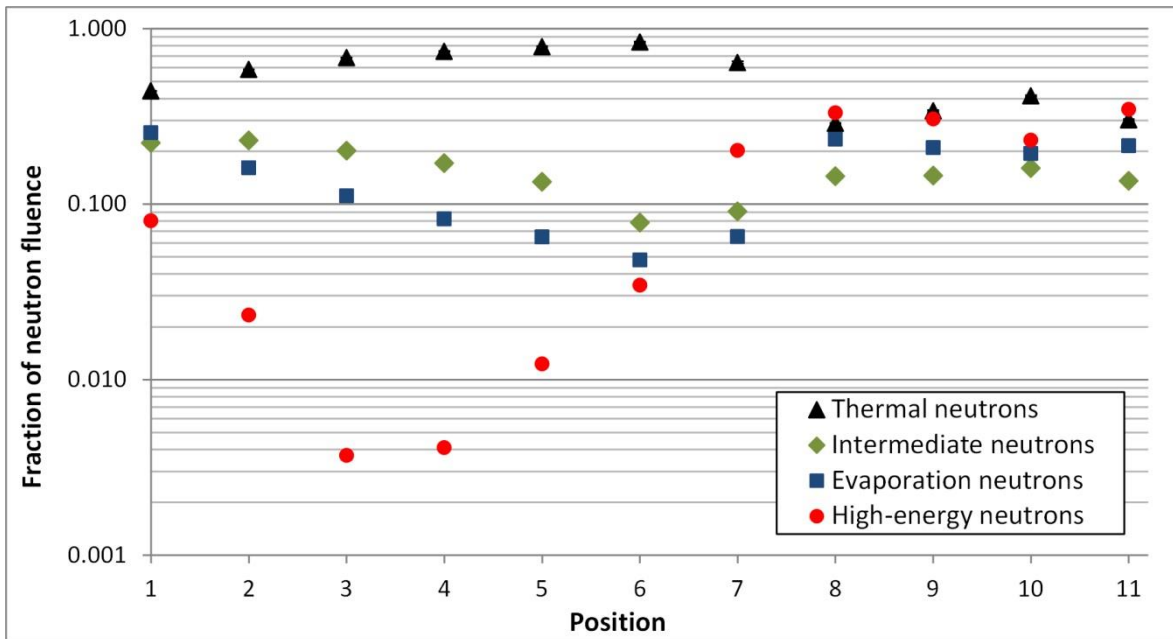
*Figure III-26 - Fractions of the simulated neutron fluence that are due to 'thermal',
'intermediate', 'evaporation' and 'high-energy' neutrons, in the positions inside and around the
gantry room operated in PBS (simulation with gantry front ring).*
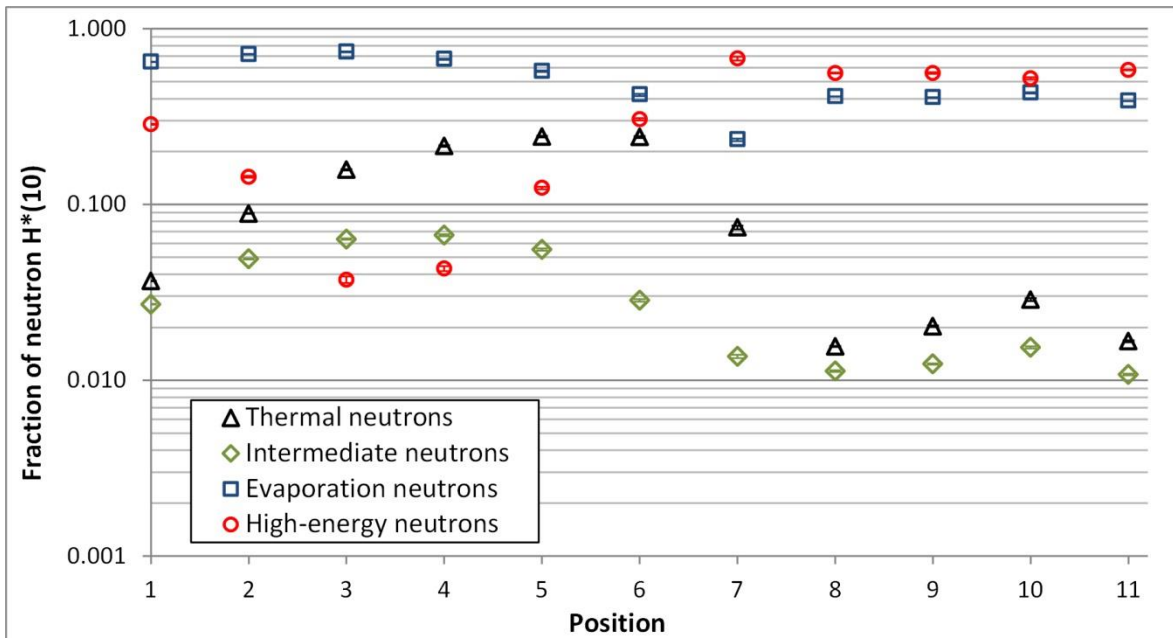
Figure III-27 - Fractions of the simulated neutron H(10) that are due to 'thermal',
'intermediate', 'evaporation' and 'high-energy' neutrons , in the positions inside and around the
gantry room operated in PBS (simulation with gantry front ring).*

Table III-6 – Neutron H*(10) obtained in the PBS simulations, without and with the gantry front ring. The results are expressed in µSv/(nA.h), where the nA.h refer to the proton charge delivered to the phantom. The given uncertainties are the MCNPX statistical uncertainties (1σ). The third column contains the H*(10) variation factors for the insertion of the gantry front ring in the simulated geometry.

Position	$H^*(10)$ [µSv/(nA.h)] without gantry ring	$H^*(10)$ [µSv/nA.h] with gantry ring	$\dfrac{H^*(10)_{with\ ring}}{H^*(10)_{without\ ring}}$
1	229.6 ± 0.5	284.6 ± 0.5	1.239 ± 0.003
2	45.1 ± 0.2	54.4 ± 0.2	1.21 ± 0.01
3	12.0 ± 0.1	14.3 ± 0.1	1.19 ± 0.01
4	5.45 ± 0.05	6.38 ± 0.06	1.17 ± 0.01
5	2.97 ± 0.04	3.31 ± 0.04	1.11 ± 0.02
6	1.45 ± 0.03	1.55 ± 0.03	1.07 ± 0.02
7	0.244 ± 0.007	0.243 ± 0.007	0.99 ± 0.04
8	3.26 ± 0.02	3.32 ± 0.01	1.02 ± 0.01
9	3.02 ± 0.02	1.35 ± 0.01	0.446 ± 0.005
10	0.78 ± 0.02	0.80 ± 0.02	1.02 ± 0.02
11	2.33 ± 0.02	2.36 ± 0.02	1.01 ± 0.01

The figures **III-26** and **III-27** show that:

- In most positions (all except 8 and 11), the thermal neutrons constitute the largest fraction of the fluence, but do not cause dominant H*(10) contributions.

- Inside the maze (positions 1 – 6), the largest contribution to H*(10) is due to the evaporation neutrons (~40-75%). The relative contribution from high-energy neutrons at the beginning of the maze (~15-30%) is larger than in the cyclotron maze.

- Starting from position 3, after the first maze corner, the fluence fraction of high-energy neutrons keeps increasing along the maze, but does not exceed that of the evaporation neutrons until outside the treatment room.

- Outside the treatment room, the high-energy neutrons represent ~50-60% of H*(10) and the evaporation neutrons ~25-45%. Iron parts of the gantry tend to reduce the fluence fraction of high-energy neutrons in some outside positions (see 9 and 10).

The WENDI-2 responses simulated using the response functions of figure **III-9** (p. **126**) are given in table **III-7.** The percent deviation of these simulated WENDI-2 responses with respect to the simulated H*(10) is also given in figure **III-28**.

Table III-7 - Simulated WENDI-2 responses obtained in the PBS simulation (with gantry ring), using the different versions of the response function shown in figure III-9. The results are expressed in µSv/(nA.h), where the nA.h refer to the proton charge delivered to the phantom. The given uncertainties are the MCNPX statistical uncertainties (1σ).

Position	MCNPX 2.7.0 Bertini & Dresner	GEANT4 9.6 Bertini	GEANT4 9.6 BIC	FLUKA	MCNP4B + HE QMN Olsher et al.
1	261.7 ± 0.5	271.7 ± 0.5	263.5 ± 0.4	256.6± 0.5	251.5 ± 0.4
2	53.4 ± 0.2	57.4 ± 0.2	56.3 ± 0.2	51.2 ± 0.2	54.5 ± 0.2
3	14.6 ± 0.1	15.8 ± 0.1	15.7 ± 0.1	13.4 ± 0.1	15.5 ± 0.1
4	6.50 ± 0.06	7.16 ± 0.06	7.11 ± 0.06	5.87 ± 0.06	6.91 ± 0.06
5	3.33 ± 0.04	3.73 ± 0.04	3.62 ± 0.04	3.01 ± 0.04	3.38 ± 0.04
6	1.55 ± 0.03	1.78 ± 0.03	1.63 ± 0.03	1.44 ± 0.03	1.39 ± 0.03
7	0.272 ± 0.008	0.321 ± 0.008	0.264 ± 0.007	0.273 ± 0.008	0.182 ± 0.006
8	3.56 ± 0.01	3.92 ± 0.02	3.37 ± 0.01	3.54 ± 0.01	2.60 ± 0.01
9	1.47 ± 0.01	1.63 ± 0.01	1.40 ± 0.01	1.46 ± 0.01	1.07 ± 0.01
10	0.82 ± 0.01	0.90 ± 0.01	0.79 ± 0.01	0.82 ± 0.01	0.63 ± 0.01
11	2.62 ± 0.02	2.92 ± 0.02	2.47 ± 0.02	2.59 ± 0.02	1.86 ± 0.02
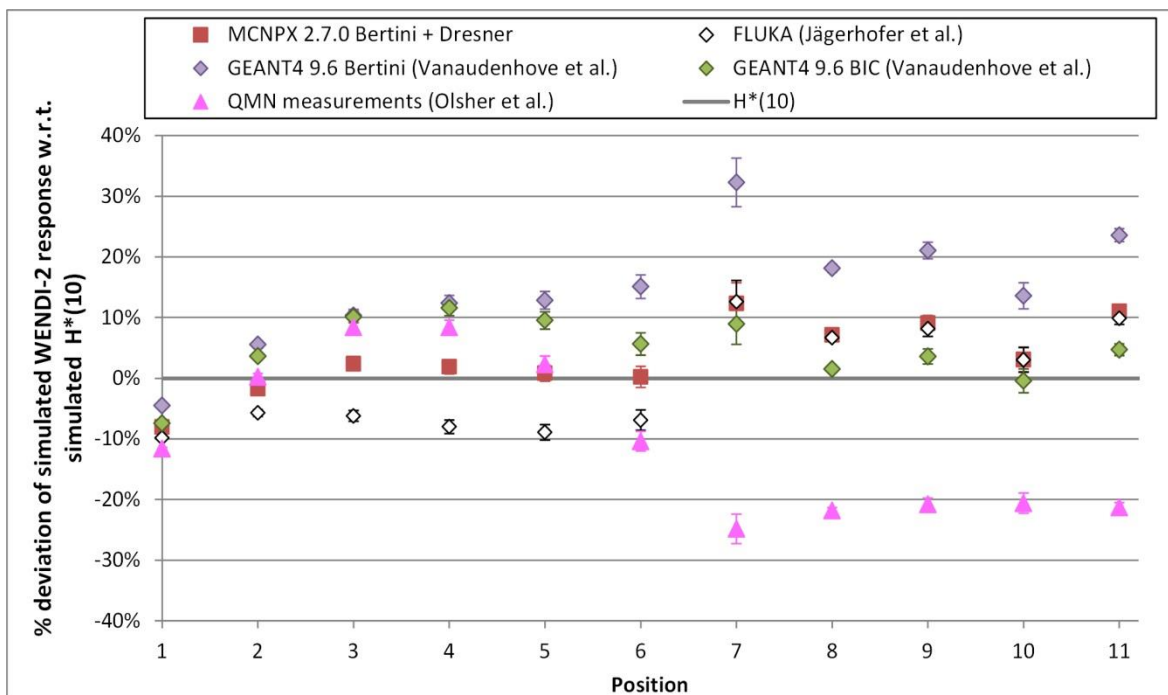
Figure III-28 - Percent deviation of the WENDI-2 response with respect to the neutron H*(10) obtained in the PBS simulation with gantry ring. The WENDI-2 response was calculated using the different versions of the response function shown in figure III-9. The uncertainty bars represent the MCNPX statistical uncertainties (1σ).

The results in figure **III-28** indicate that the WENDI-2 should allow measuring H*(10) with an accuracy better than ~15% inside the maze. The differences between the various simulated responses tend to be smaller here than in the cyclotron maze, thanks to the somewhat larger fraction of evaporation neutrons. As a reminder, evaporation neutrons correspond to the energy region where a common section, based on validation measurements, was used for the response functions (see figure **III-9**). Because of its ^{252}Cf calibration, the WENDI-2 measures the H*(10) contribution from evaporation neutrons quite accurately (see Chapter II).

In position 1, the simulation suggests that the WENDI-2 might slightly underestimate H*(10), but not by more than ~10%. This slight underestimation is related to the fraction of neutrons with energies between ~10 MeV and ~50 MeV (see figure **III-24**): these neutrons give a relatively large contribution to the response but the response functions underestimate the fluence-to-H*(10) conversion coefficients in that energy region (see figure **III-9**). For the WENDI-2 responses in the other maze positions, an experimental validation of the response function at thermal energies would help further reducing the uncertainties.

Outside the treatment room, the discrepancies between the different simulated versions of the WENDI-2 response tend to be larger than in the maze. This is related to the larger fraction of high-energy neutrons for which our knowledge of the response function is relatively imprecise. In terms of percent deviation with respect to H*(10), the results are quite similar to those obtained outside the cyclotron room (see figure **III-21**). According to the simulation results, one may assume that the WENDI-2 response will lie within at most 25% of H*(10) in the positions 8 – 11.

In position 7, behind the maze door, the uncertainties on the simulated WENDI-2 response are in fact a bit larger than in the positions 8 – 11. The cause hereof is that, next to a relatively important fraction of high-energy neutrons, the simulated spectrum also contains a large fraction of thermal neutrons, for which the response function is even less precisely determined. The present results suggest though that the WENDI-2 response should not deviate by more than 35% from H*(10) in this position.

Table **III-8** contains the results for the average simulated WENDI-2 response $R_{sim,avg}$ and its estimated total uncertainty σ_{tot}, calculated as explained in section **III-2.2**. Similarly to the case of the cyclotron room, in positions outside the gantry room (7 – 11) $R_{sim,avg}$ is very similar to the BIC-based response. The total relative uncertainty on $R_{sim,avg}$ is of 4-5 % in the maze and 7-11 % outside the treatment room. The uncertainties included in the evaluation of σ_{tot} are detailed in table **III-9**. The largest contribution comes from the uncertainties on the response function below 0.144 MeV and above 19 MeV, except for the two first positions in the maze, where the uncertainty on the contribution from evaporation neutrons predominates.

Table III-8 – Average WENDI-2 response $R_{sim,avg}$ and its total uncertainty σ_{tot} in the simulation of the gantry room operated in PBS (with gantry ring).

Position	$R_{sim,avg}$ [μSv/(nA.h)]	σ_{tot} [μSv/(nA.h)]	$\dfrac{\sigma_{tot}}{R_{sim,avg}} x\ 100\%$
1	2.6×10^2	0.1×10^2	4%
2	5.5×10^1	0.2×10^1	4%
3	1.50×10^1	0.07×10^1	5%
4	6.7×10^0	0.4×10^0	5%
5	3.4×10^0	0.2×10^0	5%
6	1.56×10^0	0.09×10^0	5%
7	2.6×10^{-1}	0.3×10^{-1}	11%
8	3.4×10^0	0.3×10^0	8%
9	1.4×10^0	0.1×10^0	8%
10	7.9×10^{-1}	0.6×10^{-1}	7%
11	2.5×10^0	0.2×10^0	9%

Table III-9 – Uncertainties on the average WENDI-2 response in the simulation of the gantry room operated in PBS (with gantry ring): the average MCNPX statistical uncertainty σ_{stat}, the systematic uncertainty σ_{exp} representing 5% of the contribution of 0.144 MeV – 19 MeV neutrons to the simulated WENDI-2 response, and the systematic uncertainty $\sigma_{resp.fct.}$ caused by the uncertainties on the WENDI-2 response function below 0.144 MeV and above 19 MeV.

Position	σ_{stat} [μSv/(nA.h)]	σ_{exp} [μSv/(nA.h)]	$\sigma_{resp.fct.}$ [μSv/(nA.h)]
1	4.5×10^{-1}	9.4×10^0	3.6×10^0
2	2.1×10^{-1}	1.9×10^0	1.1×10^0
3	9.5×10^{-2}	5.1×10^{-1}	5.3×10^{-1}
4	5.7×10^{-2}	2.0×10^{-1}	2.8×10^{-1}
5	3.7×10^{-2}	9.2×10^{-2}	1.3×10^{-1}
6	2.7×10^{-2}	3.2×10^{-2}	7.4×10^{-2}
7	7.4×10^{-3}	3.0×10^{-3}	2.7×10^{-2}
8	1.5×10^{-2}	7.1×10^{-2}	2.7×10^{-1}
9	1.3×10^{-2}	2.9×10^{-2}	1.1×10^{-1}
10	1.4×10^{-2}	1.8×10^{-2}	5.4×10^{-2}
11	1.7×10^{-2}	4.8×10^{-2}	2.1×10^{-1}

III-3.3 Gantry room operated in DS

The neutron fluence spectra simulated for the gantry room operated in DS are shown in the figures **III-29** and **III-30**. As in the previous section, these figures also show how the fluence spectra were modified after inserting the gantry front ring in the simulated geometry.

For the simulation with the gantry front ring, the neutron H*(10) spectra are shown, in black, in the figures **III-31** and **III-32**. The fluence and H*(10) fractions of thermal, intermediate, evaporation and high-energy neutrons are shown in the figures **III-33** and **III-34**. The results of the total neutron H*(10), obtained without and with the gantry front ring, are given in table **III-10**.

The evolution of the spectra along the maze is very similar to the one of the PBS simulation (see previous section). The DS irradiation causes however a much larger secondary neutron production than the PBS irradiation (see figure **III-29** *vs.* figure **III-22**). The main reason for the increased neutron production are the high-Z materials that the proton beam traverses inside the DS nozzle, such as tantalum (Z=73) and lead (Z=82). Indeed, at the considered proton energy of nearly 230 MeV, the average number of neutrons emitted per proton – called the neutron multiplicity – significantly increases with the atomic number Z of the target. The neutron multiplicity for a tantalum target is for instance larger by a factor of ~8 than for a low-Z target like human tissue, according to MCNPX simulations for stopping-length targets based on the Bertini model [79].

The larger neutron multiplicity observed for targets of increasing Z is mostly due to a larger emission of evaporation neutrons. This is for instance seen in the measurements of double differential neutron yields by Meier *et al.* [238]. This tendency might explain:

- the larger fraction of evaporation neutrons observed at the entrance of the maze, in comparison with the PBS results (see positions 12 – 13 in figure **III-29** *vs.* positions 1 – 2 in figure **III-22**);

- the lower fraction of high-energy neutrons towards the end of the maze, in comparison with the PBS results (see positions 15 – 16 in figure **III-29** *vs.* positions 5 – 6 in figure **III-22**). Indeed, most of the high-energy neutrons in these positions were transmitted through the maze wall. The relative importance of the wall-transmitted fluence, compared to the maze-scattered fluence, thus seems to be smaller in the DS case than in the PBS case. In other words, the high-Z nozzle elements cause a larger relative increase of the maze-scattered component than of the wall-transmitted component, because the former is mostly driven by evaporation neutrons and the latter by high-energy neutrons.
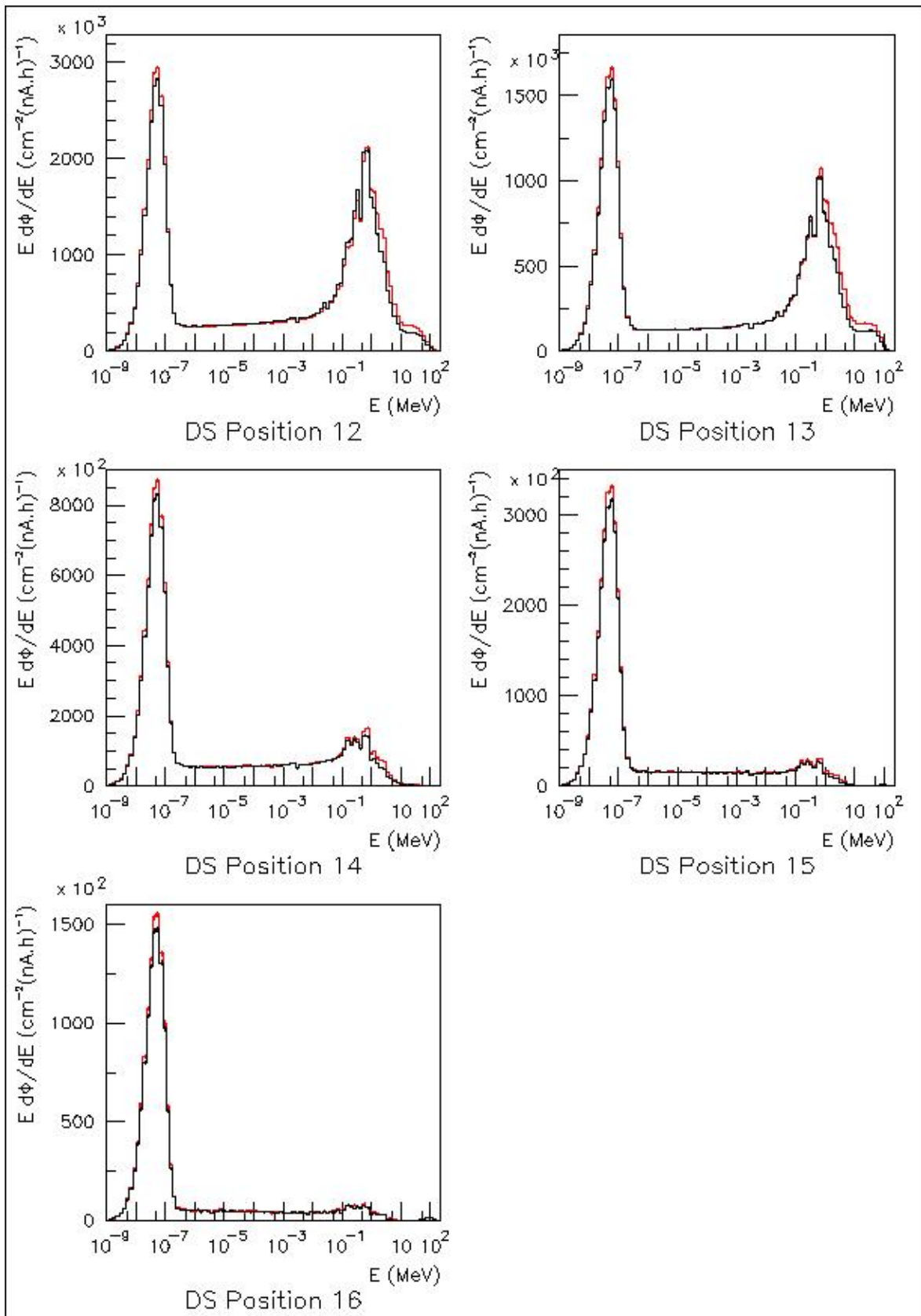
Figure III-29 - Neutron fluence spectra simulated inside the maze of the gantry treatment room operated in DS. The spectra in red were obtained without the gantry front ring, those in black <u>with</u> the gantry front ring.
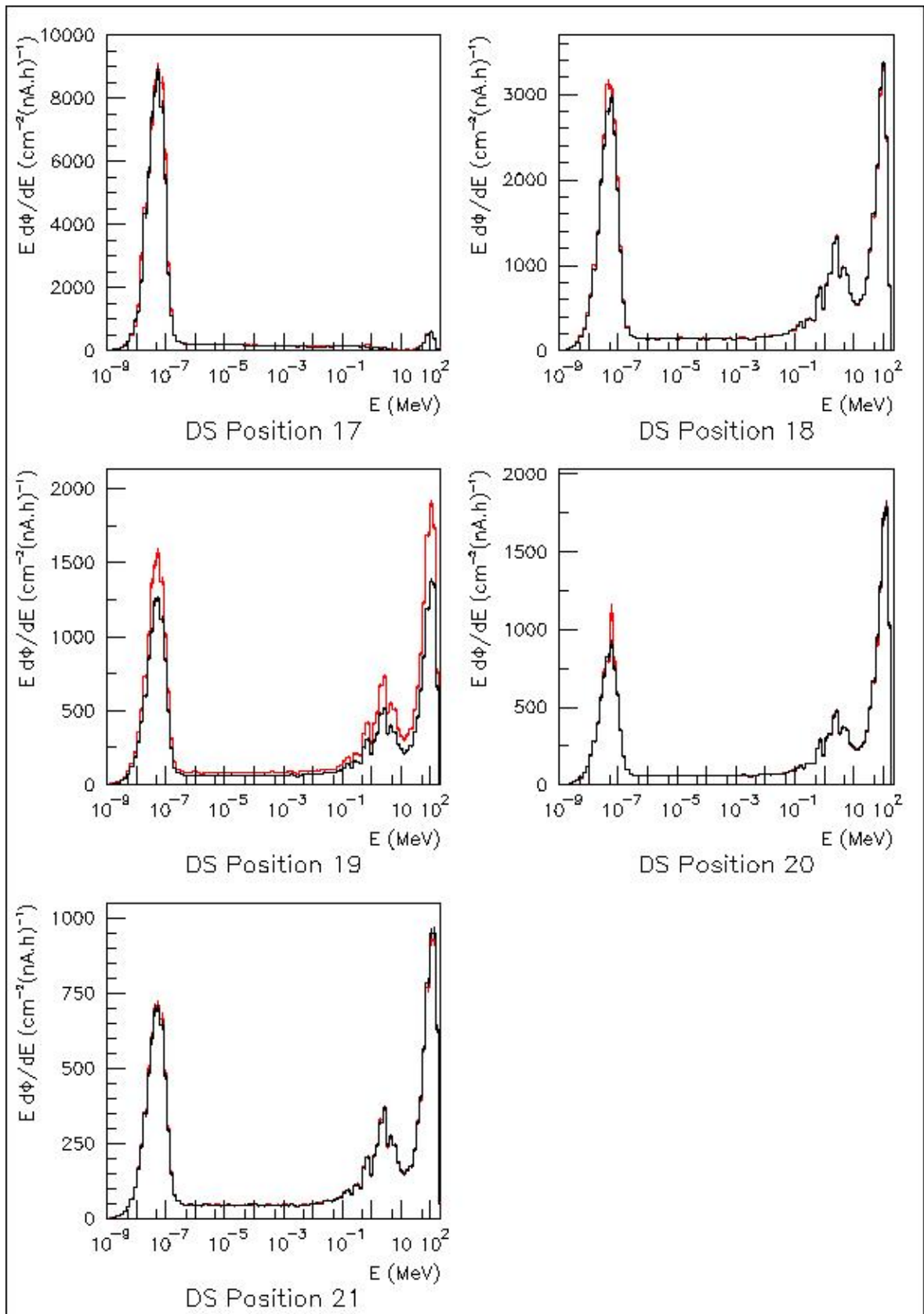
Figure III-30 - Neutron fluence spectra simulated outside the gantry treatment room operated in DS. The spectra in red were obtained without the gantry front ring, those in black __with__ the gantry front ring.
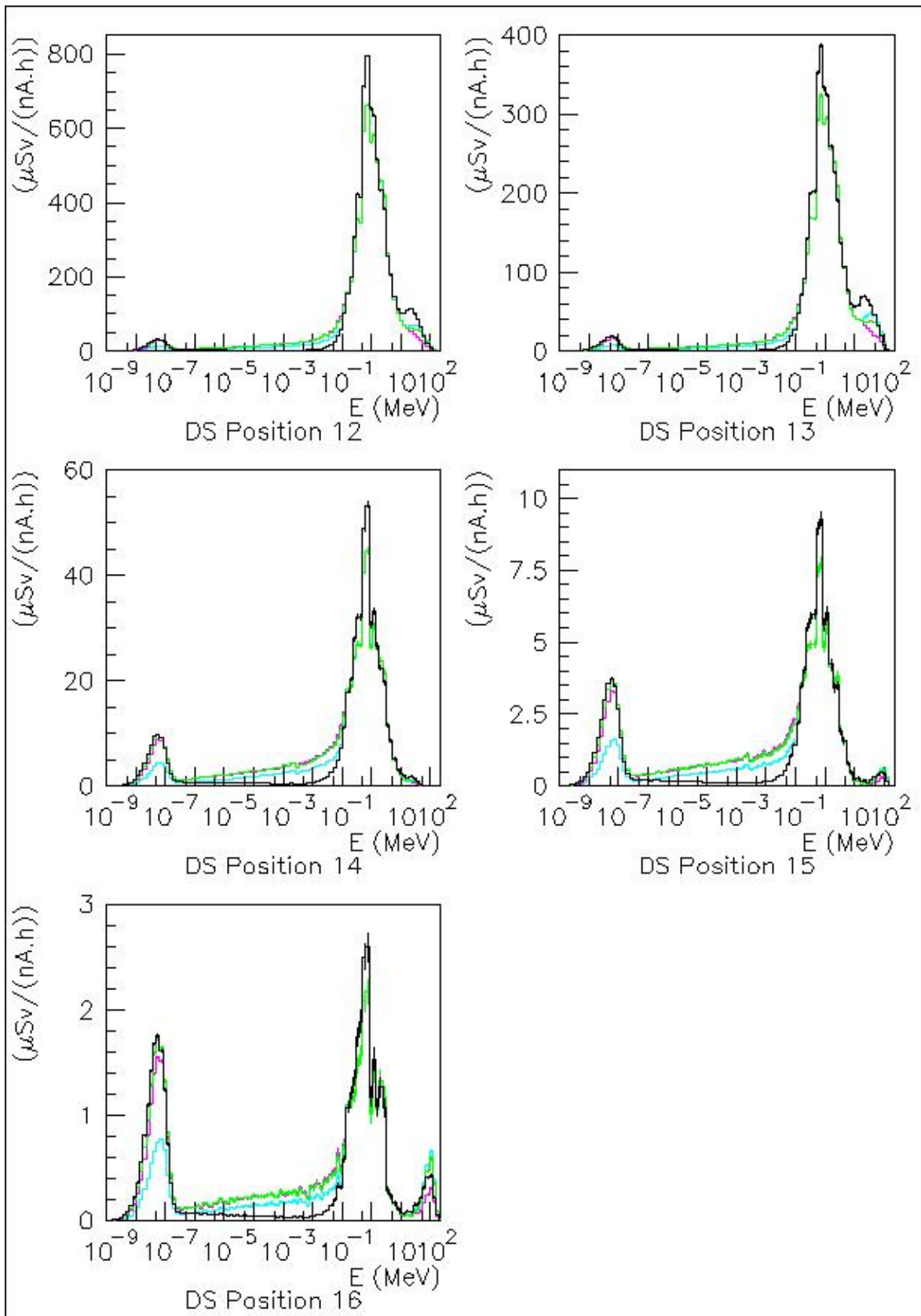
Figure III-31 - For positions inside the maze of the gantry treatment room operated in DS (with gantry ring): neutron H*(10) spectra (in black) and WENDI-2 spectra based on the GEANT4 9.6 BIC response function (in green), the FLUKA response function (in cyan) and the response function of Olsher et al. based on experimental data above 46 MeV (in pink).
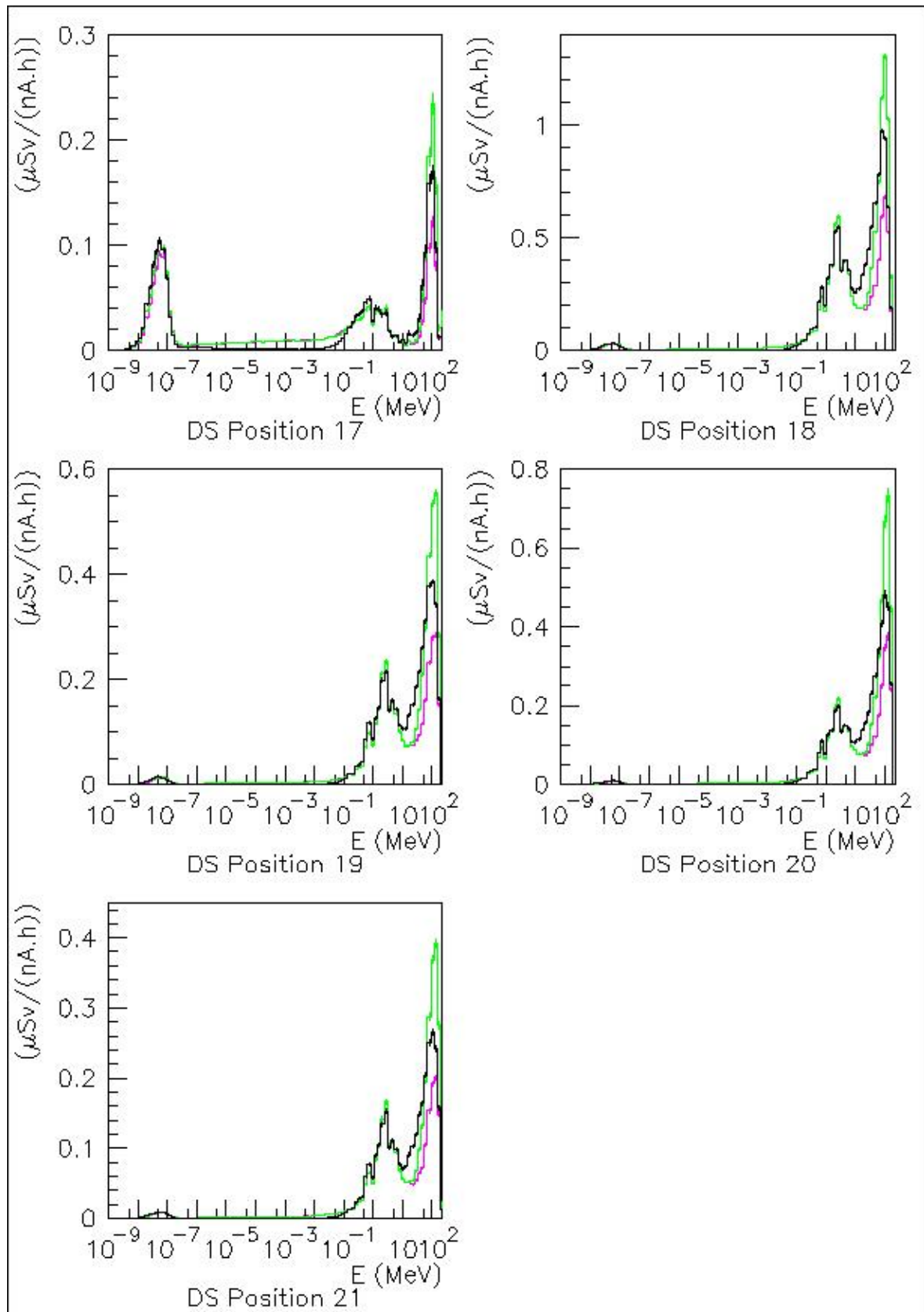
Figure III-32 - For positions outside the gantry treatment room operated in DS (with gantry ring): neutron H*(10) spectra (in black) and WENDI-2 spectra based on the GEANT4 9.6 BIC response function (in green) and the response function of Olsher et al. based on experimental data above 46 MeV (in pink).

Unlike in the maze, the neutron fluences in positions located in the control room are not increased by using DS instead of PBS (see positions 18 and 19 in figure **III-30** *vs.* positions 8 and 9 in figure **III-23**, considering the simulations <u>with</u> the gantry ring). The total neutron fluences are very similar in both cases, because they mainly depend on the production of the high-energy neutrons inside the treatment room. In fact, the multiplicity for high-energy neutrons does not increase that much with the atomic number of the proton target [238]. Moreover, as a compensating effect, a part of the high-energy neutron fluence in the DS case is also produced at a somewhat larger distance from the control room: the nozzle elements are indeed further removed from positions 8 and 9 than the water phantom (see figure **III-6**).

Concerning the positions inside the adjacent treatment room, it should be remembered that these are not situated at the same heights in the PBS and DS irradiations: positions 10 and 11 (PBS) are at ~1 m above the floor, whereas positions 20 and 21 (DS) are right on the floor. The total neutron fluence in position 20 (DS) is about 1.4 times larger than in position 10 (PBS). The difference is in this case mostly due to the fact that position 10 (at ~1 m height) is shielded by the gantry counterweight, whereas position 20 (on the floor) is not. As for the positions located closer to the proton beam axis, the total neutron fluence in position 21 (DS) is about two times smaller than in position 11 (PBS). That might be related to the fact that, in the DS irradiation, high-energy neutrons produced in the First Scatterer and the Range Modulator are attenuated by the scanning magnets of the nozzle.

With the DS irradiation, the influence of the gantry front ring is also a bit different than for the PBS case. Inside the maze, the inclusion of the gantry front ring mainly causes a small fluence decrease, mostly visible in the spectra at the level of neutrons above ~1 MeV (see figure **III-29**). A part of the gantry ring indeed intercepts neutrons that are produced in the First Scatterer and the Range Modulator and are emitted towards the entrance of the maze. From that point of view, the iron ring plays an attenuating role, via inelastic scattering (threshold in iron: 847 keV) and non-elastic interactions of high-energy neutrons. In Position 12, one can however notice a small increase in the fluence of intermediate and evaporation neutrons up to ~847 keV. This resembles the "backscattering" role of the ring observed in the PBS case, which is essentially caused by elastic scattering. In the DS case, however, the attenuating role globally exceeds the backscattering role, so that the presence of the gantry ring results in a slight decrease of the total neutron fluence in the maze. As shown in table **III-10**, H*(10) inside the maze is reduced by 9-14% due to the inclusion of the gantry front ring (positions 12 – 16).

As in the PBS case, the most important impact of the gantry front ring is observed in one position inside the control room: position 19. High-energy neutrons emitted from the water phantom towards position 19 have to travel through the ring. The effect of the ring is however much less pronounced than in the PBS case, because high-energy neutrons are also emitted from the nozzle elements and these neutrons

can reach position 19 without crossing the ring. H*(10) in position 19 is therefore "only" reduced by a factor of 1.36 (*vs.* a factor of ~2 in position 9 of the PBS case). The other positions in the control room and the adjacent treatment room are not significantly affected by the presence of the gantry front ring, like in the PBS case.
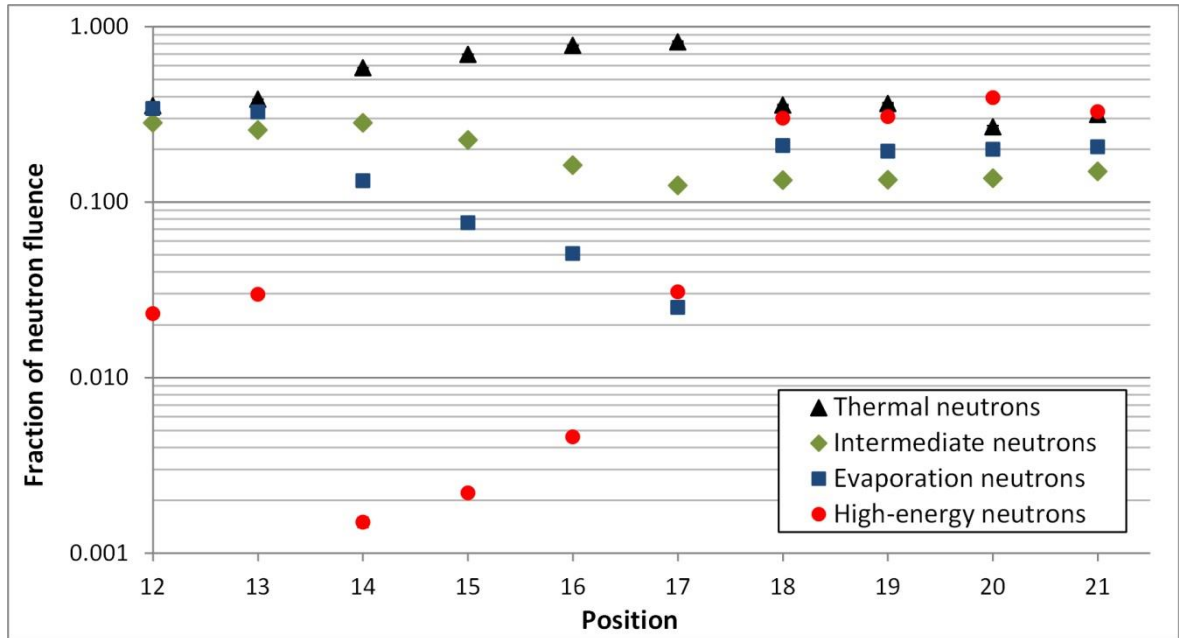
Figure III-33 - Fractions of the simulated neutron fluence that are due to 'thermal', 'intermediate', 'evaporation' and 'high-energy' neutrons, in the positions inside and around the gantry room operated in DS (simulation with gantry front ring).
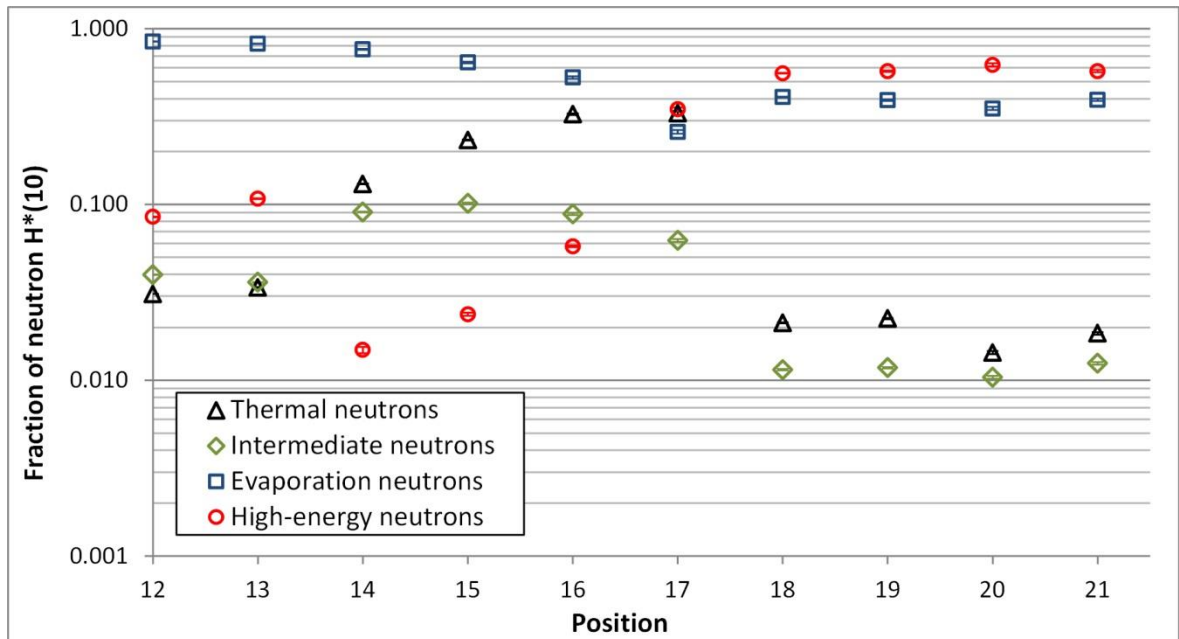
Figure III-34 - Fractions of the simulated neutron H(10) that are due to 'thermal', 'intermediate', 'evaporation' and 'high-energy' neutrons, in the positions inside and around the gantry room operated in DS (simulation with gantry front ring).*

Table III-10 - Neutron H*(10) obtained in the DS simulations, without and with the gantry front ring. The results are expressed in µSv/(nA.h), where the nA.h refer to the proton charge delivered at the nozzle entrance. The given uncertainties are the MCNPX statistical uncertainties (1σ).

Position	H*(10) [µSv/(nA.h)] without gantry ring	H*(10) [µSv/nA.h] with gantry ring	$\dfrac{H^*(10)_{with\ ring}}{H^*(10)_{without\ ring}}$
12	2228 ± 2	2020 ± 2	0.907 ± 0.001
13	1188 ± 2	1035 ± 2	0.872 ± 0.002
14	160.3 ± 0.5	138.6 ± 0.5	0.865 ± 0.004
15	33.8 ± 0.2	29.6 ± 0.2	0.877 ± 0.007
16	10.9 ± 0.1	9.9 ± 0.1	0.90 ± 0.01
17	0.57 ± 0.02	0.52 ± 0.01	0.91 ± 0.02
18	2.87 ± 0.01	2.88 ± 0.02	1.01 ± 0.01
19	1.66 ± 0.02	1.20 ± 0.01	0.72 ± 0.01
20	1.26 ± 0.04	1.27 ± 0.04	1.01 ± 0.03
21	0.82 ± 0.02	0.83 ± 0.03	1.00 ± 0.03

From the figures **III-33** and **III-34**, it appears that:

- In most positions (all except 12 and 20), the thermal neutrons constitute the largest fraction of the fluence, but do not cause dominant H*(10) contributions.

- Inside the maze (positions 12 – 16), the largest contribution to H*(10) is due to the evaporation neutrons (~50-85%). At the beginning of the maze, this H*(10) fraction is a bit larger than in the PBS case. The relative contribution from high-energy neutrons is relatively small throughout the entire maze (2-11%).

- Starting from position 14, after the first maze corner, the fluence fraction of high-energy neutrons keeps increasing along the maze, but does not exceed that of the evaporation neutrons until outside the treatment room, as in the PBS case. However, the fraction of high-energy neutrons is smaller compared to the PBS irradiation.

- Outside the treatment room, the high-energy neutrons represent ~35-60% of H*(10) and the evaporation neutrons ~25-40%, which is quite similar to the PBS case.

For the DS irradiation, the WENDI-2 responses simulated using the response functions of figure **III-9** (p. **126**) are given in table **III-11.** The percent deviation of these simulated WENDI-2 responses with respect to the simulated H*(10) is shown in figure **III-35**. The results are similar to those of figure **III-28** for the PBS case. Small differences with the PBS case can be noticed essentially inside the maze (positions 12 – 16) and behind inside the maze door (position 17). These are a logical consequence of the small differences in the energy spectra already discussed in this section.

Table III-11 - Simulated WENDI-2 responses obtained in the DS simulation (with gantry ring), using the different versions of the response function shown in figure III-9. The results are expressed in µSv/(nA.h), where the nA.h refer to the proton charge delivered at the nozzle entrance. The given uncertainties are the MCNPX statistical uncertainties (1σ).

Position	MCNPX 2.7.0 Bertini & Dresner	GEANT4 9.6 Bertini	GEANT4 9.6 BIC	FLUKA	MCNP4B + HE QMN Olsher et al.
12	1955 ± 2	2032 ± 2	2014 ± 2	1902 ± 2	1988 ± 2
13	991 ± 2	1032 ± 2	1019 ± 2	968 ± 2	999.4 ± 2
14	146.8 ± 0.4	160.8 ± 0.4	160.6 ± 0.4	135.3 ± 0.4	159.2 ± 0.4
15	31.6 ± 0.2	35.8 ± 0.2	35.6 ± 0.2	28.2 ± 0.2	34.8 ± 0.2
16	10.1 ± 0.1	11.8 ± 0.1	11.6 ± 0.1	8.8 ± 0.1	11.0 ± 0.1
17	0.51 ± 0.01	0.68 ± 0.01	0.62 ± 0.01	0.51 ± 0.01	0.50 ± 0.01
18	3.09 ± 0.02	3.42 ± 0.02	2.94 ± 0.02	3.07 ± 0.02	2.26 ± 0.01
19	1.32 ± 0.01	1.47 ± 0.02	1.25 ± 0.01	1.31 ± 0.01	0.94 ± 0.01
20	1.46 ± 0.04	1.64 ± 0.04	1.37 ± 0.03	1.44 ± 0.04	0.99± 0.03
21	0.94 ± 0.03	1.04 ± 0.03	0.88 ± 0.03	0.92 ± 0.03	0.66 ± 0.02
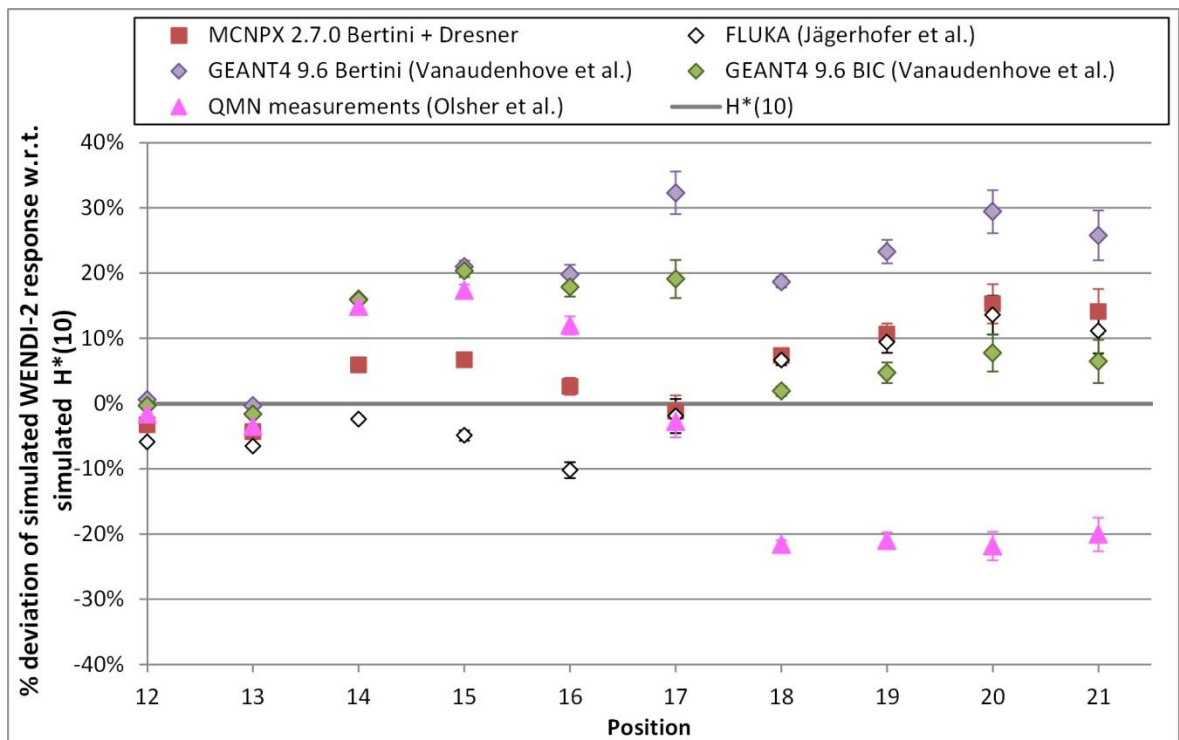
Figure III-35 – Percent deviation of the WENDI-2 response with respect to the neutron H*(10) obtained in the DS simulation with gantry ring. The WENDI-2 response was calculated using the different versions of the response function shown in figure III-9. The uncertainty bars represent the MCNPX statistical uncertainties (1σ).

Table **III-12** shows the results for the average simulated WENDI-2 response $R_{sim,avg}$ and its total uncertainty σ_{tot}, which is based on the uncertainties listed in table **III-13**. As in the previous cases, $R_{sim,avg}$ outside the room is very similar to the BIC-based response. The total relative uncertainty on $R_{sim,avg}$ is of 4-10 % depending on the positions. As in the PBS case, the largest contribution comes from the uncertainties on the response function below 0.144 MeV and above 19 MeV, except for the two first positions in the maze.

Table III-12 – Average WENDI-2 response $R_{sim,avg}$ and its total uncertainty σ_{tot} in the simulation of the gantry room operated in DS.

Position	$R_{sim,avg}$ [μSv/(nA.h)]	σ_{tot} [μSv/(nA.h)]	$\dfrac{\sigma_{tot}}{R_{sim,avg}} x\ 100\%$
12	1.98×10^3	0.08×10^3	4%
13	1.00×10^3	0.04×10^3	4%
14	1.53×10^2	0.08×10^2	5%
15	3.3×10^1	0.2×10^1	6%
16	1.07×10^1	0.07×10^1	6%
17	5.6×10^{-1}	0.4×10^{-1}	8%
18	3.0×10^0	0.2×10^0	8%
19	1.3×10^0	0.1×10^0	9%
20	1.4×10^0	0.1×10^0	10%
21	8.9×10^{-1}	0.8×10^{-1}	9%

Table III-13 – Uncertainties on the average WENDI-2 response in the simulation of the gantry room operated in DS: the average MCNPX statistical uncertainty σ_{stat}, the systematic uncertainty σ_{exp} representing 5% of the contribution of 0.144 MeV – 19 MeV neutrons to the simulated WENDI-2 response, and the systematic uncertainty $\sigma_{resp.fct.}$ caused by the uncertainties on the WENDI-2 response function below 0.144 MeV and above 19 MeV.

Position	σ_{stat} [μSv/(nA.h)]	σ_{exp} [μSv/(nA.h)]	$\sigma_{resp.fct.}$ [μSv/(nA.h)]
12	2.0×10^0	8.0×10^1	2.5×10^1
13	1.6×10^0	4.0×10^1	1.1×10^1
14	4.4×10^{-1}	4.9×10^0	5.7×10^0
15	1.7×10^{-1}	8.7×10^{-1}	1.7×10^0
16	1.0×10^{-1}	2.4×10^{-1}	6.1×10^{-1}
17	1.3×10^{-2}	6.4×10^{-3}	4.0×10^{-2}
18	1.6×10^{-2}	6.1×10^{-2}	2.3×10^{-1}
19	1.4×10^{-2}	2.4×10^{-2}	1.1×10^{-1}
20	3.5×10^{-2}	2.3×10^{-2}	1.3×10^{-1}
21	2.5×10^{-2}	1.7×10^{-2}	7.6×10^{-2}

III-3.4 Fixed-beam treatment room

The neutron fluence spectra simulated for the Fixed-Beam Treatment Room (FBTR) are shown in the figures **III-36** and **III-37**. The corresponding H*(10) spectra are shown in black in the figures **III-38** and **III-39**. The fluence and H*(10) fractions of thermal, intermediate, evaporation and high-energy neutrons are subsequently compared in the figures **III-40** and **III-41**.

The fluence spectrum of position 1b, located inside the treatment room at a small angle with respect to the proton beam axis, is characterised by a large high-energy peak because the emission of high-energy neutrons during intranuclear cascades is strongly forward-peaked (see figure **III-36**). In fact, the size of this peak quickly drops as the angle to the proton beam axis increases, as can be noticed in positions 1c (at ∼60°) and 1a (at ∼90°). The maximum of the high-energy peak also tends to progressively shift towards lower energies (starting from $E_{max} > 100$ MeV in 1c, to $E_{max} \approx 25$ MeV in 1a).

The evolution of the spectra along the maze (1c – 1g), is as expected very similar to the ones obtained in the two previous case-studies of the gantry treatment room. In terms of shape, the spectra at the beginning of the maze (1c – 1d) are more similar to those of the PBS case (see figure **III-22**; positions 1 – 2), because no scattering elements of the nozzle were used to shape the proton field in this US irradiation. The larger fraction of high-energy neutrons in position 1c, compared to PBS Position 1, is however related to (1) the smaller angle of 1c with respect to the proton beam axis and (2) the absence of an iron gantry which increases the fraction of backscattered neutrons in the PBS study.

The positions 2a – 2c – 2b located in the technical room are comparable to the positions 8 – 11 in the PBS study, because they are shielded by a concrete wall of ∼2 m in thickness and are located at angles smaller than ∼45° from the proton beam axis. Unlike in the PBS case, however, there are no solid structures – such as parts of a gantry – between the water phantom and this shielding wall, which is thus a simpler case to model. The fluence in positions 2a – 2c – 2b should for instance essentially depend on (1) the fluence of high-energy neutrons emitted from the water phantom towards the considered position, (2) the distance from the water phantom to the concrete wall along this direction, and (3) the concrete thickness along this direction.

As explained in section **III-2.1.4**, the assumption was made that equipment of the eye treatment line does not interfere significantly with the high-energy neutron flux emitted in the direction of position 2d. Since no solid elements were modelled around the water phantom, the simulated fluence spectrum in 2d will also mainly depend on the three abovementioned parameters.
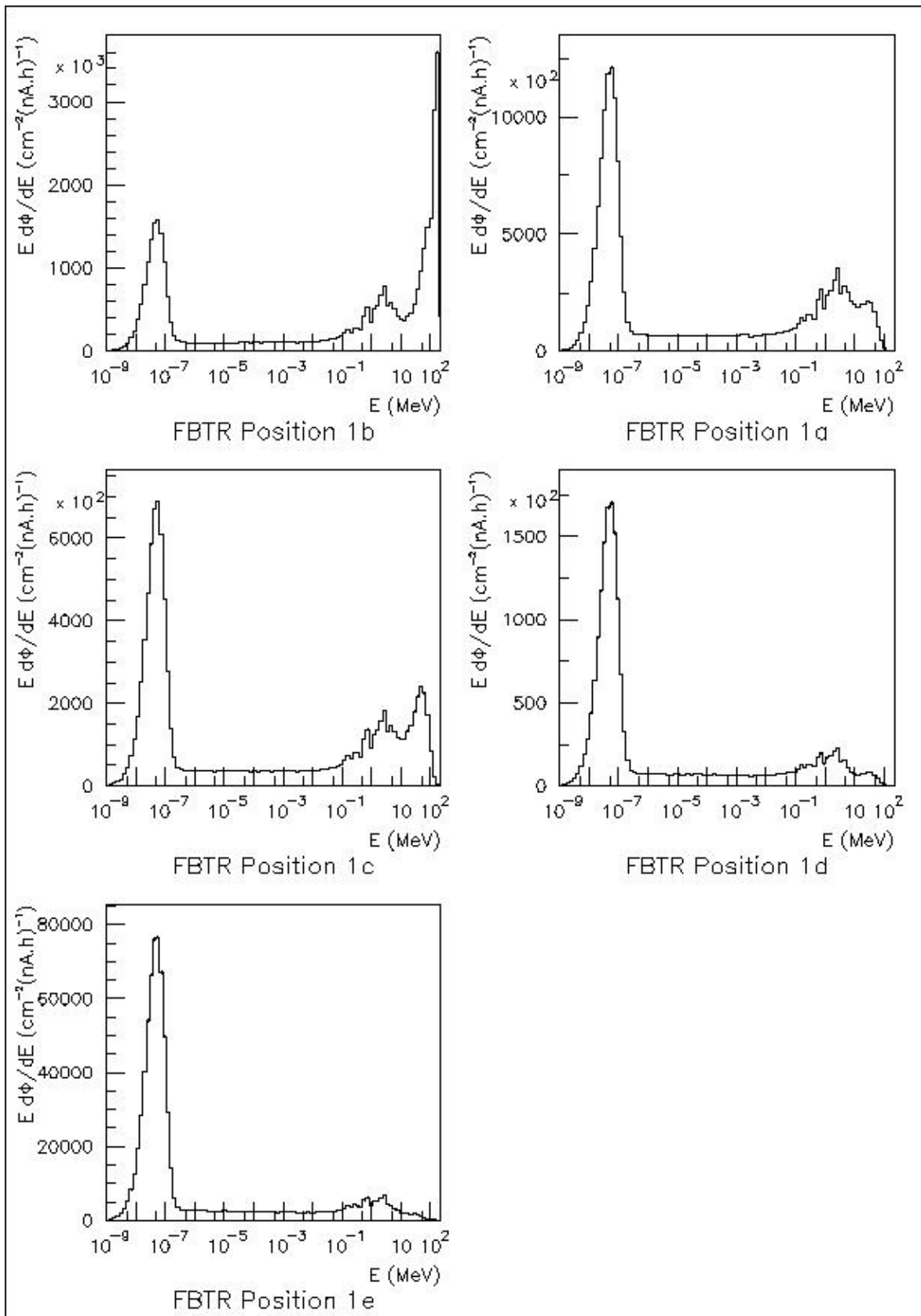
Figure III-36 - Neutron fluence spectra simulated inside the fixed-beam treatment room (positions 1a – 1e).
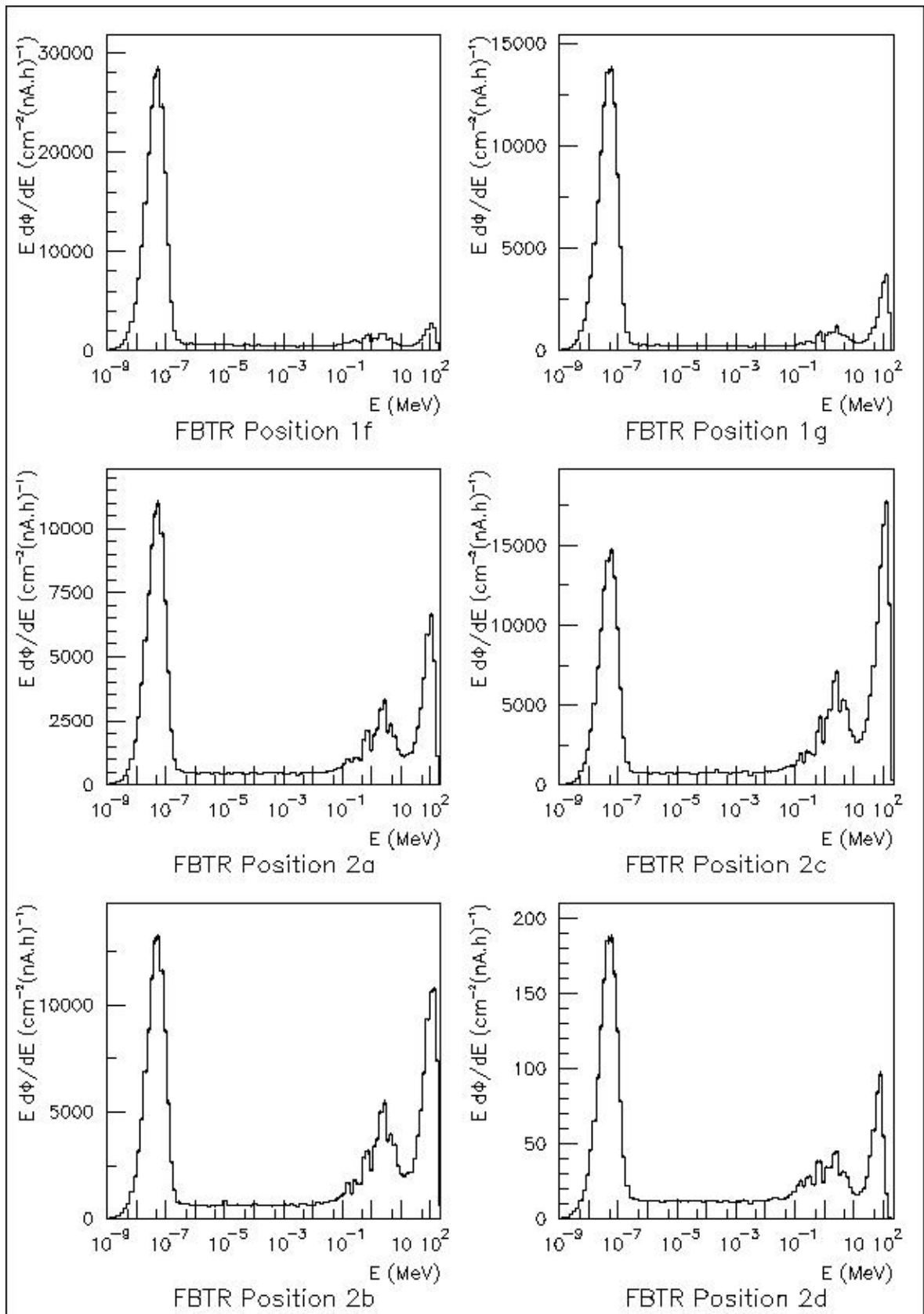
Figure III-37 - Neutron fluence spectra simulated in the maze of the fixed-beam treatment room (positions 1f, 1g), in the technical room (positions 2a, 2b, 2c). and in the adjacent treatment room (position 2d).
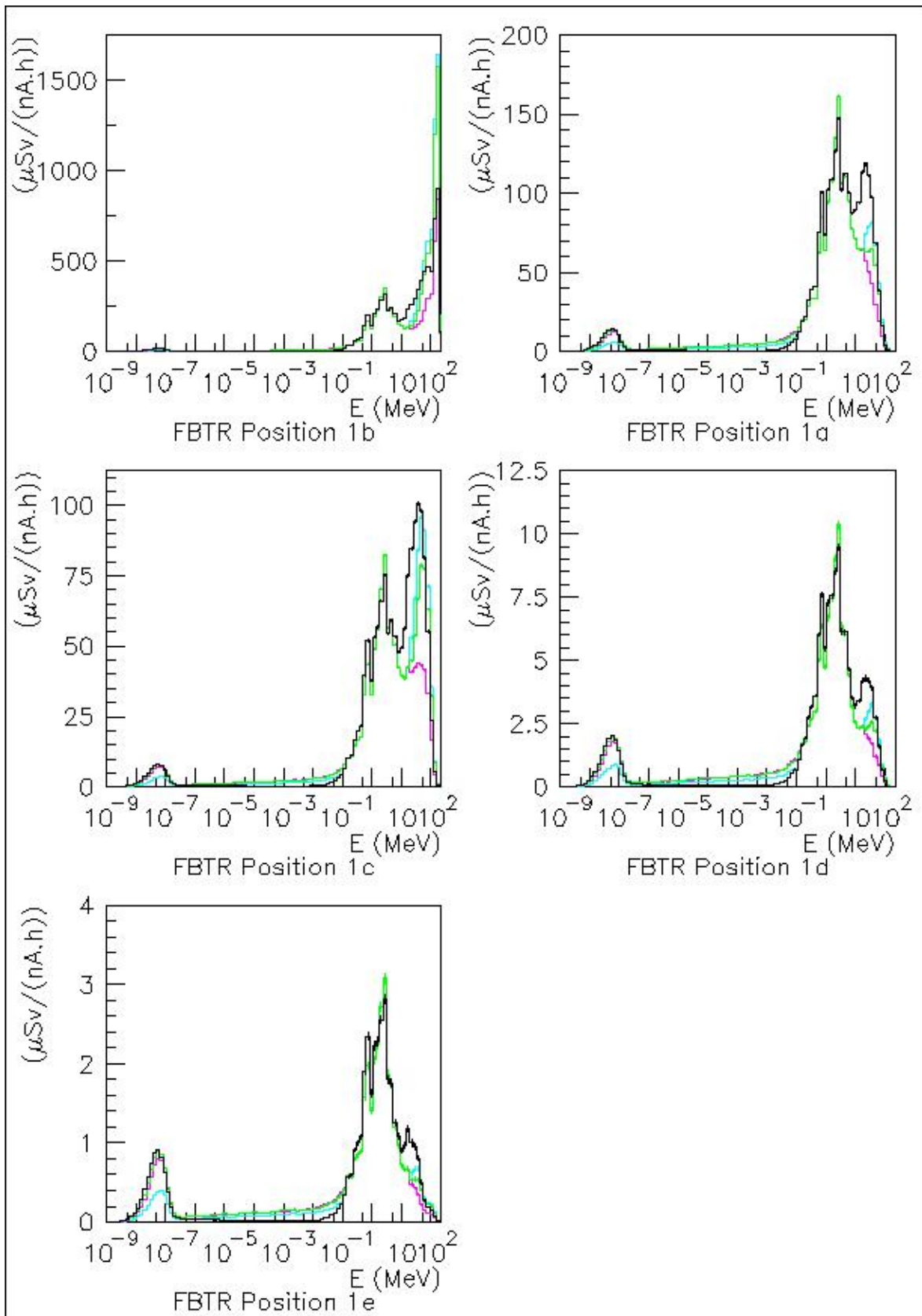
Figure III-38 - For positions 1a – 1e inside the fixed-beam treatment room: neutron H*(10) spectra (in black) and WENDI-2 spectra based on the GEANT4 9.6 BIC response function (in green), the FLUKA response function (in cyan) and the response function of Olsher et al. based on experimental data above 46 MeV (in pink).
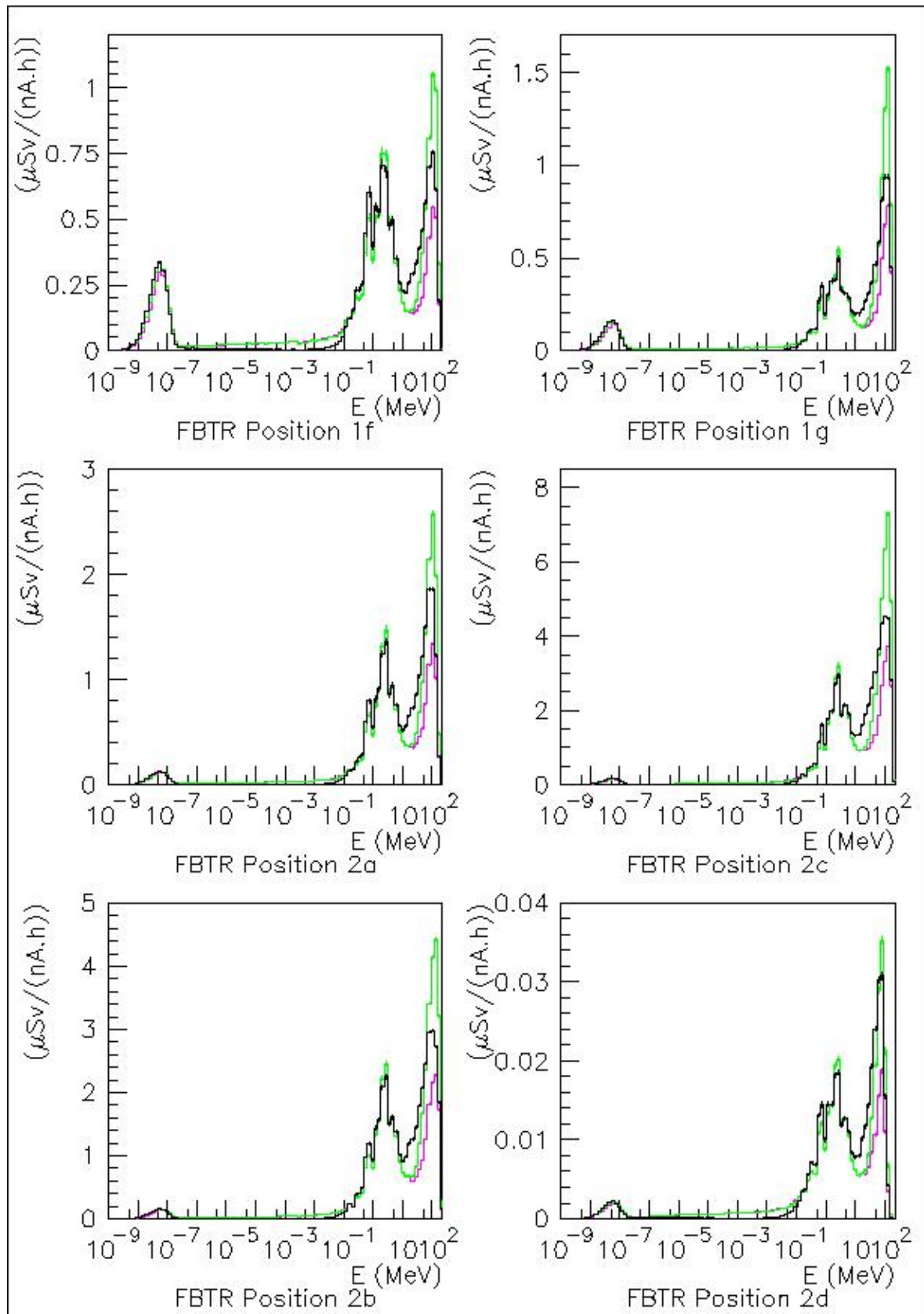
Figure III-39 - For positions 1f – 2d around the fixed-beam treatment room: neutron H*(10) spectra (in black) and WENDI-2 spectra based on the GEANT4 9.6 BIC response function (in green) and the response function of Olsher et al. based on experimental data above 46 MeV (in pink).
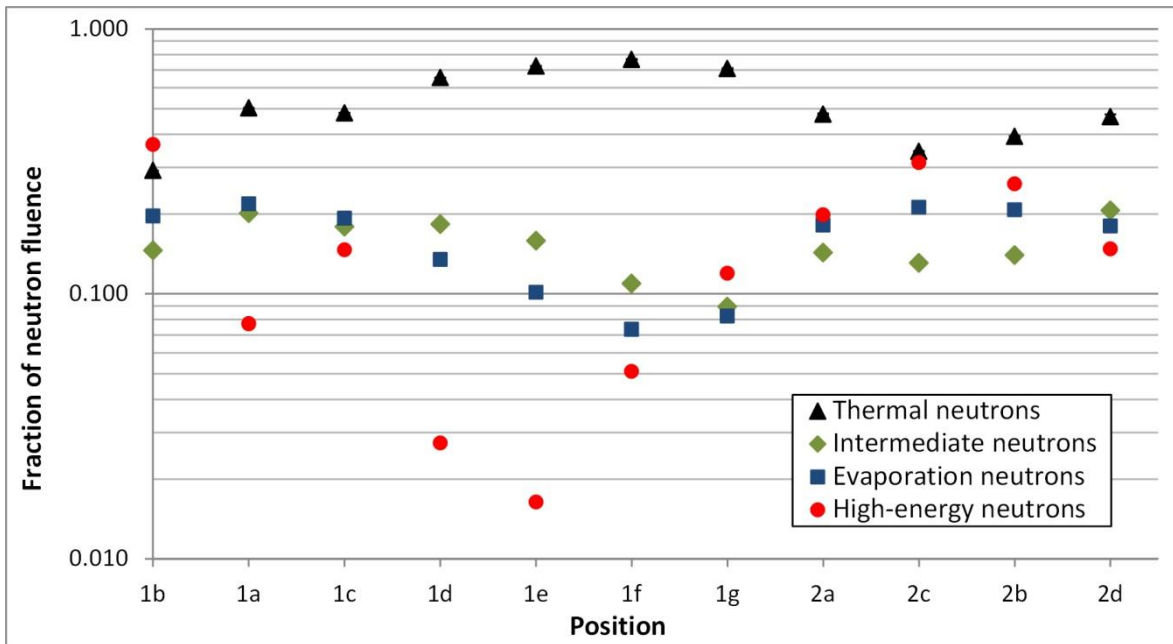
Figure III-40 - Fractions of the simulated neutron fluence that are due to 'thermal', 'intermediate', 'evaporation' and 'high-energy' neutrons, in the positions inside and around the fixed-beam treatment room.
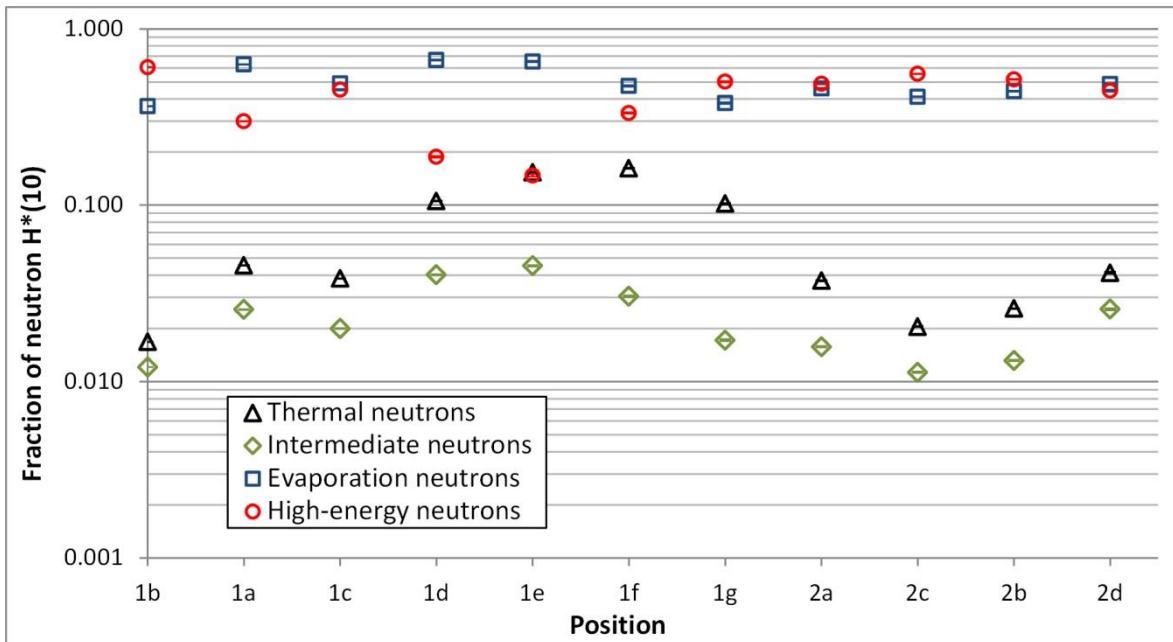
Figure III-41 - Fractions of the simulated neutron H*(10) that are due to 'thermal', 'intermediate', 'evaporation' and 'high-energy' neutrons, in the positions inside and around the fixed-beam treatment room.

The figures **III-40** and **III-41** show that:

- In all positions except 1b, the thermal neutrons constitute the largest fraction of the fluence, but do not cause dominant H*(10) contributions.

- Position 1b in front of the water phantom has the largest fraction of high-energy neutrons: 37% of the total fluence, also representing 61% of the total H*(10).

- As in the other case-studies, the largest contribution to H*(10) inside the maze is due to the evaporation neutrons (~45-65%). Position 1g is an exception, where the relative contribution from high-energy neutrons exceeds that of the evaporation neutrons.

- In the technical room (2a – 2c – 2b) and the adjacent gantry room (2d), the high-energy neutrons represent ~45-55% of H*(10) and the evaporation neutrons ~40-45%.

The total neutron H*(10) is given in table **III-14**. For positions in the technical room, it can be noted that the largest H*(10) was obtained in 2c, even though this position is situated at a larger angle from the proton beam axis than 2b. This is due to the smaller distance of 2c with respect to the water phantom and the smaller concrete thickness along the corresponding line of sight (see table **III-15**).

Table III-14 - Neutron H(10) obtained in the simulation of the fixed-beam treatment room. The results are expressed in µSv/(nA.h), where the nA.h refer to the proton charge delivered to the water phantom. The given uncertainties are the MCNPX statistical uncertainties (1σ).*

Position	H*(10) [µSv/(nA.h)]	Position	H*(10) [µSv/(nA.h)]
1b	2054 ± 1	2a	6.28 ± 0.03
1a	578.2 ± 0.6	2c	15.24 ± 0.04
1c	388.9 ± 0.5	2b	10.98 ± 0.03
1d	35.1 ± 0.1	2d	0.099 ± 0.001
1e	10.78 ± 0.05		
1f	3.74 ± 0.02		
1g	2.89 ± 0.02		

Table III-15 – Characteristics of positions 2a – 2c – 2b in the technical room and position 2d in the adjacent gantry room.

Position	2a	2c	2b	2d
Angle to the proton beam axis, measured w.r.t. isocentre	~40°	~15°	~5°	~90°
Distance from centre of water phantom to concrete wall, along line of sight [m]	4.9	4.9	5.4	5.9
Concrete thickness along line of sight [m]	2.0	2.0	2.2	≳ 2.5

The WENDI-2 responses simulated using the response functions of figure **III-9** (p. **126**) are given in table **III-16.** The percent deviation of these simulated WENDI-2 responses with respect to the simulated H*(10) is shown in figure **III-42**.

In Position 1b, in front of the water phantom, the discrepancies between the different versions of the simulated WENDI-2 response are comparable to those obtained in positions located behind the 2m thick shielding walls (1g, 2a,2c,2b, 2d), because of the comparable fraction of high-energy neutrons. On the whole, the results for the positions in the maze and behind the shielding walls are very similar to those of figure **III-28** for the PBS case. Position 1c at the entrance of the maze contains however a larger fraction of high-energy neutrons compared to PBS Position 1, which leads to a somewhat larger uncertainty in the simulated WENDI-2 response. Position 1a is in fact more similar to PBS Position 1 in this case, because their angles with respect to the proton beam axis are more alike.

Table **III-17** shows the results for the average simulated WENDI-2 response $R_{sim,avg}$ and its total uncertainty σ_{tot}. The uncertainties included in the calculation of σ_{tot} are listed in table **III-18**. $R_{sim,avg}$ behind the shielding walls is obviously very similar to the BIC-based response, as in the PBS case. The total relative uncertainty on $R_{sim,avg}$ is of 4 – 9 %. In most positions, the largest contribution to this uncertainty is due to the uncertainties on the response function below 0.144 MeV and above 19 MeV. The exceptions are positions 1a, 1d and 1e, where the uncertainty on the response to evaporation neutrons is larger.

Table III-16 - Simulated WENDI-2 responses obtained in the simulation of the fixed-beam treatment room, using the different versions of the response function shown in figure III-9. The results are expressed in µSv/(nA.h), where the nA.h refer to the proton charge delivered to the phantom. The given uncertainties are the MCNPX statistical uncertainties (1σ).

Position	MCNPX 2.7.0 Bertini & Dresner	GEANT4 9.6 Bertini	GEANT4 9.6 BIC	FLUKA	MCNP4B + HE QMN Olsher et al.
1b	2460 ± 1	2758 ± 2	2289 ± 1	2385 ± 1	1667 ± 1
1a	530.8 ± 0.5	555.0 ± 0.5	537.4 ± 0.5	521.8 ± 0.5	510.8 ± 0.5
1c	373.3 ± 0.4	382.7 ± 0.5	354.7 ± 0.4	358.3 ± 0.5	312.2 ± 0.4
1d	33.2 ± 0.1	35.9 ± 0.1	35.2 ± 0.1	32.1 ± 0.1	33.9 ± 0.1
1e	10.28 ± 0.05	11.28 ± 0.05	11.11 ± 0.05	9.75 ± 0.05	10.71 ± 0.05
1f	3.88 ± 0.02	4.37 ± 0.02	3.98 ± 0.02	3.67 ± 0.02	3.38 ± 0.02
1g	3.25 ± 0.02	3.68 ± 0.02	3.15 ± 0.02	3.11 ± 0.02	2.41 ± 0.02
2a	6.67 ± 0.03	7.35 ± 0.03	6.44 ± 0.03	6.59 ± 0.02	5.14 ± 0.02
2c	17.10 ± 0.04	18.99 ± 0.04	16.14 ± 0.04	16.83 ± 0.04	12.24 ± 0.03
2b	12.13 ± 0.03	13.41 ± 0.03	11.55 ± 0.03	11.93 ± 0.03	8.98 ± 0.03
2d	0.099 ± 0.001	0.108 ± 0.001	0.098 ± 0.001	0.098 ± 0.001	0.082 ± 0.001
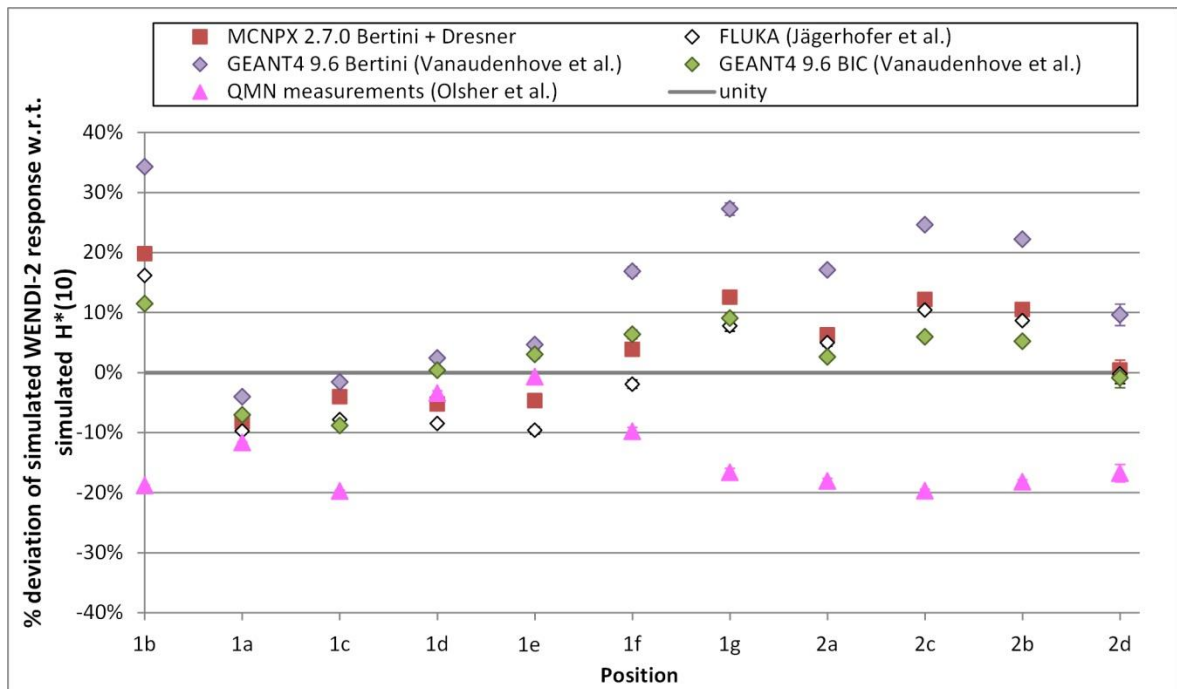
Figure III-42 – Percent deviation of the WENDI-2 response with respect to the neutron H*(10) obtained in the simulation of the fixed-beam treatment room. The WENDI-2 response was calculated using the different versions of the response function shown in figure III-9. The uncertainty bars represent the MCNPX statistical uncertainties (1σ).

Table III-17 – Average WENDI-2 response $R_{sim,avg}$ and its total uncertainty σ_{tot} in the fixed-beam treatment room simulation.

Position	$R_{sim,avg}$ [μSv/(nA.h)]	σ_{tot} [μSv/(nA.h)]	$\dfrac{\sigma_{tot}}{R_{sim,avg}} x\ 100\%$
1b	2.3×10^3	0.2×10^3	9%
1a	5.3×10^2	0.2×10^2	4%
1c	3.6×10^2	0.2×10^2	5%
1d	3.4×10^1	0.1×10^1	4%
1e	1.06×10^1	0.05×10^1	4%
1f	3.9×10^0	0.2×10^0	5%
1g	3.1×10^0	0.2×10^0	8%
2a	6.4×10^0	0.5×10^0	7%
2c	1.6×10^1	0.1×10^1	8%
2b	1.16×10^1	0.09×10^1	8%
2d	9.7×10^{-2}	0.6×10^{-2}	6%

Table III-18 – Uncertainties on the average WENDI-2 response in the fixed-beam treatment room simulation: the average MCNPX statistical uncertainty σ_{stat}, the systematic uncertainty σ_{exp} representing 5% of the contribution of 0.144 MeV – 19 MeV neutrons to the simulated WENDI-2 response, and the systematic uncertainty $\sigma_{resp.fct.}$ caused by the uncertainties on the WENDI-2 response function below 0.144 MeV and above 19 MeV.

Position	σ_{stat} [μSv/(nA.h)]	σ_{exp} [μSv/(nA.h)]	$\sigma_{resp.fct.}$ [μSv/(nA.h)]
1b	1.3×10^0	3.9×10^1	2.1×10^2
1a	5.4×10^{-1}	1.9×10^1	7.9×10^0
1c	4.4×10^{-1}	1.0×10^1	1.5×10^1
1d	1.0×10^{-1}	1.2×10^0	6.6×10^{-1}
1e	4.7×10^{-2}	3.5×10^{-1}	2.9×10^{-1}
1f	2.0×10^{-2}	8.8×10^{-2}	1.7×10^{-1}
1g	1.9×10^{-2}	5.6×10^{-2}	2.4×10^{-1}
2a	2.5×10^{-2}	1.5×10^{-1}	4.3×10^{-1}
2c	3.7×10^{-2}	3.3×10^{-1}	1.3×10^0
2b	3.3×10^{-2}	2.5×10^{-1}	8.7×10^{-1}
2d	1.3×10^{-3}	2.4×10^{-3}	5.0×10^{-3}

III-4 Conclusion

Monte Carlo simulations were carried out with MCNPX 2.7.0 to compute neutron fluence spectra inside and around four different rooms of the proton therapy facility of Essen: the cyclotron room, a gantry room operated in PBS, a gantry room operated in DS and the fixed-beam treatment room operated in US. In these simulations, the same conservative choices were made as in the original shielding design simulations for this facility:

- the MCNPX physics model selected for the intranuclear cascade was the one that leads to the highest neutron doses at forward angles, namely the Bertini model;

- the concrete density was set to 2.30 g/cm^3, a slightly lower value than the minimum density which was officially requested to the concrete provider when building the Essen facility: 2.35 g/cm^3.

No specific information was available on the average elemental composition of the concrete used at Essen, so a standard composition defined by the NIST for ordinary 'Portland' concrete was selected, like in the original shielding design simulations.

With the abovementioned assumptions, one expects that the simulated neutron doses will overestimate the true neutron doses behind the shielding walls, which would confirm that this methodology provided a legitimate basis for the shielding design. It will be the goal of our next chapter to verify this, by comparing our simulation results to on-site neutron dose measurements performed with a WENDI-2.

Since most ambient neutron dosimeters in use today – the WENDI-2 included – were designed to measure the operational quantity H*(10), our simulated neutron spectra were folded with the appropriate conversion coefficients of ICRP Publication 74 to compute H*(10) at the positions of interest.

However, as we explained in the previous chapter, the WENDI-2 does not possess an ideal response function and caution should be taken when using the detector in neutron fields with energy distributions that differ strongly from the ^{252}Cf calibration spectrum. Therefore, an attempt was made in this chapter to predict the response of the WENDI-2 at the positions of interest, in order to verify its agreement with H*(10). Because large uncertainties exist on the WENDI-2 response function at thermal energies and above 20 MeV, a systematic study was carried out in which the neutron spectra were folded with five different versions of the WENDI-2 response function presented in Chapter II. From these results, an average WENDI-2 response and its total uncertainty was determined for each position.

The discrepancies between the five versions of the simulated WENDI-2 response were evidently the largest in positions characterised by:

- a large fluence fraction of high-energy neutrons, such as the FBTR Position 1b in front of the water phantom and positions located in adjacent rooms, and/or

- a large fluence fraction of thermal neutrons, such as positions located near the maze door of treatment rooms or, similarly, Position 7 in the middle of the cyclotron maze.

In such positions, all simulated WENDI-2 responses regardless of the used response function agreed with H*(10) within at most 30-35 %.

The smallest discrepancies between different versions of the simulated WENDI-2 response were obtained in positions where the contribution of evaporation neutrons strongly dominates the response. These are positions located inside the room at ~90° or more from the proton beam axis, e.g. at the beginning of the maze in the gantry rooms and the cyclotron room, or in the FBTR Position 1a. In these positions, the simulated WENDI-2 responses agree with H*(10) within 10-15 %.

Our simulation results in general thus suggest that, in spite of its imperfect response function, the WENDI-2 is indeed relatively well-suited for performing H*(10) measurements inside proton therapy facilities.

Nevertheless, because the uncertainties on the simulated WENDI-2 response are non-negligible, the on-site measurements in Chapter IV will not be compared directly to the simulated H*(10) but rather to the average simulated WENDI-2 responses and their estimated uncertainty (4% – 11% at 1σ).

CHAPTER IV
WENDI-2 measurements in the proton therapy facility of Essen

IV-1 Introduction

This chapter describes the neutron measurements performed with a WENDI-2 inside and around four rooms of the proton therapy facility of Essen. A comparison will be made with the corresponding simulation results from Chapter III.

The MCNPX simulations described in Chapter III were made following the methodology used in the original shielding design simulations for this facility. As previously explained, this methodology involves conservative choices regarding the defined concrete density and the selected physics models (conservative at forward angles). The simulated neutron doses behind the shielding walls are therefore expected to overestimate the measurements. An important goal of this chapter will be to verify this expected conservative nature of the simulations.

IV-2 Experimental set-up

IV-2.1 Cyclotron room

In February 2012, a series of WENDI-2 measurements was carried out at the Essen facility in the access maze and behind the vault door of the cyclotron room, as well as in the main control room (see positions indicated in figure **III-1** on p. **117**). The WENDI-2 was placed on a trolley at ~1m above the floor, except in the positions outside the cyclotron room (1 – 3) where the device stood directly on the floor.

The proton beam was extracted from the cyclotron at an intensity of 300 nA with a duty cycle of 50%, which corresponds to an average intensity of 150 nA. As represented in the MCNPX simulations, the extracted beam was stopped inside the nickel beam stop of the degrader wheel. The irradiations were launched before starting the WENDI-2 measurement and ended after the WENDI-2 stopped counting.

Operated in counter mode, the WENDI-2 counted the triggered impulses during a preselected measuring time of 1 min and automatically displayed an average dose rate at the end of the measuring time. Dividing this average dose rate by the built-in calibration factor of 0.317 nSv/c [155] and multiplying it by the pre-set measuring time, the number of recorded counts N and the Poisson counting uncertainty $\sqrt{N}$ was retrieved.

Given the 50% duty cycle, the beam intensity was actually zero during 50% of the measuring time, so the effective count rate, corresponding to a beam intensity of 300 nA, was estimated as N divided by 30s. The neutron background was considered negligible, since no count was recorded during 60s while the beam was off. Dead-time loss corrections for the effective count rates were estimated following the Feller model for a non-paralyzable detector (see section **II-4.1.2**), assuming a dead-time of 1.8 μs [155]. The estimated dead-time losses were negligible in all positions except for the two that are the closest to the beam stop. In positions 4 and 5, the dead-time losses were estimated to 88% and 19% of the measured effective count rate, respectively. The dead-time corrected count rates were then normalized to the beam intensity of 300 nA, for the comparison with the simulation results (expressed in μSv/(nA.h)).

IV-2.2 Gantry room operated in PBS

Two series of WENDI-2 measurements were performed around the Gantry Treatment Room 4 at the WPE. The first measurement series was acquired in May 2012. Measurements were carried out in all positions indicated in figure **III-4** on p. **119**. In positions 1 – 7, inside the maze and behind the door, the detector stood at ~25 cm above the floor. In positions 8 – 11, in the control room and the adjacent gantry room, the detector stood at ~1 m above the floor. The second series was acquired in May 2013, for the positions 1 and 7 – 11.

In both cases, a water phantom was positioned and irradiated in PBS as described in section **III-2.1.2**. The used beam intensity was of ~2 nA. Under these irradiation conditions, the WENDI-2 count rates in all measurement positions were well within the measuring range specified by the manufacturer of the WENDI-2 [154], so dead-time losses were negligible. The neutron background measured with the WENDI-2 before starting the irradiations was negligible as well.

For both series of measurements, the relative counting uncertainties were estimated from the number of counts N following Poisson's law ($N^{-1/2}$). The measured doses, corresponding to N multiplied by the built-in calibration factor of 0.317 nSv/c [155], were normalized to the delivered proton charge, in order to be compared to the simulation results.

During the first series, the WENDI-2 was operated in counter mode with a pre-set measuring time of 1 min. All irradiations delivered the same pre-set proton charge and lasted slightly less than 1 min. Each WENDI-2 measurement was started just before the irradiation and ended just after it. The number of WENDI-2 counts N was retrieved by dividing the dose rate displayed at the end of the measurement by 0.317 nSv/c [155] and multiplying it by the pre-set measuring time. The delivered

proton charge was monitored by means of the Monitor Units (MU) of the ionization chamber 'IC2-3' inside the treatment nozzle (manufacturer: IBA, [239]). Based on calibration data provided by IBA:

- 1 MU corresponded to a collected electron charge of 3 nC on the primary integral plan of the IC2-3, and

- the ratio of this collected electron charge to the delivered proton charge was of 138.8 ± 3.5.

The delivered proton charge was thus calculated as follows:

$$Q_p\,[nA.h] = \frac{MU \times 3 \times 10^{-9}C}{138.8} \times \frac{1\,nA.h}{3.6 \times 10^{-6}C}$$

The relative uncertainty on Q_p was estimated to 2.5% (private communication, Gilles Mathot, IBA).

During the second series, a longer measuring time was selected for the WENDI-2 measurements and the length of the irradiations depended on the measurement position. The irradiations were launched right after starting the measuring time and were stopped manually after at least 100 WENDI-2 counts could be recorded. The displayed number of counts N at the end of the irradiation was written down before the display automatically switched to the average dose rate at the end of the measuring time. The delivered proton charge was monitored in an independent way, using a Bragg Peak Chamber Type 34070 (an ionization chamber manufactured by PTW [240]) placed at the isocentre. The proton charge was determined as:

$$Q_p\,[nA.h] = N_p \times 1.602 \times 10^{-19}C \times \frac{1\,nA.h}{3.6 \times 10^{-6}C}$$

$$\text{with} \quad N_p = \frac{Q_e[C] \times \frac{w}{e}\left[\frac{J}{C}\right]}{S_{coll}\left[\frac{MeV}{cm}\right] \times d\,[cm] \times 1.602 \times \frac{10^{-13}J}{MeV}}$$

where Q_e is the electron charge collected in the Bragg Peak Chamber, w/e = 34.4 J/C the mean energy expended in air per unit liberated electron charge [241], d = 0.2 cm the gap thickness of the Bragg Peak Chamber [240], and S_{coll} = 0.00445 MeV/cm the stopping power in air of 225 MeV protons (product of the mass stopping power of 3.69 MeV.cm^2/g [241], and the air density at NTP conditions of 1.205 x 10^{-3} g/cm^3).

In this case, the relative uncertainty on Q_p was estimated to 4.0%, taking into account the following relative uncertainties: 3.0% on the Bragg Peak Chamber gap thickness [240], 2.0% on the mass stopping power [241], 1.4% on the air density and 1.2% on w/e [241]. In this second series of PBS measurements, the overall uncertainty on Q_p is thus a bit larger than in the first series (4.0% vs. 2.5%). This is mainly due to the mechanical tolerance on the gap thickness of the used ionization

chamber: the relative uncertainty on the gap thickness is about 3 times larger for the Bragg Peak Chamber than for the IC2-3.

For both measurement series, the total relative uncertainty on R_i, the measured WENDI-2 response normalized to the delivered proton charge, was calculated by combining the relative statistical uncertainty on the WENDI-2 counts and the relative uncertainty on Q_p as follows:

$$\frac{\sigma_{R_i}}{R_i} = \sqrt{\left(\frac{1}{\sqrt{N}}\right)^2 + \left(\frac{\sigma_{Q_p}}{Q_p}\right)^2}$$

The results of the two measurement series were eventually combined by calculating their averages weighted by the uncertainties σ_{Ri}:

$$R = \left(\frac{R_1}{(\sigma_{R_1})^2} + \frac{R_2}{(\sigma_{R_2})^2}\right)\bigg/\left(\frac{1}{(\sigma_{R_1})^2} + \frac{1}{(\sigma_{R_2})^2}\right) \text{ with } \sigma_R = \left(\frac{1}{(\sigma_{R_1})^2} + \frac{1}{(\sigma_{R_2})^2}\right)^{-1/2}$$

IV-2.3 Gantry room operated in DS

In May 2013, WENDI-2 measurements were also performed around the Gantry Treatment Room 3 at Essen. A water phantom was irradiated with a simple DS configuration, as already described in section **III-2.1.3**. The proton beam intensity at the nozzle entrance was of ~18 nA. The measurement positions for the WENDI-2 are indicated in figure **III-6** on p. **121**. The detector stood on a trolley at ~1m above the floor, except in the adjacent gantry room (positions 29 and 30) where it was placed on the floor.

The WENDI-2 was operated in counter mode, in the same way as in the second series of PBS measurements (see previous section). At least a few hundred counts were recorded in each measurement position.

To normalize the measurements for the comparison with the simulation results, it was necessary to determine the delivered proton charge at the entrance of the treatment nozzle. The proton source defined in the MCNPX simulation is indeed located just in front of the First Scatterer (see section **III-2.1.3**). Since an ionization chamber could not be inserted at the nozzle entrance, the MUs of the built-in ionization chamber 'IC2-3', located just downstream the collimating jaws, were recorded instead. In the used DS configuration, the proton field at that location is however too large with respect to the sensitive area of the IC2-3, so the MUs could only correspond to a limited fraction of the total proton charge. The relationship between the proton charge at the nozzle entrance and the MUs of the IC2-3 had to be determined through a preliminary series of measurements in which the treatment nozzle was set in 'pass-through' mode, *i.e.* the scattering elements of the DS mode

CHAPTER IV

were taken out of the beam path. In pass-through mode, the proton charge at the nozzle entrance could be measured with an ionization chamber placed at the isocentre. The used ionization chamber was a Bragg Peak Chamber Type 34070 [240]. Without modifying the beam intensity, successive irradiations of 1 min were performed, alternately with the nozzle in pass-through mode (to measure the proton charge with the Bragg Peak Chamber) and in DS mode (to record the MUs of IC2-3). Thanks to the good beam stability, the repeatability of these preliminary measurements was satisfactory (see table **IV-1**). The irradiations were carried out at a lower beam intensity of ~3 nA to avoid any saturation effects in the Bragg Peak Chamber. The proton charge crossing the Bragg Peak Chamber was determined from the collected electron charge as outlined in the previous section for the second series of PBS measurements.

The obtained coefficient for the conversion of the MUs into the proton charge at the nozzle entrance was of **$2.44 \cdot 10^{-4}$ nA.h/MU**. The relative uncertainty on this conversion coefficient, and thus on the delivered proton charge, was estimated to 4.2%. This combines the following uncertainties: 3.0% on the gap thickness of the Bragg Peak Chamber [240], 2.0% on the mass stopping power of the protons [241], 1.4% on the air density, 1.2% on *w/e* [241], 1% on the electron charge collected per minute in the Bragg Peak Chamber (see table **IV-1**), and 0.5% on the number of MUs delivered per minute (see table **IV-1**).

As for the PBS measurements, the relative Poisson uncertainty on the number of WENDI-2 counts and the relative uncertainty on the delivered proton charge were then combined in "root-sum-of-squares", to provide the relative uncertainty on the measured WENDI-2 response per unit delivered proton charge.

Table IV-1 – Preliminary calibration measurements: electron charge collected during 1 min in the Bragg Peak Chamber, with the nozzle set in pass-through mode, and MUs delivered during 1 min as recorded by the IC2-3, with the nozzle set in the DS configuration.

Electron charge collected in Bragg Peak Chamber [nC]	IC2-3 [MU]
82.6	215
81.4	218
84.2	218
80.1	
Average : 82.1 ± 0.9	**Average : 217 ± 1**

182 |

IV-2.4 Fixed-beam treatment room

In April 2014, WENDI-2 measurements were carried out inside and around the fixed-beam treatment room at Essen. The fixed-beam line was used to irradiate a water phantom in US mode as described in section **III-2.1.4**. No beam scatterer was used in this irradiation. The beam spot was simply scanned over a predefined area of ~19 cm x 22 cm at the entrance of the phantom. The shape of the proton field is shown in Figure **IV-1**, which is the scan of a GafChromic sheet that was temporarily placed on the vertical entrance plane of the phantom and irradiated with the selected US field during one full cycle of 1 min. The beam intensity was of ~2.5 nA for neutron measurements performed inside the treatment room and its maze. It was increased to ~25 nA for neutron measurements performed inside the technical room or the adjacent gantry room. The measurement positions are indicated in figure **III-8** on p. **124**. All of them were situated at ~150 cm above the floor, except for 2d (on the floor).

The WENDI-2 was operated in counter mode, in the same way as in the second series of PBS measurements. The irradiations were long enough to ensure at least a few hundred WENDI-2 counts in each measurement position.
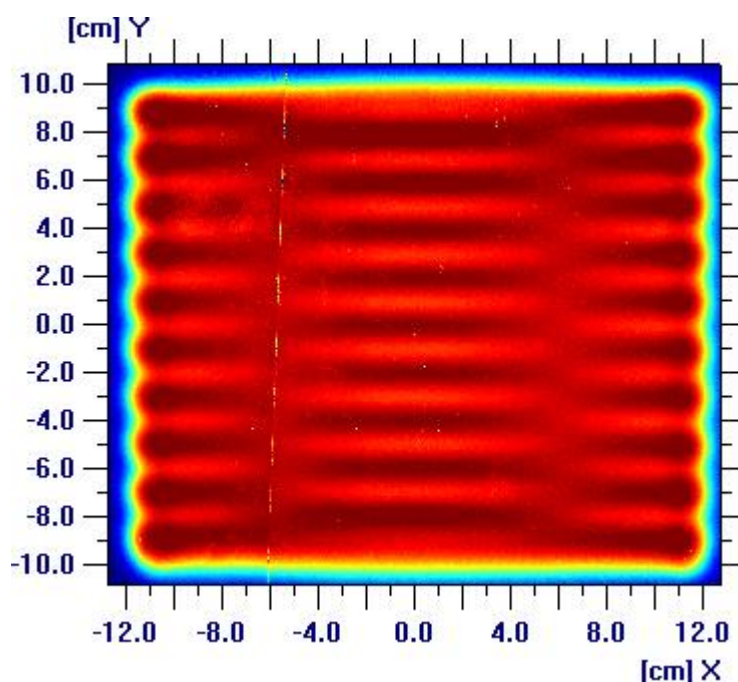
Figure IV-1 – Shape of the US field: scan of the irradiated GafChromic on the vertical entrance plane of the water phantom.

During this experiment, measurements were performed not only with a WENDI-2, but also with several other types of neutron detectors. The latter were operated by two collaborating research teams, one from CERN and the other from the SCK-CEN. Their results will be discussed in Chapter VI. Here, we would mainly like to stress the fact that a large number of irradiations had to be delivered during this shift.

The total irradiation time was of ~2 h, which is nearly ten times more than in one average day of treatment. The total delivered proton charge was therefore large, also because for measurements performed behind the shield the beam intensity was roughly five times the typical treatment intensity. In fact, it was estimated that the total proton charge delivered during the experiment would reach almost 20% the average annual treatment workload for this beam line, which constituted the main reason for choosing the US delivery mode. Indeed, scanning the beam into a field of ~400 cm² reduces by a factor of ~20 the proton charge that crosses the small ionization chamber 'IC2-3' inside the nozzle (manufacturer: IBA). This 'IC2-3' is relatively fragile since it has an average lifetime of about 1 year in regular treatment conditions, which usually involve scanned fields. Concentrating the whole proton charge into a small fixed spot through the 'IC2-3', by keeping the scanning magnets switched off, would have induced a very high risk of destroying this chamber during our experiment.

Similarly to the DS case (see previous section), no available ionization chamber was large enough to encompass the entire proton field of 19 cm x 22 cm. Therefore, the delivered proton charge was indirectly monitored by means of the MUs recorded with the 'IC2-3'. The relationship between these MUs and the real proton charge delivered to the water phantom was established through a preliminary measurement with a Bragg Peak Chamber Type 34070 [240] placed at the isocentre. During this test, the scanning magnets of the treatment nozzle were switched off in order to keep the proton beam spot steady within the diameter of the Bragg Peak Chamber. The test was conducted at a low intensity of ~2.5 nA to avoid saturating the Bragg Peak Chamber. The beam was thus delivered in this fixed spot during 1 min. Then, without changing the beam intensity, the scanning magnets were switched on again and the beam was delivered in US mode during 1 min, so as to record the corresponding number of MUs. The results are given in table **IV-2**. We assumed the same uncertainty on the number of MUs delivered per minute as in the DS measurements (0.5%; see table **IV-1**). The proton charge corresponding to the delivered MUs was calculated in the same way as in the second series of PBS measurements (see section **IV-2.2**).

Table IV-2 – Preliminary calibration measurements: electron charge collected during 1 min in the Bragg Peak Chamber, with the nozzle set in pass-through mode, and MUs delivered during 1 min as recorded by the IC2-3, with the nozzle set in the DS configuration.

Electron charge collected in Bragg Peak Chamber [nC]	IC2-3 [MU]
4.05×10^3	236

The obtained coefficient for the conversion of the MUs into the proton charge delivered to the water phantom was of **$1.84 \cdot 10^{-4}$ nA.h/MU**. As in the DS case, a relative uncertainty of 4.2 % was associated to this coefficient, taking into account the

same sources of uncertainties. The total uncertainty on the measured WENDI-2 response per unit delivered proton charge was then also determined in the same way as in the DS case.

IV-3 Results

IV-3.1 Cyclotron room

The results of the WENDI-2 measurements carried out inside and around the cyclotron room are summarized in table **IV-3**. In figure **IV-2**, the simulated WENDI-2 responses, from section **III-3.1**, are also compared to these measurements.

Table IV-3 – WENDI-2 measurements inside and around the cyclotron room. The cyclotron-extracted intensity was of 300 nA with a 50% duty cycle. The measuring time was of 1 min.

Position	WENDI-2 counts	Dead-time corrected count rate [cps]	Measured WENDI-2 response [μSv/(nA.h)]	Relative statistical uncertainty
4	7.80×10^6	4.89×10^5	$(1.8571 \pm 0.0007) \times 10^3$	0.04 %
5	2.64×10^6	1.05×10^5	$(3.973 \pm 0.002) \times 10^2$	0.06 %
6	1.02×10^5	3.42×10^3	$(1.300 \pm 0.004) \times 10^1$	0.3 %
7	6.48×10^3	2.16×10^2	$(8.2 \pm 0.1) \times 10^{-1}$	1 %
8	2.2×10^2	7.4×10^0	$(2.8 \pm 0.2) \times 10^{-2}$	7 %
9	2.5×10^2	8.4×10^0	$(3.2 \pm 0.2) \times 10^{-2}$	6 %
3	1.7×10^1	5.7×10^{-1}	$(2.2 \pm 0.5) \times 10^{-3}$	24 %
1	1×10^0	3×10^{-2}	$(1 \pm 1) \times 10^{-4}$	100 %
2	1×10^0	3×10^{-2}	$(1 \pm 1) \times 10^{-4}$	100 %
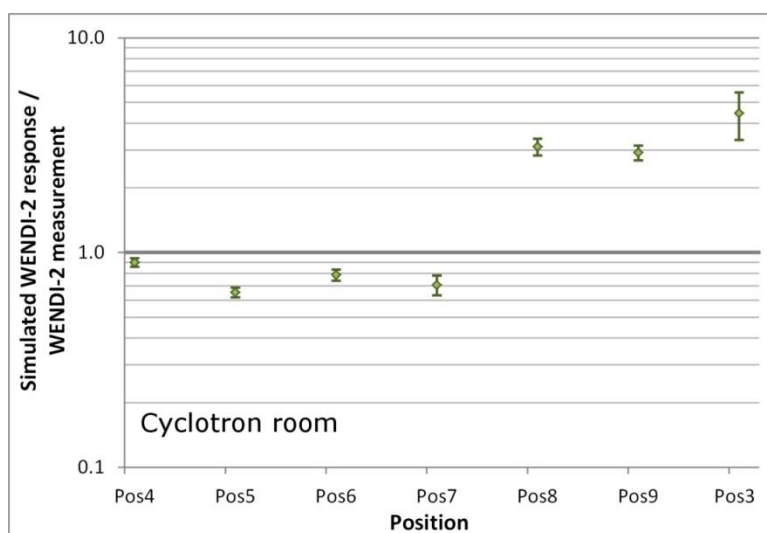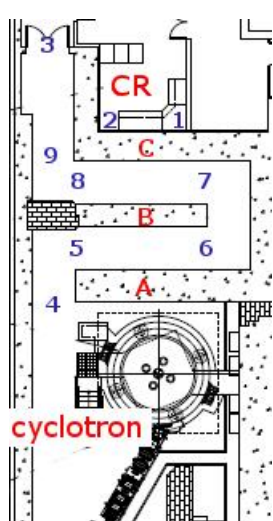
Figure IV-2 – Cyclotron room: ratio of the simulated WENDI-2 response to the WENDI-2 measurement. The uncertainties combine in "root-sum-of-squares" the relative statistical uncertainty on the WENDI-2 measurement and the relative uncertainty on the simulated WENDI-2 response determined in Chapter III.

The simulation-to-measurement comparison in figure **IV-2** is not shown for positions 1 and 2 because of the insufficient measurement statistics: the WENDI-2 only registered one count in one minute in these positions. These measured values are nevertheless given in table **IV-3** to indicate that the neutron dose rates in the main control room were very low even though the experiment was conducted at maximum levels of secondary neutron production. The highest beam intensity was indeed selected and the cyclotron-extracted protons were fully stopped on the degrader wheel. The main control room is in fact particularly well-shielded thanks to a concrete shield of ~3.50 m in total thickness and a location at backward angles with respect to the direction of the cyclotron-extracted proton beam (implying a reduced high-energy neutron flux emitted towards the control room).

In terms of agreement between the simulated and measured WENDI-2 responses, the considered positions seem to fall into two categories:

1) Positions 4 – 7, in the first half of the maze, are characterised by a relatively good simulation-to-measurement agreement. The simulated responses are smaller than the measurements by at most ~35%. As explained in section **III-3.1**, the neutron fluence in these positions originates mainly from neutrons that have been scattered throughout the maze. Neutrons transmitted directly through maze wall 'A', on the contrary, do not give a significant contribution to the response. The satisfactory results in these positions thus suggest that, from a global point of view, the neutron production and scattering inside the cyclotron room has been relatively well modelled in the simulations. The cause of the slight underestimate of the simulation results with respect to the measurements is difficult to identify because many parameters influence the simulated spectra, such as e.g. the proton and neutron interaction cross-sections and physics models, the distribution of the proton losses inside the cyclotron, material definitions and the modelling of all the equipment pieces which may significantly influence the neutron flux distributions inside the room.

2) Positions 8 – 9 in the second half of the maze, and position 3 behind the maze door, are characterised by an overestimate of a factor of 3 – 4 of the simulated responses with respect to the measurements. According to the simulation results in section **III-3.1**, the maze-scattered fluence component is already strongly attenuated and fully thermalized in position 8, so that in comparison the fluence component transmitted through wall 'B' becomes more significant. This transmitted component originates mainly from a small amount of high-energy neutrons emitted at ~135° by the protons impinging on the beam stop. These high-energy neutrons travel in nearly straight line through wall 'B', and probably through the corner of wall 'A' as well. The few interactions that these high-energy neutrons undergo inside the walls lead to the generation of evaporation neutrons, which also appear in the spectra of positions 8 and 9. As shown in section **III-3.1**, these evaporation and high-energy neutrons that emerge from wall 'B' strongly determine H*(10) and the WENDI-2 response in the

last part of the maze and behind the maze door. The overestimate by a factor of 3 – 4 of the simulation can thus be linked to this wall-transmitted component, for which the simulations were indeed expected to be conservative.

A combination of uncertainties affecting several simulation parameters should explain the observed overestimate. The neutron flux emerging from wall 'B' near positions 8 – 9 is mainly influenced by:

- the high-energy neutron flux entering wall 'B',
- the concrete composition and density,
- the traversed concrete thickness, and
- the cross-sections for the neutron interactions within the wall.

The simulated high-energy neutron flux entering wall 'B' certainly depends a lot on the double-differential neutron production cross-section at ∼135° for nickel, the material of the beam stop. This cross-section was based on the Bertini model, above 150 MeV, and the endf70prot library in the range of ∼10 MeV – 150 MeV. Its accuracy is difficult to verify since little corresponding experimental data is available. It should however be noted that at backward angles the Bertini model is in fact not the most conservative model amongst those available in MCNPX 2.7.0 (this will be shown in Chapter V).

A metallic cupboard, which was not modelled in the simulations, intersects the straight lines from the beam stop to positions 8 – 9 (see picture in figure **IV-3**). This cupboard contains electrical equipment (e.g. transformers) belonging to the final power amplifier (FPA) of the cyclotron RF system. It might perhaps attenuate the high-energy neutron flux in a non-negligible way so as to cause a non-negligible reduction of H*(10) in positions 8 – 9.
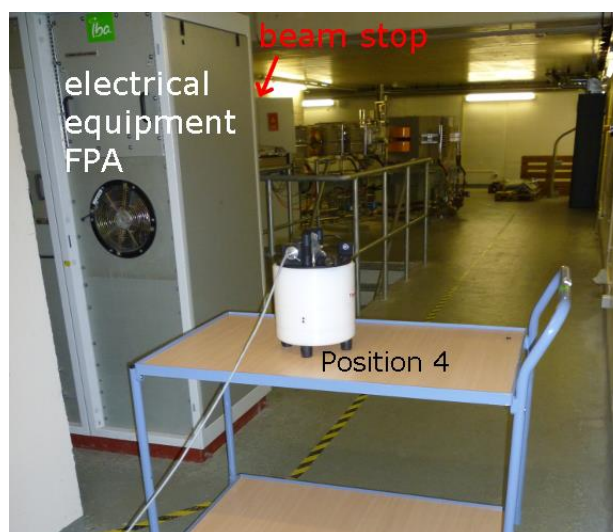
Figure IV-3 – Picture of the cyclotron room showing the FPA cupboard standing between the cyclotron and the entrance of the maze, as well as the position of the beam stop (behind a protection panel)

Furthermore, the influence of the defined concrete composition and density on the simulation results in positions 8, 9 and 3 might be unexpectedly large, as will be shown in Chapter V too.

Uncertainties on the traversed concrete thickness may also play a role, since in practice a constructed building is never the perfect reflection of its architectural plans. These uncertainties may not necessarily be large, but are most probably non-negligible for such a thick concrete shield.

As for the variance reduction technique necessary to achieve the statistical consistency for the wall-transmitted fluence, we assume that it must not have introduced a significant bias in the simulation results since it was applied according to the general recommendations of the field (see section **III-2.4**).

Finally, uncertainties on the positioning of the detector and its angular response were not formally evaluated in this work by lack of time. These uncertainties are both thought to be relatively small (on the order of a few percent). The uncertainties on the delivered proton beam intensity, which may have fluctuated over time, were not estimated either.

IV-3.2 Gantry room operated in PBS

Two series of WENDI-2 measurements were performed around the gantry room operated in PBS. The results of the first series are given in table **IV-4**, those of the second series in table **IV-5**. The results of both series are compatible with each other within 1σ or 2σ for all positions, except for position 8 (agreement within 4σ).

Table IV-4 – First series of PBS measurements: recorded number of WENDI-2 counts (N) and its relative statistical uncertainty; delivered proton charge Q_p in one minute (corresponding to 5698.2 MUs) and its relative uncertainty; measured WENDI-2 response per unit delivered proton charge (R_1) and its relative uncertainty.

Position	N	$\frac{1}{\sqrt{N}}$ x 100 %	Delivered proton charge Q_p [nA.h]	$\frac{\sigma_{Q_p}}{Q_p}$ x 100%	Measured WENDI-2 response R_1 [µSv/(nA.h)]	$\frac{\sigma_{R_1}}{R_1}$ x 100%
1	3.40×10^4	0.5 %	3.42×10^{-2}	2.5 %	3.14×10^2	2.6 %
2	7.87×10^3	1.1 %	3.42×10^{-2}	2.5 %	7.28×10^1	2.7 %
3	2.02×10^3	2.2 %	3.42×10^{-2}	2.5 %	1.87×10^1	3.3 %
4	7.8×10^2	3.6 %	3.42×10^{-2}	2.5 %	7.2×10^0	4.4 %
5	4.3×10^2	4.8 %	3.42×10^{-2}	2.5 %	4.0×10^0	5.4 %
6	2.0×10^2	7.2 %	3.42×10^{-2}	2.5 %	1.8×10^0	7.6 %
7	1.7×10^1	7.8 %	3.42×10^{-2}	2.5 %	1.5×10^{-1}	8.2 %
8	1.4×10^2	8.5 %	3.42×10^{-2}	2.5 %	1.3×10^0	8.9%
9	3.6×10^1	17 %	3.42×10^{-2}	2.5 %	3.3×10^{-1}	17%
10	1.8×10^1	24 %	3.42×10^{-2}	2.5 %	1.7×10^{-1}	24%
11	7.7×10^1	11 %	3.42×10^{-2}	2.5 %	7.1×10^{-1}	12%

Table IV-5 – Second series of PBS measurements: recorded number of WENDI-2 counts (N) and its relative statistical uncertainty; delivered proton charge (Q_p) and its relative uncertainty; measured WENDI-2 response per unit delivered proton charge (R_2) and its relative uncertainty.

Position	N	$\dfrac{1}{\sqrt{N}}$ x 100 %	Delivered proton charge Q_p [nA.h]	$\dfrac{\sigma_{Q_p}}{Q_p}$ x 100%	Measured WENDI-2 response R_2 [µSv/(nA.h)]	$\dfrac{\sigma_{R_2}}{R_2}$ x 100%
1	3.17×10^4	0.6 %	3.1×10^{-2}	4.0 %	3.2×10^2	4.1 %
6	4.0×10^2	5.0 %	7.2×10^{-2}	4.0 %	1.8×10^0	6.4 %
7	1.0×10^2	10 %	2.9×10^{-1}	4.0 %	1.1×10^{-1}	11 %
8	8.0×10^2	3.5 %	3.6×10^{-1}	4.0 %	7.0×10^{-1}	5.4 %
9	3.0×10^2	5.8 %	3.4×10^{-1}	4.0 %	2.8×10^{-1}	7.1 %
10	2.0×10^2	7.1 %	2.4×10^{-1}	4.0 %	2.6×10^{-1}	8.1 %
11	3.0×10^2	5.8 %	1.3×10^{-1}	4.0 %	7.2×10^{-1}	7.1 %

Table **IV-6** contains the weighted averages of the two series. The ratio of the simulated WENDI-2 responses (from section **III-3.2**) to these average measurements is shown in figure **IV-4**, for the two versions of the PBS simulations; without and with the gantry front ring.

Figure **IV-4** shows that the insertion of the gantry front ring in the modelled geometry improves the agreement of the simulated WENDI-2 response with the measurements, both in position 9 (in the control room) and in positions 1 – 6 inside the maze. A discussion of the impact of this ring on the simulation results has been given in section **III-3.2**.

Table IV-6 – PBS measurements: Average measured WENDI-2 response per unit delivered proton charge, and its relative uncertainty

Position	Average measured WENDI-2 response R [µSv/(nA.h)]	$\dfrac{\sigma_R}{R}$ x 100 %
1	$(3.17 \pm 0.07) \times 10^2$	2.2 %
2	$(7.3 \pm 0.2) \times 10^1$	2.7 %
3	$(1.87 \pm 0.06) \times 10^1$	3.3 %
4	$(7.2 \pm 0.3) \times 10^0$	4.4 %
5	$(4.0 \pm 0.2) \times 10^0$	5.4 %
6	$(1.78 \pm 0.09) \times 10^0$	4.9 %
7	$(1.1 \pm 0.1) \times 10^{-1}$	9.9 %
8	$(7.6 \pm 0.4) \times 10^{-1}$	4.7 %
9	$(2.9 \pm 0.2) \times 10^{-1}$	6.5 %
10	$(2.4 \pm 0.2) \times 10^{-1}$	7.8 %
11	$(7.2 \pm 0.4) \times 10^{-1}$	6.0 %
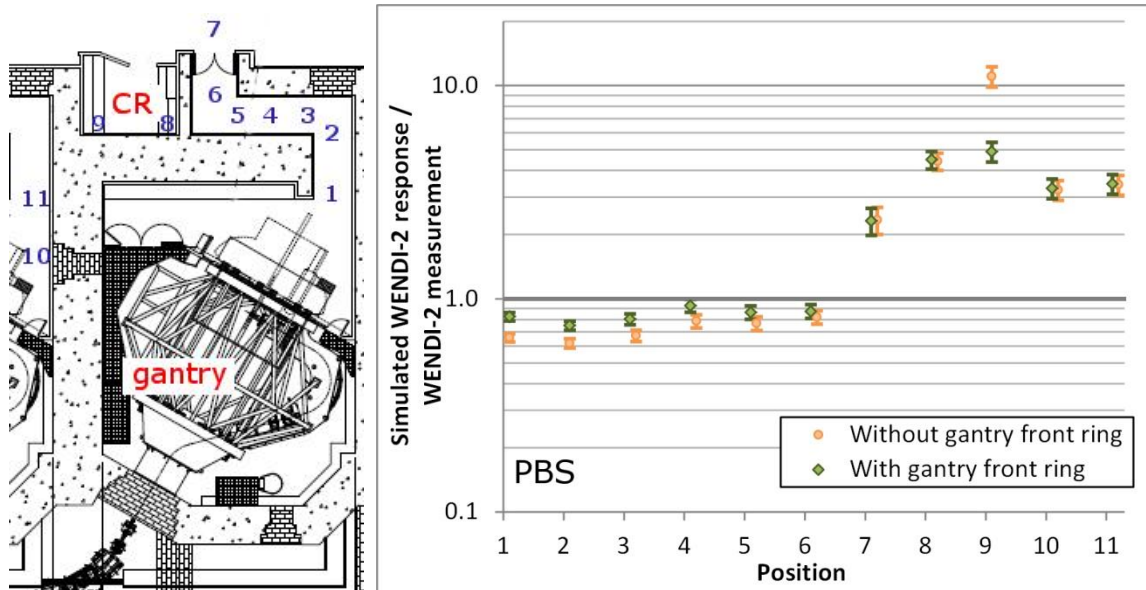
Figure IV-4 – Gantry room operated in PBS: ratio of the simulated WENDI-2 response to the WENDI-2 measurement. The uncertainties combine in "root-sum-of-squares" the relative uncertainty on the measured WENDI-2 response per unit delivered proton charge and the relative uncertainty on the simulated WENDI-2 response determined in Chapter III.

The trend already observed in the case of the cyclotron room exists as well in the results of the PBS case-study:

1) The maze of the gantry room is in fact comparable to the first 'S' of the cyclotron maze (CYCL positions 4 – 7). For the PBS positions 1 – 6, a relatively good agreement is indeed obtained between the simulated and measured WENDI-2 responses.

In the first part of the maze (1 – 3), the simulated responses underestimate the measurements by 20-25 % (for the simulation with the gantry front ring). In these positions, the WENDI-2 response is almost entirely determined by the maze-scattered fluence. As previously discussed for the cyclotron maze, multiple parameters may cause this slight underestimate. Unmodelled iron parts of the gantry could perhaps play a determining role in this case, judging for instance by the positive impact that the modelling of the gantry front ring has had in these positions.

In the second part of the maze (4 – 6), the simulated responses agree with the measurements within 2σ or 3σ. As explained in section **III-3.2**, the contribution of the wall-transmitted neutron flux increases towards the end of the maze. The better simulation-to-measurement agreement in these positions is perhaps a consequence of a compensating effect in the simulation between an overestimate on the wall-transmitted component and the slight underestimate on the maze-scattered component.

2) For positions located outside the treatment room (7 – 11), the simulated WENDI-2 responses overestimate the measurements by a factor of 2 – 5 (see simulation with the gantry front ring). As in the case of the cyclotron room, the overestimate is clearly linked to the wall-transmitted neutron fluxes.

Many possible causes of the overestimate have already been enumerated in the previous section. In this case, the high-energy neutrons were however produced inside a water phantom. The simulation results in the positions 7 – 11 are thus sensitive to, amongst others, the accuracy in the high-energy region of the double-differential neutron production cross-sections for oxygen, at forward angles. These were also based on the Bertini model, above 150 MeV, and the evaluated data of the endf70prot library below 150 MeV.

IV-3.3 Gantry room operated in DS

Table **IV-7** shows the results of the WENDI-2 measurements performed inside and around the gantry room operated in DS. The ratio of the simulated WENDI-2 responses (from section **III-3.3**) to these measurements is shown in Figure **IV-5**, for the simulations without and with the gantry front ring.

The results are very similar to those of the gantry room operated in PBS. The insertion of the gantry front ring into the simulated geometry also improved the agreement between the simulated WENDI-2 responses and the measurements, although the impact was a bit smaller than in the PBS case (see discussion in section **III-3.3**).

Concerning the simulation with the gantry front ring, we observe that:

1) In positions 12 – 16, inside the maze, the simulated responses are in very good agreement with the measurements (agreement within 1σ or 2σ). The maze-scattered fluence, which gives the dominant contribution to the responses all along the maze (see section **III-3.3**), was thus simulated with good accuracy.
Unlike in PBS, no underestimate of the simulated responses is noted in this DS case. Therefore, it seems possible that the simulation overestimates the contribution (production) from the additional neutron sources inside the DS nozzle, which involve several target materials much heavier than water. These overestimates, if indeed they exist, seem to "compensate" for the underestimate observed in the PBS case.

2) In positions 17 – 21, outside the gantry room, the simulated WENDI-2 responses overestimate the measurements by a factor of 2 – 6. Like in the two previous case-studies, the simulation was thus as expected conservative with respect to the wall-transmitted neutron fluxes.

Table IV-7 – DS measurements: recorded number of WENDI-2 counts (N) and its relative statistical uncertainty; delivered proton charge (Q_p) and its relative uncertainty; measured WENDI-2 response per unit delivered proton charge (R) and its relative uncertainty.

Position	N	$\dfrac{1}{\sqrt{N}}$ x 100 %	Delivered proton charge Q_p [nA.h]	$\dfrac{\sigma_{Q_p}}{Q_p}$ x 100%	Measured WENDI-2 response R [μSv/(nA.h)]	$\dfrac{\sigma_R}{R}$ x 100%
12	6.72×10^5	0.1 %	1.2×10^{-1}	4.2 %	$(1.85 \pm 0.08) \times 10^3$	4.2 %
13	3.67×10^5	0.2 %	1.3×10^{-1}	4.2 %	$(9.2 \pm 0.4) \times 10^2$	4.2 %
14	5.47×10^4	0.4 %	1.3×10^{-1}	4.2 %	$(1.35 \pm 0.06) \times 10^2$	4.2 %
15	2.43×10^4	0.6 %	2.6×10^{-1}	4.2 %	$(2.9 \pm 0.1) \times 10^1$	4.3 %
16	9.13×10^3	1.0 %	2.7×10^{-1}	4.2 %	$(1.1 \pm 0.5) \times 10^1$	4.3 %
17	4.7×10^2	4.6 %	4.6×10^{-1}	4.2 %	$(3.3 \pm 0.2) \times 10^{-1}$	6.2 %
18	1.57×10^3	2.5 %	5.3×10^{-1}	4.2 %	$(9.4 \pm 0.5) \times 10^{-1}$	4.9 %
19	3.9×10^2	5.1 %	5.4×10^{-1}	4.2 %	$(2.3 \pm 0.2) \times 10^{-1}$	6.6 %
20	2.9×10^2	5.9 %	2.8×10^{-1}	4.2 %	$(3.2 \pm 0.2) \times 10^{-1}$	7.2 %
21	2.7×10^2	6.1 %	2.8×10^{-1}	4.2 %	$(3.0 \pm 0.2) \times 10^{-1}$	7.4 %
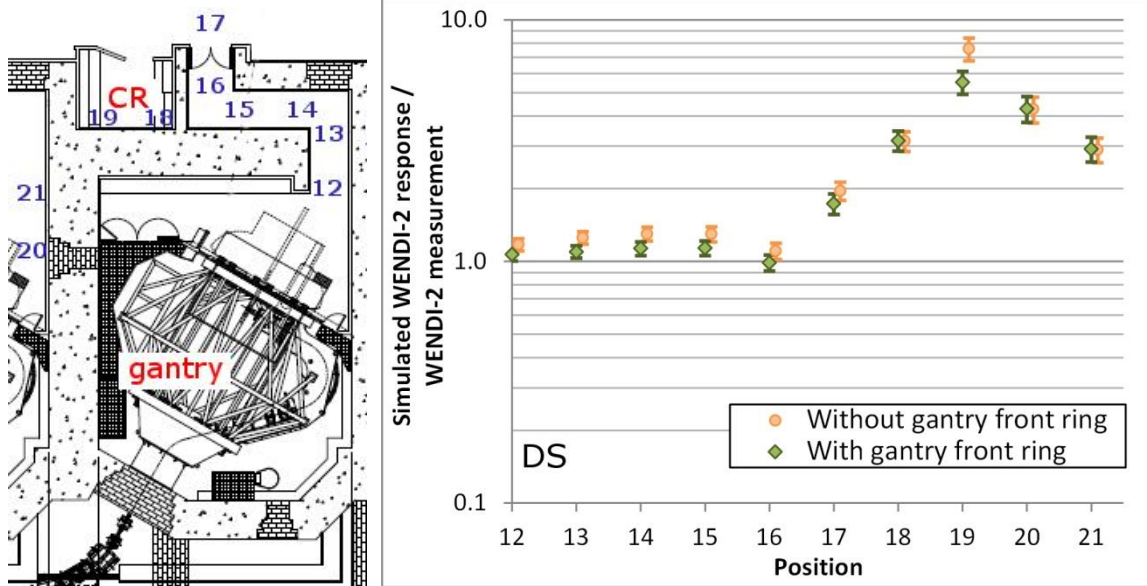
Figure IV-5 – Gantry room operated in DS: ratio of the simulated WENDI-2 response to the WENDI-2 measurement. The uncertainties combine in "root-sum-of-squares" the relative uncertainty on the measured WENDI-2 response per unit delivered proton charge and the relative uncertainty on the simulated WENDI-2 response determined in Chapter III.

IV-3.4 Fixed-beam treatment room

The WENDI-2 measurements performed inside and around the fixed-beam treatment room are summarized in table **IV-8**. Figure **IV-6** shows the ratio of the simulated WENDI-2 responses (from section **III-3.4**) to these measurements.

Table IV-8 – FBTR measurements: recorded number of WENDI-2 counts (N) and its relative statistical uncertainty; delivered proton charge (Q_p) and its relative uncertainty; measured WENDI-2 response per unit delivered proton charge (R) and its associated total relative uncertainty.

Position	N	$\frac{1}{\sqrt{N}}$ $x\ 100\ \%$	Delivered proton charge Q_p [nA.h]	$\frac{\sigma_{Q_p}}{Q_p}$ $x\ 100\%$	Measured WENDI-2 response R [µSv/(nA.h)]	$\frac{\sigma_R}{R}$ $x\ 100\%$
1b	2.40×10^5	0.2 %	3.7×10^{-2}	4.2 %	$(2.03 \pm 0.09) \times 10^3$	4.2 %
1a	6.88×10^4	0.4 %	3.7×10^{-2}	4.2 %	$(5.8 \pm 0.2) \times 10^2$	4.2 %
1c	7.20×10^4	0.4 %	6.1×10^{-2}	4.2 %	$(3.8 \pm 0.2) \times 10^2$	4.2 %
1d	9.28×10^3	1.0 %	8.1×10^{-2}	4.2 %	$(3.6 \pm 0.2) \times 10^1$	4.3 %
1e	2.51×10^3	2.0 %	7.6×10^{-2}	4.2 %	$(1.04 \pm 0.05) \times 10^1$	4.7 %
1f	7.3×10^2	3.7 %	8.3×10^{-2}	4.2 %	$(2.8 \pm 0.2) \times 10^0$	5.6 %
1g	3.4×10^2	5.4 %	7.7×10^{-2}	4.2 %	$(1.4 \pm 0.1) \times 10^0$	6.8 %
2a	4.76×10^3	1.4 %	5.6×10^{-1}	4.2 %	$(2.7 \pm 0.1) \times 10^0$	4.5 %
2c	9.80×10^3	1.0 %	5.5×10^{-1}	4.2 %	$(5.6 \pm 0.2) \times 10^0$	4.3 %
2b	5.51×10^3	1.3 %	4.4×10^{-1}	4.2 %	$(3.9 \pm 0.2) \times 10^0$	4.4 %
2d	1.28×10^2	6.3 %	7.7×10^{-1}	4.2 %	$(5.3 \pm 0.3) \times 10^{-2}$	7.5 %
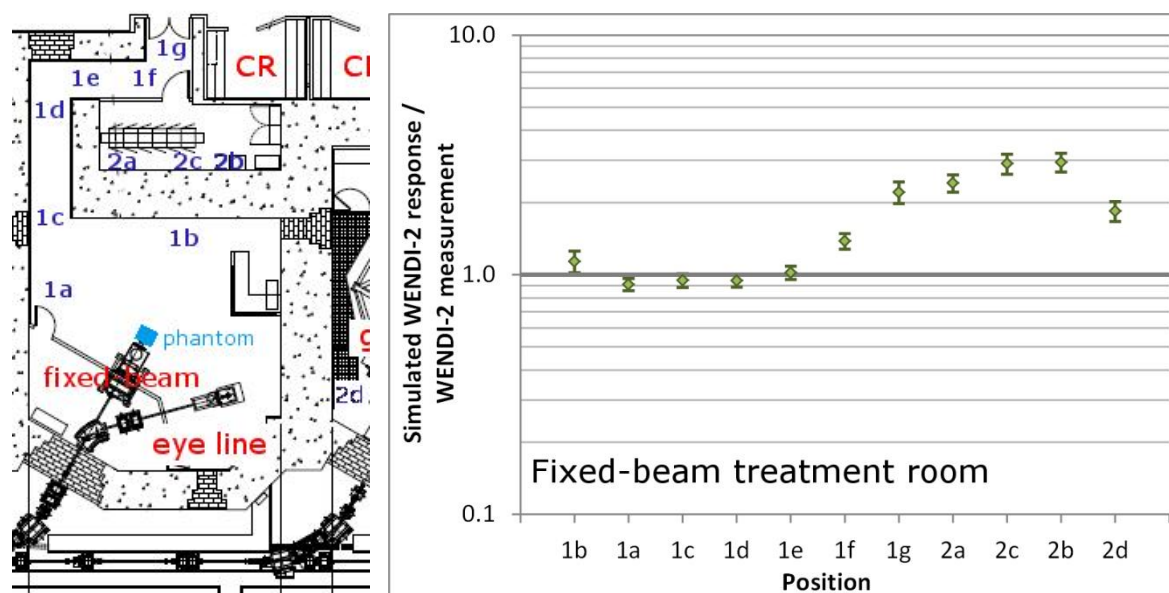
Figure IV-6 – Fixed-beam treatment room: ratio of the simulated WENDI-2 response to the WENDI-2 measurement. The uncertainties combine in "root-sum-of-squares" the relative uncertainty on the measured WENDI-2 response per unit delivered proton charge and the relative uncertainty on the simulated WENDI-2 response determined in Chapter III.

The trend observed in the results of the fixed-beam treatment room is consistent with those already observed in the three previous case-studies:

1) Inside the treatment room (1a, 1b) and in the part of the maze where the maze-scattered neutrons mostly determine the response (1c - 1e, see spectra in section **III-3.4**), the simulated responses and the measurements are in very good agreement with each other (agreement within 1σ, or nearly so).

2) In the technical room (2a, 2c, 2b) and in the adjacent gantry room (2d), the simulated WENDI-2 responses overestimate the measurements by a factor of 2 – 3. The responses in these positions are mostly determined by the wall-transmitted neutron fluxes, for which the simulation was thus conservative, as expected.

In this case, it is certain that there were no equipment parts or cupboards at all between the water phantom and the wall of the technical room. In principle, the overestimate in the simulation results for positions 2a, 2c and 2b should thus not be caused by unmodelled objects inside the treatment room. That might perhaps explain the slightly better simulation-to-measurement agreement compared to the results obtained around the gantry treatment rooms.

It is also interesting to note that the overestimate seems to be a bit larger for position 2b than for position 2d, even though the traversed concrete thickness is actually smaller for 2b (see table **III-15** on p. **173**). This suggests that some uncertainties which are unrelated to the simulated concrete walls are significant at least for position 2b. One hypothesis for instance is that, in the simulation of the proton interactions with the oxygen nuclei of the phantom, the production of high-energy neutrons is slightly overestimated, and that this overestimate is larger for the near-0° emission than for the near-90° emission. We will come back on this hypothesis when discussing the neutron spectrometry measurements in Chapter VI.

3) Concerning the end of the maze: the maze-scattered fluence component is strongly attenuated and the contribution from neutrons transmitted through the wall of the technical room becomes increasingly important in positions 1f and 1g (see spectra in section **III-3.4**). Compared to the other rooms, the angle of the maze door with respect to the proton beam is actually the smallest for this room (~25°). This causes a somewhat larger emission of high-energy neutrons in the direction of the maze door. In terms of simulation-to-measurement agreement, positions 1f and 1g are in fact quite similar to the positions located behind the maze doors of the gantry rooms (PBS Position 7 and DS Position 17).

IV-4 Conclusion

WENDI-2 measurements were performed inside and around four rooms at the proton therapy facility of Essen: the cyclotron room, the Gantry Treatment Room 4 operated in PBS, the Gantry Treatment Room 3 operated in DS, and the Fixed-Beam Treatment Room operated in US.

In this chapter, we have compared these measurements to the corresponding simulated WENDI-2 responses obtained in Chapter III. As a reminder, the MCNPX simulations were made following a methodology based on conservative choices which was adopted in the original shielding design simulations for this facility. Our main goal in this chapter has been to assess the conservative nature of these simulations, *i.e.* to verify that the simulated neutron doses behind the shielding walls are indeed overestimated. The results of the comparison have confirmed this assumption for the four rooms. The simulated WENDI-2 responses indeed overestimate the measurements by at least a factor of ~2 in every position located outside the room in operation.

However, in positions located inside the room, or in (a part of) the access maze – where the contribution of wall-transmitted neutrons is rather small –, the simulated WENDI-2 responses are in good agreement with the measurements. In general, the production of secondary neutrons, especially evaporation neutrons, is thus relatively well modelled in the simulations, as is the scattering of these neutrons throughout the room and the maze.

For the gantry rooms, it has nevertheless been shown that adding the iron gantry front ring into the simulated geometry allows further improving the simulation-to-measurement agreement inside the maze, especially in the PBS case. The ring also drastically improved the agreement for one specific position located outside the treatment room, in the "shadow" of the ring with respect to the water phantom (from the point of view of high-energy neutrons, which travel in nearly straight line). This improvement was particularly large in the PBS case, in which all secondary neutrons originated from the water phantom.

So far, it has thus been confirmed that the simulations of Chapter III were conservative with respect to the wall-transmitted neutron fluxes. The largest overestimates, obtained inside the control room of the gantry rooms, were of a factor of 5 – 6 (when the gantry front ring was added into the model). Similar results were obtained by Satoh *et al.* in a recent study conducted at the Fukui proton therapy centre, with a 235 MeV proton beam impinging on a water phantom [242].

The overestimates obtained outside the rooms are thought to be mostly related to a combination of uncertainties that affect several parameters of the simulations. As a non-exhaustive list of these, let us mention:

- uncertainties on the double differential neutron production cross-sections of protons, especially on their high-energy end, because high-energy neutrons mostly drive the dose attenuation profile through the shield.
  For protons of more than 150 MeV, the cross-sections were calculated according to the Bertini intranuclear cascade model and the Dresner evaporation model.
  Amongst the different intranuclear cascade models available in MCNPX 2.7.0, the Bertini model constitutes the most conservative choice for the calculation of the neutron doses at forward angles in these simulations.
  The uncertainties on these model-based cross-sections might be larger than for the cross-sections below 150 MeV, because the latter were based on evaluated data (*i.e.* partially based on experimental data). However, the uncertainties on the evaluated data are probably larger in the range of 20 MeV – 150 MeV than below 20 MeV, due to the lower availability of experimental data and their often larger measuring uncertainties.
- uncertainties on the interaction cross-sections of the neutrons. Similarly to those of the protons, these cross-sections were based on evaluated data below 150 MeV and on the Bertini & Dresner models above 150 MeV.
- uncertainties related to unmodelled objects that could cause a non-negligible attenuation of the high-energy neutron flux;
- uncertainties on the average concrete composition;
- the uncertainty on the average concrete density (in a conservative approach, a density of 2.30 g/cm^3 was defined in the simulations ,while the true density should in principle be ≥ 2.35 g/cm^3);
- uncertainties on the traversed concrete thicknesses;
- uncertainties related to presence of steel reinforcing bars and potential inhomogeneities in the concrete;
- uncertainties on the positioning of the WENDI-2;
- uncertainties on the angular response of the WENDI-2;
- uncertainties potentially related to the applied statistical treatment and variance reduction technique;

Future work should be dedicated to estimating the different uncertainties on these shielding simulations. As a first step in this direction, sensitivity analyses regarding the selected physics models and the concrete composition will be presented in the following chapter.

CHAPTER V
Sensitivity analyses for the MCNPX simulations

V-1 Introduction

As explained in Chapter IV, several sources of uncertainty affect the Monte Carlo simulations of secondary neutrons inside proton therapy facilities. Due to some of these uncertainties, the simulated neutron doses behind the ~2 m thick shielding are overestimated by at least a factor of ~2 with respect to on-site measurements. It is however unclear which sources of uncertainty play the most important role in these overestimates. In this chapter, we will try to assess the impact of two main simulation parameters:

- the choice of the physics models for the interactions of protons and neutrons of more than 150 MeV. In MCNPX, several models are indeed available for the intranuclear cascade and for the evaporation.

- the average elemental composition of the concrete and its density.

V-2 Methodology

V-2.1 Modelled geometry

Our sensitivity analyses for the MCNPX simulations of proton therapy rooms were carried out for a simplified geometrical model, consisting of a spherical concrete shell with an inner radius of 5 m and a thickness of 3 m, as shown in figure **V-1**. A 60 x 60 x 60 cm^3 water phantom at the centre of the sphere was irradiated by a thin proton beam of 230 MeV (a pencil beam as in section **III-2.1.2**).

Ten-degree polar-angle intervals were defined with respect to the Z-axis (the proton beam axis; see figure **V-1**). Within these eighteen polar-angle intervals, the neutron fluence spectra were calculated at different depths inside the concrete shell and were folded with the fluence-to-H*(10) conversion coefficients from ICRP Publication 74 to obtain the neutron H*(10).
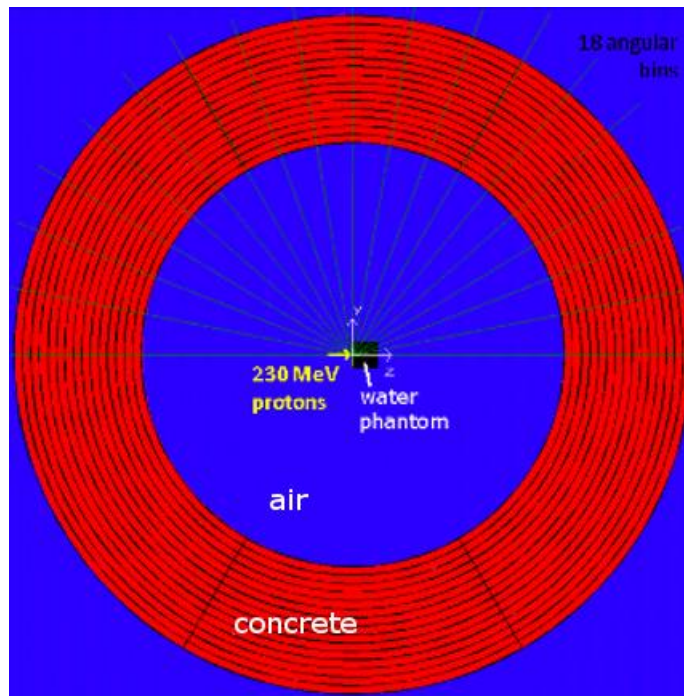
Figure V-1 – ZY cut through the modelled geometry representing a water phantom irradiated by a 230 MeV proton pencil beam, inside a spherical concrete shell with an inner radius of 5 m and a thickness of 3m.

For the calculation of the neutron fluence spectra, F4:n tallies in association with an E card were defined inside 2 cm thick cells, situated entirely inside the concrete, except for those at 3 m depth (which were defined in the surrounding air). In what follows, a spectrum calculated in a tally cell defined between a depth of x meter and $(x + 0.02)$ meter will simply be referred to as "the spectrum at x meter depth".

V-2.2 Materials and cross-sections

The material definitions of the NIST 'Portland' concrete, the water and the air were the same as in Chapter III. The same evaluated cross-section libraries for proton and neutron interactions were used (see table **III-1 on p. 128**):

- For most isotopes, evaluated cross-sections were used up to 150 MeV (mainly from the endf70prot [100,192] and endf70 [100,218] libraries).

- For some isotopes, evaluated data was only available up to 20 MeV.

When defining other concrete compositions, for the sensitivity study of section **V-2.3**, a maximum use of recent evaluated cross-section data was sought too.

High-energy interactions for which no evaluated cross-section data was available were simulated with built-in physics models for the intranuclear cascade, the pre-equilibrium and the evaporation (or the Fermi break-up for light nuclei). For the intranuclear cascade and the evaporation, the MCNPX user can choose amongst

several models. In the sensitivity study regarding physics models, both the intranuclear cascade and the evaporation models were systematically varied. In the sensitivity study regarding the concrete composition, the default physics settings, *i.e.* the Bertini model for the intranuclear cascade and the Dresner model for the evaporation, were used like in the simulations of Chapter III.

V-2.3 Sensitivity to the physics models

To assess the influence of the selected physics models on the simulation results, a simulation was run for each possible combination of the intranuclear cascade and evaporation models (used for proton and neutron interactions above 150 MeV). These combinations have already been listed previously, in table **II-2** on **p. 58**. A brief description of these models has also been given in section **I-5.4**. The CEM03 model cannot be combined with other models because it handles not only the intranuclear cascade, but also the pre-equilibrium and the evaporation.

In these simulations, the same concrete composition was used as in our simulations of Chapter III, namely the NIST composition of ordinary 'Portland' concrete.

V-2.4 Sensitivity to the concrete composition

Concrete is a composite material consisting mostly of:

- aggregates; typically a mix of coarse aggregates, such as gravel or crushed stone, and fine aggregates, like sand. The aggregates generally represent 60 – 75% of the concrete volume (or 70 – 85 % by mass) [243].

- a binder that holds the aggregates together: e.g. hardened cement paste, which is obtained by mixing cement powder with water.

Next to these components, concrete may also contain a few admixtures, e.g. $CaCl_2$ or synthetic organic molecules, which modify certain of its properties related, for instance, to its workability, setting or hardening.

Aggregates are usually a mixture of minerals and rocks. Minerals have a relatively well-defined chemical composition and a specific internal structure, whereas rocks consist of a combination of several minerals. A large number of minerals and rocks can potentially constitute naturally occurring aggregates (see table **V-1**). Many elements are represented in these, such as O, Si, Al, Ca, Na, K, Fe, Mg, C, H, S …

In the case of Portland concrete, the main component of cement powder is pulverized clinker. For the production of clinker, several raw materials are used as sources of calcium, silica (SO_2), alumina (Al_2O_3) and/or iron. Examples of these raw materials are clay, limestone, calcite, marl, shale, sand, fly ash, iron ore *etc.* [244]. Clinker is produced by making the grinded raw materials react chemically under high temperatures. The resulting product consists mostly of hydraulic calcium silicates ($3CaO.SiO_2$ and $2CaO.SiO_2$), and, to a lesser extent, of calcium aluminates ($3CaO.Al_2O_3$) and calcium aluminoferrites ($4CaO.Al_2O_3.Fe_2O_3$) [245]. Eventually, the clinker is pulverized and mixed with a small amount of gypsum ($CaSO_4.2H_2O$) to obtain cement powder [245].

Table V-1 – Mineral and rock constituents in aggregates [243].

Minerals	Igneous rocks	Metamorphic rocks
Silica	Granite	Marble
Quartz	Syenite	Metaquartzite
Opal	Diorite	Slate
Chalcedony	Gabbro	Phyllite
Tridymite	Peridotite	Schist
Cristobalite	Pegmatite	Amphibolite
Silicates	Volcanic glass	Hornfels
Feldspars	Obsidian	Gneiss
Ferromagnesian	Pumice	Serpentinite
Hornblende	Tuff	
Augite	Scoria	
Clay	Perlite	
Illites	Pitchstone	
Kaolins	Felsite	
Chlorites	Basalt	
Montmorillonites		
Mica	**Sedimentary rocks**	
Zeolite	Conglomerate	
Carbonate	Sandstone	
Calcite	Quartzite	
Dolomite	Graywacke	
Sulfate	Subgraywacke	
Gypsum	Arkose	
Anhydrite	Claystone, siltstone,	
Iron sulfide	argillite, and shale	
Pyrite	Carbonates	
Marcasite	Limestone	
Pyrrhotite	Dolomite	
Iron oxide	Marl	
Magnetite	Chalk	
Hematite	Chert	
Goethite		
Imenite		
Limonite		

When mixing water with cement powder, a chemical reaction called hydration occurs in several stages. A saturated ion solution is formed and, progressively, different crystallization phases start to appear. An overview of the primary compound formation processes is given in table **V-2**. These phases evolve over time and as a function of the environmental humidity and temperature. The initial set of the concrete, in which the paste loses its plasticity, is largely due to the hydration of tricalcium silicate ($3CaO.SiO_2$). The latter also plays a role in the early strength gain. The hydration of dicalcium silicate ($2CaO.SiO_2$) is a slower process that contributes a lot to the strength development after the first week [244]. For the complete hydration of Portland cement, a water-to-cement ratio of 0.40 in mass is required [244]. With a lower ratio, some cement will remain unhydrated, whereas with a larger ratio, the excess water remains in capillary pores or may evaporate. Eventually, the water-to-cement ratio and the way in which the cement paste crystallizes influence the bulk density of the concrete. Concrete is thus a relatively complex material, of which the elemental composition and density depend on many parameters, such as the selected raw materials and admixtures, the mixing ratios, the placing methods, the moisture and temperature conditions during the hardening, the aging processes *etc*.

Table V-2 – Main chemical processes in the hydration of Portland cement [244]

2 ($3CaO•SiO_2$) Tricalcium silicate	+ 11 H_2O Water	= $3CaO•2SiO_2•8H_2O$ Calcium silicate hydrate (C-S-H)	+ 3 ($CaO•H_2O$) Calcium hydroxide
2 ($2CaO•SiO_2$) Dicalcium silicate	+ 9 H_2O Water	= $3CaO•2SiO_2•8H_2O$ Calcium silicate hydrate (C-S-H)	+ $CaO•H_2O$ Calcium hydroxide
$3CaO•Al_2O_3$ Tricalcium aluminate	+ 3 ($CaO•SO_3•2H_2O$) Gypsum	+ 26 H_2O Water	= $6CaO•Al_2O_3•3SO_3•32H_2O$ Ettringite
2 ($3CaO•Al_2O_3$) Tricalcium aluminate	+ $6CaO•Al_2O_3•3SO_3•32H_2O$ Ettringite	+ 4 H_2O Water	= 3 ($4CaO•Al_2O_3•SO_3•12H_2O$) Calcium monosulfoaluminate
$3CaO•Al_2O_3$ Tricalcium aluminate	+ $CaO•H_2O$ Calcium hydroxide	+ 12 H_2O Water	= $4CaO•Al_2O_3•13H_2O$ Tetracalcium aluminate hydrate
$4CaO•Al_2O_3•Fe_2O_3$ Tetracalcium aluminoferrite	+ 10 H_2O Water	+ 2 ($CaO•H_2O$) Calcium hydroxide	= $6CaO•Al_2O_3•Fe_2O_3•12H_2O$ Calcium aluminoferrite hydrate

In this study, the sensitivity of the MCNPX shielding simulation to the selected concrete composition was studied by means of elemental compositions found in literature. Twenty-nine ordinary concrete types, including 'NIST Portland', were compared. Their elemental composition, expressed in mass fractions, and their density are given in table **V-3** [236,246–253]. Ordinary concretes are commonly considered to contain up to 2% of hydrogen in mass [177]. In the present selection of compositions, the percentage mass of hydrogen ranges from 0.2% up to 2.0%. The densities vary between 2.10 g/cm^3 and 2.58 g/cm^3.

Composition (density in [g/cm³])	1 H	6 C	7 N	8 O	11 Na	12 Mg	13 Al	14 Si	15 P	16 S	17 Cl	19 K	20 Ca	22 Ti	24 Cr	25 Mn	26 Fe
Walker_01 (2.33)	0.002078	0.055823	0.000000	0.493391	0.000000	0.002087	0.005110	0.188081	0.000000	0.000824	0.000000	0.000000	0.249487	0.000000	0.000000	0.000000	0.003118
Walker_0-HW2 (2.26)	0.003100	0.000000	0.000000	0.440655	0.018158	0.037644	0.060673	0.215678	0.000886	0.000886	0.000000	0.006643	0.130647	0.004872	0.000000	0.001329	0.078831
Magnuson (2.14)	0.003319	0.105320	0.000000	0.499428	0.001411	0.094200	0.007859	0.042101	0.000000	0.002483	0.000523	0.009445	0.226317	0.001488	0.000000	0.000512	0.005595
Hanford dry (2.18)	0.004000	0.000000	0.000000	0.482102	0.002168	0.014094	0.069387	0.277549	0.000000	0.000000	0.000000	0.013010	0.080229	0.000000	0.000000	0.000000	0.057461
Los Alamos MCNP (2.25)	0.004530	0.000000	0.000000	0.512600	0.015270	0.000000	0.035550	0.360360	0.000000	0.000000	0.000000	0.000000	0.057910	0.000000	0.000000	0.000000	0.013780
Walker_02-b (2.20)	0.005230	0.001046	0.000000	0.513188	0.016735	0.002274	0.035471	0.352433	0.000000	0.000000	0.000000	0.013597	0.045475	0.000000	0.000000	0.000000	0.014552
Ordinary NBS 04 (2.35)	0.005558	0.000000	0.000000	0.498076	0.017101	0.002565	0.045746	0.315092	0.000000	0.001283	0.000000	0.019239	0.082941	0.000000	0.000000	0.000000	0.012398
Fermilab ordinary (2.34)	0.006000	0.000000	0.000000	0.498000	0.017000	0.003000	0.046000	0.315000	0.000000	0.001000	0.000000	0.019000	0.083000	0.000000	0.000000	0.000000	0.012000
SLAC A230 (2.30)	0.006100	0.054800	0.000000	0.510200	0.001100	0.043500	0.007000	0.202600	0.000000	0.002600	0.000000	0.002100	0.160200	0.000000	0.000000	0.000000	0.009800
Agosteo TSF-5.5 (2.31)	0.006152	0.174349	0.000000	0.408009	0.000000	0.032492	0.011610	0.034324	0.000000	0.000000	0.000000	0.000000	0.325373	0.000000	0.000000	0.000000	0.007690
Oak Ridge ORNL (2.30)	0.006187	0.175193	0.000000	0.410184	0.000271	0.032649	0.010830	0.034479	0.000000	0.000000	0.000000	0.001138	0.321287	0.000000	0.000000	0.000000	0.007784
Walker_0-HW1 (2.33)	0.006443	0.000000	0.000000	0.454038	0.017612	0.036512	0.058849	0.209192	0.000859	0.000859	0.000000	0.006443	0.126718	0.004725	0.000000	0.001289	0.076460
Gencel_HC20 (2.584)	0.007390	0.000000	0.000000	0.370260	0.000040	0.088510	0.007400	0.040940	0.000000	0.002400	0.000000	0.000070	0.352490	0.000040	0.000000	0.000240	0.130220
Rocky Flats (2.32)	0.007500	0.055200	0.000200	0.484900	0.006300	0.012500	0.021700	0.155000	0.000000	0.001900	0.000000	0.013700	0.230000	0.001000	0.000000	0.000000	0.010100
Gencel_HC10 (2.495)	0.007630	0.000000	0.000000	0.373450	0.000040	0.101160	0.007540	0.042370	0.000000	0.002550	0.000000	0.000080	0.395530	0.000020	0.000000	0.000120	0.069510
Gencel_PC00 (2.4)	0.007880	0.000000	0.000000	0.376840	0.000050	0.114640	0.007690	0.043890	0.000000	0.002720	0.000000	0.000090	0.441420	0.000000	0.000000	0.000000	0.004780
Walker_03 (2.39)	0.008368	0.049372	0.000000	0.476569	0.000000	0.023849	0.035565	0.143096	0.002929	0.002929	0.000000	0.001674	0.243515	0.000000	0.000000	0.001255	0.010879
Ordinary NBS 03 (2.35)	0.008485	0.050064	0.000000	0.473483	0.000000	0.024183	0.036063	0.145100	0.000000	0.002970	0.000000	0.001697	0.246924	0.000000	0.000000	0.000000	0.011031
Walker_05 (2.51)	0.008773	0.003190	0.000000	0.490888	0.011564	0.000798	0.052239	0.251226	0.000000	0.001475	0.000000	0.009969	0.096503	0.006779	0.000000	0.017945	0.048650
Ordinary Bashter (2.30)	0.009400	0.000900	0.000000	0.536600	0.004600	0.001200	0.013200	0.367400	0.000000	0.000800	0.000000	0.003100	0.056500	0.000000	0.000000	0.000000	0.006300
Walker_02-a (2.30)	0.009991	0.000999	0.000000	0.529974	0.015986	0.002172	0.033884	0.336664	0.000000	0.000000	0.000000	0.012989	0.043440	0.000000	0.000000	0.000000	0.013901
Regular Petrie (2.30)	0.010000	0.000000	0.000000	0.532000	0.029000	0.000000	0.034000	0.337000	0.000000	0.000000	0.000000	0.000000	0.044000	0.000000	0.000000	0.000000	0.014000
NIST Portland (2.30)	0.010000	0.001000	0.000000	0.529107	0.016000	0.002000	0.033872	0.337021	0.000000	0.000000	0.000000	0.013000	0.044000	0.000000	0.000000	0.000000	0.014000
Ordinary Aminian (2.35)	0.010000	0.001000	0.000000	0.532000	0.029000	0.000000	0.034000	0.339000	0.000000	0.000000	0.000000	0.003000	0.044000	0.000000	0.000000	0.000000	0.008000
Ordinary Yarar (2.41)	0.010000	0.002920	0.000000	0.517846	0.013140	0.001620	0.033664	0.304956	0.000000	0.000673	0.000000	0.009490	0.091830	0.000000	0.000000	0.000000	0.013861
Hanford wet (2.35)	0.012309	0.000000	0.000000	0.513359	0.002001	0.013009	0.064045	0.256179	0.000000	0.000000	0.000000	0.012008	0.074052	0.000000	0.000000	0.000000	0.053037
Hematite-serpentine Bashter (2.5)	0.012900	0.000000	0.000000	0.435100	0.000000	0.066400	0.016600	0.105300	0.000000	0.000900	0.000000	0.000000	0.059700	0.000000	0.000000	0.000000	0.303100
Serpentine Shultis (2.10)	0.015909	0.000909	0.000000	0.511818	0.004091	0.135000	0.019091	0.209091	0.000000	0.000000	0.000000	0.004091	0.068182	0.000000	0.000909	0.000000	0.030909
NIST ordinary (2.30)	0.022100	0.002484	0.000000	0.574930	0.015208	0.001266	0.019953	0.304627	0.000000	0.000000	0.000000	0.010045	0.042951	0.000000	0.000000	0.000000	0.006435

Table V-3 – Elemental composition, expressed in mass fractions, and density of the different concrete compositions found in literature.

'Hanford dry', containing 0.4% of hydrogen, represents a concrete that, initially, had the 'Hanford wet' composition (1.2% of hydrogen, see table **V-3**), but has been ageing for decades in a dry environment [236].

The concrete compositions containing serpentine minerals (e.g. $Mg_3(OH)_4Si_2O_5$) tend to have larger hydrogen contents thanks to the presence of hydroxyl groups in their aggregates. Serpentine minerals were originally formed during hydrothermal metamorphism at convergent plate boundaries under the oceans. They are particularly abundant at the oceanic crust/mantle boundary, but can also be found worldwide in places where remnants of an oceanic plate are exposed at the Earth's surface, such as in mountain chains (the Alps in Europe, for instance) or coastal regions [254,255]. Serpentine concrete is a fairly common choice for the shielding of nuclear reactors [256].

V-2.5 Variance reduction and statistical treatment

The variance reduction technique referred to as "geometry splitting and Russian roulette" was applied like in the simulations of Chapter III (see description in section **III-2.4**). The distribution of neutron importances adopted in this case is shown in figure **V-2**.

For each simulation, twenty-five runs with different pseudorandom number sequences were submitted in parallel and the results were combined by computing averages weighted by the MCNPX statistical uncertainties, in the same way as described in section **III-2.4**.

Twenty million histories were simulated in each of the twenty-five runs. For every individual run, the statistical uncertainties on the neutron H*(10) tallies were smaller than 10% at all depths and all polar angles up to at least 130°-140°.

A good sampling of the fluence spectra at high energies is particularly important because these neutrons drive the attenuation through the shield and generate most of the lower-energy neutrons present at large depths. At backward angles, the high-energy neutrons play this crucial role even though they are only present in very few numbers at the entrance of the shield. In the simulations based on the Bertini model, the sampling of the high-energy neutron fluence was satisfactory for polar angles up to 130°-140°. In the worst case (at 130°-140°, at 3 m depth), only the four energy bins between 88 MeV and 230 MeV had statistical uncertainties larger than 10% in the individual runs. The contribution of these bins to the simulated H*(10) was of ~15% at 3 m depth. For the simulation based on the CEM03 model, the sampling of the high-energy neutron fluence at 130°-140° was a little less satisfactory: at 3 m depth, the uncertainties on the results of the individual runs were of ~15% on all bins up to 88 MeV and of 20 – 50% on the four last bins. At 80°-90°, the sampling was however fully satisfactory at all depths.
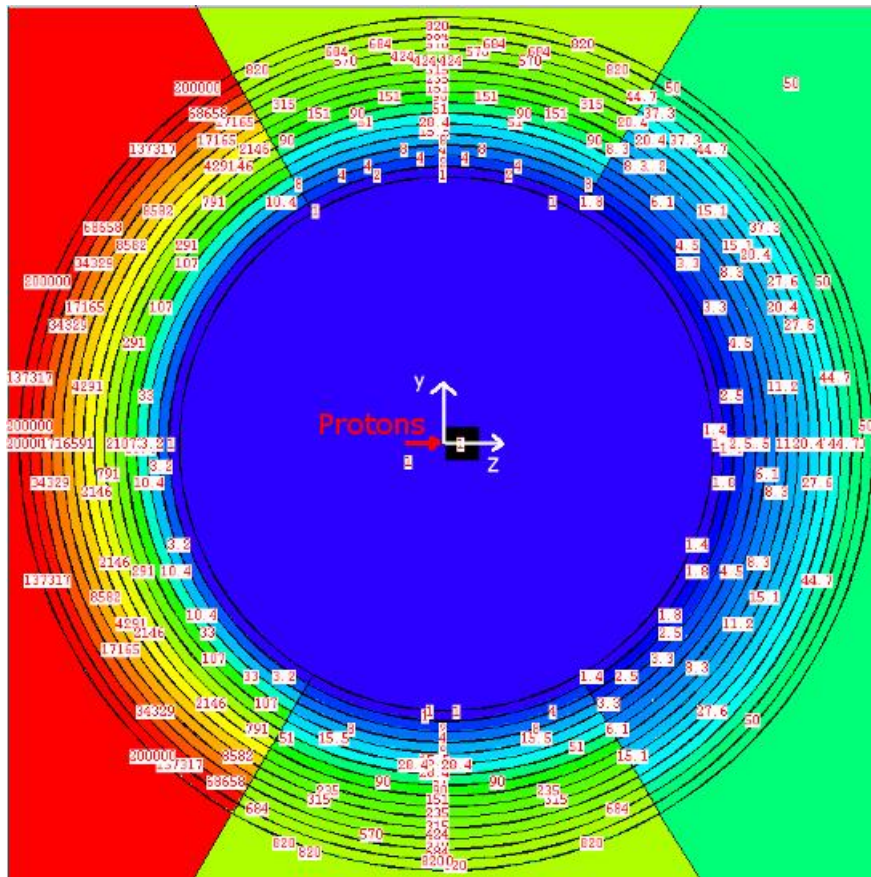
Figure V-2 – Variance reduction for the neutron transport through the spherical concrete shield.

V-3 Results

V-3.1 Sensitivity to the physics models

The figures **V-3**, **V-4**, **V-5** and **V-6** show simulation results obtained with the intranuclear cascade models Bertini, Isabel, INCL4 and CEM03, respectively. In each figure, the attenuation of the neutron H*(10) as a function of depth in the concrete is compared for the polar-angle intervals of 0° - 10°, 40° - 50°, 80° - 90° and 130° - 140°. Similar results for thick iron targets obtained with MCNPX, FLUKA or GEANT4 can be found in [257], [90,257] and in Chapter 2 of [184], respectively.

The results obtained with the Dresner and ABLA evaporation models are presented together in the figures **V-3**, **V-4** and **V-5**. The choice of the evaporation model has no significant impact on the simulated H*(10).

The choice of the intranuclear cascade model, on the contrary, does have a significant impact on H*(10). The figures **V-7** to **V-10** show that:

- The differences between the H*(10) simulated with different intranuclear cascade models tend to increase as a function of depth in the concrete.

- The Bertini model is, as expected, the most conservative model at forward emission angles, up to ~40°. At larger polar angles, however, the INCL4 model becomes the most conservative.

- The CEM03 model produces the smallest H*(10) at all considered polar angles and is thus the least conservative model in this case.

- At 0 m depth, the differences between the H*(10) obtained with the Bertini, Isabel and INCL4 models are quite small at any polar angle. Compared to the CEM03 results, they are larger by a factor of 1.2 – 1.3 at forward angles (up to ~90°). At backward angles, these differences become smaller.

- At 2 – 3 m depth, the Bertini model leads to H*(10) values that are larger than the CEM03 results by a factor of 1.5 – 1.8.

- With the Isabel model, the simulated H*(10) values globally follow the same trend as the Bertini results, but are a bit smaller (by factor of ~1.1).

- At 2 – 3 m depth, the differences between the INCL4 and the CEM03 results strongly depend on the polar angle. The smallest differences were obtained at 10° – 20°, where the INCL4 results are larger by a factor of 1.2 – 1.3 compared to the CEM03 results. The differences then quickly increase as a function of the polar angle, reaching a factor of ~3 at 80°- 90° and a factor of ~5 at 130°- 140°. The difference at 130°-140° could be a bit underestimated here due to the poorer sampling of the high-energy neutrons in the CEM03 simulation (which possibly resulted in a slight overestimate of H*(10) at large depths).
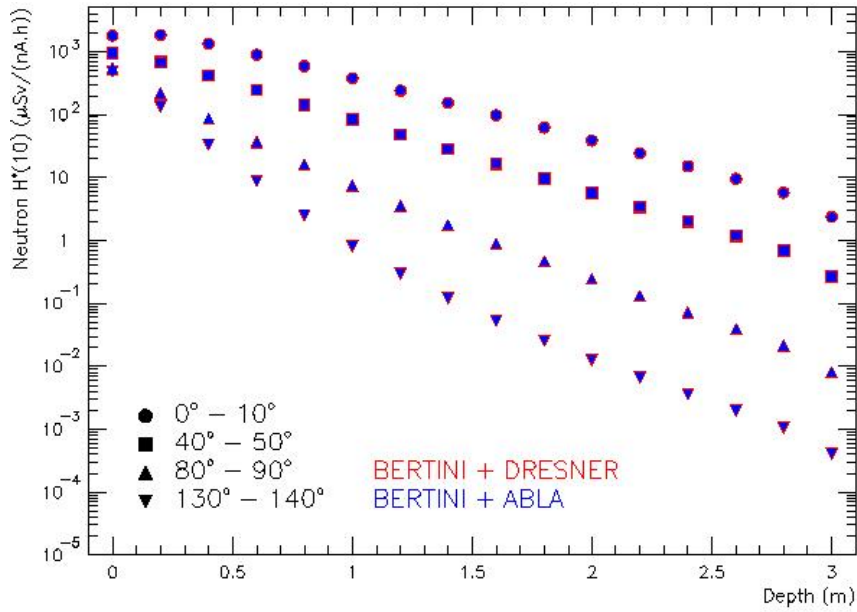
Figure V-3 – Neutron H*(10) attenuation curves for different polar-angle intervals, as simulated with the Bertini intranuclear cascade model. Concerning the evaporation, no significant differences were obtained when using the ABLA model (blue markers) instead of the Dresner model (red markers).
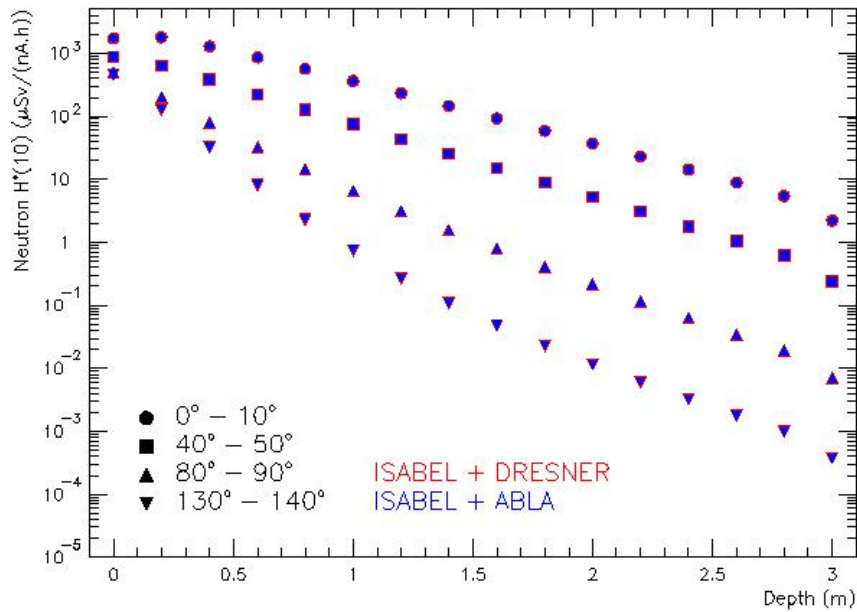
Figure V-4 – Neutron H*(10) attenuation curves for different polar-angle intervals, as simulated with the Isabel intranuclear cascade model. Concerning the evaporation, no significant differences were obtained when using the ABLA model (blue markers) instead of the Dresner model (red markers).
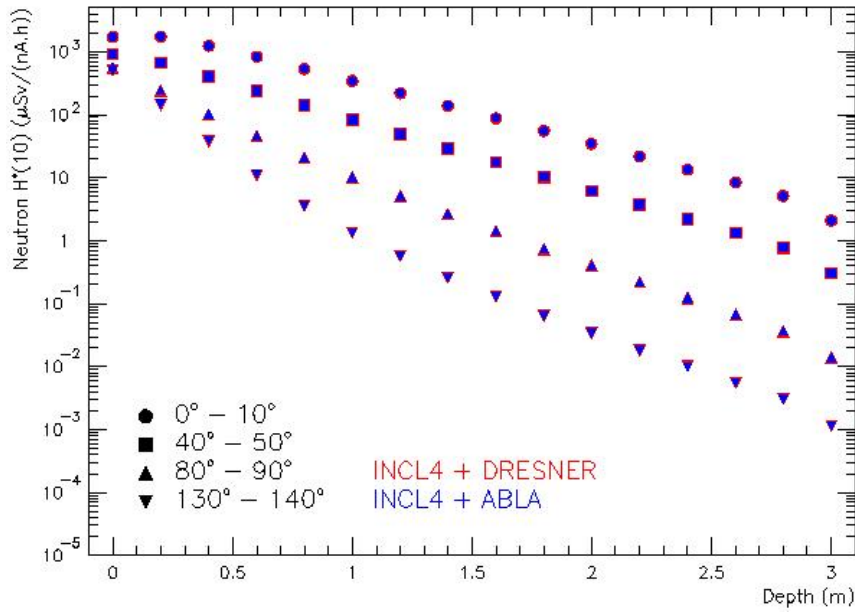
Figure V-5 – Neutron H*(10) attenuation curves for different polar-angle intervals, as simulated with the INCL4 intranuclear cascade model. Concerning the evaporation, no significant differences were obtained when using the ABLA model (blue markers) instead of the Dresner model (red markers).
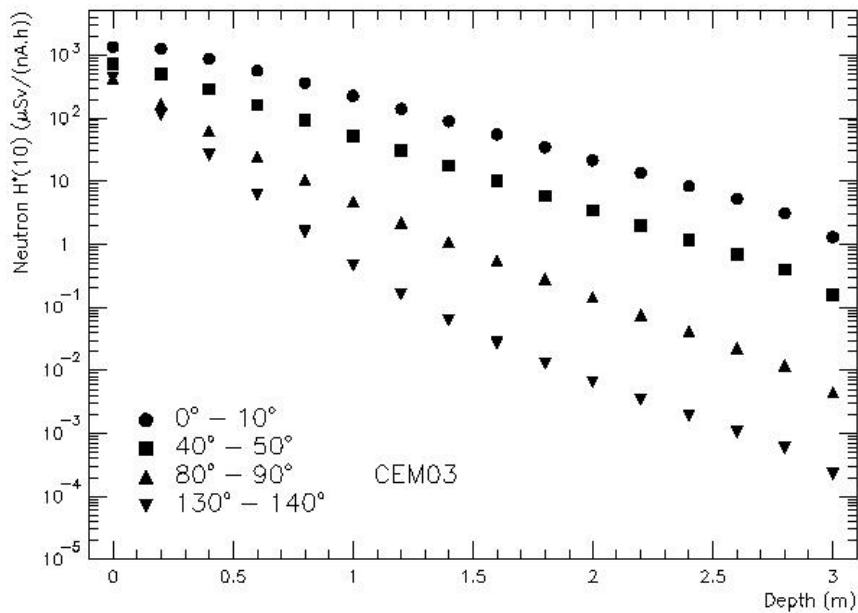
Figure V-6 – Neutron H*(10) attenuation curves for different polar-angle intervals, as simulated with the CEM03 model.
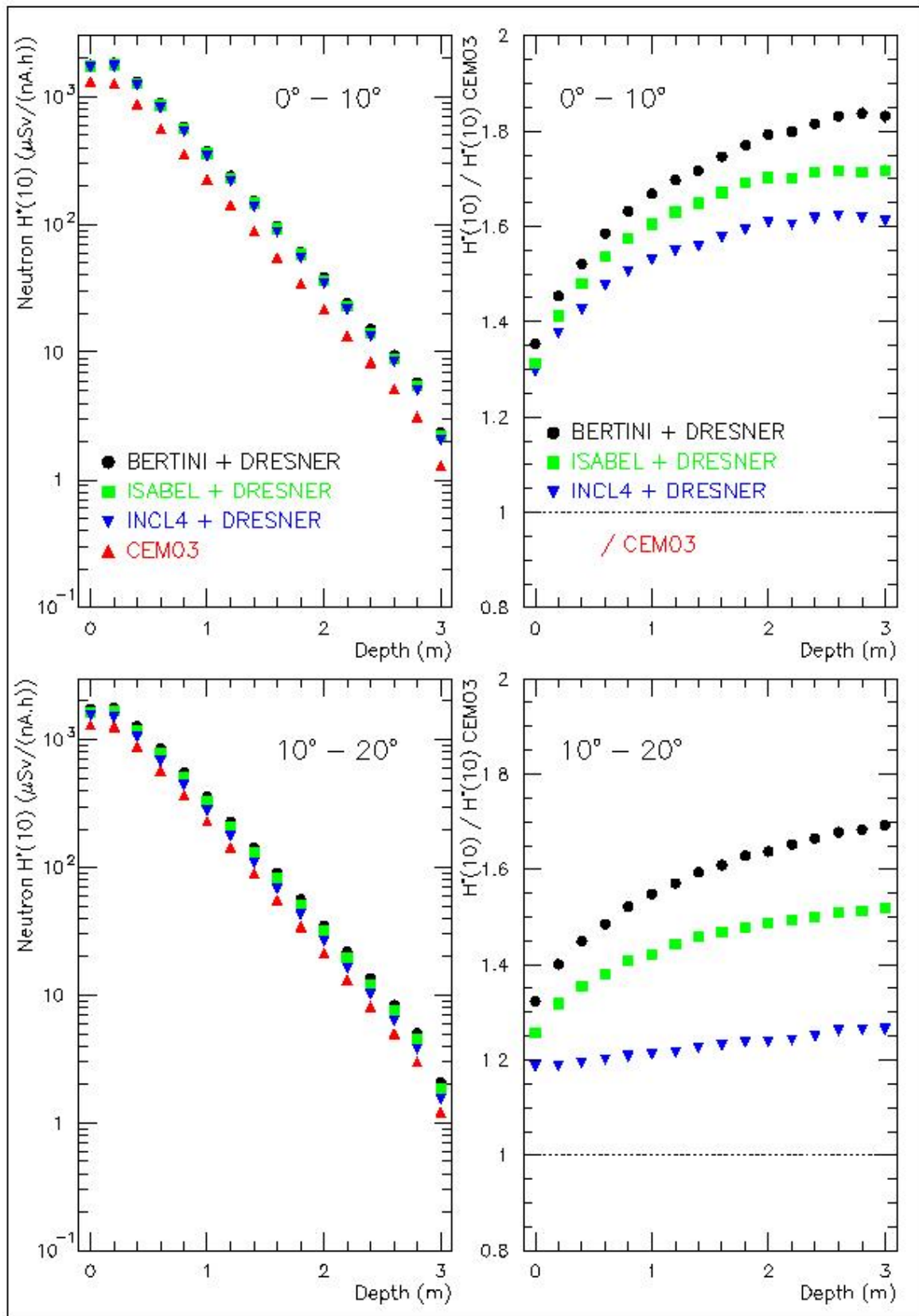
Figure V-7 – For the polar-angle intervals of 0°-10° and 10°-20° : (Left) Comparison of the neutron H*(10) attenuation profiles obtained with the different intranuclear cascade models: Bertini, Isabel, INCL4 and CEM03. (Right) Ratio of the neutron H*(10) attenuation profile obtained with the Bertini, Isabel or INCL4 model to the one obtained with the CEM03 model.
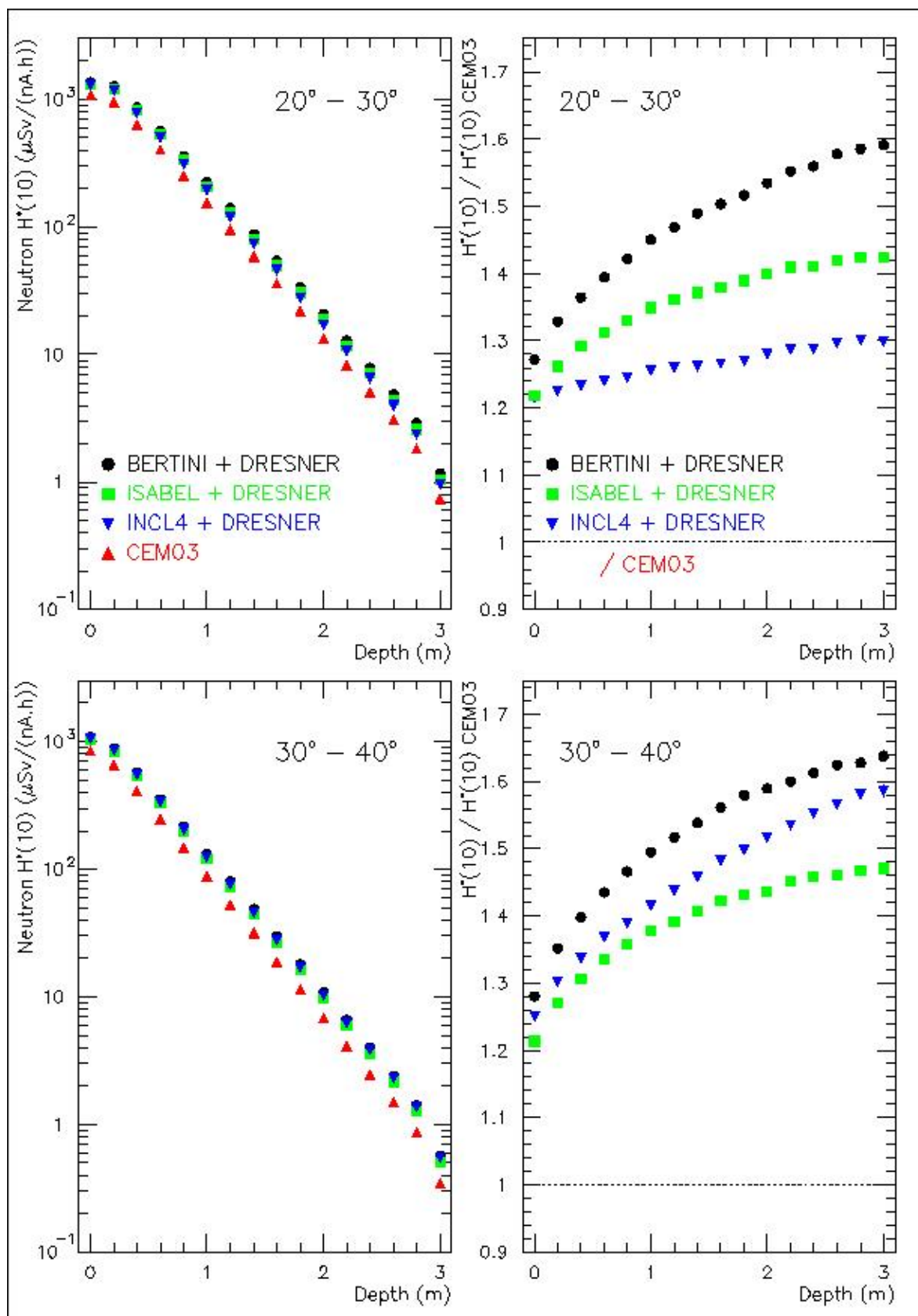
Figure V-8 – For the polar-angle intervals of 20°-30° and 30°-40° : (Left) Comparison of the neutron H*(10) attenuation profiles obtained with the different intranuclear cascade models: Bertini, Isabel, INCL4 and CEM03. (Right) Ratio of the neutron H*(10) attenuation profile obtained with the Bertini, Isabel or INCL4 model to the one obtained with the CEM03 model.
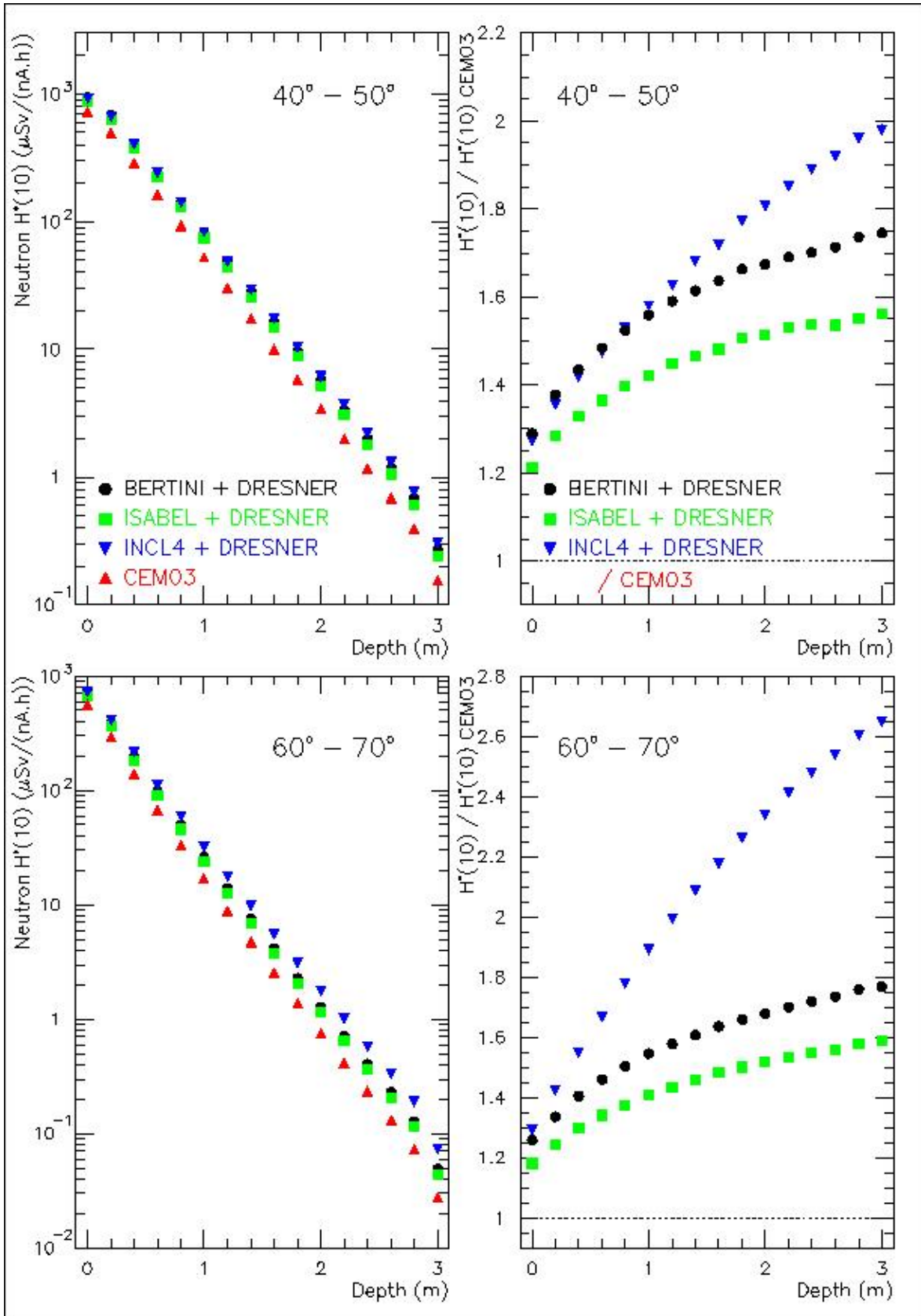
Figure V-9 – For the polar-angle intervals of 40°-50° and 60°-70° : (Left) Comparison of the neutron H*(10) attenuation profiles obtained with the different intranuclear cascade models: Bertini, Isabel, INCL4 and CEM03. (Right) Ratio of the neutron H*(10) attenuation profile obtained with the Bertini, Isabel or INCL4 model to the one obtained with the CEM03 model.
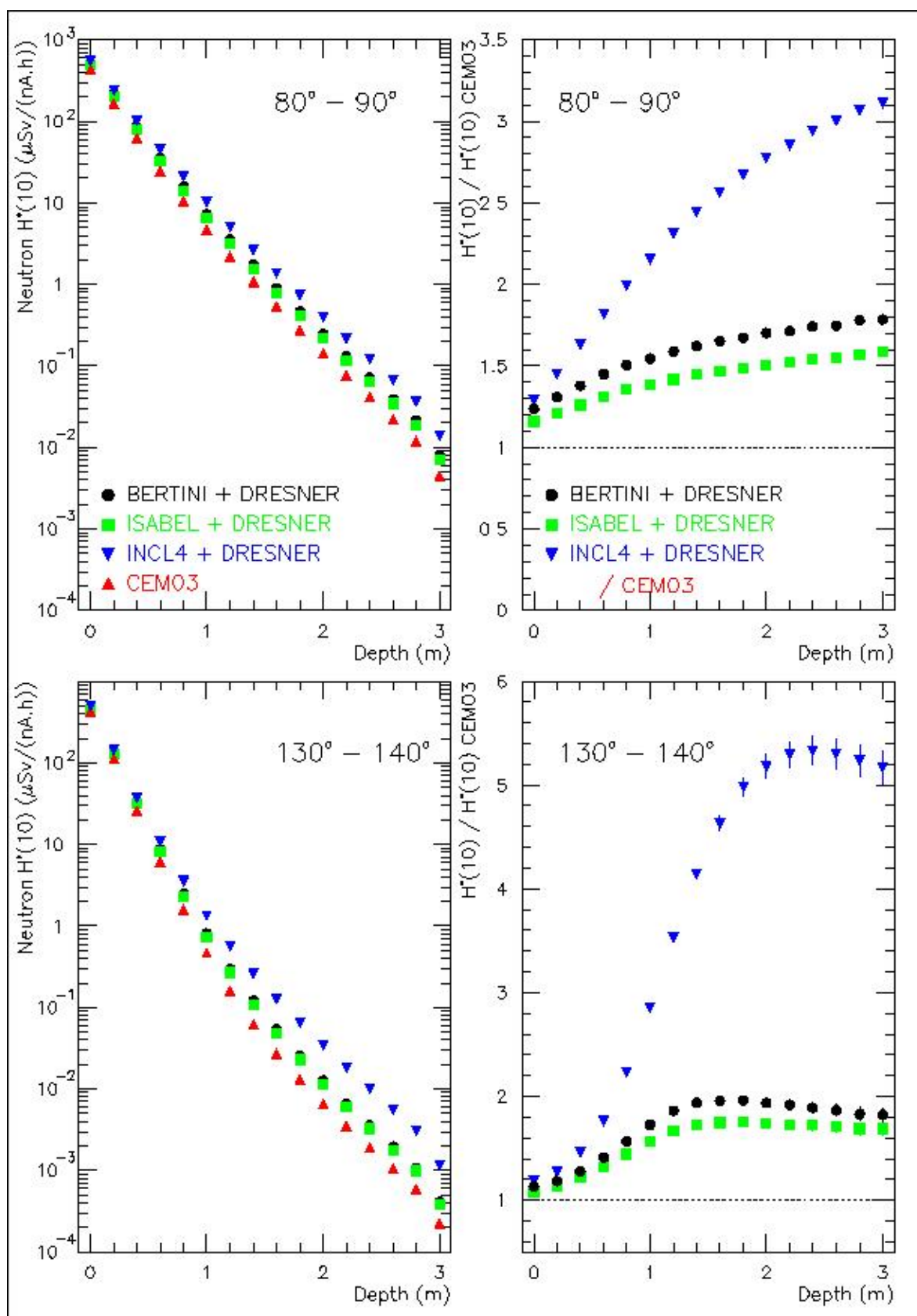
Figure V-10 – For the polar-angle intervals of 80°-90° and 130°-140° : (Left) Comparison of the neutron H*(10) attenuation profiles obtained with the different intranuclear cascade models: Bertini, Isabel, INCL4 and CEM03. (Right) Ratio of the neutron H*(10) attenuation profile obtained with the Bertini, Isabel or INCL4 model to the one obtained with the CEM03 model.

A comparison of the neutron spectra obtained with each intranuclear cascade model at different depths is presented in the figures **V-11**, **V-12** and **V-13**, for the polar-angle intervals of 0° – 10°, 80° – 90° and 130° – 140°, respectively.

In the spectra at 0 m depth, large differences due to the choice of the intranuclear cascade model mostly appear for neutrons of more than ~100 MeV at forward angles, and neutrons of more than ~50 MeV at backward angles (see close-ups in figure **V-14**). In these high-energy bins, the fluence can vary by up to a factor of a few (or more) depending on the selected intranuclear cascade model.

Neutrons of more than ~50 MeV are capable of a creating a chain of intranuclear cascades throughout the shield. As a consequence, they continuously generate evaporation neutrons at all depths. Even when they are present in very few numbers in the spectrum at 0 m depth, nearly all evaporation neutrons and lower-energy neutrons present at 2 – 3 m depth have been generated by them in outer layers of the shield. Therefore, these high-energy neutrons produced in the water phantom strongly determine the total neutron fluence behind 2 – 3 m of concrete.

When selecting an intranuclear cascade model that increases the production of high-energy neutrons by the protons, it leads to an increased production of evaporation neutrons inside the shield. In other words, the differences that mostly affect the high-energy neutron fluence at 0 m depth create differences on the rest of the spectrum, which progressively increase as a function of depth. This is for instance illustrated in figure **V-15**, which shows the ratio of the spectrum obtained with the Bertini model to the spectrum obtained with the CEM03 model, for different depths in the concrete.

Somehow, this phenomenon is a sort of "less pronounced version" of the one that causes an increase as a function of depth of the discrepancies between the H*(10) at different polar angles. For example, at 0 m depth, the difference between H*(10) values at 0°-10° and 130°-140° is smaller than one order of magnitude, whereas at 2 – 3 m depth this difference becomes larger than three orders of magnitude (see for instance figure **V-3**). This is a drastic example since, at 0 m depth, the fluence of neutrons of more than 100 MeV is more than three orders of magnitude larger at 0°-10° than at 130°-140° (see figure **V-14**).

In the same way, it appeared in this study that the ratio of H*(10) values obtained at 3 m depth with two different intranuclear cascade models is approximately equal to the ratio of the fluences at 0 m depth of neutrons with energies greater than ~100 MeV. Concerning the production of these neutrons by the protons, the largest differences between the various intranuclear cascade models of MCNPX are obtained at backward angles. For this reason, the differences between H*(10) behind the shield are thus larger at backward angles than at forward angles.
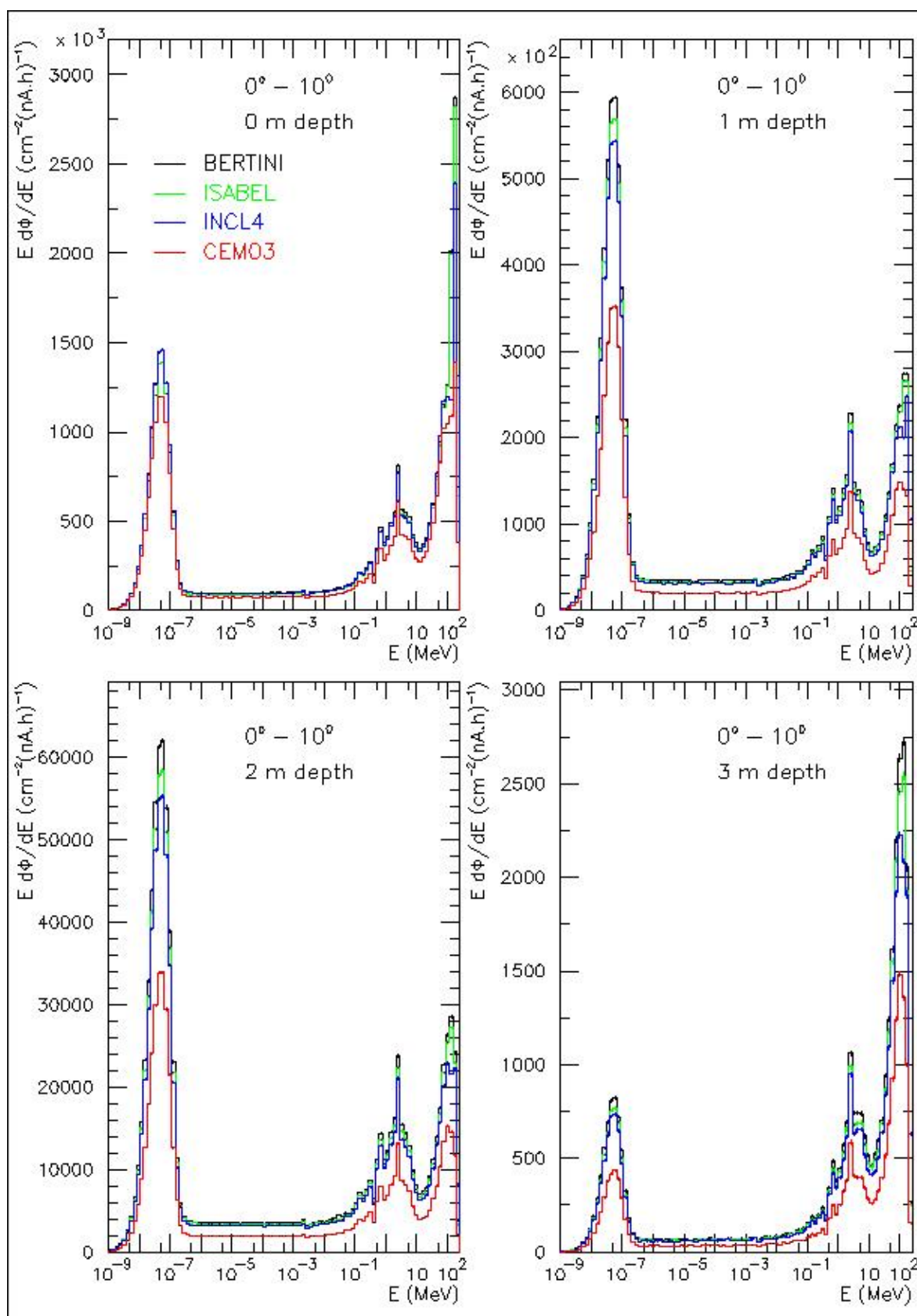
Figure V-11 – Comparison of the neutron fluence spectra in the 0° - 10° polar-angle interval simulated with each intranuclear cascade model (Bertini, Isabel, INCL4 and CEM03), at 0 m, 1 m, 2 m and 3 m depth in the concrete.
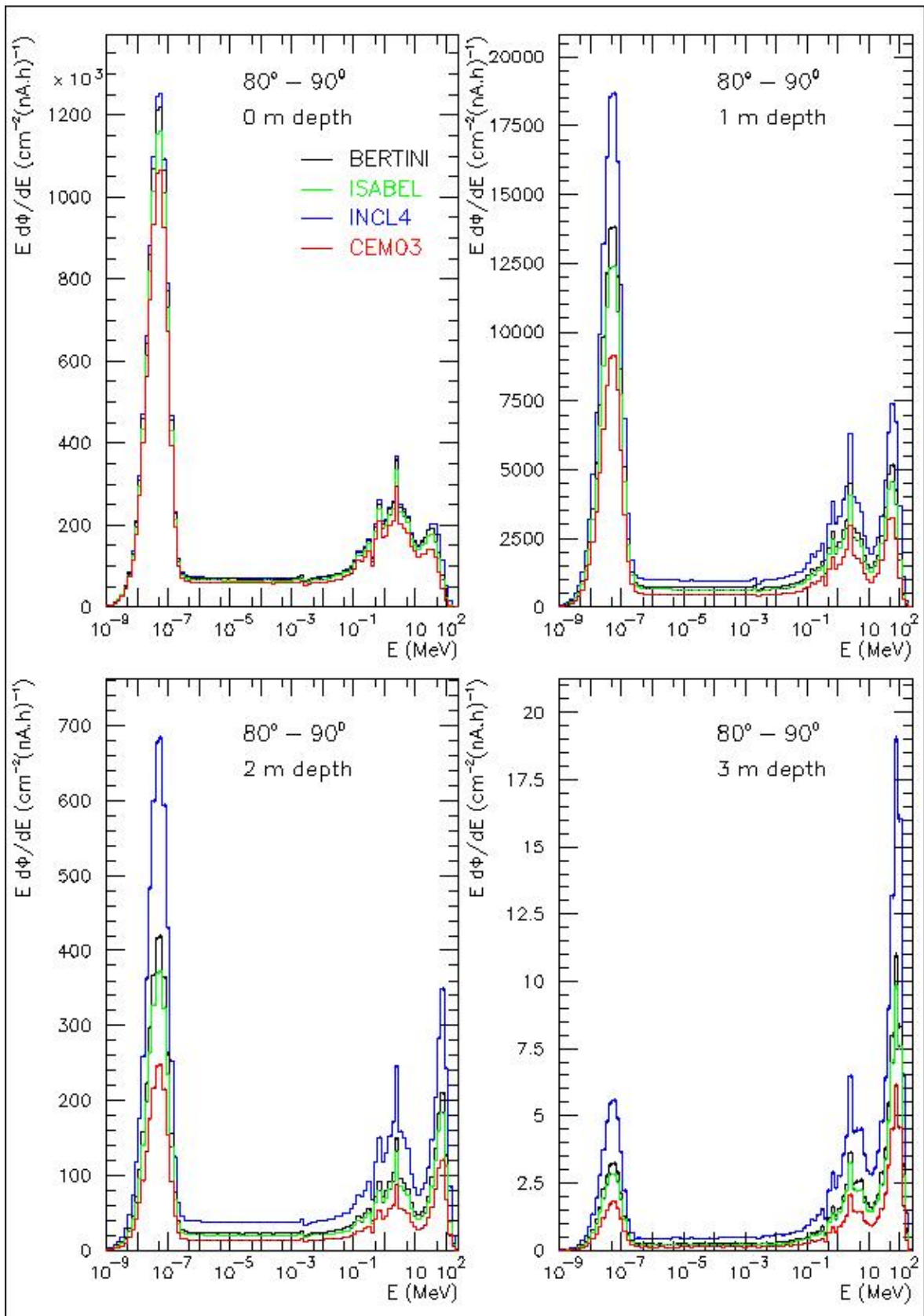
Figure V-12 – Comparison of the neutron fluence spectra in the 80° - 90° polar-angle interval simulated with each intranuclear cascade model (Bertini, Isabel, INCL4 and CEM03), at 0 m, 1 m, 2 m and 3 m depth in the concrete.
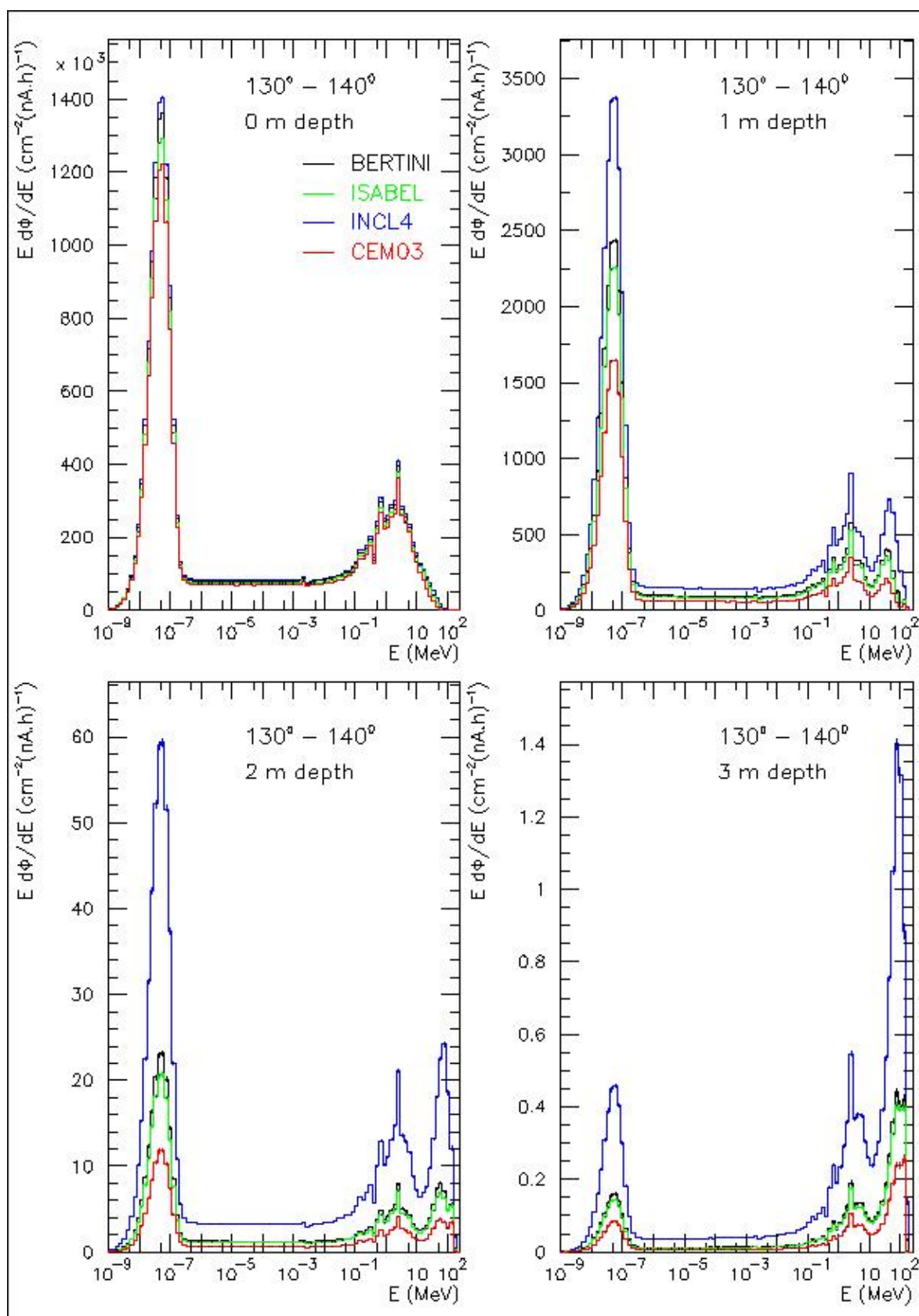
Figure V-13 – Comparison of the neutron fluence spectra in the 130° - 140° polar-angle interval simulated with each intranuclear cascade model (Bertini, Isabel, INCL4 and CEM03), at 0 m, 1 m, 2 m and 3 m depth in the concrete.
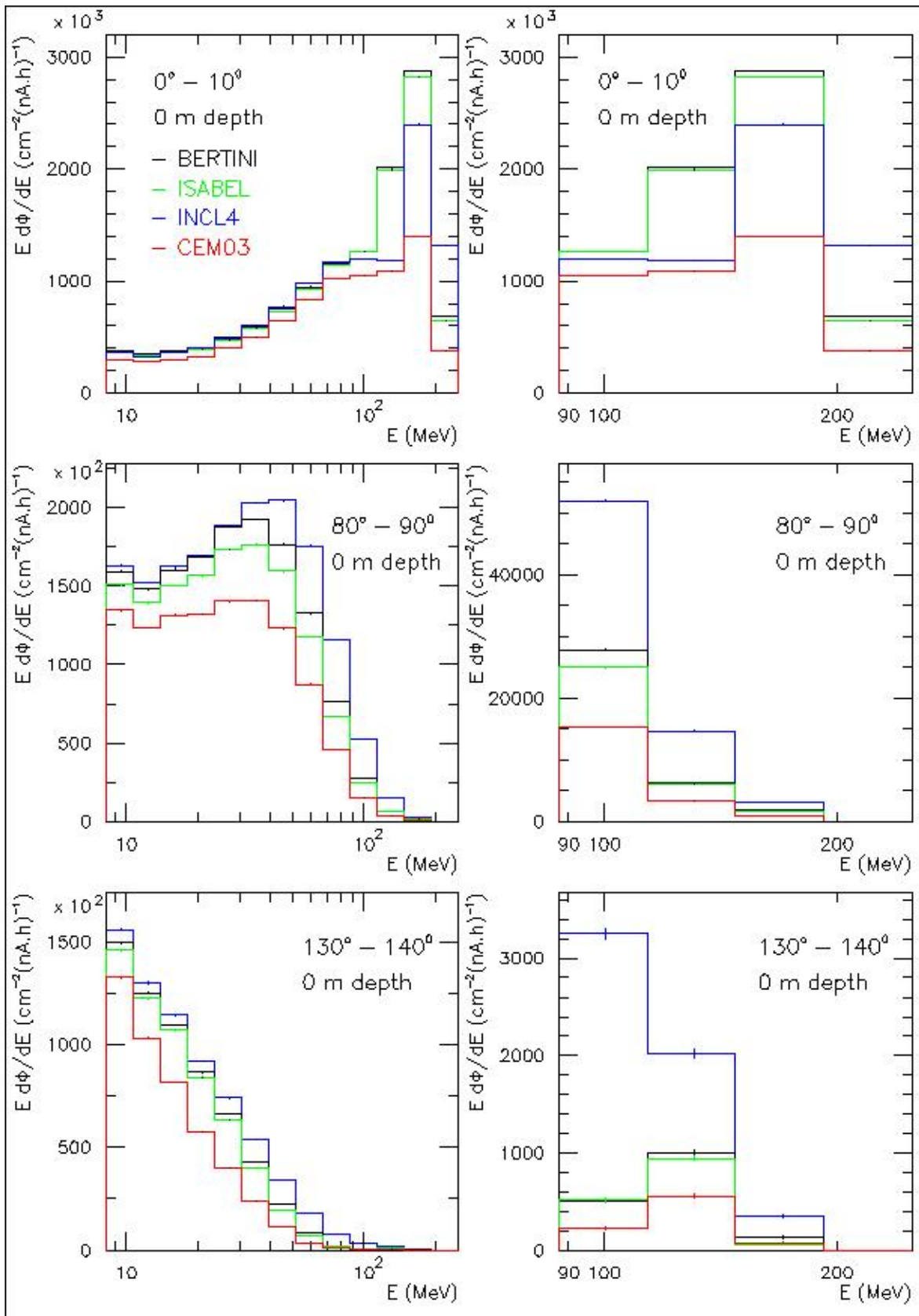
Figure V-14 – Close-ups on the high-energy part of the neutron fluence spectra simulated with each intranuclear cascade model (Bertini, Isabel, INCL4 and CEM03) at 0 m depth, in three different polar-angle intervals (0° - 10° ; 80° - 90° ; 130° - 140°).
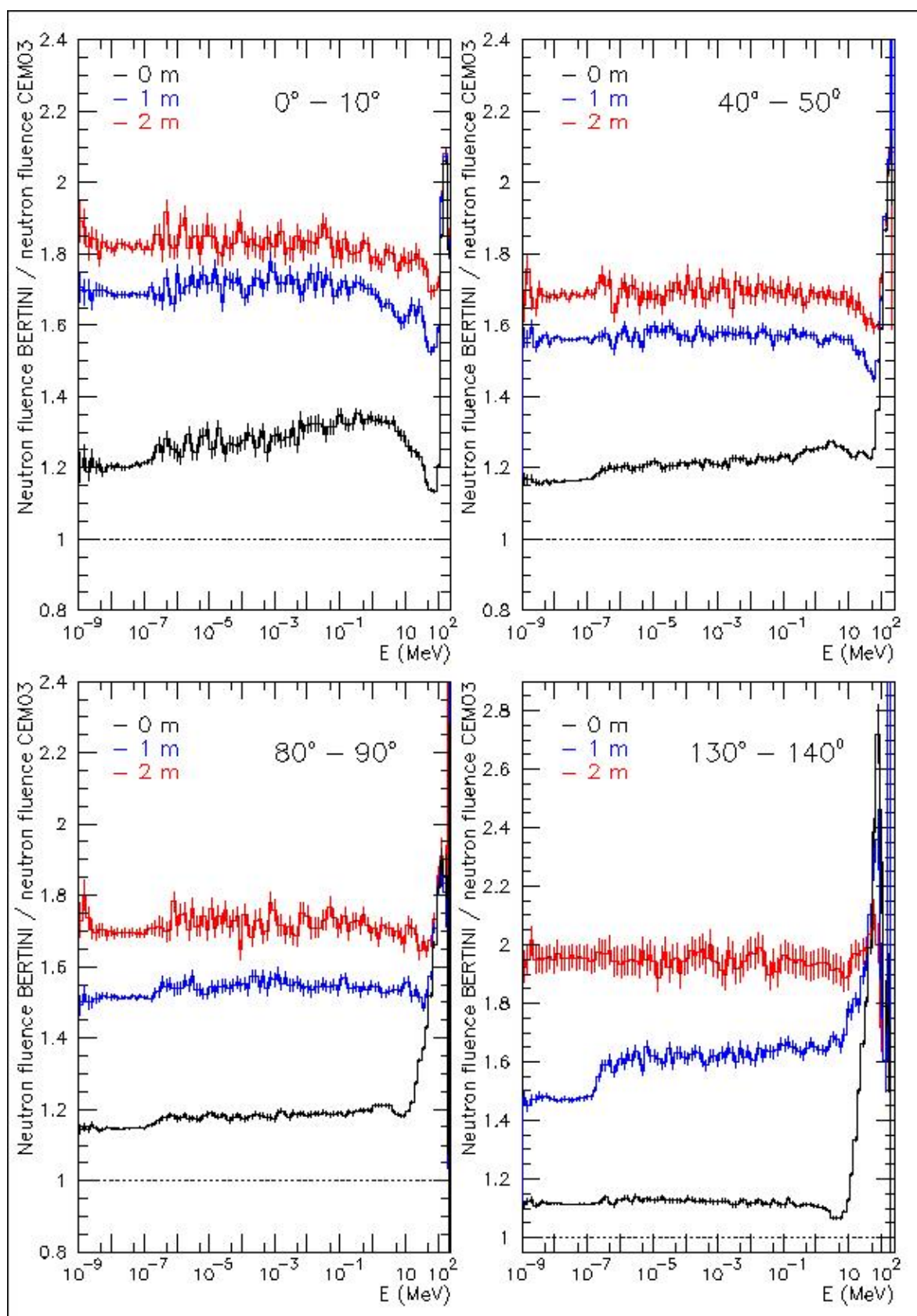
Figure V-15 – Ratio of the spectrum simulated with the Bertini model to the spectrum simulated with the CEM03 model, at different depths in the concrete (0m, 1m, 2m) and in different polar-angle intervals (0° - 10° ; 40° - 50° ; 80° - 90° ; 130° - 140°).

V-3.2 Sensitivity to the concrete composition

In figure **V-16**, the tested concrete compositions are ranked according to their shielding effectiveness, based on the simulated neutron H*(10) at 2 m depth in the concrete shell (in the polar-angle interval of 0°-10°). The elemental compositions of these concretes, in atoms per unit volume, are also graphically represented in figure **V-17**. Amongst these compositions, the most effective neutron shielding is obtained with 'NIST ordinary', the least effective with 'Hanford dry'. 'NIST ordinary' has an average density of 2.30 g/cm^3, but is the composition with the largest hydrogen content (2% in mass). 'Hanford dry' combines a small density (2.18 g/cm^3) and a small hydrogen content (0.4% in mass), but does neither have the smallest density nor the smallest hydrogen content.

Our results show that the effectiveness of the neutron shielding depends on a complex interplay of the different elements and the mass density. No absolute rule can be established with respect to the content of one element alone, although the hydrogen content does seem to constitute a particularly sensitive parameter. Figure **V-18** shows, amongst others, the hydrogen content as a function of H*(10) at 2 m depth in the 0°-10° polar angle interval (red curve). Hydrogen has one of the largest total cross-sections on average for thermal and intermediate neutrons. For evaporation neutrons up to ~1 MeV, its total cross-section is also relatively large. Moreover, hydrogen is the lightest element and thus allows for the largest energy transfers during elastic scattering. For these reasons, hydrogen has an excellent moderating power for neutrons up to ~1 MeV. It has in fact already been widely acknowledged that the hydrogen content of a concrete has a high impact on the attenuation of neutrons of less than ~20 MeV. Much fewer studies have however been published about the influence of the concrete composition on the attenuation of neutrons with wider energy distributions, ranging from thermal energies up to 230 MeV. The results of this study are however compatible with those of Brandl *et al.*, who published a similar study restricted to concrete thicknesses of 50 cm [258].

In figure **V-18**, other elements have been grouped according to their similar atomic masses and total neutron cross-sections. For energies up to ~1 MeV, carbon and oxygen have smaller total neutron cross-sections on average than hydrogen, but they are light elements. That makes them in principle better neutron moderators than elements such as e.g. silicon and calcium, which are not only heavier but also have smaller cross-sections below ~1 MeV. Heavy elements such as iron are, despite their relatively large total cross-sections, inefficient moderators below ~10 MeV since the energy transfers in elastic scattering tend to be small. Their neutron capture cross-section at thermal energies is however quite large, which means they are relatively good absorbers of thermalized neutrons. They also have the largest total cross-sections above 10 MeV, but the non-elastic neutron reactions lead to the generation of additional neutrons in the evaporation stage. On the whole, these heavy elements,

which are often present in small quantities, do not seem to have a determining impact on the shielding effectiveness. However, for the two serpentine concretes, which have very similar compositions, a larger iron content at the expense of magnesium and silicon appears to have a positive impact on the shielding effectiveness: see 'Hematite-serpentine Bashter' (30% iron in mass) and 'Serpentine Shultis' (3% iron in mass) in figure **V-17.**
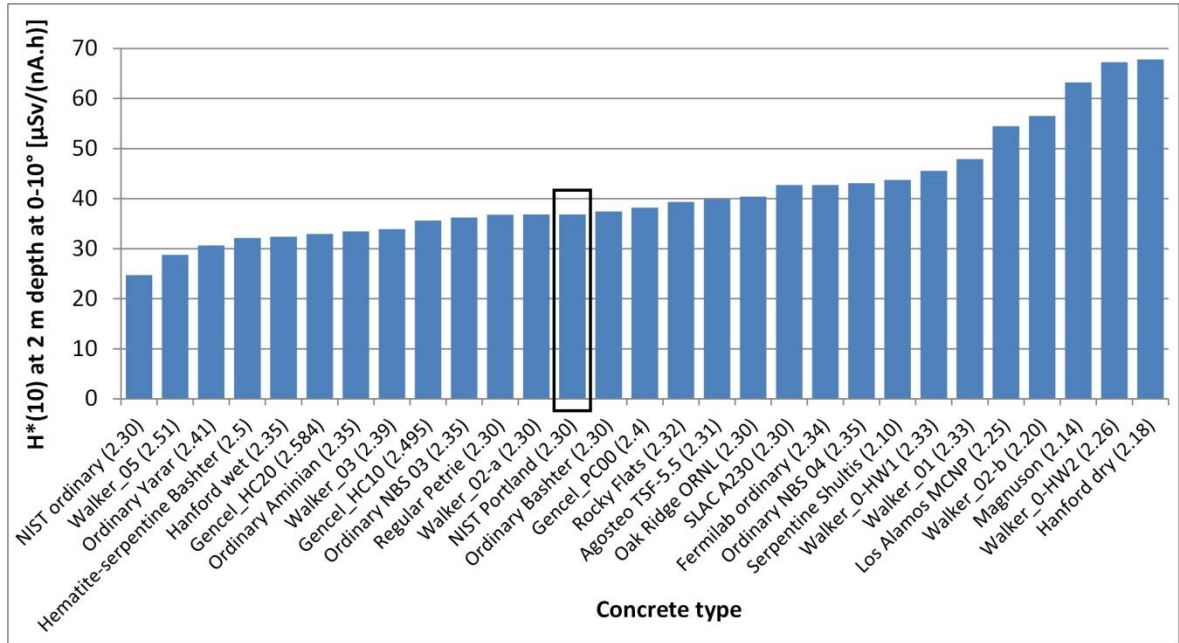
Figure V-16 – Neutron H*(10) at 2 m depth in the 0°-10° polar-angle interval, as a function of the selected concrete composition.
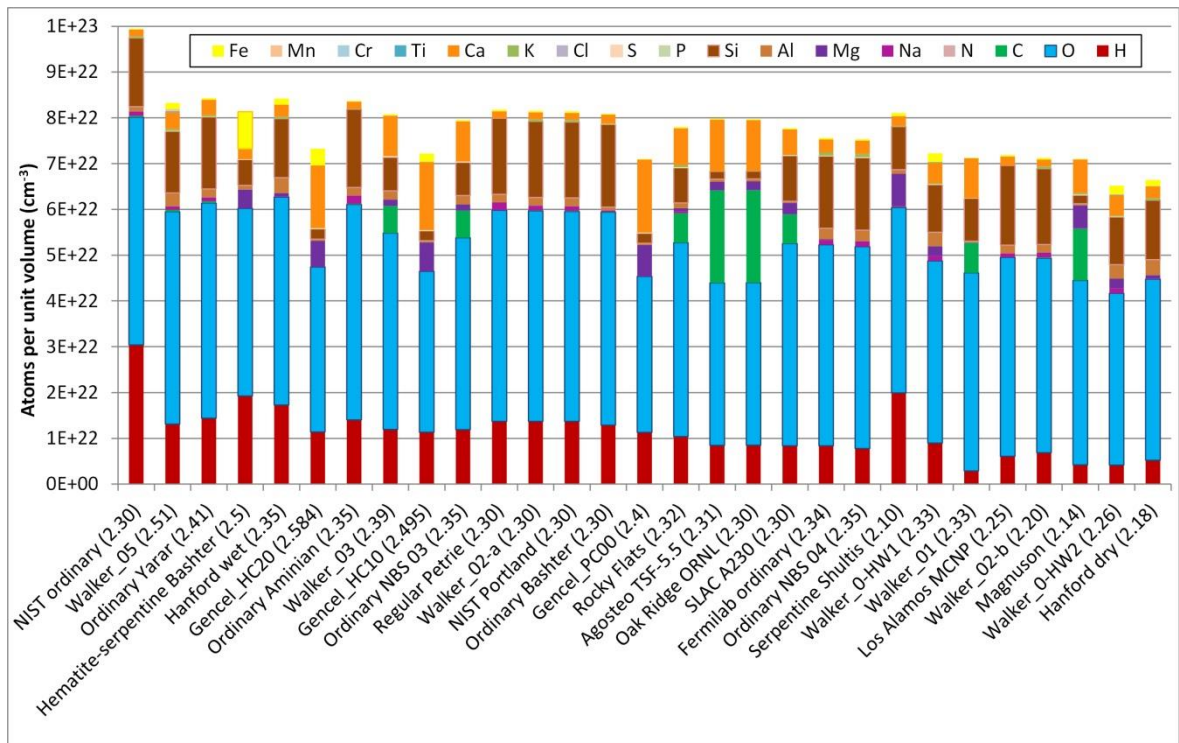
Figure V-17 – Overview of the elemental compositions in atoms per unit volume for the concrete types cited in the previous figure.
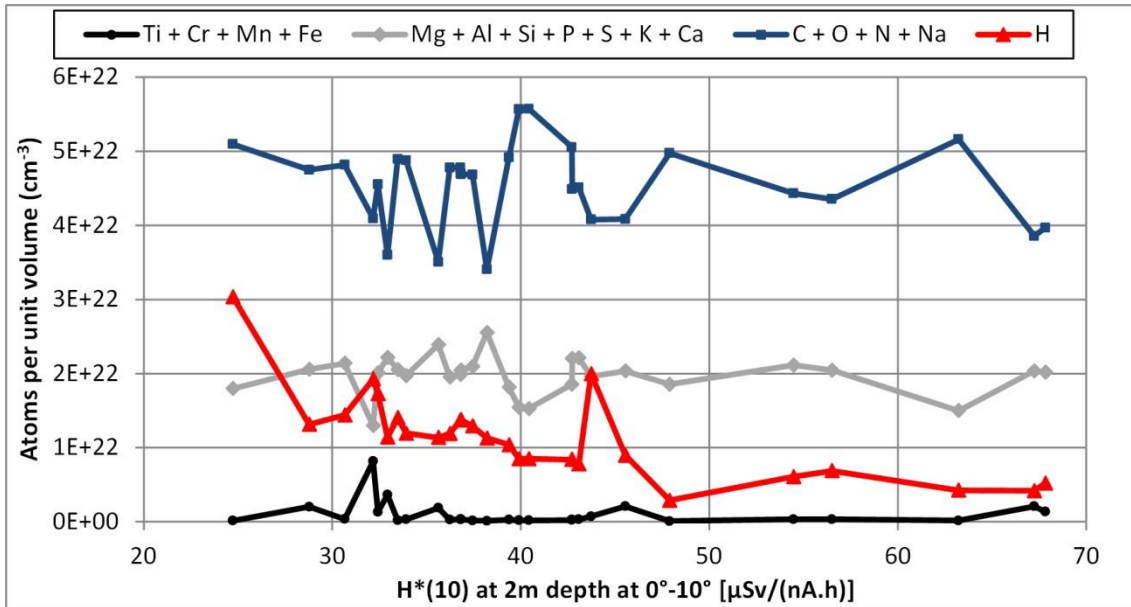
Figure V-18 – Relationship between the number of atoms per unit volume, for three groups of elements having similar total neutron cross-sections, and the neutron H*(10) obtained with the corresponding concrete composition at 2 m depth in the 0° - 10° polar-angle interval. The lines connecting the dots are only a guide for the eye.

In our selection of ordinary concrete compositions, the concretes with larger mass densities tend to provide the best neutron shields, but the relationship between the density and H*(10) at 2 m depth is far from monotonic, due to compensating effects related mostly to the hydrogen content (see figure **V-19**).
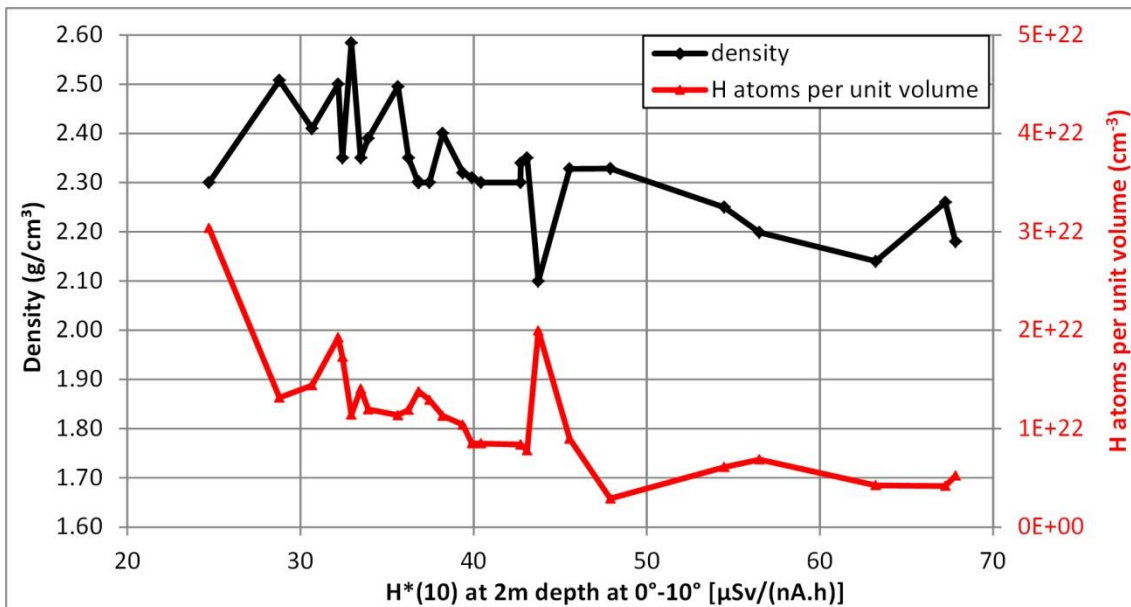
Figure V-19 – Mass density and hydrogen content (in atoms per unit volume) of the concrete, as a function of the neutron H*(10) obtained with the corresponding concrete composition at 2 m depth in the 0° - 10° polar-angle interval. The lines connecting the dots are only a guide for the eye.

The neutron H*(10) attenuation profiles through the concrete, in different polar-angle intervals, are shown in the figures **V-20** and **V-21** for the concrete compositions 'NIST ordinary' and 'Hanford dry', as well as for the composition of reference, 'NIST Portland'. The ratios of the H*(10) profile obtained with 'NIST Portland' concrete to those obtained with 'NIST ordinary' or 'Hanford dry' are also shown in these figures.

At forward angles, the discrepancies between the H*(10) values obtained with different concrete compositions increase monotonically as a function of depth in the concrete. At 130°-140°, however, this increase remains monotonic only up to a depth of ~60 cm (see figure **V-21**). In the first ~60 cm of concrete, the H*(10) discrepancies increase faster for larger polar angles. Softer source spectra seem thus to be more sensitive to the studied variations of composition than harder source spectra. This is not surprising because the most obvious differences between the three considered concrete compositions concern the number of hydrogen atoms per unit volume (see figure **V-17**), and hydrogen is the most efficient moderator of neutrons below ~1 MeV.

The non-zero differences between H*(10) values at 0 m depth obtained with different concrete compositions (see figures **V-20** and **V-21**, right side) are probably due to the "cross-talk effect" from the inner surface of the spherical concrete shell. This effect, studied by Agosteo *et al.* in [90], refers to neutrons that were backscattered at the entrance of shield and then re-entered it in a different angular bin. By this mechanism, the concrete composition has an influence on the neutron spectrum even at 0 m depth. This effect mostly concerns low-energy neutrons, which are very sensitive to an increase in the hydrogen content of the concrete.

In the figures **V-20** and **V-21** (right side), one can also notice a drop in the H*(10) discrepancies behind the outer surface of the spherical shell, at 3 m depth. This drop is caused by the fact that fewer neutrons are being backscattered by the air and fewer evaporation neutrons are also being produced than inside the concrete shield. The emission of evaporation neutrons is indeed an isotropic process, which means that some of the neutrons produced in the concrete are emitted towards the inner surface of the shield. Due to this contribution of neutrons travelling in opposite direction with respect to the main neutron current, the H*(10) calculated at a depth $d < 3$ m inside the concrete shell is a bit larger than if the value had been calculated just behind the outer surface of a concrete shell of thickness d. Compared to the "equilibrium spectrum" inside the shield, the fluence fraction of neutrons below 10 MeV is smaller in the spectrum just outside the shield. The influence of the hydrogen content is therefore smaller as well.
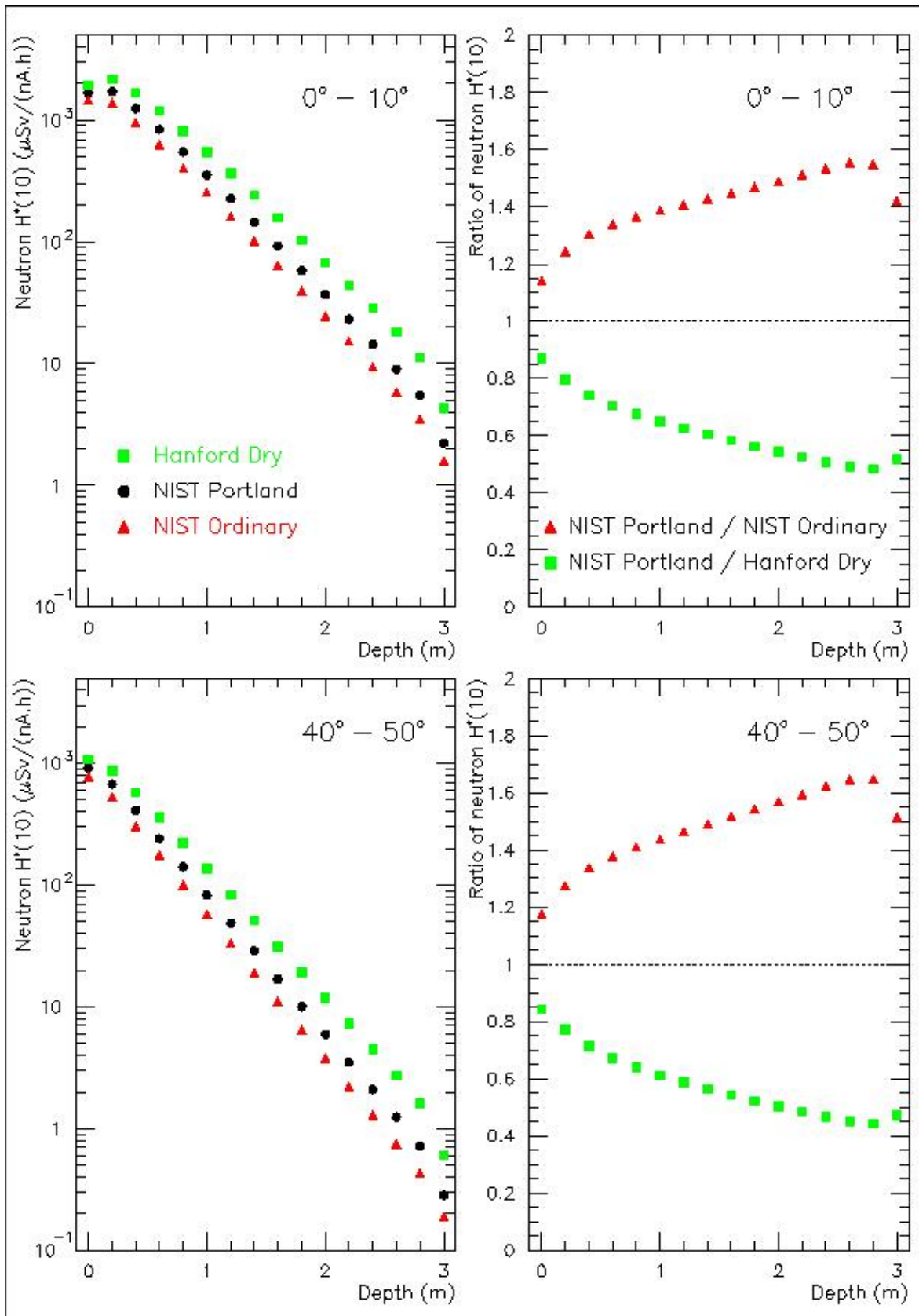
Figure V-20 – For the polar-angle intervals of 0°-10° and 40°-50° : (Left) Comparison of the neutron H*(10) attenuation profiles obtained with the concrete compositions 'Hanford Dry', 'NIST Portland' and 'NIST Ordinary'. (Right) Ratio of the neutron H*(10) attenuation profile obtained with 'NIST Portland' concrete to the one obtained with 'NIST Ordinary' or 'Hanford Dry' concrete.
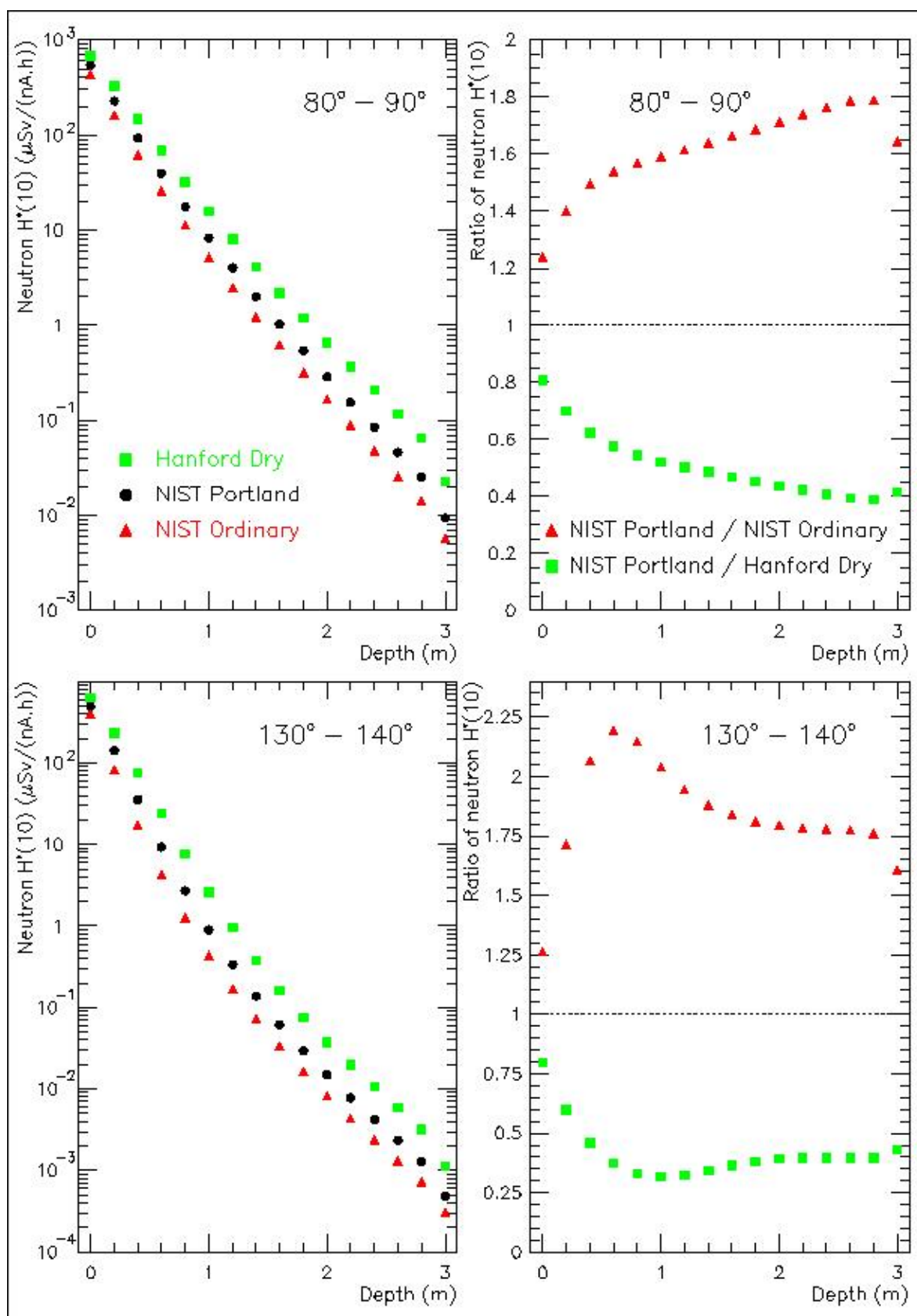
Figure V-21 – For the polar-angle intervals of 80°-90° and 130°-140° : (Left) Comparison of the neutron H*(10) attenuation profiles obtained with the concrete compositions 'Hanford Dry', 'NIST Portland' and 'NIST Ordinary'. (Right) Ratio of the neutron H*(10) attenuation profile obtained with 'NIST Portland' concrete to the one obtained with 'NIST Ordinary' or 'Hanford Dry' concrete.

The most correct way to estimate the influence of the concrete composition on H*(10) behind the shield would be to repeat this study for concrete shells of different thicknesses (e.g. 2.00 m, 2.20 m, 2.40 m *etc.*). By lack of time, we will assume in the present study that the percentage drop in the H*(10) discrepancies observed at the outer surface of the shield would be approximately the same when considering other concrete thicknesses between 2 m and 3 m. This percentage drop is of ~15 % for the comparison 'Hanford dry'/'NIST ordinary', and ~10% for 'NIST Portland'/'NIST ordinary'.

The reference composition 'NIST Portland' leads to H*(10) values behind a 2 – 3 m thick shield which, at polar angles of 0°-10°, are larger by a factor of 1.3 – 1.4 with respect to the most effective neutron shield based on 'NIST ordinary' concrete. These differences increase as a function of the polar angle, up to a factor of 1.6 at 130°-140° (see table **V-4:** H*(10)$_{\text{NIST Portland}}$ / H*(10)$_{\text{NIST ordinary}}$).

When comparing the least effective neutron shield ('Hanford dry') to the most effective neutron shield ('NIST ordinary), the differences between H*(10) behind the shield reach a factor of 2.3 – 2.7 at polar angles of 0°-10°, and 3.8 at 130°-140° (see table **V-5**: H*(10)$_{\text{Hanford dry}}$ / H*(10)$_{\text{NIST ordinary}}$).

Table V-4 – Ratios of the H(10) values obtained behind a shield of 2 m or 3 m in thickness when comparing the reference concrete ('NIST Portland' concrete) to the most effective neutron shield ('NIST ordinary' concrete), as a function of the polar angle.*

shielding thickness [m]	0°-10°	40°-50°	80°-90°	130°-140°
2.00	1.3	1.4	1.5	1.6
3.00	1.4	1.5	1.6	1.6

Table V-5 – Ratios of the H(10) values obtained behind a shield of 2 m or 3 m in thickness when comparing the least effective neutron shield ('Hanford dry' concrete) to the most effective neutron shield ('NIST ordinary' concrete), as a function of the polar angle.*

shielding thickness [m]	0°-10°	40°-50°	80°-90°	130°-140°
2.00	2.3	2.6	3.4	3.8
3.00	2.7	3.2	4.0	3.8

V-4 Conclusion

Sensitivity studies with respect to the selected high-energy physics models and the definition of the concrete composition were conducted for MCNPX shielding simulations of proton therapy rooms. For the shield, a simplified spherical geometry was adopted with an inner radius of 5 m and a concrete thickness of 3 m, in which the neutron H*(10) was calculated at different depths in 10° polar-angle intervals. A thick water phantom at the centre of the spherical room was irradiated by a proton pencil beam of 230 MeV.

V-4.1 Sensitivity to the physics models

The high-energy physics models used for the interactions of protons and neutrons above 150 MeV were systematically varied. The study showed that the simulation results do not depend on the selected evaporation model (Dresner or ABLA). However, when changing the intranuclear cascade model, significant differences were observed in the neutron H*(10) values at 2 – 3 m depth in the concrete.

The Bertini model was, as expected, the most conservative model at forward angles. For angles larger than ~40°, the INCL4 model was however the most conservative. The least conservative model at all polar angles was the CEM03 model.

Behind a concrete shield of 2 – 3 m in thickness, the H*(10) values of the Bertini model are larger than those of the CEM03 model by a factor of 1.5 – 1.8, depending on the angular bin. With the INCL4 model, the discrepancies with respect to the CEM03 model are of a factor of 1.2 – 1.3 at forward angles, but increase up to a factor of ~3 near 90° and (at least) a factor of ~5 near 135°. These discrepancies approximately reflect those observed at 0 m depth for the fluence of neutrons above ~100 MeV.

The neutron H*(10) values behind the shield are thus quite sensitive to the high-energy end of the double differential neutron production cross-sections of protons of 150 – 230 MeV in water. At forward angles, the impact of the choice of the intranuclear cascade model is however lower than a factor of 2. Therefore, it seems very unlikely that the uncertainties on these cross-sections could entirely explain the overestimate of the simulation results with respect to the WENDI-2 measurements in Chapter IV (for positions located behind the shielding). They may nevertheless contribute to these overestimates in a non-negligible way.

Obtaining accurate and precise measurements of the double differential neutron production cross-section for protons of 150 – 230 MeV on oxygen (or double differential neutron yield measurements for thick water targets) would be valuable for a benchmark of the intranuclear cascade models available in MCNPX. Similar

measurements for proton energies of 20 – 150 MeV would also be useful to investigate possible overestimates in the ENDF-B/VII evaluated data. For the non-elastic interactions of protons of 50 – 250 MeV with oxygen, these evaluated cross-sections are indeed based on very few experimental data [118].

V-4.2 Sensitivity to the concrete composition

The sensitivity to the selected concrete composition was studied by performing the same simulation for twenty-nine ordinary concrete compositions found in literature, of which the hydrogen mass percentage varied between 0.2% and 2.0% and the density between 2.10 g/cm^3 and 2.58 g/cm^3.

The effectiveness of the neutron shielding depends on a complex interplay of the different elements and the mass density. The hydrogen content is however one of the most sensitive parameters, thanks to its excellent moderating power for neutrons below ~1 MeV.

The largest differences in H*(10) behind a shield of 2 – 3 m in thickness were obtained between the compositions 'Hanford dry' (0.4% of hydrogen; 2.18 g/cm^3) and 'NIST ordinary' (2.0% of hydrogen; 2.30 g/cm^3). They range from a factor of 2.3 – 2.7 at polar angles of 0°-10° to a factor of 3.8 at 130°-140°.

With the composition of reference 'NIST Portland' (1.0% of hydrogen; 2.30 g/cm^3), used in the simulations of Chapter III, the neutron H*(10) values behind a 2 – 3m thick shield at 0°-10° are larger by a factor of 1.3 – 1.4 compared to those obtained with the most effective shielding ,'NIST ordinary'. These differences increase up to a factor of 1.6 at 130°-140°. Based on these results, it seems that the uncertainties related to the concrete composition could be significant for the neutron doses behind the shielding in the simulations of Chapter III. They can however not be the single cause of the corresponding simulation-to-measurement ratios obtained in Chapter IV.

CHAPTER VI
Additional measurements with a BSS, a TEPC and an LB 6411 in the proton therapy facility of Essen

VI-1 Introduction

In Chapter IV, WENDI-2 measurements performed in several positions inside and around the fixed-beam treatment room at Essen were presented. In some of these positions, additional neutron measurements were also acquired by two other research groups:

- a group from CERN, under the supervision of Marco Silari, carried out neutron spectrometry measurements [259–261] with an extended-range BSS [159]. Measuring the neutron spectrum is the best way to obtain reference H*(10) values for the in-field calibration of rem meters used around proton accelerators.

- A group from SCK-CEN, coordinated by Filip Vanhavere, performed ambient dosimetry measurements with a conventional rem meter LB 6411, microdosimetry measurements with a TEPC, as well as personal dosimetry measurements using different technologies. An overview of these results can be found in [262].

This chapter is largely based on a common paper which is currently under review for publication in Radiation Measurements, and of which I am the first author [263].

VI-2 Methodology

VI-2.1 MCNPX simulations

In Chapter V, we have shown that the intranuclear cascade model used to simulate the nuclear interactions of the high-energy protons and neutrons can have a significant impact on the neutron doses calculated behind the concrete walls of a proton therapy room. The simulation of the fixed-beam treatment room presented in Chapter III was based on the Bertini model, which is the most conservative intranuclear cascade model available in MCNPX for the emission of neutrons at forward angles with respect to the proton beam. The same simulation was run again using the CEM03 model instead of the Bertini & Dresner models, in order to also

compare the neutron measurements to the least conservative simulated neutron doses. These simulation results were processed in the same way as described in Chapter III.

VI-2.2 Overview of the measurement positions

Table **VI-1** provides an overview of the measurement positions inside and around the fixed-beam treatment room for the different types of detectors.
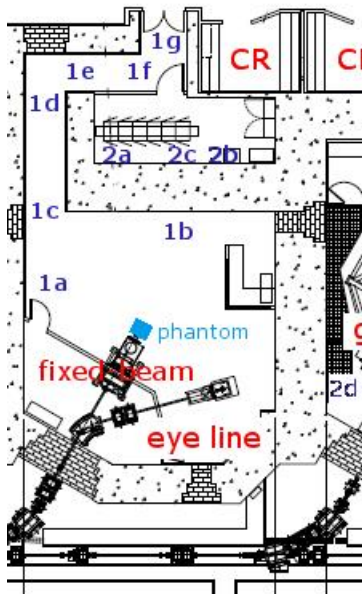
Table VI-1 – Overview of the measurement positions for the WENDI-2 (see Chapter IV), the LB 6411, the BSS and the TEPC. The measurement positions are indicated by a 'Y' in the table

Position	WENDI-2	LB 6411	BSS	TEPC
1b	Y	Y	Y	Y
1a	Y	Y	Y	Y
1c	Y	-	-	-
1d	Y	-	-	-
1e	Y	-	-	-
1f	Y	-	-	-
1g	Y	-	Y	-
2a	Y	Y	Y	-
2c	Y	Y	-	-
2b	Y	Y	-	Y
2d	Y	-	-	-

VI-2.3 BSS measurements

The CERN BSS [159,264] is composed of seven spheres: five polyethylene spheres with outer diameters of 81, 108, 133, 178, 233 mm and two additional spheres, nicknamed *Stanlio* and *Ollio*, containing a lead shell in order to extend the response up to several hundred MeV. The thermal neutron detector placed at the centre of each sphere is a 2 atm (202.65 kPa) spherical ^{3}He proportional counter.

Our collaborators from CERN performed Monte Carlo simulations with the 2011.2b version of the FLUKA code [105,107] in order to recalculate, by following the same methodology, the BSS response matrix calculated several years ago with the 1998 version of FLUKA [159]. The new simulations confirmed the old response matrix, improving its energy resolution (thanks to the new 260 group structure of the neutron cross-sections below 20 MeV) and reducing significantly the statistical uncertainties on the response of the two largest spheres, labelled as *233 mm* and *Ollio* (from maximum 10-20% [159] to < 5% in this work) [261]. The new response matrix

is shown in figure **VI-1**. The experimental validation of the BSS response functions between 144 keV and 19 MeV was performed at PTB in March 2002 [159].
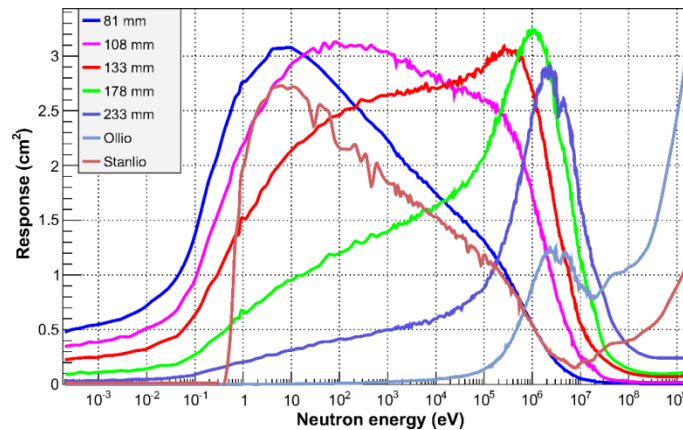
Figure VI-1 – BSS response functions, obtained via FLUKA simulations.
Figure provided by our collaborators from CERN [261].

The neutron spectrum is derived by unfolding the measured number of counts, normalised to the number of protons impinging on the phantom, with the BSS response matrix [158]. The group from CERN used two numerical unfolding codes: MAXimum Entropy Deconvolution (MAXED) [265] and GRAVEL [266]. The first code was designed especially for the unfolding of multi-sphere neutron spectrometer data, whereas the second has more general applications.

These two codes need an *a priori* estimation of the true spectrum, called guess spectrum. MAXED and GRAVEL calculate estimated counts for each sphere by folding the response matrix with the guess spectrum. By means of their own specific algorithm, they iteratively alter this guess spectrum in order to reach the best agreement between the measured and the estimated counts.

In this case, the guess spectra used for unfolding the BSS data were the neutron spectra simulated with MCNPX using the Bertini & Dresner models (see Chapter III). For position 1b, where the shape of the simulated spectrum depends more strongly on the selected physics models, the unfolding was also performed using the CEM03 spectrum as a guess.

The measured neutron spectra were folded with the ICRP fluence-to-H*(10) conversion coefficients [87] to obtain the neutron H*(10), for the comparison with the response of the other detectors.

The uncertainty bars associated to the spectra unfolded with MAXED were calculated using the IQU code (UMG package) [267][268]. The sensitivity analysis and uncertainty propagation calculation was based on the statistical counting uncertainties (1%), the uncertainty on the number of delivered protons (4.2%) and the uncertainty on the response matrix (5%). The IQU code cannot be used for the unfolding analysis with GRAVEL [268]. However, because of the similarities between

the unfolding algorithms, the same uncertainties were assumed here for the MAXED and GRAVEL spectra.

Since the BSS response matrix has not yet been validated in quasi-monoenergetic neutron beams of high energy, the uncertainties associated to the neutron fluxes above 20 MeV were assumed to be larger than those calculated using the IQU code, which does not deal in detail with the uncertainties associated to the response functions of the spheres. According to two studies about the influence of the BSS response functions on the unfolded spectra [269,270], the neutron flux above 20 MeV measured by a BSS outside the shielding of high-energy particle accelerators could show variations up to 20%, depending on the Monte Carlo code and the selected in-built physics models used for the calculation of the response functions. This could result in variations up to 10% in the associated H*(10) rate [269,270]. Taking also this aspect into account, the global uncertainties associated to the neutron H*(10) measured with the BSS were evaluated at 12%.

VI-2.4 LB 6411 measurements

The LB 6411 probe (Berthold Technologies) is a conventional rem meter. It consists of a polyethylene moderator sphere (25 cm in diameter) with internal Cd-absorbers and perforations, which surrounds a cylindrical ^{3}He proportional counter [271]. The ^{252}Cf calibration factor of 0.353 nSv/count is used to convert the counts into H*(10) values. This monitor is designed to measure neutrons from thermal energies up to 20 MeV. It is known to have a strongly decreasing sensitivity to neutrons above 20 MeV. The relative dose response function (relative to H*(10)) of the LB 6411 as calculated by Burgkhardt *et al.* up to 20 MeV [271] is shown in figure **VI-2**.
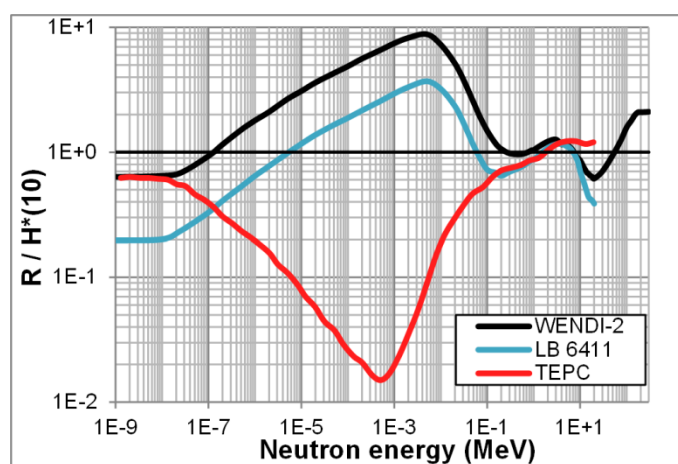
Figure VI-2 – Relative dose response functions of the LB 6411 and the TEPC [84]*, compared to that of the WENDI-2 (simulated with MCNPX using the Bertini & Dresner models* [190]*).*

The LB 6411 was operated by our collaborators from the SCK-CEN. The global uncertainties associated with these measurements (4.2-4.5%) include the standard

uncertainty for Poisson counting (0.1-1.5%) and the uncertainty on the number of delivered protons (4.2%).

VI-2.5 TEPC measurements

The TEPC Model LET-SW5 (Far West Technology) is spherical, with an internal diameter of 12.55 cm and a 2 mm thick shell of A-150 tissue-equivalent plastic. The TEPC was filled with propane tissue-equivalent gas at a pressure of 8.8 mbar to simulate a tissue site size of 2 μm [161]. Figure **VI-2** shows the relative dose response function (relative to H*(10)) of this type of detector, as calculated up to 20 MeV by D.J. Thomas [84].

Our collaborators from the SCK-CEN operated the TEPC and analysed its results. They constructed microdosimetric dose distributions, as a function of equal logarithmic intervals of the lineal energy y (keV/μm), by applying the principles explained in [161]. Their calibration of the microdosimetric spectra was based on the proton edge, which is a distinctive feature in the spectra defined as the maximum lineal energy imparted over the full chord length. For a 2 μm simulated site size, this quantity equals 136 keV/μm [161]. In the proton edge region, the microdosimetric spectra were fitted with a Fermi-like function and the value of 136 keV/μm was assigned to the intercept of the tangent at the inflexion point of this function [272]. The measured lineal energy range spanned from 2 keV/μm to 230 keV/μm.

The absorbed dose distribution was obtained with the following formula [273]:

$$D_i\,(Gy) = \frac{y_i\,d(y_i)\,[keV/\mu m]\ \times\ l\,[\mu m]}{\rho\,[kg/m^3]\ \times\ V\,[m^3]} \times 1.602 \times 10^{-16}\left[\frac{J}{keV}\right]$$

where the mean chord length l = 1.333 μm (*i.e.* 4/3 of the 1 μm radius of the simulated spherical tissue site), the gas density ρ = 0.0157 kg/m^3 and the gas volume V = 0.001073 m^3.

The dose equivalent H was calculated as the integral of the product of the absorbed dose distribution with the quality factor function Q [274].

The uncertainties on H include the standard deviation of three consecutive measurements (normalized per MU) acquired in the same position (1.4%-2.4%) and the uncertainty on the number of protons delivered per MU (4.2%).

VI-3 Results

VI-3.1 Simulations with a proton source

For the simulations based either on the Bertini & Dresner models or on the CEM03 model, the results of the average WENDI-2 response and the neutron H*(10) are listed in table **VI-2**. For the simulation based on the Bertini & Dresner models, the data is simply recapitulated from Chapter III (table **III-17**).

The figures **VI-3** to **VI-7** show the corresponding simulated neutron spectra, obtained with the Bertini & Dresner models and the CEM03 model, in the positions 1a, 1b, 2a and 1g. These figures also show the BSS unfolding results, which will be discussed in section **VI-3.2**.

The Bertini & Dresner neutron spectra are larger than the CEM03 spectra on the whole energy range. For positions inside the treatment room, the differences are more pronounced in the high-energy peak (10 MeV – 230 MeV) than at lower energies:

- For energy bins above 10 MeV: the differences are of a factor of 1.2 – 2.0 in position 1b, and 1.2 – 2.6 in position 1a;

- For energy bins below 10 MeV: the differences are of a factor of ~1.3 in position 1b, and ~1.2 in position 1a.

Due to the propagation mechanisms of the intranuclear cascade through the concrete shield, a lot of neutrons are produced at all depths and the initial surplus of high-energy neutrons in the Bertini & Dresner spectrum in front of the shielding eventually results in an overestimation factor that affects the whole energy range relatively uniformly, behind the shield. This effect has already been discussed in Chapter V. In position 2a, for example, both simulated spectra have very similar shapes, the Bertini & Dresner spectrum being larger than the CEM03 spectrum by a factor of ~1.6-1.7 at all energies (see figure **VI-6**). Position 1g is also partially affected by this effect (see figure **VI-7**) because the neutron flux at the end of the maze originates both from scattering inside the access maze and direct transmission through the walls of the technical room.

The discrepancies in the H*(10) values obtained with the Bertini & Dresner models *vs.* the CEM03 model are of a factor of:

- 1.35 in position 1b and 1.21 in position 1a;
- 1.66 in position 2a and 1.60 in position 1g.

The discrepancies are relatively consistent with those of the related systematic study for a spherical geometry, presented in section **V-3.1**.

Table VI-2 – Simulation results for the average WENDI-2 response and the neutron H*(10), obtained either with the Bertini & Dresner models or with the CEM03 model, with the proton source in front of the water phantom. The data is expressed in µSv/(nA.h). The standard uncertainties associated to the neutron H*(10) values are statistical uncertainties. For the WENDI-2 response, the uncertainties on the WENDI-2 response function were combined with the statistical uncertainties, like in Chapter III.

Posi-tion	Average simulated WENDI-2 response		Simulated neutron H*(10)	
	Spectra: Bertini	Spectra: CEM03	Spectra: Bertini	Spectra: CEM03
1b	$(2.3 \pm 0.2) \times 10^3$	$(1.6 \pm 0.1) \times 10^3$	$(2.054 \pm 0.001) \times 10^3$	$(1.526 \pm 0.009) \times 10^3$
1a	$(5.3 \pm 0.2) \times 10^2$	$(4.44 \pm 0.05) \times 10^2$	$(5.782 \pm 0.006) \times 10^2$	$(4.773 \pm 0.005) \times 10^2$
1c	$(3.6 \pm 0.2) \times 10^2$	$(2.8 \pm 0.1) \times 10^2$	$(3.889 \pm 0.005) \times 10^2$	$(3.088 \pm 0.004) \times 10^2$
1d	$(3.4 \pm 0.1) \times 10^1$	$(2.79 \pm 0.07) \times 10^1$	$(3.51 \pm 0.01) \times 10^1$	$(2.83 \pm 0.01) \times 10^1$
1e	$(1.06 \pm 0.05) \times 10^1$	$(8.3 \pm 0.3) \times 10^0$	$(1.078 \pm 0.005) \times 10^1$	$(8.33 \pm 0.04) \times 10^0$
1f	$(3.9 \pm 0.2) \times 10^0$	$(2.6 \pm 0.1) \times 10^0$	$(3.74 \pm 0.02) \times 10^0$	$(2.54 \pm 0.02) \times 10^0$
1g	$(3.1 \pm 0.2) \times 10^0$	$(1.9 \pm 0.1) \times 10^0$	$(2.89 \pm 0.02) \times 10^0$	$(1.81 \pm 0.02) \times 10^0$
2a	$(6.4 \pm 0.5) \times 10^0$	$(3.9 \pm 0.3) \times 10^0$	$(6.28 \pm 0.03) \times 10^0$	$(3.78 \pm 0.02) \times 10^0$
2c	$(1.6 \pm 0.1) \times 10^1$	$(9.7 \pm 0.8) \times 10^0$	$(1.52 \pm 0.04) \times 10^1$	$(9.13 \pm 0.03) \times 10^0$
2b	$(1.16 \pm 0.09) \times 10^1$	$(6.3 \pm 0.5) \times 10^0$	$(1.10 \pm 0.03) \times 10^1$	$(6.03 \pm 0.03) \times 10^0$
2d	$(9.7 \pm 0.6) \times 10^{-2}$	$(5.7 \pm 0.3) \times 10^{-2}$	$(9.9 \pm 0.1) \times 10^{-2}$	$(5.75 \pm 0.05) \times 10^{-2}$
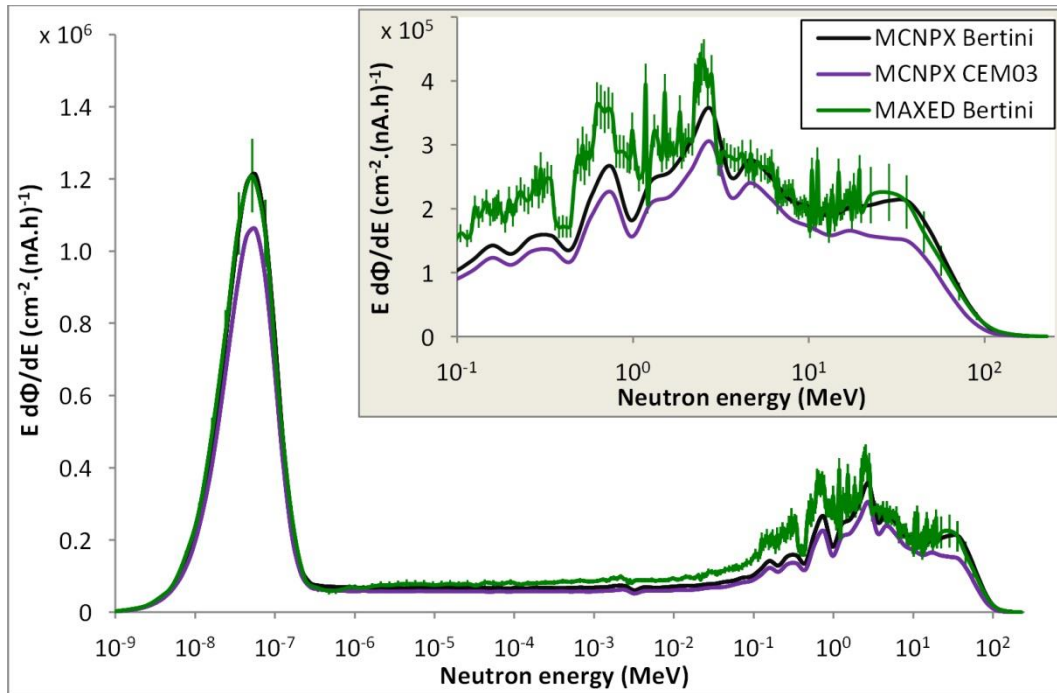
Figure VI-3 – Neutron spectrum in position 1a, as obtained by the MCNPX simulations, using the Bertini & Dresner and the CEM03 models, respectively, and as obtained by unfolding of the BSS data using MAXED with the MCNPX Bertini & Dresner spectrum as a guess.The uncertainties on the experimental spectrum correspond, below 20 MeV, to those calculated with the IQU code and, above 20 MeV, to 20% of the bin values.The statistical uncertainties on the simulated spectra are ≤ 1% for bins up to 70 MeV and ≤ 10% for bins above 70 MeV.
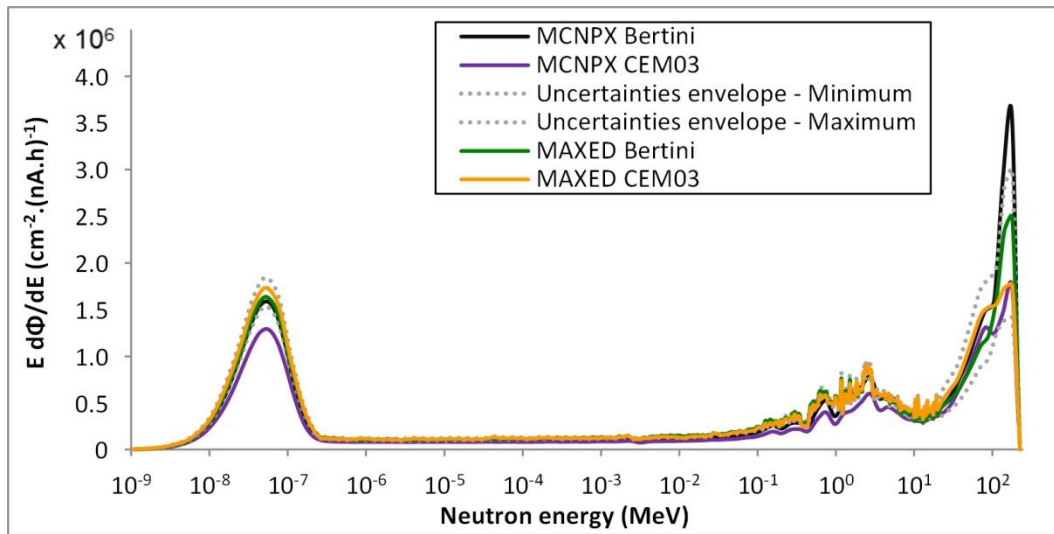
Figure VI-4 –Neutron spectrum in position 1b, as obtained by the MCNPX simulations, using the Bertini & Dresner and the CEM03 models, respectively, compared to the unfolded BSS spectra obtained using MAXED with as a guess (a) the MCNPX Bertini & Dresner spectrum, and (b) the MCNPX CEM03 spectrum. In grey dotted lines: the envelope of the uncertainties associated to the two BSS spectra unfolded with MAXED. Uncertainties on the simulated spectra are ≤ 1% for all bins.
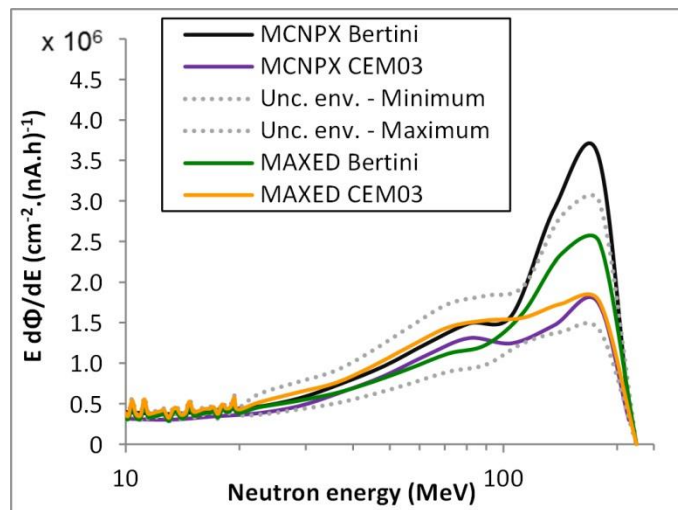
Figure VI-5 – Zoom on the high-energy peak of the spectra shown in the previous figure.
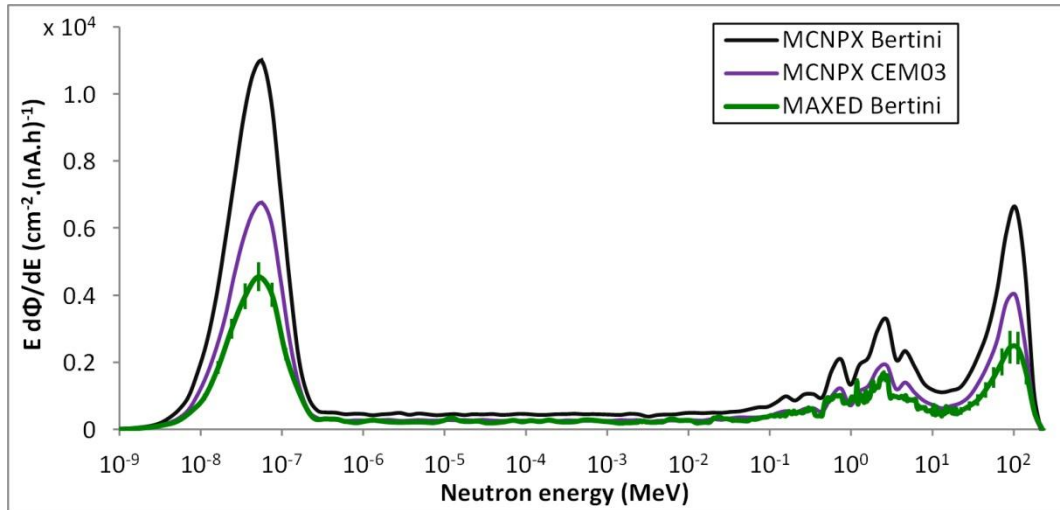
Figure VI-6 – Neutron spectrum in position 2a, as obtained by the MCNPX simulations, using the Bertini & Dresner and the CEM03 models, respectively, and as obtained by unfolding of the BSS data using MAXED with the MCNPX Bertini & Dresner spectrum as a guess. The uncertainties on the experimental spectrum correspond, below 20 MeV, to those calculated with the IQU code and, above 20 MeV, to 20% of the bin values. The statistical uncertainties on the simulated spectra are ≤ 3% for all bins.
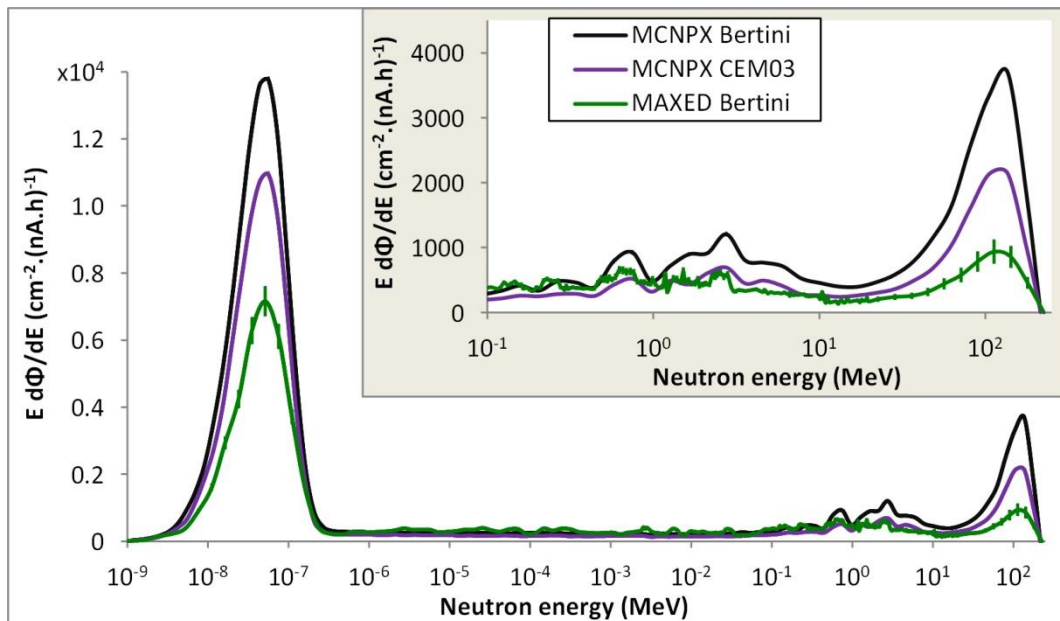
Figure VI-7 – Neutron spectrum in position 1g, as obtained by the MCNPX simulations, using the Bertini & Dresner and the CEM03 models, respectively, and as obtained by unfolding of the BSS data using MAXED with the MCNPX Bertini & Dresner spectrum as a guess. The uncertainties on the experimental spectrum correspond, below 20 MeV, to those calculated with the IQU code and, above 20 MeV, to 20% of the bin values. The statistical uncertainties on the simulated spectra are ≤ 3% for all bins.

VI-3.2 BSS spectra *vs.* simulated spectra

The unfolding results of the BSS data are compared to the simulated spectra in the figures **V-3** to **V-7**. The uncertainties associated to the spectra unfolded with MAXED are those calculated with the IQU code [268], except for energies above 20 MeV where 20% relative uncertainties were considered. For all positions, the spectra unfolded with GRAVEL matched with the MAXED results within 1σ uncertainties. For the sake of readability, only the MAXED spectra are shown.

VI-3.2.1 Inside the treatment room

In Position 1a (figure **VI-3**), situated at roughly 90° from the proton beam axis, the guess spectrum – simulated with the Bertini & Dresner models – matches the unfolded spectra very well for neutrons with energies larger than ~5 MeV. In the intermediate energy range and in the evaporation peak up to ~5 MeV, the guess spectrum is smaller than the unfolded spectra by ~20%. The agreement is better than for the spectrum simulated with the CEM03 model, which underestimates the unfolded spectra by ~30% in the intermediate, evaporation and high-energy regions.

For Position 1b, located in the direction of forward neutron emission, the simulated and measured spectra are compared in figure **VI-4** and a zoom on the high-energy peak is shown in figure **VI-5**. For the sake of readability, the uncertainty bars of the two spectra unfolded with MAXED (using different guess spectra) are replaced in the plots by two dotted curves that delimit their envelope. The comparison of the unfolding results obtained with the two different guess spectra brings out the fact that, as predicted by [275], the energy resolution of the BSS at high energies is not sufficient to determine the exact shape of the high-energy peak without ambiguity. Nevertheless, it is interesting to note that the spectrum simulated with the Bertini & Dresner models agrees very well with the unfolded spectra at all energies except in the high-energy peak, where an overestimate appears above 150 MeV. The spectrum simulated with the CEM03 model, however, only matches with the unfolding results in the high-energy peak and underestimates them at all other energies.

VI-3.2.2 Outside the treatment room

In Position 2a, located at roughly 40° from the proton beam axis, the unfolded spectra (figure **VI-6**) are lower than the simulated spectra by a factor that remains relatively constant on the entire energy range: a factor of ~2.3 with respect to the Bertini & Dresner spectrum and ~1.4 with respect to the CEM03 spectrum. In this aspect, the results are similar to those of Satoh et al. [242], obtained with the simulation code PHITS and the DARWIN spectrometer at the Fukui Proton Therapy Centre.

At the end of the access maze, in position 1g, the neutron spectrum (see figure **VI-7**) is mainly characterised by a large thermal peak as well as a relatively small high-energy peak. The simulated spectra are larger than the average BSS results on the whole energy range, but the overestimation factor is actually larger on the high-energy peak (contribution from neutrons directly transmitted through the technical room) than on the thermal peak (main contribution from neutrons scattering inside the access maze).

VI-3.3 WENDI-2 measurements *vs.* simulation results

Figure **VI-8** shows the ratios of the simulation results to the WENDI-2 measurements. These measurements as well as the simulation results obtained with the Bertini & Dresner models have already been presented in Chapter IV. They are compared here to additional simulation results based on the CEM03 model.

VI-3.3.1 Inside the treatment room

Inside the treatment room (1a, 1b) and the first part of the maze (1c, 1d, 1e), the simulated WENDI-2 responses based on the Bertini & Dresner spectra agree with the WENDI-2 measurements within one to two standard uncertainties. The agreement is better than for the simulation results based on the CEM03 model, which underestimate the measurements by a factor of 1.2 – 1.3. This is globally consistent with our observations on the BSS spectra (see section **VI-3.2.1**).

In position 1b, characterised by a large high-energy peak with a maximum above 100 MeV, the average simulated WENDI-2 response based on the Bertini & Dresner spectrum slightly overestimates the WENDI-2 measurement. This might reflect the slight overestimate on the high-energy peak observed with respect to the BSS results above 100 MeV (see figures **VI-4** and **VI-5**).

VI-3.3.2 Outside the treatment room

In the adjacent rooms (2a, 2b, 2c, 2d) and at the end of the maze (1g), both the simulations results obtained with the Bertini & Dresner models and the CEM03 model overestimate the WENDI-2 measurements. The overestimate ranges up to a factor of ~3 with the Bertini & Dresner models, and up to a factor of ~1.7 with the CEM03 model.

In both cases, the overestimates are larger for positions located at forward angles (2b, 2c, 2a) than for position 2d at ~90° with respect to the proton beam.
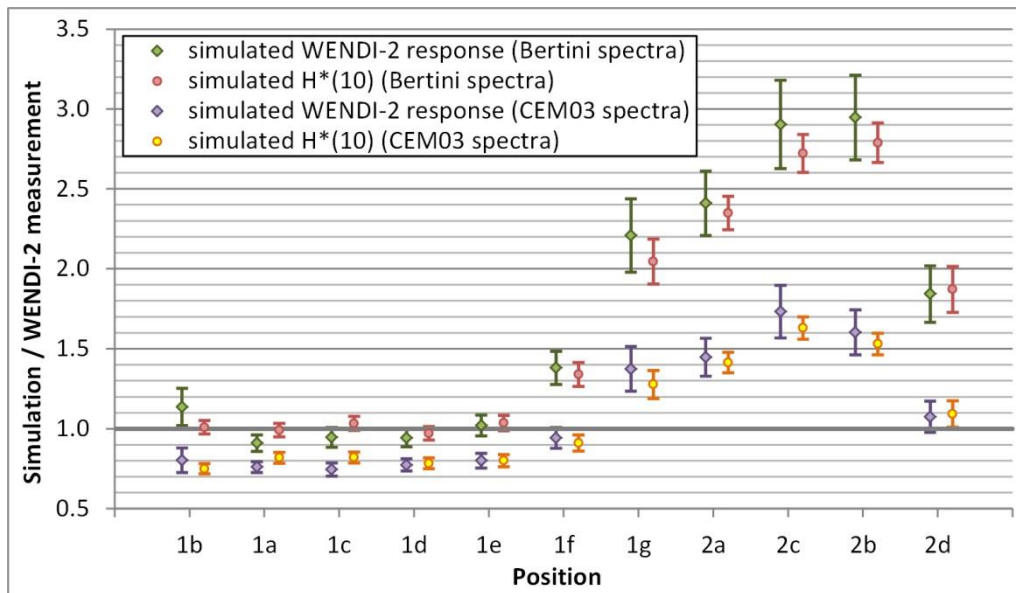
Figure VI-8 – The following quantities are given in ratio to the WENDI-2 measurements: (a) the average simulated WENDI-2 response based on the Bertini & Dresner spectra, (b) the neutron H*(10) rates based on the Bertini & Dresner spectra, (c) the average simulated WENDI-2 response based on the CEM03 spectra, (d) the neutron H*(10) rates based on the CEM03 spectra.

VI-3.4 Global intercomparison of the measurements

The neutron H*(10) rates obtained by unfolding the BSS data with MAXED and GRAVEL are in good agreement with each other in all positions (see table **VI-3**). In the case of position 1b, a good agreement also exists between the H*(10) rates calculated using the unfolded spectra using the Bertini and the CEM03 guess spectra.

The WENDI-2 measurements agree within ~10% with the H*(10) rates of the BSS data in the four types of neutron fields (positions 1a, 1b, 1g, 2a; see table **VI-4**). It corresponds to an agreement within one standard uncertainty. There thus seems to be little need to introduce position-specific calibration correction factors, based on the local neutron spectrum, to improve the accuracy of the H*(10) measurements performed with the WENDI-2.

Compared to the WENDI-2, the conventional rem meter LB 6411 measures values lower by 40% in position 1b and by 27%-28% in positions 2a, 2b and 2c, located at forward polar angles behind the shielding (see table **VI-4**). The low response to high energy neutrons of the LB 6411 thus causes an underestimate of the measured H*(10) rates in these positions in which the proportion of neutrons with more than 20 MeV lies between ~15% and ~30%, according to the MCNPX simulations. These results are comparable to the discrepancies observed in measurements at GSI [149], at the CERF facility [276] and at the CERN Proton Synchrotron [277]. In position 1a, however, a better agreement was found between the LB 6411 measurement and the WENDI-2 and BSS data. According to the MCNPX simulations, neutrons with more than 20 MeV constitute only ~5% of the total

neutron flux in this position. It seems that the LB 6411 can be used for area monitoring of neutrons inside proton therapy facilities, but accurate neutron H*(10) measurements behind the shielding and in "forward" positions inside the treatment room would actually require the calculation of a position-specific calibration correction factor. To determine such a correction factor, the shape of the local neutron spectrum needs to be well characterised and the response function of the LB6411 must be known up to 230 MeV.

The TEPC measures the dose equivalent *H* and was not calibrated for measuring H*(10) in these specific neutron fields. The results nevertheless agree with the other detector responses within at most two standard uncertainties in all positions (see table **VI-4**). Compared to the WENDI-2 and BSS measurements, the TEPC results tend to be lower by 20 – 30%.

Table VI-3 – H(10) results in µSv/(nA.h) from the BSS data unfolded with GRAVEL and MAXED using the Bertini & Dresner guess spectrum, and – for position 1b – the BSS data unfolded with GRAVEL and MAXED using the CEM03 guess spectrum.*
With thanks to our collaborators from CERN who provided these results.

Position	Bertini guess spectrum		CEM03 guess spectrum	
	GRAVEL	MAXED	GRAVEL	MAXED
1b	1860 ± 223	1890 ± 227	1930 ± 232	1944 ± 233
1a	647 ± 78	648 ± 78	-	-
1g	1.46 ± 0.18	1.30 ± 0.16	-	-
2a	2.76 ± 0.33	2.78 ± 0.33	-	-

Table VI-4 – Measurements with the WENDI-2, the LB 6411 and the TEPC, compared to the average H(10) measured with the BSS. The results are expressed in µSv/(nA.h).*

Position	BSS H*(10) (Average)	WENDI-2	LB 6411	TEPC
1b	$(1.9 ± 0.2) \times 10^3$	$(2.03 ± 0.09) \times 10^3$	$(1.23 ± 0.05) \times 10^3$	$(1.66 ± 0.07) \times 10^3$
1a	$(6.5 ± 0.8) \times 10^2$	$(5.8 ± 0.2) \times 10^2$	$(5.5 ± 0.2) \times 10^2$	$(4.5 ± 0.2) \times 10^2$
1g	$(1.4 ± 0.2) \times 10^0$	$(1.4 ± 0.1) \times 10^0$	-	-
2a	$(2.8 ± 0.3) \times 10^0$	$(2.7 ± 0.1) \times 10^0$	$(1.96 ± 0.09) \times 10^0$	-
2c	-	$(5.6 ± 0.2) \times 10^0$	$(4.1 ± 0.2) \times 10^0$	-
2b	-	$(3.9 ± 0.2) \times 10^0$	$(2.8 ± 0.1) \times 10^0$	$(3.4 ± 0.5) \times 10^0$

VI-3.5 Simulations based on BSS spectra

VI-3.5.1 Impact on results outside the treatment room

As explained in Chapter V, the neutrons of more than ~100 MeV produced in the water phantom strongly determine the neutron H*(10) obtained outside the treatment room. According to the spectrum measured with the BSS in position 1b, the Bertini model slightly overestimates this production at small polar angles (see figure **VI-5**). This overestimate is expected to have a non-negligible impact on the simulated neutron H*(10) in position 2b, which is located behind the shielding on approximately the same line-of-sight as 1b with respect to the water phantom.

To show this, an MCNPX simulation was run in which the proton source was replaced by a neutron source in position 1b, with an energy distribution corresponding to the measured spectrum. In this case, the BSS data unfolded with MAXED using the Bertini & Dresner guess spectrum was used. The source was actually positioned just in front of the 1b tally sphere, between the water phantom and this sphere. It emitted neutrons towards the technical room, with a uniform distribution for angles of 0° to 90° with respect to the line-of-sight of 1b. This angular distribution of the source allowed reproducing approximately the same neutron shape in position 2b as in the simulation with the proton source impinging on the water phantom. The default Bertini & Dresner models were used for the high-energy interactions of the neutrons.

Since MCNPX automatically normalizes the simulation results per source-emitted particle, the spectrum calculated for position 2b was expressed in (neutrons/cm^2)/neutron. In order to compare that spectrum to those obtained with the simulations involving the proton source, a normalization factor thus had to be estimated. Therefore, the same simulation was run using the MCNPX Bertini spectrum of 1b as energy distribution for the neutron source. In this simulation, the shape of the spectra in the positions 1b and 2b was faithfully reproduced with respect to the corresponding proton-source simulation. For position 2b, the total fluence in the "neutron-source simulation" was then divided by the total fluence in the "proton-source simulation", to provide the required normalization factor of 3.12 x 10^{-13} neutron/(nA.h).

The neutron spectrum simulated in 2b, using the neutron source in 1b with an energy distribution corresponding to the BSS spectrum, is shown in figure **VI-9**. The results are, as expected, intermediate to those obtained with the Bertini & Dresner models and the CEM03 model in the proton-source simulations, due to the intermediate fluence of neutrons above 100 MeV in 1b (see the 'MAXED Bertini' curve in figure **VI-5**). The ratio of the simulated H*(10) to the WENDI-2 measurements, for positions 1b and 2b, is also shown in figure **VI-10** (green circles).
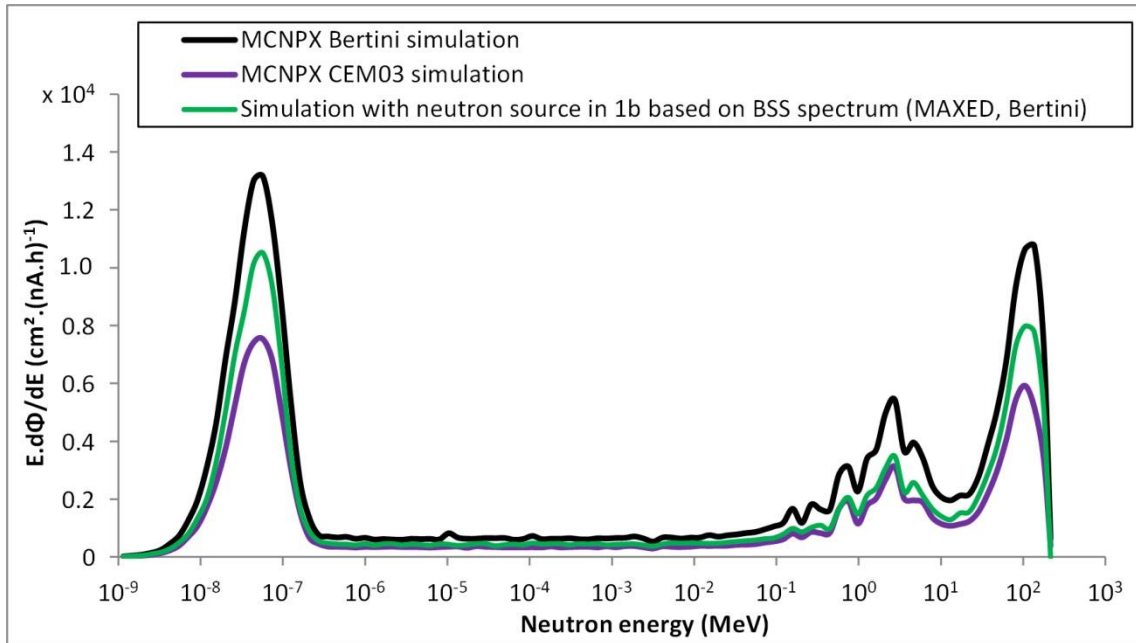
Figure VI-9 – Neutron spectrum in position 2b behind the shield, as obtained in three different MCNPX simulations: the two simulations that involve a proton source in front of the water phantom, based on (1) the Bertini & Dresner models and (2) the CEM03 model; and (3) the simulation that involves a neutron source positioned in 1b with an energy distribution corresponding to the BSS spectrum in that position (unfolded with MAXED using the Bertini & Dresner spectrum as a guess). The statistical uncertainties are ≤ 3% for all bins.
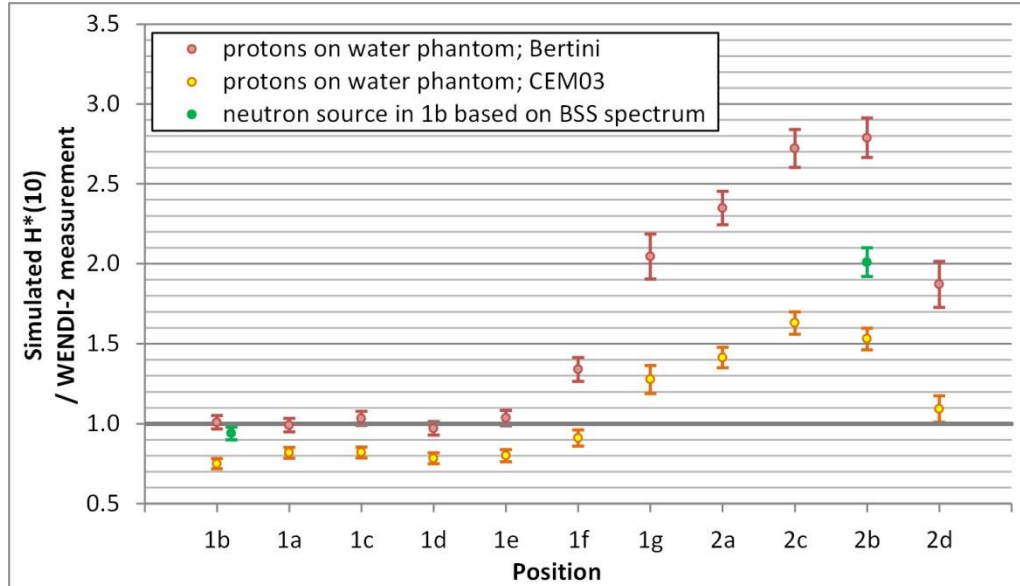
Figure VI-10 – The ratio of the simulated neutron H*(10) to the corresponding WENDI-2 measurement, for three different MCNPX simulations: the two simulations that involve a proton source in front of the water phantom, which are based on (1) the Bertini & Dresner models and (2) the CEM03 model (same results as in figure VI-8); and (3) results given for positions 1b and 2b only: the simulation that involves a neutron source positioned in 1b with an energy distribution corresponding to the BSS spectrum in that position (unfolded with MAXED using the Bertini & Dresner spectrum as a guess).

In the proton-source simulation based on the Bertini & Dresner models, the neutron H*(10) in position 2b is larger by a factor of 1.4 compared to the neutron-source simulation based on the BSS spectrum (MAXED, Bertini). This overestimate corresponds closely to the initial overestimate on the neutron fluence above 100 MeV in front of the shielding (see data for position 1b in table **VI-5**). As explained in Chapter V, this overestimate which only affects the high-energy neutrons inside the treatment room eventually spreads out over the entire width of the neutron spectrum due to the propagation mechanisms of the neutrons through the concrete shield.

Table VI-5 – Neutron fluence above 100 MeV inside the treatment room, according to the two simulations that involve a proton source in front of the water phantom, and which are based on (1) the Bertini & Dresner models and (2) the CEM03 model. Comparison with the same quantity in the BSS spectrum unfolded with MAXED (using the Bertini & Dresner spectrum as a guess).

Position	Neutron fluence above 100 MeV $[n/(cm^2.nA.h)]$			% deviation with respect to BSS result	
	MCNPX Bertini	MCNPX CEM03	BSS MAXED (Bertini)	MCNPX Bertini	MCNPX CEM03
1b	2.04×10^6	1.11×10^6	1.49×10^6	+37%	-26%
1a	3.78×10^3	1.84×10^3	3.41×10^3	+11%	-46%

Unfortunately, the uncertainties on the measured neutron fluence above 100 MeV are large, because the BSS response matrix has not yet been validated at high energies and the unfolding is also quite sensitive to the shape of the guess spectrum. Taking the uncertainty envelope of figure **VI-5** into account, the simulation based on the Bertini & Dresner models overestimates the measured neutron fluence above 100 MeV by a factor of 1.7 ± 0.5 in position 1b. Judging by our example, this causes an overestimate by the same factor on the neutron H*(10) in position 2b. At forward angles with respect to the proton beam direction, the conservative nature of the shielding simulations seems thus indeed to be partially caused by an overestimate on the production of high-energy neutrons by 230 MeV protons in water.

The overestimate of the Bertini model for the production of neutrons of more than 100 MeV could perhaps be less pronounced at angles of ~90° than at forward angles (see table **VI-5**). If so, it could perhaps explain why the overestimate of the simulated neutron H*(10) is larger in 2b than in 2d, despite that the traversed concrete thickness is smaller for 2b.

VI-3.5.2 Validation of the WENDI-2 response function

The measurements in position 1b are also useful to the study of the WENDI-2 response function at high energies, thanks to the large fraction of high-energy neutrons in this spectrum: ~10-15% of the neutrons have energies above 100 MeV and ~15-20% are in the range of 10 MeV – 100 MeV. The five different versions of the WENDI-2 response function from figure **III-9** (on p. **126**) were therefore folded with the BSS spectrum and the results were compared to the WENDI-2 measurement in 1b. This procedure was repeated for four versions of the BSS spectrum shown in figure **VI-4**:

- the unfolding results based on the Bertini & Dresner guess spectrum,
- the unfolding results based on the CEM03 guess spectrum,
- the upper boundary of the uncertainty envelope,
- the lower boundary of the uncertainty envelope.

The ratios of these simulated WENDI-2 responses to the WENDI-2 measurement are shown in figure **VI-11**. Using the unfolding results based on the Bertini & Dresner guess spectrum or the CEM03 guess spectrum leads to nearly identical results for the simulated WENDI-2 response in 1b. In both cases, the response function based on the GEANT4 BIC model yields the best agreement with the WENDI-2 measurement. When using the upper boundary of the uncertainty envelope associated to these spectra, the results suggest that the actual WENDI-2 response function is intermediate to the one based on the GEANT4 BIC model and the one based on the high-energy measurements of Olsher *et al*. These results are thus consistent with our conclusions of Chapter II regarding the WENDI-2 measurements performed in high-energy QMN beams at the TSL. This is however not the case for the results obtained when using the lower boundary of the uncertainty envelope, which might thus underestimate the true high-energy neutron fluence in 1b.
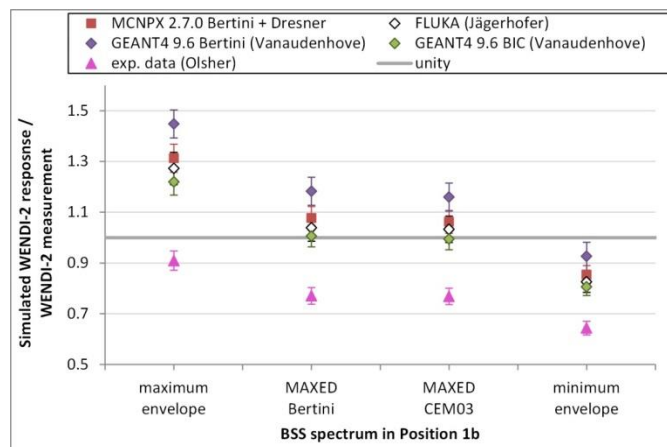
*Figure VI-11 – Ratio of the simulated WENDI-2 response to the WENDI-2 measurement in position 1b. The simulated WENDI-2 response was calculated by folding the BSS spectrum results for position 1b with each of the different versions of the WENDI-2 response function shown in figure **III-9** on p. **126**. Four versions of the BSS spectrum (see figure **VI-4**) were used, to take the uncertainties on the unfolding parameters into account.*

VI-4 Conclusion

Additional measurements with a BSS, an LB 6411 and a TEPC were performed inside and around the fixed-beam treatment room. The MCNPX simulation for this room, which had previously been run with the Bertini & Dresner models (see Chapter III), was also run with the least conservative model in this case, namely the CEM03 model.

In positions located both inside and outside the treatment room, the WENDI-2 measurements agreed within ~10% with the neutron H*(10) measured with the BSS. It confirms that, in these neutron fields, the WENDI-2 allows measuring H*(10) with a satisfactory accuracy without applying any field-specific calibration correction factor.

Measurements with an LB 6411, however, require such correction factor in positions located at forward angles with respect to the proton beam direction, to avoid underestimating H*(10) by ~25-40%.

The TEPC dose equivalent measurements were globally consistent with the other measurements. The values were however lower by ~20-30% compared to the H*(10) measured with the BSS and the WENDI-2.

The comparison of the simulation results with the WENDI-2 and BSS measurements for positions inside the treatment room showed that the CEM03 model seems to underestimate the global neutron production inside the treatment room by a factor of ~1.3. The Bertini & Dresner models lead to a better agreement in general with these measurements. However, at forward angles, the Bertini model (unlike the CEM03 model) overestimates the production of neutrons with energies above 100 MeV, which leads to a non-negligible increase of the neutron H*(10) simulated behind the shielding (estimated to a factor of 1.7 ± 0.5). It could perhaps partially explain why, for positions behind the shielding, the discrepancies between the simulated H*(10) and the WENDI-2 measurements are larger at forward angles than at ~90° with respect to the proton beam direction.

Finally, the BSS spectrum with the largest fraction of high-energy neutrons (position 1b) was also folded with five versions of the response function of the WENDI-2, and the results were compared to the WENDI-2 measurement in the same position. The GEANT4 BIC-based response function seems to provide the best agreement, which is relatively consistent with the conclusions of our high-energy QMN measurements presented in Chapter II. A firm conclusion can however not be drawn due to the relatively large uncertainties on the high-energy neutron fluence.

CHAPTER VII
Conclusions

Proton therapy uses advantageous properties of proton beams, such as their finite range in matter and the Bragg peak at the end of their depth-dose distribution, to deliver a highly conformal dose to a cancerous tumour. Compared to X-ray therapy, proton therapy allows a reduction of the unnecessary dose delivered to the surrounding healthy tissues and offers the possibility to spare critical organs located behind the tumour.

Protons beams used in proton therapy typically have energies in the range of 70 MeV – 230 MeV. At these energies, protons have a small but significant probability of undergoing non-elastic nuclear reactions, which result in the unwanted production of secondary particles such as neutrons, protons, light ions and gamma photons. The production of such particles occurs, for instance, inside the proton accelerator, the beam line, the treatment nozzle and the patient. Many of the secondary particles fall into the category of ionizing radiation. People exposed to this radiation are therefore at risk of developing, on the long-term, adverse health effects such as, for example, cancer. For the patient, the secondary doses can in principle be reduced by using an active beam delivery technique (e.g. PBS) instead of a passive scattering technique (like DS). To protect the staff and members of the public inside the facility, the stray radiation field should be attenuated by appropriate shielding walls. The shielding design should ensure that the effective doses outside the shielding do not exceed the national legal limits for occupational (or public) exposure.

The thicknesses of the shielding walls are in the first place determined with respect to the secondary neutrons, which give by far the largest contribution to the effective dose outside the shielding. Today, the shielding design for proton therapy facilities often relies on neutron doses calculated through Monte Carlo simulations. The latter involve complex geometries and depend on many parameters. Several of these parameters, e.g. related to particle source characteristics, material compositions and interaction cross-sections (at high energies, especially), can often not be controlled in a precise way. It is also hardly possible to model all the details of the building and its equipment. As a consequence, the global uncertainties on simulated neutron doses outside the shielding may be rather large.

Conservative choices are generally made for several parameters of the shielding design simulations. Because of these conservative choices, the simulated neutron doses are expected to be overestimated outside the shielding. If that is indeed the case, it means an implicit safety margin is being taken into account in the shielding design.

Given the complexity of the simulations and the many sources of uncertainties, it is actually important to experimentally verify that these simulations are indeed conservative. Ideally, one would also like to understand which aspects of the simulations really contribute to this conservativeness, and to what extent. There are, however, surprisingly few studies in literature which focus on the comparison between shielding design simulations and neutron dose measurements performed behind the shielding walls in the constructed proton therapy facilities.

In this work, we have presented such comparisons for the proton therapy facility of Essen. Most of the measurements were performed with a WENDI-2, which possesses a good sensitivity over the entire width of the neutron spectra, including their high-energy component of 10 MeV – 230 MeV. This is particularly important since the literature indicated that conventional rem meters, which have a decreased sensitivity to neutrons above ~10 MeV, might underestimate the neutron H*(10) by up to a factor of ~2 inside proton therapy facilities.

A first part of this work focussed on the study of the WENDI-2 response function and its comparison with the fluence-to-H*(10) conversion coefficients. The goal hereafter was to use this information to theoretically assess the accuracy in terms of H*(10) of our WENDI-2 measurements performed at Essen.

We used MCNPX 2.7.0 to simulate the WENDI-2 response function and our results were found to be consistent with those of other authors obtained with different Monte Carlo codes (MCNPX 2.1.5, FLUKA, GEANT4 9.6) [152,183,184]. Relatively large differences were however noted amongst these other results, especially at thermal energies (factors of 2 – 3) and in the range of 20 MeV – 230 MeV (factors of 1.3 – 1.5).

In the experimental validation of the WENDI-2 response function, our focus lied on the energy range of evaporation and high-energy neutrons, because they give the dominant contributions to the H*(10) outside the shielding of proton therapy rooms. Concerning the range of evaporation neutrons, our measurements with ^{252}Cf and AmBe sources were in good agreement with the simulated responses, especially the one based on the FLUKA response function [183]. They were also fully consistent with the monoenergetic neutron beam measurements of Olsher *et al.* (within their standard uncertainties of 5%) [152]. At high energies, measurements were performed with quasi-monoenergetic neutron beams at the TSL, for peak energies of 21.8 MeV, 93.1 MeV and 173.4 MeV. Only the fluence of the peak neutrons could be measured in this case. Due to the difficulty to obtain a precise characterisation of the neutron spectra, the estimated uncertainties on the total neutron fluence, and thus on the measured WENDI-2 responses, were as large as 20% – 30%. We compared these measurements to simulated responses obtained by folding available evaluations of the neutron spectra with the different versions of the simulated WENDI-2 response function. The measurements tended to be lower than the simulated responses, but

smaller discrepancies were obtained than with previous experimental results by Olsher *et al.* [182] (which were lower than the simulated responses by a factor of ~2 on average). In general, our measurements agreed within at most two standard uncertainties with the responses based on the BIC model of GEANT4 9.6 [184]. They also agreed mostly within three standard uncertainties with the other simulated responses, except the one based on the Bertini model of GEANT4 9.6 [184].

The Monte Carlo simulations of the neutron fields inside the proton therapy facility of Essen were carried out with MCNPX 2.7.0. Four rooms were modelled: the cyclotron room, a gantry treatment room operated in PBS, a gantry room operated in DS, and the fixed-beam treatment room operated in US. The same conservative choices were made as in the original shielding design simulations for this facility. For example, the intranuclear cascade model that leads to the highest calculated neutron doses at forward angles (the Bertini model) was selected. The concrete density defined in the simulation (2.30 g/cm^3) was also slightly lower than the minimum density that the concrete provider had to ensure for this building (2.35 g/cm^3).

The neutron spectra simulated at the measurement positions were folded with the different versions of the WENDI-2 response function (including also the one based on the high-energy measurements of Olsher *et al.*)*.* The obtained responses were compared to the simulated H*(10), obtained by folding the spectra with the fluence-to-H*(10) conversion coefficient of ICRP Publication 74. From this comparison, we predicted that the accuracy of the WENDI-2 measurements in terms of H*(10) would be better than 30-35% in all considered positions. This was however a theoretical prediction based on simulated spectra not yet validated by spectral measurements. It was obviously also limited by the uncertainties on the WENDI-2 response function. The results were nevertheless consistent with our expectations, knowing the results of the CONRAD experiment relative to hadron therapy [149,177,178] and the prediction of Jägerhofer *et al.* based on measurements in high-energy quasi-monoenergetic neutron beams [181].

For the comparison of the MCNPX simulations to the WENDI-2 measurements, we computed the average of the simulated WENDI-2 responses in each position. The associated relative standard uncertainties were estimated to 4% – 11%. These included the uncertainties on the WENDI-2 response function and the statistical uncertainties on the simulated neutron spectra.

When comparing the average simulated WENDI-2 responses to the WENDI-2 measurements, the same trend was observed for the three treatment rooms and the cyclotron room. A relatively good agreement was obtained in positions located inside the room and in the access maze (or at least, in the parts of it where the maze-scattered neutrons cause the dominant H*(10) contribution). Outside the treatment rooms and in the last arm of the cyclotron maze, *i.e.* where wall-transmitted neutrons essentially determine H*(10), the simulated WENDI-2 responses overestimated the

measurements by factors of 2 – 6. Our results thus confirmed the expected conservative nature of the MCNPX simulations with respect to the wall-transmitted neutron fluxes.

The overestimates tended to be larger around the gantry treatment rooms than the fixed-beam treatment room. This could perhaps be due to unmodelled objects inside the gantry rooms which significantly attenuate the high-energy neutron fluence. We found for instance that adding the front ring of the iron gantry into the simulated geometry significantly reduced the overestimate in one position outside the shielding (by a factor of 2 in the PBS case and 1.4 in the DS case). In the fixed-beam treatment room, however, there were no equipment parts or cupboards between the water phantom and the measurement positions outside the shielding. In this case, the overestimates were limited to factors of 2 – 3.

The MCNPX simulations were based on a standard composition of ordinary concrete referred to as 'NIST Portland', which has a density of $2.30 \, g/cm^3$ and a hydrogen content of 1.0% in mass. Unfortunately, we did not have the possibility of determining the true composition of the concrete in the Essen facility. Instead, we carried out a sensitivity study on the MCNPX simulations by testing 29 concrete compositions found in literature, of which the densities ranged between $2.10 \, g/cm^3$ and $2.58 \, g/cm^3$ and the hydrogen mass percentages between 0.2% and 2.0%. The study showed that errors on the concrete composition and density can lead to non-negligible over- or underestimates of the neutron H*(10) outside the shielding. They can however not be the single cause of the overestimates we observed for the Essen facility. With 'NIST Portland' as a reference composition, the possible overestimates seemed indeed to be limited to a factor of 1.3 – 1.4 at forward angles, and 1.6 at lateral angles.

A sensitivity study was also carried out with respect to the physics models selected for the proton and neutron interactions above 150 MeV. We observed that the choice of the evaporation model (Dresner or ABLA) has no significant influence on the simulation results. The choice of the intranuclear cascade model (Bertini, Isabel, CEM03 or INCL4) can however significantly impact the results, especially outside the shielding. Inside the room, the differences in the neutron H*(10) are not so large (within a factor of 1.3), because the intranuclear cascade model only has an important impact on the high-energy end of the spectra. Inside the shield, these high-energy neutrons however produce additional neutrons of lower energy. Due to this mechanism, the differences that mostly affect the high-energy neutron fluence in front of the shield eventually create differences on the rest of the spectrum, which increase as a function of depth in the concrete. The differences between the H*(10) simulated with different intranuclear cascade models thus increase significantly with depth. At 2 – 3 m depth, they are about as large as those observed in the source spectra for the neutron fluence above ~100 MeV. With the Bertini model, the simulated H*(10) are the largest at forward angles (up to ~40°), whereas the INCL4

model is the most conservative at larger angles. Compared to the least conservative simulation (based on CEM03), the H*(10) values obtained with the Bertini model after 2 – 3 m of concrete are larger by factors of 1.5 – 1.8. With the INCL4 model at backward angles (>90°), these differences exceed a factor of 3.

When using the Bertini model in the MCNPX simulation of the fixed-beam treatment room, the average simulated WENDI-2 responses reproduced the measurements quite well inside the room. With the CEM03 model, on the other hand, the average simulated responses were underestimated by factors of 1.2 – 1.3. The global secondary neutron production in the water phantom thus appeared to be more accurately predicted by the Bertini model than the CEM03 model.

The WENDI-2 measurements did however not inform us on the accuracy of the simulated neutron fluence above 100 MeV specifically. Spectrometry measurements were then acquired with an extended-range BSS in these same positions. In general, the measured spectra agreed better with the Bertini spectra than the CEM03 spectra, except in the high-energy peak at forward angle. For the interactions of the protons with water, the Bertini model appeared to overestimate the forward-angle production of neutrons with energies above 100 MeV. We expect this to cause an overestimate of approximately the same magnitude on the neutron H*(10) outside the shielding (at forward angle). For the considered position, this overestimate was estimated to a factor of 1.7 ± 0.5. A more precise estimate could unfortunately not be obtained due to the large uncertainties on the BSS response matrix at high energies and the limited energy resolution of the BSS.

By folding the BSS spectra with the fluence-to-H*(10) conversion coefficients, we could experimentally assess the accuracy in terms of H*(10) of the WENDI-2 measurements in a few positions, located inside and outside the treatment room. The WENDI-2 measurements agreed with the BSS H*(10) rates within ~10% in each position. It thus confirmed that the WENDI-2 allows measuring H*(10) with satisfactory accuracy in these neutron fields.

A few comparisons were also made with measurements acquired with a conventional rem meter LB 6411 and a TEPC. We observed that the LB 6411 underestimates the H*(10) by ~25-40% in positions characterised by a relatively large fraction of high-energy neutrons. These are located outside the shielding or at forward angles with respect to the proton beam direction inside the treatment room. The results thus tended to confirm the underestimates reported in literature regarding conventional rem meter measurements inside proton therapy facilities [175,242]. As for the TEPC, the measured dose equivalents were lower than the BSS H*(10) and WENDI-2 measurements by 20 – 30%. Other authors [46,176] reported similar results, but for irradiations with proton beams of 178 MeV (*vs.* 227 MeV in our experiment).

During the course of this project, two similar experimental validation studies for Monte Carlo shielding simulations of proton therapy facilities were published. The first study was conducted by Satoh *et al.* at the Fukui proton therapy centre [242]. Their Monte Carlo simulations were carried out with PHITS, using the high-energy nuclear data file JENDL/HE-2007 [278] for protons and neutrons in the range of 20 MeV – 235 MeV. The second study, relative to the Essen proton therapy facility, was carried out by our colleague Thibault Vanaudenhove with GEANT4 (using the Bertini model) [184]. For the simulated neutron H*(10) outside the shielding, both studies reported overestimates that are similar to our own.

The causes behind the conservativeness of the shielding simulations regarding the wall-transmitted neutron fluxes need to be further investigated. Overlooked objects in the simulated geometry and uncertainties on the concrete composition can have a significant effect on the simulation results, but they cannot fully explain the simulation-to-measurement ratios that we observed outside the shielding.

Our work indicated that, for the non-elastic interactions of protons of 150 MeV – 230 MeV in water, the Bertini model probably overestimates the forward production of high-energy neutrons. This could significantly contribute to the overestimates of the H*(10) outside the shielding. Future work should be dedicated to quantifying this overestimate more precisely. The present results could be improved by reducing the uncertainties on the BSS response matrix above 20 MeV. This could probably be attained by means of a thorough experimental validation of the BSS response functions, using for instance well-characterised high-energy quasi-monoenergetic neutron beams that have recently become available at the RCNP of Osaka.

Ideally, precise measurements of the double differential neutron yield for protons of 20 MeV – 230 MeV on thick water targets (and other targets of interest) should be obtained, for instance by means of time-of-flight spectrometry. Benchmark exercises should then be run for the la150h library, the pre-equilibrium exciton model and the intranuclear cascade models of MCNPX. It should be noted that a few measurements are already available in literature (e.g. [238,279]), but there seems to be a specific lack of experimental data for neutron emissions at the most-forward angle.

It also seems important to investigate whether other simulation parameters may significantly influence the neutron attenuation length in the concrete. It could be interesting to perform shielding experiments in which both the neutron source spectrum and the concrete composition are well-characterised. The neutron spectrum should be measured behind increasing thicknesses of concrete and compared to corresponding MCNPX simulations. If the neutron cross-sections (or other simulation aspects?) lead to an overestimate of the attenuation length, increasing differences should appear as a function of the shielding thickness. The

experiment could be repeated for source spectra ranging up to e.g. 70 MeV, 150 MeV and 230 MeV, so as to potentially separate the influence from the physics models and the evaluated cross-section data.

References

[1]   **L. Pray**, *DNA Replication and Causes of Mutation*, Nature Education 1, 214, *2008*.

[2]   **R.A. Weinberg**, Chapter 2: *The nature of cancer*, in: The biology of cancer, second edition, R.A. Weinberg (Ed.), Garland Science (Taylor & Francis Group), ISBN: 0815340761, 31–70, *2014*.

[3]   **B.W. Stewart, C.P. Wild**, *World Cancer Report 2014*, International Agency for Research on Cancer, World Health Organization, ISBN: 978-9-28320-429-9, *2014*.

[4]   **E. Chan, J.B. Berlin**, *Section I - 4. Principles of chemotherapy*, in: Textbook of surgical oncology, G.J. Poston, R.D. Beauchamp, T.J.M. Ruers (Eds.), Informa UK, ISBN: 978-1-84184-507-4, 21–32, *2007*.

[5]   **P. Jain, A. Saleem, P. Price**, *Section I - 3. Principles of adjuvant radiotherapy*, in: Textbook of surgical oncology, G.J. Poston, R.D. Beauchamp, T.J.M. Ruers (Eds.), Informa UK, ISBN: 978-1-84184-507-4, 11–20, *2007*.

[6]   **E.M. Zeman**, Chapter 1: *Biological basis of radiation oncology*, in: Clinical Radiation Oncology, D. Meloni, A. Byrne (Eds.), Churchil Livingstone (Elsevier), ISBN: 978-1-4377-1637-5, 3–46, *2007*.

[7]   **D. Becker, M.D. Sevilla**, *The chemical consequences of radiation damage to DNA*, Advances in Radiation Biology 17, 121–180, *1993*.

[8]   **M.E. Lomax, L.K. Folkes, P. O'Neill**, *Biological consequences of radiation-induced DNA damage: relevance to radiotherapy*, Clinical Oncology 25, 578–585, *2013*.

[9]   **G. Steel**, Chapter 7: *Radiobiology of tumours*, in: Handbook of radiotherapy physics: theory and practice, P. Mayles, A. Nahum, J.C. Rosenwald (Eds.), CRC Press (Taylor & Francis Group), ISBN: 978-0-75030-860-1, 127–148, *2007*.

[10]   **W.D. Newhauser, R. Zhang**, *The physics of proton therapy*, Physics in Medicine and Biology 60, R155–R209, *2015*.

[11]   **P.J. Hoskin, C. Coyle**, Chapter 1: *Introduction*, in: Radiotherapy in practice - Brachytherapy, second edition, P.J. Hoskin, C. Coyle (Eds.), Oxford University Press, ISBN: 978-0-19960-090-8, 1–4, *2011*.

[12]   **J.F. Eary**, Chapter 1: *Principles of therapy with unsealed sources*, in: Nuclear medicine therapy, J.F. Eary, W. Brenner (Eds.), Informa Healthcare USA, ISBN: 978-0-82472-876-2, 1–8, *2007*.

[13]   **P.J. Hoskin**, Chapter 1: *Introduction*, in: Radiotherapy in practice - External beam therapy, P.J. Hoskin (Ed.), Oxford University Press, ISBN: 978-0-19-969656-7, 1–5, *2012*.

[14] **W. Strydom, W. Parker, M. Olivares**, Chapter 8: *Electron beams: physical and clinical aspects*, in: Radiation oncology physics: a handbook for teachers and students, E.B. Podgorsak (Ed.), IAEA, ISBN: 92-0-107304-6, 273–300, *2005*.

[15] **M.W. McDonald, M.M. Fitzek**, *Proton Therapy*, Current Problems in Cancer 34, 257–296, *2010*.

[16] **International Commission on Radiation Units & measurements**, *Quantities and units in radiation protection dosimetry, ICRU Report 51*, *1993*.

[17] **International Commission on Radiation Units & measurements**, *Fundamental quantities and units for ionizing radiation (revised), ICRU report 85*, *2011*.

[18] **International Commission on Radiological Protection**, *The 2007 recommendations of the international commission on radiological protection - ICRP Publication 103*, Annals of the ICRP 37, 1–332, *2007*.

[19] **E.B. Podgorsak**, Chapter 6: *Interactions of charged particles with matter*, in: Radiation physics for medical physics, second edition, E. Greenbaum (Ed.), Springer, ISBN: 978-3-642-00874-0, 227–275, *2010*.

[20] **N. Laulainen, H. Bichsel**, *Energy removed by delta rays from finite volumes in passage of charged particles*, Nuclear Instruments and Methods 104, 531–539, *1972*.

[21] **E.B. Podgorsak**, Chapter 1: *Basic radiation physics*, in: Radiation oncology physics: a handbook for teachers and students, E.B. Podgorsak (Ed.), International Atomic Energy Agency, ISBN: 92-0-107304-6, *2005*.

[22] **International Commission on Radiation Units & measurements**, *Linear Energy Transfer, ICRU report 16*, *1970*.

[23] **B.R. Martin, G. Shaw**, *Section 4.3 - Particle interactions with matter*, in: Particle Physics, Third edition, John Wiley & Sons, ISBN: 978-0-470-03293-0, 83–91, *2008*.

[24] **National Institute of Standards and Technology**, *ESTAR database: stopping powers and ranges for electrons*, URL: http://physics.nist.gov/PhysRefData/Star/Text/ESTAR.html, .

[25] **International Commission on Radiation Units & measurements**, *Stopping power and ranges for protons and alpha particles, ICRU Report 49*, *1993*.

[26] **J.F. Ziegler**, *Stopping of energetic light ions in elemental matter*, Journal of Applied Physics 85, 1249–1272, *1999*.

[27] **National Institute of Standards and Technology**, *PSTAR database: stopping powers and ranges for protons*, URL: http://physics.nist.gov/PhysRefData/Star/Text/PSTAR.html, .

[28] **P. Sigmund**, *Errata and addenda for ICRU Report 73, Stopping of ions heavier than helium*, *2009*.

[29] **F.H. Attix**, Chapter 8: *Charged-particle interactions in matter*, in: Introduction to radiological physics and radiation dosimetry, John Wiley & Sons, ISBN: 0-471-01146-0, 160–202, ***1986***.

[30] **E.B. Podgorsak**, *Section 1.4 - Photon interactions with matter*, in: Radiation oncology physics: a handbook for teachers and students, IAEA, ISBN: 92-0-107304-6, 26–42, ***2005***.

[31] **F.H. Attix**, Chapter 7: *Gamma- and X-ray interactions in matter*, in: Introduction to radiological physics and radiation dosimetry, John Wiley & Sons, ISBN: 0-471-01146-0, 124–159, ***1986***.

[32] **M. Amichetti**, *The Actual interest in radiotherapy for the utilization of proton beam, Highlighting physics basis, technology and common clinical indications*, Journal of Tumor 4, 378–385, ***2016***.

[33] **IAEA, ICRU**, *Relative Biological Effectiveness in Ion Beam Therapy - Technical Reports Series n° 461*, ISBN: 978-92-0-107807-0, ***2008***.

[34] **H. Paganetti**, Chapter 19: *The physics of proton biology*, in: Proton Therapy Physics, H. Paganetti (Ed.), CRC Press (Taylor & Francis Group), ISBN: 978-1-4398-3644-6, 593–626, ***2012***.

[35] **H. Giap, B. Giap**, *Historical perspective and evolution of charged particle beam therapy*, Translational Cancer Research 1, 127–136, ***2012***.

[36] **R.R. Wilson**, *Radiological use of fast protons*, Radiology 47, 487–491, ***1946***.

[37] **J.H. Lawrence**, *Proton irradiation of the pituitary*, Cancer 10, 795–798, ***1957***.

[38] **H. Paganetti**, Chapter 1: *Proton therapy : history and rationale*, in: Proton Therapy Physics, H. Paganetti (Ed.), CRC Press (Taylor & Francis Group), 1–18, ***2012***.

[39] **J.M. Slater, J.O. Archambeau, D.W. Miller, M.I. Notarus, W. Preston, J.D. Slater**, *The proton treatment center at Loma Linda University Medical Center: rationale for and description of its development*, International Journal of Radiation Oncology, Biology and Physics 22, 383–389, ***1992***.

[40] **Particle Therapy Co-Operative Group (PTCOG)**, *Particle therapy facilities in operation*, URL: http://www.ptcog.ch/index.php/facilities-in-operation, **accessed: June 25, 2015**.

[41] **Particle Therapy Co-Operative Group (PTCOG)**, *Particle therapy facilities under construction*, URL: http://www.ptcog.ch/index.php/facilities-under-construction, **accessed: June 25, 2015**.

[42] **F. Stichelbaut, Y. Jongen**, *Properties of an energy degrader for light ions*, Progress in Nuclear Science and Technology 4, 272–275, ***2014***.

[43] **Ion Beam Applications**, *Proteus PLUS brochure*, ***2016***.

[44] **Proton therapy center of Prague**, *Treatment rooms*, URL:

http://www.proton-cancer-treatment.com/proton-center/treatment-technology-and-diagnostics/treatment-rooms/, **accessed: June 9, 2016**.

[45] **B. Gottschalk**, Chapter 2: *Physics of proton interactions in matter*, in: Proton Therapy Physics, H. Paganetti (Ed.), CRC Press (Taylor & Francis Group), 19–60, *2012*.

[46] **R. Sayah**, Evaluation des doses dues aux neutrons secondaires reçues par les patients de différents âges traités par protonthérapie pour des tumeurs intracrâniennes, Université Paris XI, *2013*.

[47] **H. Paganetti, T. Bortfeld**, *Proton beam radiotherapy - The state of the art, New Technologies in Radiation Oncology (Medical Radiology Series)*, ISBN: 3-540-00321-5, *2005*.

[48] **Massachusetts General Hospital Cancer Center**, *What is proton beam therapy? Principles of proton beam therapy*, URL: http://www.massgeneral.org/radiationoncology/AboutProtonTherapy.aspx, **accessed: June 9, 2016**.

[49] **D. Nichiporov, W. Hsi, J. Farr**, *Beam characteristics in two different proton uniform scanning systems: a side-by-side comparison*, Medical physics 39, 2559–2568, *2012*.

[50] **Ion Beam Applications**, *Proteus PLUS brochure*, *2012*.

[51] **B. Marchand, D. Prieels, B. Bauvir, R. Sépulche, M. Gérard**, IBA proton pencil beam scanning: an innovative solution for cancer treatment, in: Proc. Eur. Part. Accel. Conf., Vienna, *2000*: pp. 2539–2541.

[52] **D.F. Measday, C. Richard-Serre**, *Loss of protons by nuclear interactions in various materials, CERN Yellow Report 69 – 17*, *1969*.

[53] **M.B. Chadwick**, *Nuclear Models for Radiotherapy Applications - LA-UR-98-1157*, *1998*.

[54] **B.R. Martin**, Nuclear and particle physics - an introduction, (*2006*).

[55] **L.E. Moritz**, *Radiation protection at low energy proton accelerators*, Radiation protection dosimetry 96, 297–309, *2001*.

[56] **V. Weisskopf**, *Statistics and nuclear reactions*, Physical Review 52, 295–302, *1937*.

[57] **W. Hauser, H. Feshbach**, *The inelastic scattering of neutrons*, Physical Review 87, 366–373, *1952*.

[58] **E. Fermi**, *High energy nuclear events*, Progress of Theoretical Physics 5, 570–583, *1950*.

[59] **M. Blann**, *Preequilibrium decay*, Annual Review of Nuclear Science 25, 123–166, *1975*.

[60] **S. Pedoux**, Extension of the Liège Intranuclear Cascade Model to the 2-15 GeV

Incident Energy Range, PhD thesis, University of Liège, *2012*.

[61] **J.J. Griffin**, *Statistical model of intermediate structure*, Physical Review Letters 17, 478–481, *1966*.

[62] **I. Ribanský, P. Obložinský, E. Běták**, *Pre-equilibrium decay and the exciton model*, Nuclear Physics A 205, 545–560, *1973*.

[63] **R. Serber**, *Nuclear reactions at high Energies*, Physical Review 72, 1114–1115, *1947*.

[64] **V.S. Barashenkov, H.W. Bertini, K. Chen, G. Friedlander, G.D. Harp, A.S. Iljinov, et al.**, *Medium energy intranuclear cascade calculations: a comparative study*, Nuclear Physics A 187, 531–544, *1972*.

[65] **A. Ferrari, P. Sala**, The Physics of High Energy Reactions, in: A. Gandini, G. Reffo (Eds.), Proc. Work. Nucl. React. Data Nucl. React. Physics, Des. Saf. (April-May 1996), World Scientific, Trieste, *1998*.

[66] **H.W. Bertini**, *Low-energy intranuclear cascade calculation*, Physical Review C 131, 1801, *1963*.

[67] **H.W. Bertini**, *Intranuclear-cascade calculation of the secondary nucleon spectra from nucleon-nucleus interactions in the energy range 340 to 2900 MeV and comparisons with experiment*, Physical Review C 188, 1711, *1969*.

[68] **K.K. Gudima, S.G. Mashnik, V.D. Toneev**, *Cascade-exciton model of nuclear reactions*, Nuclear Physics A 401, 326–361, *1983*.

[69] **S.G. Mashnik, K.K. Gudima, R.E. Prael, A.J. Sierk, M.I. Baznat, N.V. Mokhov**, *CEM03.03 and LAQGSM03.03 event generators for the MCNP6, MCNPX, and MARS15 transport codes, LA-UR-08-2931*, *2008*.

[70] **Y. Yariv, Z. Fraenkel**, *Intranuclear cascade calculation of high-energy heavy-ion interactions*, Physical Review C 20, 2227–2243, *1979*.

[71] **Y. Yariv, Z. Fraenkel**, *Intranuclear cascade calculation of high energy heavy ion collisions: effect of interactions between cascade particles*, Physical Review C 24, 488–494, *1981*.

[72] **J. Cugnon, T. Mizutani, J. Vandermeulen**, *Equilibration in relativistic nuclear collisions. A Monte Carlo calculation*, Nuclear Phys 352, 505–534, *1981*.

[73] **J. Cugnon, C. Volant, S. Vuillier**, *Improved intranuclear cascade model for nucleon-nucleus interactions*, Nuclear Physics A 620, 475–509, *1997*.

[74] **Y. Yariv, T. Aoust, A. Boudard, J. Cugnon, J.C. David, S. Lemaire, et al.**, Intranuclear cascade models at low energy?, in: Int. Conf. Nucl. Data Sci. Technol. 2007, , *2008*: pp. 1125–1128.

[75] **T. Aoust**, Améliorations du modèle de cascade intranucléaire de Liège en vue de l'étude de cibles de spallation pour les systèmes hybrides, PhD thesis, University of Liège, *2007*.

[76] **D.J. Brenner, E.J. Hall**, *Secondary neutrons in clinical proton radiotherapy: a charged issue*, Radiotherapy and Oncology 86, 165–170, **2008**.

[77] **B. Clasie, A. Wroe, H. Kooy, N. Depauw, J. Flanz, H. Paganetti, et al.**, *Assessment of out-of-field absorbed dose and equivalent dose in proton fields*, Medical Physics 37, 311–321, **2010**.

[78] **S.J. Dowdell**, Pencil beam scanning proton therapy: the significance of secondary particles, PhD thesis, University of Wollongong, **2011**.

[79] **F. Stichelbaut**, *Shielding Calculations for PT Center in Essen, Germany (internal presentation at IBA)*, **2009**.

[80] **P. Reuss**, Chapter 9: *Thermalisation of neutrons*, in: Neutron physics, EDP Sciences, ISBN: 9782759800414, 259–284, **2008**.

[81] **N.E. Ipe**, Chapter 17: *Neutron interactions & shielding aspects for proton therapy*, in: Proton Therapy Physics, CRC Press edition, H. Paganetti (Ed.), ISBN: 978-1-4398-3644-6, 525–554, **2012**.

[82] **International Commission on Radiological Protection**, *Relative biological effectiveness (RBE), quality factor (Q), and radiation weighting factor (wR), ICRP Publication 92*, **2003**.

[83] **S. Agosteo, M. Silari, L. Ulrici**, *Instrument response in complex radiation fields*, Radiation Protection Dosimetry 137, 51–73, **2009**.

[84] **D.J. Thomas**, *The system of radiation protection for neutrons: does it fit the purpose?*, Radiation protection dosimetry 161, 3–10, **2014**.

[85] **International Commission on Radiological Protection**, *1990 Recommendations of the International Commission on Radiological Protection, ICRP Publication 60*, **1991**.

[86] **International Commission on Radiological Protection**, *Conversion coefficients for radiological protection quantities for external radiation exposures, ICRP Publication 116*, **2010**.

[87] **International Commission on Radiological Protection**, *Conversion coefficients for use in radiological protection against external radiation, ICRP Publication 74*, **1996**.

[88] **A.V. Sannikov, E.N. Savitskaya**, *Ambient dose equivalent conversion factors for high energy neutrons based on the ICRP 60 recommendations*, Radiation protection dosimetry 70, 383–386, **1997**.

[89] **M. Pelliccioni**, *Overview of fluence-to-effective dose and fluence-to-ambient dose equivalent conversion coefficients for high energy radiation calculated using the FLUKA code*, Radiation Protection Dosimetry 88, 279–297, **2000**.

[90] **S. Agosteo, M. Magistris, A. Mereghetti, M. Silari, Z. Zajacova**, *Shielding data for 100–250 MeV proton accelerators: Double differential neutron distributions and attenuation in concrete*, Nuclear Instruments and Methods in Physics

Research B 265, 581–598, *2007*.

[91]   **IAEA**, *Compendium of neutron spectra and detector responses - Technical Reports Series No. 403 - Supplement to Technical Reports Series No. 318*, *2001*.

[92]   **M. Silari, G.R. Stevenson**, *Radiation protection at high energy proton accelerators.*, Radiation protection dosimetry 96, 311–321, *2001*.

[93]   **IAEA**, *Radiological Safety Aspects of the Operation of Proton Accelerators, Technical Reports Series no. 283*, *1988*.

[94]   **W.D. Newhauser, U. Titt, D. Dexheimer, X. Yan, S. Nill**, *Neutron shielding verification measurements and simulations for a 235-MeV proton therapy center*, Nuclear Instruments and Methods in Physics Research A 476, 80–84, *2002*.

[95]   **U. Titt, W.D. Newhauser**, *Neutron shielding calculations in a proton therapy facility based on Monte Carlo simulations and analytical models: criterion for selecting the method of choice*, Radiation protection dosimetry 115, 144–148, *2005*.

[96]   **M.R. Folkert**, Monte Carlo Simulation of Neutron Shielding for Proton Therapy Facilities, Master thesis, MIT, *1998*.

[97]   **A.F. Bielajew**, *Fundamentals of the Monte Carlo method for neutral and charged particle transport, class notes*, University of Michigan, *2001*.

[98]   **X-5 Monte Carlo Team**, *MCNP - A General Monte Carlo N-Particle Transport Code, Version 5 - Volume I: Overview and Theory, LA-UR-03-1987*, *2003*.

[99]   **N.E. Ipe, G. Fehrenbacher, I. Gudowska, H. Paganetti, J.M. Schippers, S. Roesler, et al.**, *PTCOG Publications Sub-Committee Task Group on Shielding Design and Radiation Safety of Charged Particle Therapy Facilities*, *2010*.

[100] **D.B. Pelowitz**, *MCNPX User's Manual Version 2.7.0, LA-CP-11-00438*, *2011*.

[101] **T. Goorley, M. James, T. Booth, F. Brown, J. Bull, L.J. Cox, et al.**, Features of MCNP6, in: Jt. Int. Conf. Supercomput. Nucl. Appl. Monte Carlo, , *2013*.

[102] **S. Agostinelli, J. Allison, K. Amako, J. Apostolakis, H. Araujo, P. Arce, et al.**, *GEANT4 - A simulation toolkit*, Nuclear Instruments and Methods in Physics Research A 506, 250–303, *2003*.

[103] **J. Allison, K. Amako, J. Apostolakis, H. Araujo, P.A. Dubois, M. Asai, et al.**, *GEANT4 developments and applications*, IEEE Transactions on Nuclear Science 53, 270–278, *2006*.

[104] **S. Jan, G. Santin, D. Strul, S. Staelens, K. Assié, D. Autret, et al.**, *GATE: a simulation toolkit for PET and SPECT*, Physics in Medicine and Biology 49, 4543–4561, *2004*.

[105] **A. Ferrari, P.R. Sala, A. Fassò, J. Ranft**, *Fluka: a multi-particle transport code, CERN 2005-010, INFN TC_05/11, SLAC-R-773*, *2005*.

[106] **G. Battistoni, F. Cerutti, A. Fassò, A. Ferrari, S. Muraro, J. Ranft, et al.**, *The

FLUKA code: description and benchmarking, AIP Conference Proceedings 896, 31–49, **2007**.

[107] **T.T. Böhlen, F. Cerutti, M.P.W. Chin, A. Fassò, A. Ferrari, P.G. Ortega, et al.**, *The FLUKA Code: Developments and challenges for high energy and medical applications*, Nuclear Data Sheets 120, 211–214, **2014**.

[108] **T. Sato, K. Niita, N. Matsuda, S. Hashimoto, Y. Iwamoto, S. Noda, et al.**, *Particle and Heavy Ion Transport code System*, Journal of Nuclear Science and Technology 50, 913–923, **2013**.

[109] **G.W. McKinney, J.W. Durkee, J.S. Hendricks, M.R. James, D.B. Pelowitz, L.S. Waters, et al.**, *MCNPX Overview - LA-UR-06-6206*, **2006**.

[110] **U.S.A.. National Nuclear Data Center (Brookhaven**, *Cross Section Evaluation Working Group*, URL: http://www.nndc.bnl.gov/csewg/, **accessed: June 17, 2016**.

[111] **R.C. Haight**, *Medium energy neutron and proton nuclear data for therapy*, Radiochimica Acta 89, 289–296, **2001**.

[112] **M.B. Chadwick, M. Herman, P. Obložinský, M.E. Dunn, Y. Danon, A.C. Kahler, et al.**, *ENDF/B-VII.1 Nuclear data for science and technology: cross sections, covariances, fission product yields and decay data*, Nuclear Data Sheets 112, 2887–2996, **2011**.

[113] **M.B. Chadwick, S.C. Frankle, R.C. Little, P.G. Young**, *New high-energy evaluated nuclear data libraries for the Accelerator Production of Tritium program - LA-UR-08-07576*, **1996**.

[114] **P.G. Young, E.D. Arthur**, *GNASH: A preequilibrium, statistical nuclear model code for calculation of cross, Los Alamos - LA-6947*, **1977**.

[115] **E.D. Arthur, P.G. Young**, *New developments in the GNASH nuclear theory code - LA-UR-88-1739*, **1988**.

[116] **P.G. Young, E.D. Arthur, M.B. Chadwick**, *Comprehensive nuclear model calculations: introduction to the theory and use of the GNASH code - LA-12343-MS*, **1992**.

[117] **P.G. Young, M.B. Chadwick**, Improvements to the nuclear model code GNASH for cross section calculations at higher energies, in: Proc. Nucl. Data Sci. Technol. 1994 Conf. Gatlinbg., , **1994**.

[118] **M.B. Chadwick**, *Neutron, proton, and photonuclear cross-sections for radiation therapy and radiation protection - LA-UR-98-4139*, **1998**.

[119] **M.B. Chadwick, P.G. Young, S. Chiba, S.C. Frankle, G.M. Hale, H.G. Hughes, et al.**, *Cross-section evaluations to 150 MeV for accelerator-driven systems and implementation in MCNPX*, Nuclear Science and Engineering 131, 293–328, **1999**.

[120] **J. Raynal**, *Optical-model and coupled-channel calculations in nuclear physics,*

IAEA-SMR-9/8, **1971**.

[121] **International Commission on Radiation Units & measurements**, *Nuclear data for neutron and proton radiotherapy and for radiation protection, ICRU Report 63*, **2000**.

[122] **M.B. Chadwick, P. Obložinský, M. Herman, N.M. Greene, R.D. McKnight, D.L. Smith, et al.**, *ENDF/B-VII.0: Next Generation Evaluated Nuclear Data Library for Nuclear Science and Technology*, Nuclear Data Sheets 107, 2931–3060, **2006**.

[123] **D.J. Brenner, R.E. Prael, J.F. Dicello, M. Zaider**, Improved calculations of energy deposition from fast neutrons, in: Proc. Fourth Symp. Neutron Dosim., Munich-Neuherberg, **1981**.

[124] **R.E. Prael**, *A summary of the hadron reaction models for use in LANL Monte Carlo transport codes, LA-UR-02-4967*, **2002**.

[125] **L.S. Waters**, *MCNPX User's Manual Version 2.3.0, LA-UR-02-2607*, **2002**.

[126] **S.G. Mashnik, A.J. Sierk**, *Improved cascade-exciton model of nuclear reactions - LA-UR-98-5999*, **1998**.

[127] **D. Filges, F. Goldenbaum**, Handbook of spallation research - theory, experiments and applications, (**2009**).

[128] **S.G. Mashnik, A.J. Sierk, K.K. Gudima, M.I. Baznat**, CEM03 and LAQGSM03 - new modeling tools for nuclear applications, in: J. Phys. Conf. Ser., , **2006**: pp. 340–351.

[129] **V.S. Barashenkov, V.D. Toneev**, *Interaction of high energy particle and nuclei with atomic nuclei, (1972)*, **1972**.

[130] **J. Cugnon**, *Proton nucleus interaction at high-energy*, Nuclear Physics A 462, 751–780, **1987**.

[131] **J. Cugnon, M.-C. Lemaire**, *Medium effects in pion production*, Nuclear Physics A 489, 781–802, **1988**.

[132] **A. Boudard, J. Cugnon, S. Leray, C. Volant**, *Intranuclear cascade model for a comprehensive description of spallation reaction data*, Physical Review C 66, 44615-1-4615–28, **2002**.

[133] **R.E. Prael, M. Bozoian**, *Adaptation of the Multistage Pre-equilibrium Model for the Monte Carlo method - LA-UR-88-3238*, **1998**.

[134] **Y.A. Korovin, A.A. Natalenko, A.Y. Konobeyev, A.Y. Stankovskiy, S.G. Mashnik**, *High energy activation data library (HEAD-2009) - LA-UR-10-01397*, **2009**.

[135] **L. Dresner**, *EVAP - A Fortran program for calculating the evaporation of various particle evaporation from excited nuclei, ORNL-TM-196*, **1961**.

[136] **F. Atchison**, Spallation and Fission in Heavy Metal Nuclei under Medium Energy Proton Bombardment," in , Kernforschungsanlage Julich GmbH (January

1980)., in: Targets Neutron Beam Spallation Sources, Jul-Conf-34, Kernforschungsanlage Jülich GmbH, Jülich, *1980*.

[137] **J. Barish, T.A. Gabriel, F.S. Alsmiller, R.G. Alsmiller**, *HETFIS High-Energy nucleon-meson Transport code with Fission - ORNL-TM-7882*, *1981*.

[138] **J.D. Bowman, W.J. Swiatecki, C.F. Tsang**, *Abrasion and ablation of heavy ions - LBL-2908*, *1973*.

[139] **A.R. Junghans, M. de Jong, H.-G. Clerc, A.V. Ignatyuk, G.A. Kudyaev, K.-H. Schmidt**, *Projectile-fragment yields as a probe for the collective enhancement in the nuclear level density*, Nuclear Physics A 629, 635–655, *1998*.

[140] **J. Benlliure, A. Grewe, M. de Jong, K.-H. Schmidt, S. Zhdanov.**, *Calculated nuclide production yields in relativistic collisions of fissile nuclei. Nucl. Phys. A, 628(3):458, 1998.*, Nuclear Physics A 628, 458–478, *1998*.

[141] **A. Leprince, J.-C. David, D. Ene, S. Leray**, *Reliability and use of INCL4.6-Abla07 spallation model in the frame of European Spallation Source target design*, Progress in Nuclear Science and Technology 4, 491–495, *2014*.

[142] **S. Furihata**, *Statistical analysis of light fragment production from medium energy proton-induced reactions*, Nuclear Instruments and Methods B 171, 251–258, *2000*.

[143] **T.E. Booth**, *A sample problem for variance reduction in MCNP, LA-10363-MS*, *1985*.

[144] **M. Cosack, H. Lesiecki**, *Dose equivalent survey meters*, Radiation protection dosimetry 10, 111–199, *1985*.

[145] **ISO/TC85**, *International Standard ISO/DIS 8529-1 - Reference Neutron Radiations Part 1: Characteristics and Methods of Production*, *2000*.

[146] **M. Silari, P. Bilski, J. Blomgren, A. Esposito, G. Fehrenbacher, A. Fuchs, et al.**, *Complex workplace radiation fields at European high-energy accelerators and thermonuclear fusion facilities*, *2006*.

[147] **C.R. Hirning, A.J. Waker**, *Needs and performance requirements for neutron monitoring in the nuclear power industry*, Radiation protection dosimetry 70, 67–72, *1997*.

[148] **V. Mares, A.V. Sannikov, H. Schraube**, *Response functions of the Andersson-Braun and extended range rem counters for neutron energies from thermal to 10 GeV*, Nuclear Instruments and Methods in Physics Research, Section A 476, 341–346, *2002*.

[149] **M. Silari, S. Agosteo, P. Beck, R. Bedogni, E. Cale, M. Caresana, et al.**, *Intercomparison of radiation protection devices in a high-energy stray neutron field. Part III: Instrument response*, Radiation Measurements 44, 673–691, *2009*.

[150] **C. Birattari, A. Ferrari, C. Nuccetelli, M. Pelliccioni, M. Silari**, *An extended range neutron rem counter*, Nuclear Instruments and Methods in Physics

Research A 297, 250–257, **1990**.

[151] **C. Birattari, A. Esposito, A. Ferrari, M. Pelliccioni, T. Rancati, M. Silari**, *The extended range neutron rem counter "LINUS": overview and latest developments*, Radiation protection dosimetry 76, 135–148, **1998**.

[152] **R.H. Olsher, H.H. Hsu, A. Beverding, J.H. Kleck, W.H. Casson, D.G. Vasilik, et al.**, *WENDI: an improved neutron rem meter*, Health Physics 79, 170–181, **2000**.

[153] **Thermo Scientific**, *FHT 762 WENDI-2 Product Specifications*, **2007**.

[154] **Thermo Scientific**, *Datasheet WENDI-2 FHT 762 - 42540/85*, **2009**.

[155] **Thermo Scientific**, *Test protocol WENDI-2 FHT 762 - 42540/85 - serial number 344*, **2008**.

[156] **Thermo Fisher Scientific**, *FH 40 G Multi-Purpose Digital Survey Meter*, URL: https://www.thermofisher.com/order/catalog/product/4254002, **accessed: June 4, 2016**.

[157] **D.J. Thomas, A.V. Alevra**, *Bonner sphere spectrometers - A critical review*, Nuclear Instruments and Methods in Physics Research, Section A 476, 12–20, **2002**.

[158] **M. Matzke**, *Unfolding procedures*, Radiation protection dosimetry 107, 155–174, **2003**.

[159] **C. Birattari, E. Dimovasili, A. Mitaroff, M. Silari**, *A Bonner Sphere Spectrometer with extended response matrix*, Nuclear Instruments and Methods in Physics Research A 620, 260–269, **2010**.

[160] **M. Silari**, *Workplace characterisation in mixed neutron-gamma fields, specific requirements and available methods at high-energy accelerators*, Radiation Protection Dosimetry 124, 230–244, **2007**.

[161] **A.J. Waker**, *Principles of experimental microdosimetry*, Radiation protection dosimetry 61, 297–308, **1995**.

[162] **International Commission on Radiation Units & measurements**, *Microdosimetry, ICRU Report 36*, **2016**.

[163] **J.V. Siebers**, Shielding measurements for a 230 MeV proton beam, University of Wisconsin-Madison, **1990**.

[164] **A. Mazal, K. Gall, J.F. Bottollier-Depois, S. Michaud, D. Delacroix, P. Fracas, et al.**, *Shielding measurements for a proton therapy beam of 200 MeV: Preliminary results*, Radiation protection dosimetry 70, 429–436, **1997**.

[165] **W.K. Hagen, B.L. Colborn, T.W. Armstrong**, *Radiation shielding calculations for the Loma Linda Proton Therapy Facility - SAIC 87/1072*, ISBN: 9788578110796, **1987**.

[166] **W.K. Hagen, B.L. Colborn, T.W. Armstrong, M. Allen**, *Radiation shielding calculations for a 70-250 MeV Proton Therapy Facility*, Nuclear Science and

Engineering 98, 272–278, *1988*.

[167] **T.W. Armstrong, B.L. Colborn**, *A thick-target radiation transport computer code for low-mass heavy ion beams*, Nuclear Instruments and Methods 169, 161–172, *1980*.

[168] **W.W. Engle**, *A user's manual for ANISN - a one dimensional discrete ordinates transport code with anisotropic scattering*, ISBN: 9788578110796, *1967*.

[169] **R.E. Prael**, *The LAHET code system: introduction, development and benchmarking*, *1993*.

[170] **R.G. Alsmiller, R.T. Santoro, J. Barish**, *Shielding calculations for a 200 MeV proton accelerator and comparisons with experimental data*, Particle Accelerators 7, 1–7, *1975*.

[171] **R. Tayama, H. Handa, K. Hayashi, H. Nakano, N. Sasamoto, H. Nakashma, et al.**, *Benchmark calculations of neutron yields and dose equivalent from thick iron target for 52-256 MeV protons*, Nuclear Engineering and Design 213, 119–131, *2002*.

[172] **J.C. Polf, W.D. Newhauser, U. Titt**, *Patient neutron dose equivalent exposures outside of the proton therapy treatment field*, Radiation Protection Dosimetry 115, 154–158, *2005*.

[173] **J.C. Polf, W.D. Newhauser**, *Calculations of neutron dose equivalent exposures from range-modulated proton therapy beams*, Physics in medicine and biology 50, 3859–3873, *2005*.

[174] **R. Tayama, Y. Fujita, M. Tadokoro, H. Fujimaki, T. Sakae, T. Terunuma**, *Measurement of neutron dose distribution for a passive scattering nozzle at the Proton Medical Research Center (PMRC)*, Nuclear Instruments and Methods in Physics Research A 564, 532–536, *2006*.

[175] **E. Hohmann, S. Safai, C.H. Bula, R. Lüscher, C. Harm, S. Mayer, et al.**, *Investigation of the neutron stray radiation field produced by irradiating a water phantom with 200 MeV protons*, Nuclear Technology 175, 77–80, *2011*.

[176] **J. Farah, F. Martinetti, R. Sayah, V. Lacoste, L. Donadille, F. Trompier, et al.**, *Monte Carlo modeling of proton therapy installations: a global experimental method to validate secondary neutron dose calculations*, Physics in medicine and biology 59, 2747–2765, *2014*.

[177] **S. Rollet, S. Agosteo, G. Fehrenbacher, C. Hranitzky, T. Radon, M. Wind**, *Intercomparison of radiation protection devices in a high-energy stray neutron field, Part I: Monte Carlo simulations*, Radiation Measurements 44, 649–659, *2009*.

[178] **B. Wiegel, S. Agosteo, R. Bedogni, M. Caresana, A. Esposito, G. Fehrenbacher, et al.**, *Intercomparison of radiation protection devices in a high-energy stray neutron field, Part II: Bonner sphere spectrometry*, Radiation Measurements 44, 660–672, *2009*.

[179] **G. Fehrenbacher, B. Wiegel, H. Iwase, T. Radon, D. Schardt, H. Schuhmacher, et al.**, *Spectrometry behind concrete shielding for neutrons produced by 400 MeV/u 12C ions impinging on a thick graphite target, GSI-2004-06/EXT-2004-084*, ***2004***.

[180] **H. Iwase, B. Wiegel, G. Fehrenbacher, D. Schardt, T. Nakamura, K. Niita, et al.**, *Comparison between calculation and measured data on secondary neutron energy spectra by heavy ion reactions from different thick targets*, Radiation Protection Dosimetry 116, 640–646, ***2005***.

[181] **L. Jägerhofer, E. Feldbaumer, D. Forkel-Wirth, C. Theis, H. Vincke, Y. Iwamoto, et al.**, *Characterization of the WENDI-II REM Counter for its Application at MedAustron*, Progress in NUCLEAR SCIENCE and TECHNOLOGY 2, 258–262, ***2011***.

[182] **R.H. Olsher, T.D. McLean**, *High-energy response of the PRESCILA and WENDI-II neutron rem meters*, Radiation Protection Dosimetry 130, 510–513, ***2008***.

[183] **L. Jägerhofer, E. Feldbaumer, C. Theis, S. Roesler, H. Vincke**, *A new method to calculate the response of the WENDI-II rem counter using the FLUKA Monte Carlo Code*, Nuclear Instruments and Methods in Physics Research A 691, 81–85, ***2012***.

[184] **T. Vanaudenhove**, Shielding study against high-energy neutrons produced in a proton therapy facility by means of Monte Carlo codes and on-site measurements, PhD thesis, Université Libre de Bruxelles, ***2014***.

[185] **ISO/TC85**, *International Standard ISO/DIS 8529-2 - Reference neutron radiations - (a) Part 2: Calibration fundamentals of radiation protection devices related to the basic quantities characterizing the radiation field*, ***2000***.

[186] **ISO/TC85**, *International Standard ISO/DIS 8529-3 - Reference neutron radiations - Part 3: Calibration of area and personal dosimeters and determination of their response as a function of neutron energy and angle of incidence*, ***1998***.

[187] **H. Harano, R. Nolte**, *Quasi-monoenergetic high-energy neutron standards above 20 MeV*, Metrologia 48, S292–S303, ***2011***.

[188] **LND**, *Datasheet LND 252180 He3 neutron detector*, LND, n.d.

[189] **S. Tolo**, Monte Carlo simulation of the WENDI-2 neutron dosimeter, Master thesis, Università di Bologna, ***2012***.

[190] **V. De Smet, I. Gerardy, F. Stichelbaut, S. Tolo**, *MCNPX simulations of the response of the extended-range rem meter WENDI-2*, Nuclear Technology and Radiation Protection 29(Suppl.), 25–30, ***2014***.

[191] **Japan Charged-Particle Nuclear Reaction Data Group**, *PENDL: plotter for evaluated nuclear data libraries*, URL: http://www.jcprg.org/endf/, **accessed: February 12, 2016**.

[192] **R.C. Little, H.R. Trellue, R.E. MacFarlane, A.C. Kahler, M.B. Lee, M.C. White**,

New neutron, proton, and S(α,β) MCNP data libraries based on ENDF/B-VII, in: Proc. Int. Conf. Phys. React. 'Nuclear Power A Sustain. Resour. Interlaken, , **2008**.

[193] **A. Heikkinen, N. Stepanov, J.P. Wellisch**, Bertini intra-nuclear cascade implementation in Geant4, in: Comput. High Energy Nucl. Phys. 2003 Conf. Proc., , **2003**.

[194] **GEANT4 Online Manual**, *The GEANT4 Binary Cascade*, URL: http://geant4.web.cern.ch/geant4/G4UsersDocuments/UsersGuides/PhysicsReferenceManual/html/node130.html, **accessed: February 1, 2016**.

[195] **G. Folger, V.N. Ivanchenko, J.P. Wellisch**, *The Binary Cascade*, The European Physical Journal A 21, 407–417, **2004**.

[196] **GEANT4 Online Manual**, *Precompound model*, URL: http://geant4.web.cern.ch/geant4/G4UsersDocuments/UsersGuides/PhysicsReferenceManual/html/node148.html, **accessed: February 1, 2016**.

[197] **GEANT4 Online Manual**, *Evaporation Model*, URL: http://geant4.web.cern.ch/geant4/G4UsersDocuments/UsersGuides/PhysicsReferenceManual/html/node153.html, **accessed: February 1, 2016**.

[198] **GEANT4 Online Manual**, *Fermi break-up model*, URL: http://geant4.web.cern.ch/geant4/G4UsersDocuments/UsersGuides/PhysicsReferenceManual/html/node166.html, **accessed: February 1, 2016**.

[199] **FLUKA Online Manual**, *Low - energy neutrons in FLUKA*, URL: http://www.fluka.org/fluka.php?id=man_onl&sub=96, **accessed: February 1, 2016**.

[200] **A. Ferrari, P.R. Sala**, A new model for hadronic interactions at intermediate energies for the FLUKA code, in: Proc. MC93 Int. Conf. Monte Carlo Simul. High Energy Nucl. Phys., Tallahassee, **1994**.

[201] **M. Blann**, *Hybrid model for pre-equilibrium decay in nuclear reactions*, Physical Review Letters 27, 337–339, **1971**.

[202] **M. Blann**, *Importance of the nuclear density distribution on pre-equilibrium decay*, Physical Review Letters 28, 757–759, **1972**.

[203] **M. Blann, H.K. Vonach**, *Global test of modified precompound decay models*, Physical Review C 28, 1475–1492, **1983**.

[204] **M. Blann**, *Precompound analyses of spectra and yields following nuclear capture of stopped π*, Physical Review C 28, 1648–1662, **1983**.

[205] **FLUKA Online Manual**, *History of FLUKA*, URL: http://www.fluka.org/fluka.php?id=man_onl&sub=103, **accessed: February 1, 2016**.

[206] **J.B. Hunt**, *The calibration of neutron sensitive spherical devices*, Radiation Protection Dosimetry 8, 239–251, **1984**.

[207] **A.V. Prokofiev, J. Blomgren, O. Byström, C. Ekström, S. Pomp, U. Tippawan, et al.**, *The TSL neutron beam facility*, Radiation protection dosimetry 126, 18–22, **2007**.

[208] **Y. Naitou, Y. Watanabe, S. Hirayama, M. Hayashi, A.V. Prokofiev, A. Hjalmarsson, et al.**, *Characterization of ANITA and QMN Neutron Beams at TSL Using Proton Recoil Techniques*, Journal of the Korean Physical Society 59, 1439–1442, **2011**.

[209] **W. Feller**, *On probability problems in the theory of counters*, in: R. Courant Anniversary volume, Studies and Essays, Interscience, New York, 105–115, **1948**.

[210] **A.V. Prokofiev**, *Neutron monitors at the TSL neutron facility - TSL Technical Note 060829-1*, **2006**.

[211] **L. Tommasino, N. Klein, P. Solomon**, *Fission fragment detection by thin film capacitors — I Breakdown counter*, Nuclear Track Detection 1, 63–70, **1977**.

[212] **A.N. Smirnov, V.P. Eismont**, *Investigations of physical properties of MOS-structure heavy ion counters*, Nuclear Instruments and Methods 154, 471–476, **1978**.

[213] **A.G. Donichkin, A.N. Smirnov, V.P. Eismont**, *Heavy-ion detection properties of thin dielectric film breakdown counters*, Nuclear Tracks 3, 205–211, **1979**.

[214] **V.P. Eismont, A.V. Prokofiev, A.N. Smirnov**, *Thin-film breakdown counters and their applications (review)*, Radiation Measurements 25, 151–156, **1995**.

[215] **A.V. Prokofiev, A.N. Smirnov, P.-U. Renberg**, *A Monitor of Intermediate-Energy Neutrons Based on Thin Film Breakdown Counters (TSL/ISV-99-0203)*, **1999**.

[216] **A.D. Carlson, S. Chiba, F.-J. Hambsch, N. Olsson, A.N. Smirnov**, *International Nuclear Data Committee Report INDC(NDS)-368 - Update to nuclear data standards for nuclear measurements*, **1997**.

[217] **V.P. Eismont, A.V. Prokofiev, A.N. Smirnov, K. Elmgren, J. Blomgren, H. Condé, et al.**, *Relative and absolute neutron-induced fission cross sections of in the intermediate energy region Pb , Bi , and*, Physical Review C 53, 2911–2918, **1996**.

[218] **H.R. Trellue, R.C. Little, M.C. White, R.E. MacFarlane, A.C. Kahler**, *ENDF70: a continuous-energy MCNP neutron data library based on ENDF/B-VII.0*, Nuclear Technology 168, 832–836, **2009**.

[219] **F.B. Brown**, *A Tutorial on Merging Tallies From Separate MCNP5 Runs, LA-UR-08-0249*, **2008**.

[220] **B.N. Taylor, C.E. Kuyatt**, *Guidelines for Evaluating and Expressing the Uncertainty of NIST Measurement Results. NIST Technical Note 1297*, **1994**.

[221] **S.G. Mashnik, M.B. Chadwick, P.G. Young, R.E. MacFarlane, L.S. Waters**, *Li*

(p,n) Nuclear Data Library for Incident Proton Energies to 150 MeV, LA-UR-00-1067, **2000**.

[222] **S.G. Mashnik, J.S. Bull**, *MCNP6 simulation of quasi-monoenergetic 7Li(p,n) neutron sources below 150 MeV*, Nuclear Data Sheets 118, 323–325, **2014**.

[223] **Y. Uwamino, T.S. Soewarsono, H. Sugita, Y. Uno, T. Nakamura, T. Shibata, et al.**, *High-energy p-Li neutron field for activation experiment*, Nuclear Instruments and Methods in Physics Research A 389, 463–473, **1997**.

[224] **J.F. Ziegler, M.D. Ziegler, J.P. Biersack**, *SRIM - The stopping and range of ions in matter (2010)*, Nuclear Instruments and Methods in Physics Research B 268, 1818–1823, **2010**.

[225] **A.V. Prokofiev, M. Chadwick, S.G. Mashnik, N. Olsson, L. Waters**, *Development and validation of the 7Li(p,n) nuclear data library and its application in monitoring of intermediate energy neutrons*, Journal of Nuclear Science and Technology Supplement, 112–115, **2002**.

[226] **M. Baba, Y. Nauchi, T. Iwasaki, T. Kiyosumi, M. Yoshioka, S. Matsuyama, et al.**, *Characterization of a 40-90 MeV 7Li(p,n) neutron source at TIARA using a proton recoil telescope and a TOF method*, Nuclear Instruments and Methods in Physics Research A 428, 454–465, **1999**.

[227] **G.G. Ohlsen**, *Kinematic relations in reactions of the form A+B→C+D+E*, Nuclear Instruments and Methods 37, 240–248, **1965**.

[228] **S. Neumann**, Aktivierungsexperimente mit Neutronen mittlerer Energien und die Produktion kosmogener Nuklide in extraterrestrischer Materie, PhD thesis, University of Hannover, **1999**.

[229] **S. Dangtip, A. Ataç, B. Bergenwall, J. Blomgren, K. Elmgren, C. Johansson, et al.**, *A facility for measurements of nuclear cross sections for fast neutron cancer therapy*, Nuclear Instruments and Methods in Physics Research Section A 452, 484–504, **2000**.

[230] **R. Bevilacqua, S. Pomp, V. Simutkin, M. Hayashi, S. Hirayama, Y. Naitou, et al.**, *Medley spectrometer for light ions in neutron-induced reactions at 175MeV*, Nuclear Instruments and Methods in Physics Research A 646, 100–107, **2011**.

[231] **S. Pomp, U. Tippawan**, *An iterative procedure to obtain inverse response functions for thick-target correction of measured charged-particle spectra*, Nuclear Instruments and Methods in Physics Research Section A 572, 893–898, **2007**.

[232] **Y. Iwamoto, M. Hagiwara, H. Iwase, H. Yashima, D. Satoh, T. Matsumoto, et al.**, *Characterization of quasi-monoenergetic neutron source using 137, 200, 246 and 389 MeV 7Li(p,n) reactions*, Progress in Nuclear Science and Technology 4, 657–660, **2014**.

[233] **Y. Iwamoto, M. Hagiwara, D. Satoh, S. Araki, H. Yashima, T. Sato, et al.**, *Characterization of high-energy quasi-monoenergetic neutron energy spectra and ambient dose equivalents of 80–389MeV 7Li(p,n) reactions using a time-of-*

flight method, Nuclear Instruments and Methods in Physics Research Section A: Accelerators, Spectrometers, Detectors and Associated Equipment 804, 50–58, **2015**.

[234] **V. De Smet, F. Stichelbaut, T. Vanaudenhove, G. Mathot, G. De Lentdecker, A. Dubus, et al.**, *Neutron H*(10) inside a proton therapy facility: comparison between Monte Carlo simulations and WENDI-2 measurements*, Radiation protection dosimetry 161, 417–421, **2014**.

[235] **D.B. Pelowitz**, *MCNPX User's Manual Version 2.5.0, LA-CP-05-0369*, **2005**.

[236] **R.J. McConn Jr, C.J. Gesh, R.T. Pagh, R.A. Rucker, R.G. Williams III**, Compendium of Material Composition Data for Radiation Transport Modeling - Revision 1, PIET-43741-TM963, PNNL-15870 Rev. 1, **2011**.

[237] **J.K. Shultis, R.E. Faw**, *An mcnp primer*, **2010**.

[238] **M.M. Meier, W.B. Amian, C.A. Goulding, G.L. Morgan, C.E. Moss**, *Neutron yields from stopping-length targets for 256-MeV protons*, Nuclear Science and Engineering 110, 299–301, **1992**.

[239] **C. Courtois, G. Boissonnat, C. Brusasco, J. Colin, D. Cussol, J.M. Fontbonne, et al.**, *Characterization and performances of a monitoring ionization chamber dedicated to IBA-universal irradiation head for Pencil Beam Scanning*, Nuclear Instruments and Methods in Physics Research A 736, 112–117, **2014**.

[240] **PTW**, *User Manual Bragg Peak Chambers Type 34070, 34073 and 34080, D797.131.00/04*, **2008**.

[241] **International Commission on Radiation Units & measurements**, *Clinical proton dosimetry - Part I: beam production, beam delivery and measurement of absorbed dose, ICRU Report 59*, **1998**.

[242] **D. Satoh, Y. Maeda, Y. Tameshige, H. Nakashima, T. Shibata, A. Endo, et al.**, *Shielding study at the Fukui Prefectural Hospital Proton Therapy Center*, Journal of Nuclear Science and Technology 49, 1097–1109, **2012**.

[243] **S.H. Kosmatka, B. Kerkhoff, W.C. Paranese**, Chapter 5: *Aggregates for concrete*, in: Design and control of concrete mixtures, 14th edition, Portland Cement Association, ISBN: 9780870312489, **2002**.

[244] **S.H. Kosmatka, B. Kerkhoff, W.C. Paranese**, Chapter 2: *Portland, blended, and other hydraulic cements*, in: Design and control of concrete mixtures, 14th edition, Portland Cement Association, **2002**.

[245] **P.K. Mehta, P.J.M. Monteiro**, Concrete: microstructure, properties, and materials, Concrete (**2006**).

[246] **R.L. Walker**, *A summary of shielding constants for concrete*, **1961**.

[247] **J.D. Cossairt**, *Radiation physics for personnel and environmental protection*, **2011**.

[248] **K.. Kase, W.R. Nelson, A. Fassò, J.C. Liu, X. Mao, T.M. Jenkins, et al.**, *Measurements of accelerator-produced leakage neutron and photon transmission through concrete*, **2003**.

[249] **S. Agosteo, A. Fassò, A. Ferrari, P.R. Sala, M. Silari, P. Tabarelli de Fatis**, *Double differential distributions and attenuation in concrete for neutrons produced by 100-400 MeV protons on iron and tissue targets*, Nuclear Instruments and Methods in Physics Research B 114, 70–80, **1996**.

[250] **O. Gencel, A. Bozkurt, E. Kam, T. Korkut**, *Determination and calculation of gamma and neutron shielding characteristics of concretes containing different hematite proportions*, Annals of Nuclear Energy 38, 2719–2723, **2011**.

[251] **I.I. Bashter**, *Calculation of radiation attenuation coefficients for shielding concretes*, Annals of Nuclear Energy 24, 1389–1401, **1997**.

[252] **A. Aminian, M.R. Nematollahi, K. Haddad, S. Mehdizadeh**, Determination of shielding parameters for different types of concretes by Monte Carlo methods, in: Proc. 13th Int. Conf. Emerg. Nucl. Energy Syst. Istanbul, , **2007**.

[253] **Y. Yarar, A. Bayülken**, *Investigation of neutron shielding efficiency and radioactivity of concrete shields containing colemanite*, Journal of Nuclear Materials 212–215, 1720–1723, **1994**.

[254] *Serpentine - Geology.com*, URL: http://geology.com/minerals/serpentine.shtml, **accessed: May 27, 2016**.

[255] **M.H. Kharita, M. Takeyeddin, M. Alnassar, S. Yousef**, *Development of special radiation shielding concretes using natural local materials and evaluation of their shielding characteristics*, Progress in Nuclear Energy 50, 33–36, **2008**.

[256] **W.A. Kansouh**, *Radiation distribution through serpentine concrete using local materials and its application as a reactor biological shield*, Annals of Nuclear Energy 47, 258–263, **2012**.

[257] **R.J. Sheu, Y.F. Chen, U.T. Lin, S.H. Jiang**, *Deep-penetration calculations in concrete and iron for shielding of proton therapy accelerators*, Nuclear Instruments and Methods in Physics Research B 280, 10–17, **2012**.

[258] **A. Brandl, C. Hranitzky, S. Rollet**, *Shielding variation effects for 250 MeV protons on tissue targets*, Radiation protection dosimetry 115, 195–199, **2005**.

[259] **N. Dinar**, Détermination du spectre neutronique autour d'accélérateurs de particules de haute énergie - Master thesis, Université Joseph Fourier, **2014**.

[260] **G.P. Manessi**, Development of advanced radiation monitors for pulsed neutron fields - PhD thesis, University of Liverpool, **2015**.

[261] **E. Aza**, SpectroGEM : A novel neutron spectrometer - PhD thesis, University of Thessaloniki, **2016**.

[262] **M. De Saint-Hubert, C. Saldarragia Vargas, O. Van Hoey, W. Schoonjans, V. De Smet, G. Mathot, et al.**, *Secondary neutron doses in a proton therapy centre,*

Radiation Protection Dosimetry , DOI: 10.1093/rpd/ncv458, *2015*.

[263] **V. De Smet, M. De Saint-Hubert, N. Dinar, G.P. Manessi, E. Aza, C. Cassell, et al.**, *Secondary neutrons inside a proton therapy facility: MCNPX simulations compared to measurements performed with a Bonner Sphere Spectrometer and neutron H*(10) monitors*, in revision for publication in Radiation Measurements *2016*.

[264] **S. Agosteo, R. Bedogni, M. Caresana, N. Charitonidis, M. Chiti, A. Esposito, et al.**, *Characterization of extended range Bonner Sphere Spectrometers in the CERF high-energy broad neutron field at CERN*, Nuclear Instruments and Methods in Physics Research A 694, 55–68, *2012*.

[265] **M. Reginatto, P. Goldhagen**, *MAXED, a computer code for maximum entropy deconvolution of multisphere neutron spectrometer data*, Health physics 77, 579–583, *1999*.

[266] **M. Matzke**, *Unfolding of Pulse Height Spectra: The HEPRO program system, PTB-N-19, Physikalisch-Technische Bundesanstalt*, ISBN: 3894295430, *1994*.

[267] **M. Reginatto, P. Goldhagen, S. Neumann**, *Spectrum unfolding, sensitivity analysis and propagation of uncertainties with the maximum entropy deconvolution code MAXED*, Nuclear Instruments and Methods in Physics Research A 476, 242–246, *2002*.

[268] **M. Reginatto**, *Manual GRAVEL MAXED - UMG33 package*, *2004*.

[269] **C. Pioch, V. Mares, W. Rühm**, *Influence of Bonner sphere response functions above 20 MeV on unfolded neutron spectra and doses*, Radiation Measurements 45, 1263–1267, *2010*.

[270] **W. Rühm, V. Mares, C. Pioch, S. Agosteo, A. Endo, M. Ferrarini, et al.**, *Comparison of Bonner sphere responses calculated by different Monte Carlo codes at energies between 1 MeV and 1 GeV – Potential impact on neutron dosimetry at energies higher than 20 MeV*, Radiation Measurements 67, 24–34, *2014*.

[271] **B. Burgkhardt, G. Fieg, A. Klett, A. Plewnia, B.R.L. Siebert**, *The neutron fluence and H*(10) response of the new LB 6411 remcounter*, Radiation Protection Dosimetry 70, 361–364, *1997*.

[272] **V. Conte, D. Moro, B. Grosswendt, P. Colautti**, *Lineal energy calibration of mini tissue-equivalent gas-proportional counters (TEPC)*, AIP Conf. Proc. 1530, 171–178, *2013*.

[273] **A.J. Waker, Aslam**, *A preliminary study of the performance of a novel design of multi-element tissue equivalent proportional counter for neutron monitoring*, Radiation Measurements 45, 1309–1312, *2010*.

[274] **International Commission on Radiation Units & measurements**, *Quantities and units for use in radiation protection, ICRU Report 33*, *1980*.

[275] **M. Reginatto**, *What can we learn about the spectrum of high-energy stray neutron fields from Bonner sphere measurements?*, Radiation Measurements 44,

692–699, **2009**.

[276] **M. Caresana, M. Silari, M. Helmecke, J. Kubancak, G.P. Manessi, K. Ott, et al.**, *Instrument intercomparison in the high-energy mixed field at the CERN-EU reference field (CERF) facility*, Radiation protection dosimetry 161, 67–72, **2014**.

[277] **G.P. Manessi, E. Aza, M. Caresana, C. Cassell, V. Colombo, S. Damjanovic, et al.**, *Comparison of the performance of different instruments in the stray neutron field around the CERN proton synchrotrons*, Radiation protection dosimetry 161, 190–195, **2014**.

[278] **Y. Watanabe, K. Kosako, S. Kunieda, S. Chiba, R. Fujimoto, H. Harada, et al.**, *Status of JENDL High Energy File*, Journal of the Korean Physical Society 59, 1040–1045, **2011**.

[279] **M.M. Meier, W.B. Amian, D.A. Clark, C.A. Goulding, J.B. McClelland, G.L. Morgan, et al.**, *Differential neutron production cross sections and neutron yields from stopping-length targets for 113-MeV protons - LA-11518-MS*, **1989**.